EFFECTS OF MAGNETIC FIELD MODELS

ON CONTROL OF ELECTROMAGNETIC ACTUATORS

A Dissertation
Presented to
The Academic Faculty

by

Hungsun Son

In Partial Fulfillment
of the Requirements for the Degree
Doctor of Philosophy in the
School of Mechanical Engineering

Georgia Institute of Technology
December 2007

EFFECTS OF MAGNETIC FIELD MODELS

ON CONTROL OF ELECTROMAGNETIC ACTUATORS

Approved by:

Dr. Kok-Meng Lee, Advisor
School of Mechanical Engineering
Georgia Institute of Technology

Dr. Bill Singhose
School of Mechanical Engineering
Georgia Institute of Technology

Dr. Nader Sadegh
School of Mechanical Engineering
Georgia Institute of Technology

Dr. David G. Taylor
School of Electrical and Computer
Engineering
Georgia Institute of Technology

Dr. Eric Johnson
School of Aerospace Engineering
Georgia Institute of Technology

Date Approved: November 01, 2007

To my lovely wife, Juwon Sung
&
my daughter, Erin Son

ACKNOWLEDGEMENTS

Finally, I owe my loving thanks to my wife Juwon Sung, my daughter Erin Son. They have lost a lot due to my study abroad for many years. Without their encouragement and understanding it would have been impossible for me to complete this work. My special gratitude is due to my parents Kyoungsik Son and Meeja Lee, my sisters Youngsin Son and Geumlan Son, my parents in law Sangrye Lee and the late Youngho Sung of blessed memory, my sister and brother in law Yoonkyung Sung and Juhwan Sung for their loving support.

TABLE OF CONTENTS

LIST OF TABLES

LIST OF FIGURES

LIST OF SYMBOLS

Upper case	Descriptions
$\mathbf{B}$	Magnetic flux density
$\hat{B}$	Estimation of magnetic flux density
$\mathbf{C_b}$	Frictional torque constant matrix
E	Objective Error function of DMP method
$\mathbf{E}$	Electric field intensity
$\mathbf{D}$	Displacement current density
$\mathbf{F}$	Magnetic interaction force
$\hat{\mathbf{K}}_j$	Approximated torque constant of the jth EM
$\mathbf{T}$	Magnetic interaction Torque
$\tilde{T}_j$	Torque constant of the jth EM
$\mathbf{H}$	Magnetic flux intensity
$\mathbf{M}$	Magnetization vector
$\mathbf{L}$	Local coordinate transformation matrix
L	Length of orientation PM
I_a, I_t	Moments of inertia about z-axis (spin axis) and x or y-axis
J	Current density
J_e	Effective current density
R	Distance between a source/sink to a point
$\mathbf{W}$	Weighting matrix

Lower case	Descriptions
a	Magnet radius
c_b	Friction coefficient
k_e	Equivalent spring constant
$\mathbf{n}$	Surface normal vector
$\mathbf{q}$	Generalized coordinates

t	Time
t_w	Propagation time of magnetic wave
v	Velocity of grasper
u_j	Input current of the jth EM
$\mathbf{x}_{mi}$	Polarity vector of the ith rotor PM
$\mathbf{x}_{sj}$	Polarity vector of the jth stator EM
$\bar{a}$	Effective magnet radius
ℓ	Magnet length
$\bar{\ell}$	Effective magnet length
m	Strength of a pole
n	Index of pole in a loop
k	Index of loop for DMP
r, θ, ϕ	spherical coordinates

Greek	**Descriptions**
α, β, γ	XYZ Euler angles
$\bar{\alpha}, \bar{\beta}, \gamma$	ZYZ Euler angles
Φ	Magnetic potential
Γ	XYZ rotational coordinate transformation matrix
μ_o	Free space permeability
μ	Permeability
ε	Permittivity
δ	Magnet effective length ratio
ρ	Switching radius of EM
ε_θ	Error constant for θ-direction
ω	Angular velocity
ϖ	Ratio of rotor angular velocity and input frequency

LIST OF ABBREVIATIONS

Abbreviation	Descriptions
3D	Three dimensional
A/D	Analog to digital converter
D/A	Digital to analog converter
DOF	Degree of Freedom
DMP	Distributed Multi-Pole model
EM(s)	Electromagnet(s)
ESL	Equivalent Single Layer
FEM	Finite Element Method
SWM	Spherical Wheel Motor
MM	Moments of Method
MLM	Meshless Method
OL	Open-Loop
PD	Proportional and derivative
PDE	Partial Differential Equation
PM(s)	Permanent magnet(s)
SMB	Spherical magnetic bearing
VRSM	Variable Reluctance Spherical Motor

SUMMARY

Many applications such as automobiles, gyroscopes, machine tools, and transfer systems require orientation control of a rotating shaft. Demands for multi-degree of freedom (DOF) actuators in modern industries have motivated this research to develop a ball-joint-like, brushless, direct-drive spherical wheel motor (SWM) that offers a means to control the orientation of its rotating shaft.

This thesis presents a general method for deriving a closed-form magnetic field solution for precise torque calculation. The method, referred here as distributed multi pole (DMP) modeling, inherits many advantages of the dipole model originally conceptualized in the context of physics, but provides an effective means to account for the shape and magnetization of the physical magnet. The DMP modeling method has been validated by comparing simulated fields and calculated forces against data obtained experimentally and numerically; the comparisons show excellent agreement. The DMP models provide a basis to develop a non-contact magnetic sensor for orientation sensing and control of a rotating shaft. Three controllers have been designed and experimentally implemented for the SWM; open-loop and PD with/without an observer. The OL control system, which decouples the spin from the shaft inclination, provides the fundamental design structure for the SWM and serves as a basis for designing feedback controllers with/without an observer.

While the observer and controller designs have been developed in the context of a spherical wheel motor, these techniques along with the models and analysis tools developed in this research can be applied to design, analysis and control of most

electromagnetic devices. We expect that the analytical method along with the orientation sensor and spherical wheel motor will have broad spectrum of applications.

CHAPTER 1

INTRODUCTION

1.1   MOTIVATION

Many automated processing equipment, machine tools, mobile vehicles such as car wheels [1] [2], propellers for boats, helicopter or underwater vehicle, and gyroscopes require orientation control of a rotating shaft. The growing interests in fuel-cell technology and non-traditional industries (such as agricultural, food-processing, surgical robotics, and manufacturing machinery) along with the widely available high-coercive rare-earth permanent magnets at low cost have motivated researchers to develop application-oriented PM-based actuators capable of multi degrees-of-freedom. Existing designs are typically combined with single-axis devices; orientation control of the rotating shaft must be manipulated by an external mechanism. Since these multi-DOF actuators are generally bulky, slow in dynamic response, and lack dexterity in negotiating the orientation of the rotating shaft, they have difficulties in achieving high speed, precise motion control simultaneously. An alternative to the multi-DOF actuators is a spherical wheel motor (SWM) which is simple, compact in design, and possesses isotropic properties in motion.

Prior research effort of the spherical motor has focused on torque computation, developing non-contact sensors for measuring three-DOF orientation for feedback control. In general, the torque model involves a large number of individual torque component terms, each of which requires computation in the 3D space. Moreover, in analysis, design

1

optimization, and real-time control particularly involving the orientation feedback, both magnetic field information and force/torque models are required. However, these represent a significant computational burden. For these reasons, the primary interest is to have a better understanding of the magnetic field for efficient design and accurate motion control of the SWM. This has led us to develop a new modeling method to derive closed-form solutions.

In this research, a new modeling method referred to here as a distributed multi-pole (DMP) model is developed to characterize electromagnetic fields. The method provides a closed-form solution that is accurate and computationally inexpensive for design optimization and control of magnetic actuating devices. The effectiveness of the DMP method will be illustrated with two useful applications: The first application is a non-contact orientation sensing-mechanism that uses an assembly of Hall-effect sensors to predict the entire magnetic field and torque acting on the orientation of the rotating shaft. The second application is the SWM where the DMP models are used for designing a model-based control system for both open-loop and closed-loop control with a high-gain observer associated with the orientation sensor.

In addition to these developments, the DMP method is further shown to facilitate the development of a non-conventional actuator in diverse engineering industries, which is a permanent magnet (PM) based actuator for controlling the orientation of a live object.

This thesis contributes to the research effort at Georgia Tech through the exploration of new methods for the magnetic field analysis as closed form, torque computation, the orientation sensor and the SWM. The thesis helps the SWM research a step closer to practical industrial applications.

1.2 BACKGROUND

Existing techniques for analyzing electromagnetic fields of a multi-DOF (position and/or orientation) PM-based actuator rely primarily on three approaches; namely, analytic solutions to Laplace's equation, numerical methods and lumped-parameter analyses with some forms of equivalent circuits. Figure 1-1 shows and summarizes features of each method to analyze magnetic fields.
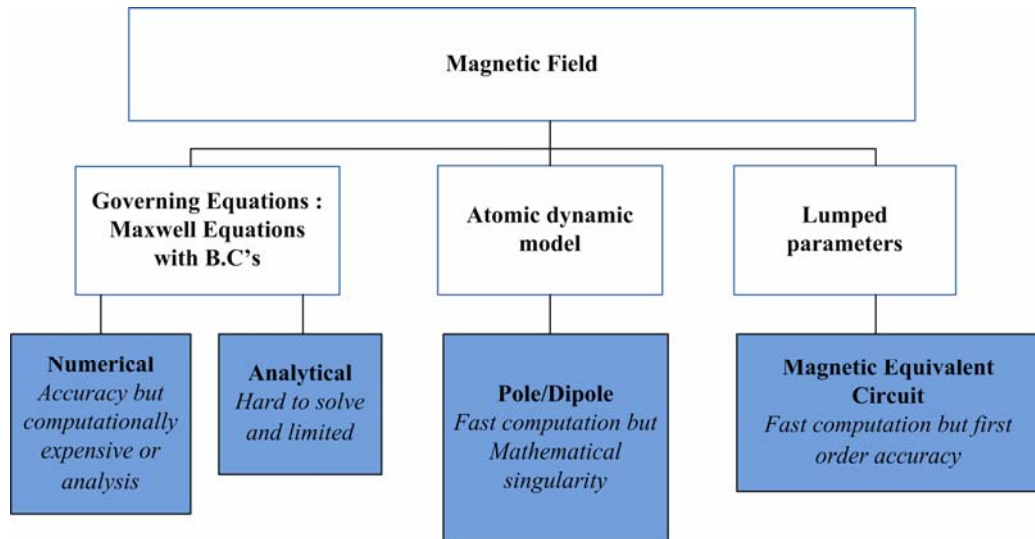
Figure 1-1 Analysis of magnetic field

The possibility of obtaining an analytical solution is often remote for devices with complex geometry. Perturbation theory and linear superposition can sometimes render a difficult problem solvable. However, even if a analytic solution is achievable, it often results in a series of space harmonics of non-elementary functions [3] [4] which have to be computed if a numeric solution to the problem is desired.

Motivated by the ability of high-speed digital computers to make repetitious computation, Harrington [5] originally proposed the concept of matrix methods (also known as the method of moments) as an unified approach to solve for the magnetic field numerically. Commonly used in antenna design and to analyze the magnetic wave propagation [6] [7], the method of moments (MM) assumes dipole moments inside a magnet canceling each other, and thus reduces the governing equation to an integral equation of surface charges. The resulting boundary value problem can then be solved with surface or volume discretization using the method of moments which provides a compact matrix formulation in the magnetic computation. However, computational time tends to grow because of the need of fully populated matrix inversion, and fine discretization for increasing numerical accuracy and stability.

During the last four decades, several other computational methods for solving magnetic field problems including finite element (FE), boundary element (BE), finite difference (FD) and mesh free methods have been very well developed. Such numerical methods offer a good prediction of the magnetic field for accurate computation of the magnetic torque [8] [9]. However, demanding computational time limits these numerical methods to off-line computation. Most of the real-time computations for optimization and motion control of electromagnetic actuators have relied on lumped parameter approaches in order to obtain a closed-form solution which generally yields only first-order accuracy. The previous approaches have difficulties in achieving both accuracy and low computation time simultaneously. These difficulties have motivated several researchers to develop an alternative method to analyze and compute magnetic fields efficiently.

4

A permanent magnet can be characterized by a set of magnetic dipoles shown in Figure 1-2. It shows a magnetized material which can be regarded as consisting of elementary magnetic dipoles. When the dipoles are aligned there is, locally, addition or subtraction of these charges such that the inside dipoles are cancelled each other. It provides a bound surface charge density.

(a)   (b)
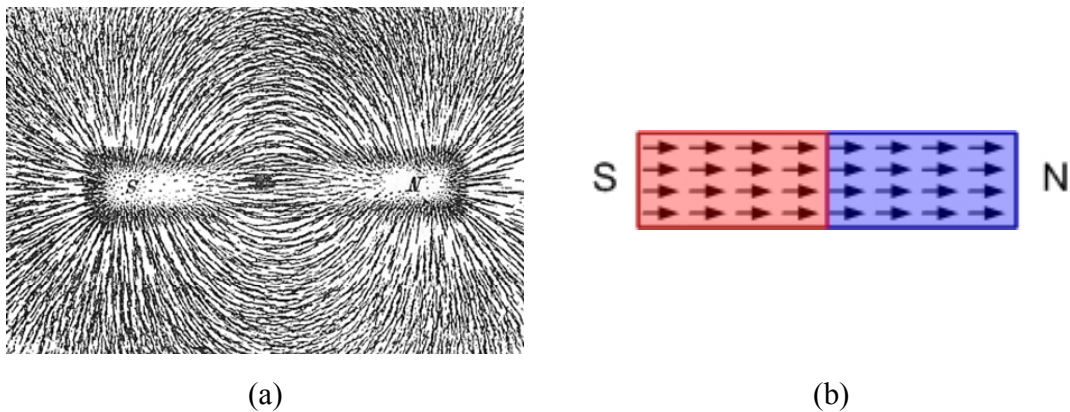
Figure 1-2 (a) Magnetic lines of a bar magnet shown by iron filings on paper [10]
(b) Schematic Magnetic dipoles model

The magnetic flux density in the outside field of the PM mainly depends on the shape of a magnet and the magnetization vector **M** (magnitude and direction) which is the net sum of magnetic dipoles. The magnetic properties of materials, expressed by the magnetization **M**, depend on two main atomistic effects, which can give rise to large and dominant local magnetic fields:

(1) Orbital motion of electrons around the nucleus, which can be seen as current loops of atomistic dimensions or as small magnetic dipole moments

(2) Intrinsic spin of the electrons (or nuclei) with the related magnetic dipole moment.

These two motions can be mathematically described by the source/sink fields and the circular fields. However, the magnetic dipole moment of the PM is mostly determined by (1), which is source and sink elementary fields.

Two models (with the magnetic dipole at the origin of magnet and the single pole at each end of magnet) have been widely used to analyze the magnetic field at a sufficiently large distance for applications such as electromagnetic wave propagation in antenna dynamics and geomagnetism for earth polarization. However, both models generally give a poor approximation when the length scale of the field is very small because

(1) Physical magnetic fields are everywhere finite. However, the end of the source/sink field model results in infinite (singular) density. Hence, errors increase as the air gap becomes smaller.

(2) Magnetic flux density (**B**) is dominantly determined by the shape of a magnet and magnetic dipole strength shown in Figure 1-3. In a hard magnet, the magnetic dipoles are strongly and completely aligned but a soft magnet has misaligned dipoles and thus leakage magnetic field along the side of the magnet. For these reasons, a single pole/dipole cannot describe the shape of a PM with physical dimensions.

Figure 1-3 Comparison of Magnetic flux density distribution with different properties

In this research, we develop a new modeling method to characterize the electromagnetic field referred here as a distributed multi-pole model (DMP). The method formulated here uses a physical modeling of a time-varying magnetic dipole but also satisfies general Maxwell governing equations. For this, the DMP model inherits many advantages of the dipole model originally conceptualized in the context of physics, but provides an effective means to account for the shape and magnetization of the physical magnet which reduces the error of magnetic field computation.

In addition, the DMP method provides a closed-form solution that is accurate and computationally inexpensive for design optimization and control of magnetic actuating devices. The advantage of being able to offer an inexpensive means to visualize the magnetic fields will make the DMP modeling method an attractive alternative to the existing methods (analytic, numerical, and lumped-parameter) for actuator and control system designs. Moreover, the simplicity of the closed-form solutions along with precise (and yet intuitive) magnetic fields of the DMP models have been demonstrated with practical examples of torque modeling and motion control of a multi-DOF actuator such as an orientation sensor and a spherical wheel motor.

1.3   REVIEW OF PRIOR AND RELATED WORKS

The following review of the prior and related publications is organized in three parts. The first part reviews analysis methods of magnetic field using a magnetic dipole and poles. Next, the latest development of multi-degree of freedom actuators is investigated. In the last part, we discuss a nonlinear control technique specially used for an electromagnetic actuator.

1.3.1 Physics-Based Magnetic Field Model

Magnetic dipole was conceptualized by Fitz Gerald in 1883, where a loop of wire with oscillating currents (called as a magnetic dipole antenna) was used to examine Maxwell's theory. In 1925, Uhlenbeck and Goudsmit introduced the concept of a spinning electron in microscopic magnetic field. The idea of a spinning electron with resultant angular momentum gave rise to a magnetic dipole moment.

(a) Dipole model   (b) Pole model   (c) Equivalent coil model
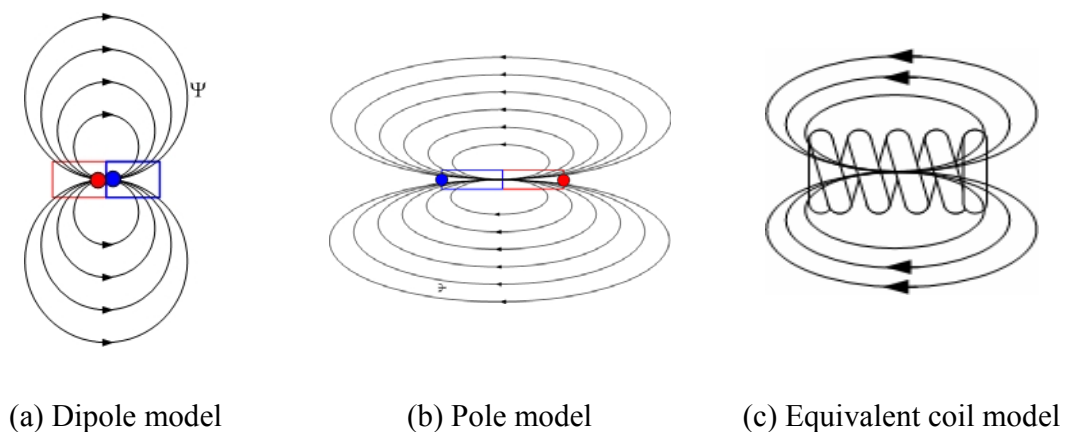
Figure 1-4 Three conventional models for a permanent magnet

From the theoretical atomic view of the origin of magnetism, three models are discussed by Craik and Harrison [10] [11] in connection with calculating the fields produced by uniformly magnetized cylinders; pole model, dipole (doublet) model, and equivalent current model shown in Figure 1-4.

The basic idea of pole and dipole models is that if dipoles are placed end to end in a chain such that opposing poles neutralizes each other, only one north pole and one south pole will remain at the ends of the chain. The same concept arises just as naturally from current loops. Each current loop is regarded as one turn in a long thin solenoid; a long thin solenoid is equivalent to a needle shaped magnet. However, when the length

scale of a computing domain is relatively small, the original pole or dipole models give a crude approximation. Thus, the field of the dipole model has been used to analyze the magnetic field of large scaled systems at a sufficiently large distance such as electromagnetic wave propagation (antenna dynamics) and geomagnetism (earth polarization), etc. However, for reasons including compact formulation and intuitive magnetic fields, many researchers continue to study and further develop the magnetic dipole models for analyzing actuator designs involving permanent magnets. Boyer [11] formulated magnetic forces using a magnetic doublet and equivalent current model. Green [12] used the current doublet theory to model the behavior of oriented permanent magnet materials, where two dimensional (2D) dipoles, quadrupoles and other higher multi-poles were suggested for modeling materials such as rare earth magnets. Also, the image current doublet model was used to deal with the iron boundary. Bennett [13] examined the current element source, its fields, and the origins of the electric and magnetic fields from a physical point of view. Coulomb's and Biot-Savart's laws were extended to include the time-varying point sources in his study.

The magnetic doublet model has been practically applied to the design of a magnetic actuator by several researchers. Nedelcu et al. [14] used the magnetic dipole model to describe the field of a permanent magnet based device, which provides concise computational formulae for the field and the energy flow within the field. However, since the model in [15] assumed that the field is a function of magnet length only, they have difficulty obtaining accurate results of the magnetic flux and force. Visschere [16] later proposed an analytical expression for the magnetic field of a 2D periodic circular array of head-to-head permanent magnets, and compared the analytical result to the dipole model.

9

His study shows how far the dipole approximation can be used for modeling a single permanent magnet.

1.3.2 Multi-Degree of Freedom Spherical Actuator

Spherical motors take a number of forms which include induction [17-19], direct-current (DC) [20-22], stepper [23], variable-reluctance (VR) [24] [25], and ultrasonic [26] motors. The first spherical induction motor was designed by Williams et al. [27]. Vachtsevanos et al. [18] [19] later proposed a three-DOF spherical induction motor for a robotic wrist and presented a detailed analysis of the relationship between the induction motor torque and flux linkages. Although the induction spherical motor generates torques in three dimensional spaces, it is difficult to realize in practice because of its complexity and stator winding design. Foggia et al. [17] designed an induction type motor (motion range of $\pm30°$ with three controllable inductors to create a magnetic field and generate torques on the armature; experimental results showed significant noise and a rather long response time of five seconds. Hollis et al. [21] developed a multi-DOF actuator based on the principle of a direct-current (DC) motor for ±4 mm in translation and ±5 degrees in orientation. A similar DC spherical motor was demonstrated by Kaneko et al. [22]. This motor could spin continuously, and the rotor orientation with a maximum inclination of 15 degrees could be measured by three encoders.

The basic concept of a spherical stepper, which has a relatively simple and compact design, was originally proposed by Lee et al. [23]. The spherical stepper offers a relatively large range of motion $\pm45°$ and possesses isotropic properties in motion. Since the maximum number of poles that can be uniformly placed on a spherical surface is

limited to 20°, Lee [28] extended the design concept of a spherical stepper to that of a variable reluctance spherical motor (VRSM) such that high-resolution motion can be achieved with a relatively small number of rotor and stator poles. Motivated by these research efforts at Georgia Tech, Wang et al. [24] [29] developed a similar spherical actuator with the spherical rotor entirely made of magnetized rare-earth magnets and a coil arrangement capable of two or three DOF motion. In [3], the relation between the hall effect sensors and the analytical results of the magnetic field are introduced to measure the three orientations of the rotor, and the results are used to design the real-time control system. Chirikjian et al. [30] at John Hopkins University designed, constructed and developed a commutation algorithm for the spherical stepper motor. Researchers in Germany [31], in Korea [32], and in Singapore [33] have recently reported and developed a spherical stepper or a VR motor with a PD controller similar in concept to the one proposed by Lee. Although the design could be easily constructed, the motor's range of inclination was limited and the motor torque constant was relatively small.

In addition to the induction, VR, and DC spherical motors just mentioned, ultrasonic spherical motors have been studied by several researchers. Shigeki et al. [26] proposed a spherical motor that uses ultrasonic vibrations of the rotor to generate torque to cause desired motion. Amano et al. [15] developed a 3-DOF ultrasonic actuator with three sets of piezoelectric elements in the stator. Two bending vibrations perpendicular to each other and a longitudinal vibration can be excited independently with three separate electrical ports. The spherical rotor is revolved on all three axes by the combination of these vibrations.

1.3.3 Nonlinear Control Design of Permanent Magnet Devices

Due to nonlinear rotor dynamics, complex magnetic fields and difficult orientation measurement, it is particularly difficult to design control techniques for a spherical motor. However, the operation principle of most existing spherical motors is similar to single-axis counterpart that may have the principle of DC, switched reluctance (SR), or permanent magnet (PM) stepper motors. The controller design technique of a single-axis actuator can be readily extended to multi-DOF spherical motors.

Recently, nonlinear control techniques for these single-axis motors (such as nonlinear observer, feedback linearization, adaptive and robust control, etc.) have been studied by numerous researchers, and the general theories of nonlinear control are also well presented in several books. Thus, the review here focused on a specific aspect of nonlinear control techniques; the design of a nonlinear and a linear high gain observer.

Ueda et al. [34] proposed a new nonlinear observer (extended linear observer) to estimate the transient state of a power system and applied it to a smooth-rotor synchronous generator, which is derived by expanding the system and measurement functions to the first order approximation about the current estimate of the state. Lawrence et al. [35] derived an identity state observer for a permanent-magnet synchronous motor, which reconstructs the electrical and mechanical states of the motor from the current and voltage measurements. The nonlinear observer operates in the rotor frame and estimates stator currents, rotor velocity, and rotor position. Later, the experimental analysis of a closed-loop adaptive velocity control system for a permanent-magnet synchronous motor (PMSM) was presented by Sepe et al. [36] which shows that the real-time observer-based adaptive velocity controller is capable of successful

operation. In [37], Chiasson et al. proposed a nontrivial full-order and reduced-order observer for a PM stepper and validated the results by experiment.

Recently, high-gain observer techniques have played an important role in the design of output feedback control of nonlinear systems. Dabroom et al. [38] proposed the digital control of nonlinear systems using high-gain observers. Closed-loop analysis validated by experimental results shows that the sampled-data controller recovers the performance of the continuous time controller as the sampling frequency and observer gain become sufficiently large. Zhu et al. [39] proposed a linearization-based controller with a nonlinear state observer which estimates the rotor position and speed. Moreover, the stability of the closed-loop system, including the observer, is confirmed through Lyapunov stability theory.

1.4 PHILOSOPHY OF THE SPHERICAL MOTOR

Of particular interest in this thesis is the further development of a spherical motor that has been invented at Georgia Tech. Prior research at Georgia Tech focused on design of mechanical structure and dynamic model by Lee, Pei [40] [41] and Zhou [42], torque characterization using lumped parameter method based on permeance models [23] and numerical method for torque computation [43] [44]. Recently, non-contact vision based sensors [45] [46], FEM and MLM torque analyses in [47] [48] have been investigated to control the orientation of the spherical motor respectively.

The vision based sensor has provided accurate measurement without mechanical contact, which does not affect the rotor dynamics. However, it required the fine grid pattern on the surface of the rotor which determines the measurement resolution and also its measurement speed is relatively low. The high measurement speed is particularly essential to control the motion accurately. Thus, the vision based sensor is not fitting to use the high spinning actuator. Motivated by such contact free sensor, we develop the orientation measurement system using a magnetic sensor. These efforts provide a means to realize the motion feasibility of spherical wheel motor (SWM) which is capable of orientation control of continuously rotating shaft.

Figure 1-5 shows the CAD model of a SWM consisting of 16 rotor PMs and 20 stator EMs equally spaced on four circular planes. The PMs and EMs are grouped in pairs and every two pole-pairs form a plane, and their magnetization axes pass radially through the center.
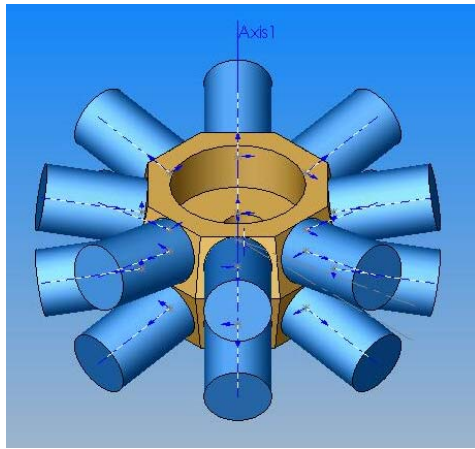
(a) Rotor
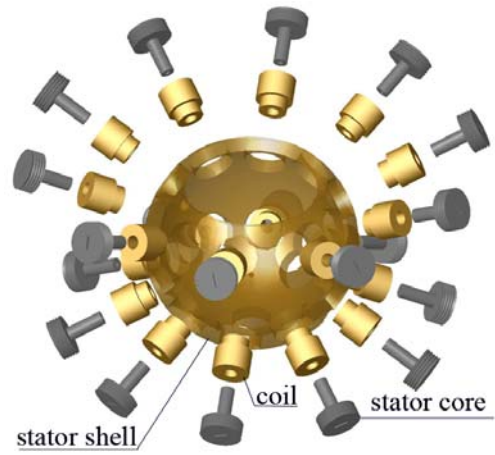
(b) Stator
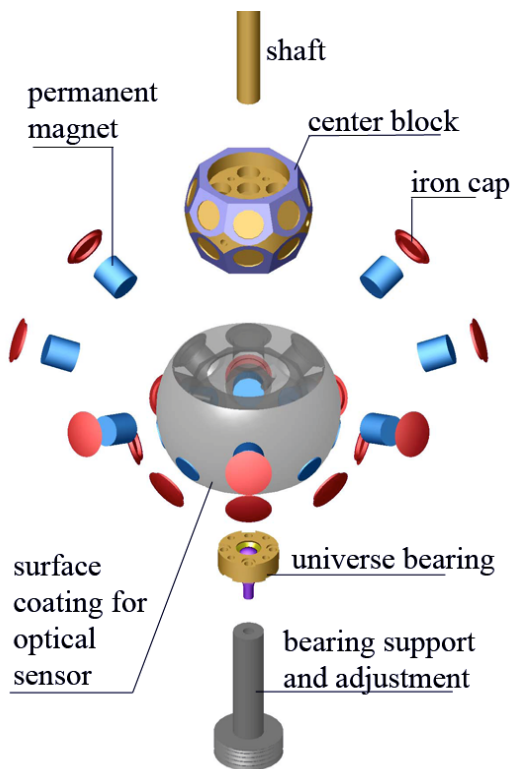
(c) Assemble
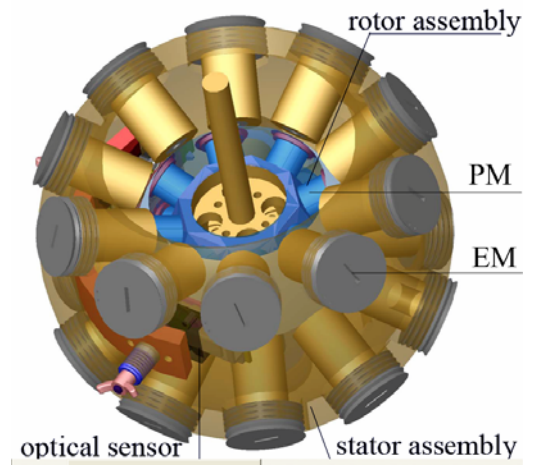
(d) SWM

Figure 1-5 CAD model of SWM [49]

A universal ball bearing supports the rotor weight and allows the rotor to rotate a certain angle uniformly. Since its rotational center is coincident to the center of gravity, the SWM structure has a well-balanced symmetry electro mechanically as shown in Figure 1-6.
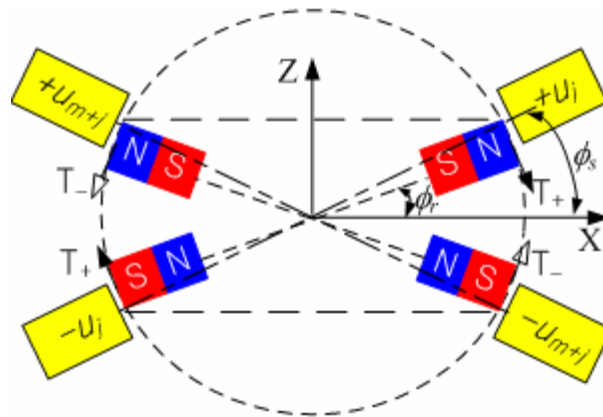
Figure 1-6 Schematics Stator and rotor pole-pairs of a SWM [50]

The rotor orientation is regulated on the principle of push-pull operation as shown in Figure 1-6. A pair of electromagnet (one side of an EM on the top and the other side of an EM under the bottom) is serially connected and thus, it generates the same magnitude of torque at the same plane but the different polarity direction. The inclination from the Z-axis is manipulated using two opposing torques, T_+ and T_-, about the axis normal to the plane that contains the current inputs u_j and u_{m+j} producing the torques. The specific polarities of the EM pole pair's depend on the PM pole pair's layout; $u_j = u_{m+j}$ to maintain the rotor at zero inclination (straight up position). Any perturbation will result in a differential torque **T** driving the rotor back to its equilibrium. This operation based on the push-pull principle can be employed to control the orientation of rotating shaft.

1.5   RESEARCH OBJECTIVES

This thesis reseach has three objectives:

The first is to develop an analytical method to characterize the magnetic field of a permanent magnet and/or an electromagnet for the design and control of electromechanical actuators.

This new method referred to here as DMP model provides a closed-form formulation of the magnetic field of an electromagnetic system consisting of permanent magnets and electromagnets. This method effectively facilitates the design analysis of an electromagnetic actuator and dynamic performance. For validation, the DMP models are compared against known solutions whenever possible obtained numerically and experimentally. In addition, a practical non-contact PM based actuator to control an orientation of a live object is demonstrated to validate the DMP model and accentuate the usefulness of the method.

The second is to develop an orientation sensor using a magnetic sensor such as Hall Effect sensor, which can predict the motion in 3D space with high accuracy but without mechanical contact.

We apply the DMP modeling method in developing an orientation sensor based on Hall Effect sensor information to predict the magnetic field, torque, and orientation of the rotating shaft. To achieve these, the DMP model should be explicitly expressed in terms of the orientation parameters and then inversely solved in the real time. Two approaches (an absolute and an incremental method) have been developed to perform in

real time applications. The absolute method uses a closed polynomial function to estimate the magnetic field to measure the orientation. The absolute method is independent of the sampling time and less sensitive to environment conditions (sensing noises), which are often critical to real time applications. The incremental method uses a Jacobian of the magnetic field in terms of the orientation. The orientation measurement is updated for every sampling period. Since the current orientation is updated from the previous orientation, the faster sampling time is one of primary parameters which affect the performance.

An apparatus with a PM is simulated to demonstrate the sensing mechanism and validate its performance. The method is finally applied to measure the orientation and design the control system of the SWM.

The third is to develop a model based open loop and closed loop control systems based on the orientation sensor of the spherical wheel motor.

This thesis extends the developments of a multi-DOF actuator developed at the Georgia Institute of Technology. Unlike previous designs which focused on controlling the orientation/displacement of a rotor, the spherical wheel motor (SWM) developed in this research offers to control the orientation of a rotating shaft. Based on the DMP model and the orientation sensor, a new model based controller and estimator system is developed for the real-time control design. The controller is expected to have better performance in controlling the rotor orientation of the SWM with smaller control effort compared with the prior control system.

1.6   OUTLINE AND ORGANIZATION OF THESIS

The remainder of the dissertation is outlined as follows.

Chapter 2 begins with a review of the fundamental magnetic field theory related to the concept of magnetic charge (pole and dipole). Then, the DMP method is developed to improve the existing models. In the DMP method, the analytical model as a closed form solution for iron free magnetic field is obtained. Then, image method is applied to handle magnetic conducting boundary conditions in the magnetic field.

Chapter 3 presents illustrative examples to validate and demonstrate the DMP model. Cylindrical permanent magnets and electromagnets are considered for illustration because of not only their simplicity but also popular interest for design of an electromagnetic actuator. Moreover, some analytical solutions and/or experimental results are available for model validation. Thus, they are used in this chapter to illustrate the DMP modeling procedure and also validate the results of the DMP method. Once the DMP method of the cylindrical PM is validated, the method is further extended to characterize a customized shape PM. Finally, two experimental setups are introduced to validate the DMP method in practice. The first one is for the magnetic field and force computation and the second is applications of magnetic actuator for the automation of live object transportation to show a practical application of the DMP model.

Chapter 4 describes a sensing methodology to determine an orientation/position of an object with a set of permanent magnets and electromagnets. The novelty behind the method fully exploits the DMP method to characterize the magnetic field distributions by a source and utilizes them for determining the object orientation/position. More than three-axis sensing of *quasi-static* magnetic fields provides information sufficient to

determine both the position and the orientation of the sensor relative to magnetic sources. However, the orientation must be determined in the real time. Despite the completeness and simplicity of the DMP method, the closed-form field solutions include nonlinear unknown parameters. Thus, a special approach must be applied to approximate the measurable magnetic field distribution for designing the absolute and the incremental sensing method. The simulation results of them are presented to show the feasibility and feature of each method.

In the Chapter 5, the dynamic model of the SWM is formulated to provide an understanding of the operation principle of the SWM presented in Chapter 1. Then, control system designs for the SWM are presented. First, we demonstrate an effective method to decouple the open-loop (OL) control of the spin rate from that of the inclination, leading to a practical OL system combining a switching (spin-rate) controller and a model-based inclination controller based the principle of push-pull operation. The OL system presented here provides the fundamental control structure for the SWM. Furthermore, we extend the design to allow feedback with a PD controller and a high-gain observer to account for un-modeled external torques.

In the Chapter 6, experimental results of both the orientation sensor and control system are compared against the simulation results in Chapter 5. Hall-effect sensors for measuring orientation are calibrated using the computed magnetic field of the DMP method. Then, each controller system developed in Chapter 5 is applied to control the orientation with and without the rotating shaft.

Finally, Chapter 7 summarized the conclusions of this thesis and recommendations for future research on the DMP model and its applications are addressed.

CHAPTER 2

MAGNETIC FIELD ANALYSIS

2.1   OVERVIEW

Design for electromagnetic actuators involves force and torque computation, which requires a good understanding of magnetic flux density distribution. In this chapter, a new modeling method based on a pole/dipole model is developed, which provides a closed form solution to describe the magnetic flux density of a set of PMs.

The remainder of this chapter is organized as follows:

1. Magnetic fields of a PM or an EM in the 2D and 3D space are reviewed to understand a concept of magnetic poles and dipoles, which provide a basis to analyze more complex magnetic field.

2. We develop a relatively complete formulation for deriving the closed-form solution to characterize the magnetic field around a PM. The method uses a limited set of known field points to construct a distributed multi-pole (DMP) model for the magnet.

3. We extend the DMP modeling method of a PM to a multi-layered electromagnet (EM). In the development, the concept of an equivalent single layer (ESL) model and an equivalent PM model is introduced, which significantly reduces computational efforts to analyze force and torque of an electromagnetic device by the Lorentz force formulation and Maxwell stress tensor respectively. In addition, the equivalent PM model also helps to visualize the interacting magnetic fields between a PM and an EM effectively.

4. To allow for material boundary conditions of magnetic field, we introduce image method and extend the DMP method involving magnetic conducting materials.

2.2   GENERAL FORMULATION OF MAGNETIC FIELD

2.2.1   Governing equation of magnetic field

The thesis begins with analyzing magnetic fields based on the following assumptions:

(1)   The property of a magnet is isotropic and linear.
(2)   The medium in the region of magnetic field is homogenous.
(3)   The induced magnetic field in one magnet exerted by another magnet is negligible.
(4)   Magnetization vector is uniformly distributed in a permanent magnet.

From (1), the magnetic flux at every point in the field is continuous and irrotational which concludes that

$$\nabla \bullet \mathbf{B} = 0 \tag{2.1}$$

$$\nabla \times \mathbf{H} = 0 \tag{2.2}$$

where $\mathbf{B}$ is the magnetic flux density and $\mathbf{H}$ is the magnetic field intensity.

Equation (2.2) is mathematically equal to the gradient of a scalar functions Φ.

$$\mathbf{H} = -\nabla\Phi \tag{2.3}$$

In addition, permeability μ is independent of field intensity as a constant based on (2) and (3), which result in linear relation:

$$\mathbf{B} = \mu\mathbf{H} \tag{2.4}$$

Equation (2.1) is combined with Equations (2.3) and (2.4) which becomes Laplace's equation:

$$\nabla^2 \Phi = 0 \qquad\qquad (2.5)$$

where Φ is the scalar magnetic potential expressed in amperes.

General magnetic field in current (electric charge) free region is reduced to Laplace's equation which is the time invariant by the Maxwell's differential laws. The equation is a second order liner partial differential equation (PDE). The fact that it is linear is particularly important, because the sum of any particular solutions of a linear differential equation is also a solution of the equation. Since the continuous and irrotational magnetic field is governed by Laplace's equation and thus, a complicated field pattern for a magnetic field can be synthesized by adding together a number of elementary fields which are also satisfying irrotational and continuous conditions expressed in Equations (2.1) and (2.2). A series of the elementary fields are suggested in different ways such that the resulting field can be expressed by adding them. Among the solutions of Laplace's equation in Equation (2.5), the 3D source and sink models shown in Figure 2-1 are given by

$$H_r = \frac{\pm m}{4\pi\left((x-x_1)^2 + (y-y_1)^2 + (z-z_1)^2\right)} \qquad\qquad (2.6)$$

where m is a constant of magnetic dipole strength; + and - indicate source and sink respectively.

For a PM, m can be assumed as a constant but for an EM, m is varying with the time t. Thus, the general expression [12] for source or sink field can be expressed in

$$H_r = \frac{\pm 1}{4\pi r^2}\left[m(t-r/c) + \frac{r}{c}\frac{\partial m(t-r/c)}{\partial t}\right] \qquad\qquad (2.7)$$

where c is the speed of light.
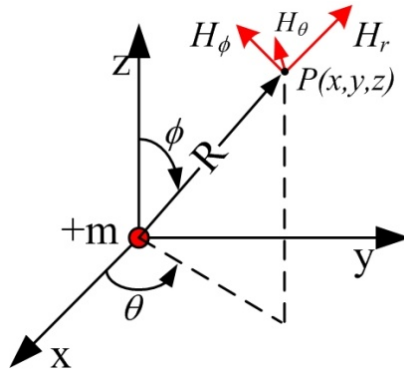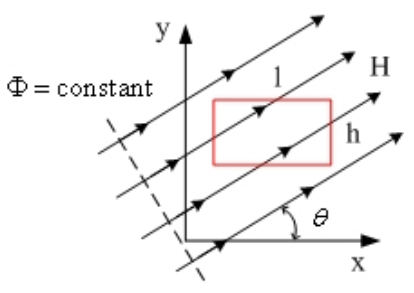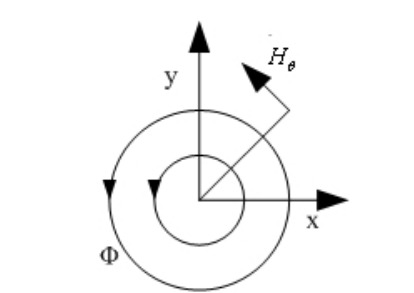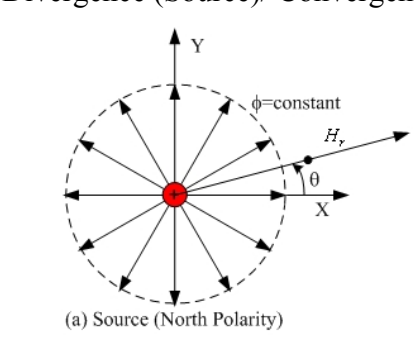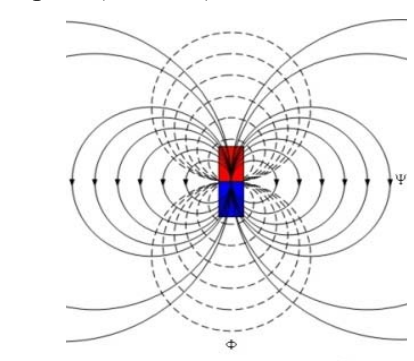
Figure 2-1 Divergence (Source)/ Convergence (Sink) field

However, the rate of change with time t in Equation (2.7) is sufficiently low as to be treated as invariant for practical purposes particularly in the design and control of PM based actuators and thus the second term $r/c = t_w \ll T$ can be assumed and $r/c = t_w$ can be neglected, where t_w physically indicates the time of magnetic wave propagation and T is the sampling time of computation. Thus, the magnetic dipole moment m in Equation (2.7) of the time varying field can be simply substituted to $m(t)$, which is implied the field as '*quasi-static*'.

In addition, other forms of elementary magnetic field models satisfying Equation (2.5) are detailed in Table 2-1.

Table 2-1 Elementary magnetic field models

Uniform field	
	$\dfrac{\partial \Phi}{\partial x} = H_x = H\cos\theta$, $\dfrac{\partial \Phi}{\partial y} = H_y = H\sin\theta (= \text{constant})$ $\Phi = -\left[\left(H\cos\theta\right)x + \left(H\sin\theta\right)y\right]$
Circular field	
	$H_r = 0$ and $H_\theta = c/r$ $\Phi = -\dfrac{I}{2\pi}\theta$
Divergence (Source)/ Convergence (Sink) field	
 (a) Source (North Polarity)	$H_r = \dfrac{c}{r}$ and $H_\theta = 0$ $\Phi = -\dfrac{m}{2\pi}\ln r = -\dfrac{m}{2\pi}\ln\sqrt{x^2 + y^2}$
Dipole (Doublet) field	
	$\Phi = -\dfrac{\kappa}{2\pi}\dfrac{\cos\theta}{r}$ where κ is constant defined as the strength of the doublet. $\dfrac{\partial \Phi}{\partial r} = H_r = \dfrac{\kappa\cos\theta}{2\pi r^2}$ and $\dfrac{1}{r}\dfrac{\partial \Phi}{\partial \theta} = H_\theta = -\dfrac{\kappa\sin\theta}{2\pi r^2}$

2.2.2 Magnetic force and torque computation

The magnetic force in *quasi-static* magnetic fields can be computed by the following two methods: Lorentz force equation or Maxwell stress tensor. Lorentz force equation is commonly used to calculate the magnetic force exerted on current-carrying conductors. Since the current vector directly used in the known field (generally generated by PM), it is not necessary to compute the magnetic flux generated by the current loop as follows:

$$\mathbf{F} = -\oint \mathbf{B} \times Id\mathbf{L} \tag{2.8}$$

where
$$I = \oiint \mathbf{J} \cdot d\mathbf{S} \, ;$$

where $\mathbf{L}$ is normalized current direction vector.

Alternatively, the magnetic force can be derived using the principle of virtual displacement:

$$\mathbf{F} = \nabla W_m \tag{2.9}$$

where
$$W_m = \frac{1}{2} \int_V \mathbf{H} \bullet \mathbf{B} dv'$$

where the volume V is taken to be sufficiently large to contain the magnetic field of an interesting object. Equation (2.9) is similarly written in terms of Maxwell stress tensor.

$$\mathbf{F} = \oint_\Gamma \mathbf{T} d\Gamma \tag{2.10}$$

where
$$\mathbf{T} = \frac{1}{\mu_0} \left(\mathbf{B}(\mathbf{B} \bullet \mathbf{n}) - \frac{1}{2} B^2 \mathbf{n} \right);$$

27

where Γ is an arbitrary boundary enclosing the body of interest; and **n** is the normal vector of the boundary surface. Equation (2.10) computes the force on the given **B** field. Once **B** is known, the force on a body can be computed from the surface integration.

2.2.3   Boundary Conditions

At the interface between two regions, the following two boundary conditions must be satisfied:

Condition I: Normal component of **B** is continuous across the boundary

$$\mathbf{B}_1 \bullet \mathbf{n} = \mathbf{B}_2 \bullet \mathbf{n} \tag{2.11}$$

Condition II: Tangential component of **H** is continuous along the boundary

$$\left(\mathbf{H}_1 - \mathbf{H}_2 \right) \times \mathbf{n} = 0 \tag{2.12}$$

where subscripts "1" and "2" denote the regions between the boundary respectively.

2.3   DISTRIBUTED MULTI-POLE MODEL

The existing methods which utilize the source and sink or dipole model to characterize the magnetic field have intrinsic disadvantages. They have mathematical singularities at the point of source/sink, and also cannot account for the shape of a PM or an EM. However, the approaches with their formulations are still very attractive not only because they provide an understanding of magnetic field but also the solution can be written in a closed-form solution reducing the computation of the 3D magnetic field. In this section, we introduce the distributed multi-pole (DMP) model [51] to characterize the magnetic field of a PM from a limited set of known field points. The magnetic field in this research satisfies the assumptions: the field is continuous and irrotational; and the

medium is homogeneous, and linear without saturation. Historically, ferromagnetic cores were commonly used in electromagnetic actuators. The widely available high-coercive rare-earth permanent magnets at low cost have begun to change that usage, and air-cored electromagnets are now commonly seen in iron-less motors. For this reason, we focus initially on examples without any magnetic conducting boundary. However, the DMP method can be extended to account for the effects of magnetic conducting boundary by incorporating image method [52] [53].

We define a dipole here as a pair of source and sink separated by a distance $\bar{\ell}$. A general DMP model of a permanent magnet with k loops (or columns) of n dipoles can be derived as follows. The potential $\Phi(x,y,z)$ at any point P(x,y,z) contributed by all the dipoles (in terms of the ith dipole in the jth loop) is thus given by

$$\Phi = \sum_{j=0}^{k}\sum_{i=0}^{n} m_{ji}\varphi_{ji} = \underline{\varphi}^{\mathrm{T}}\underline{m} \tag{2.13}$$

where $\underline{\varphi}^{\mathrm{T}} = \left[\left(\varphi_{00}\cdots\varphi_{0n}\right) \quad \left(\varphi_{10}\cdots\varphi_{1n}\right) \quad \left(\cdots\right) \quad \left(\varphi_{k0}\cdots\varphi_{kn}\right)\right]$;

$\underline{m} = \left[\left(m_{00}\cdots m_{0n}\right) \quad \left(m_{10}\cdots m_{1n}\right) \quad \left(\cdots\right) \quad \left(m_{k0}\cdots m_{kn}\right)\right]^{\mathrm{T}}$;

$\varphi_{ji} = \left[\left(1/R_{ji+}\right)-\left(1/R_{ji-}\right)\right]/\left(4\pi\right)$; and

where R_{ji+} and R_{ji-} expressed in terms of distance $\bar{\ell}$ are the distances from the source and sink to the point P respectively; and m_{ji} is the strength of the ji^{th} dipole.

Similarly, since $\nabla\left(1/R\right) = -\mathbf{a}_{R}(1/R^2)$ where $\mathbf{a}_{R} = \mathbf{R}/R$, the magnetic flux density at P can be found from Equations (2.3) and (2.13):

$$\mathbf{B} = \sum_{j=0}^{k}\sum_{i=0}^{n} m_{ji}\boldsymbol{\beta}_{ji} = \underline{\boldsymbol{\beta}}^{\mathrm{T}}\underline{m} \tag{2.14}$$

where $\underline{\boldsymbol{\beta}}^{\mathrm{T}} = \left[\left(\boldsymbol{\beta}_{00} \cdots \boldsymbol{\beta}_{0n} \right) \quad \left(\boldsymbol{\beta}_{10} \cdots \boldsymbol{\beta}_{1n} \right) \quad \left(\cdots \right) \quad \left(\boldsymbol{\beta}_{k0} \cdots \boldsymbol{\beta}_{kn} \right) \right]$;

and $\boldsymbol{\beta}_{ji} = -\dfrac{\mu_o}{4\pi} \left(\dfrac{\mathbf{a}_{Rji+}}{R_{ji+}^2} - \dfrac{\mathbf{a}_{Rji-}}{R_{ji-}^2} \right)$. Note that Equations (2.13) and (2.14) are in matrix form.

For a DMP model that has a single dipole along the magnetization axis,

$$\varphi_{j0} = \varphi_{0i} = \begin{cases} 0 & i, j \neq 0 \\ \varphi_0 & i = j = 0 \end{cases}$$

$$\text{and} \quad \beta_{j0} = \beta_{0i} = \begin{cases} 0 & i, j \neq 0 \\ \beta_0 & i = j = 0 \end{cases}$$

The unknown parameters in Equations (2.13) and (2.14) are k, n, $\overline{\ell}$ and m_{ji}.

For the purpose of deriving closed-form solutions to facilitate the design and control of PM-based devices, we seek the field solution outside the physical region of the magnet, particularly near its boundary. The problem is to find an appropriate distribution of dipoles to best approximate the field solution. To solve for the unknowns (k, n, $\overline{\ell}$ and m_{ji}), we minimize the error function given in Equation (2.15) subject to constraints imposed by the magnet geometry and a limited set of known field solutions (as fitting points):

$$E = \int_z \left[\Phi(z) - \Phi_A(z) \right]^2 dz \tag{2.15}$$

where $\Phi_A(z)$ is a known solution derived analytically, or curve-fit from solved numerical solutions or measured experimental data along the magnetization axis (say, the z-axis). The general expression of the magnetic scalar potential Φ_A created at $\mathbf{R}'(x', y', z')$ to the field point R(x, y z) is given by

$$\Phi_A = \frac{1}{4\pi} \int_V \frac{-\nabla \bullet \mathbf{M}}{|\mathbf{R} - \mathbf{R}'|} dV + \frac{1}{4\pi} \int_S \frac{\mathbf{M} \bullet \mathbf{n}}{|\mathbf{R} - \mathbf{R}'|} dS \tag{2.16}$$

where $\mathbf{n}$ is the unit surface normal. The first integral in Equation (2.16) is a volume integral over the body volume V, while the second one is a surface integral over the body boundary surface S. The corresponding magnetic flux density can also be found using Equation (2.3).

The constraints are formed from a set of specified points. For example, if the residual magnetic flux density of the magnet is specified at the surface across the magnetization axis (say at $z=z_o$), it can be used as a constraint:

$$B(z_o) = B_A(z_o) = -\mu_o \nabla \Phi_A \big|_{z=z_o} \tag{2.17}$$

which can be expressed in terms of the dipoles using Equation (2.14). Since Equation (2.13) accounts for the potential field along the magnetization axis, the $(k \times n + 1)$ constraints include Equation (2.15) and the potential along two other orthogonal directions from Equation (2.16):

$$\begin{bmatrix} \underline{\beta}_0^T \big|_{z=z_o} \\ \underline{\varphi}_1^T \\ \vdots \\ \underline{\varphi}_{(k \times n)}^T \end{bmatrix} \underline{m} = \begin{pmatrix} B_A(z_o) \\ \Phi_{A1} \\ \vdots \\ \Phi_{A(k \times n)} \end{pmatrix} \tag{2.18}$$

In Equation (2.18), the subscript "0" denotes that the dipole is at the center of surface along the magnetization vector. If the known fields are in terms of the measured magnetic flux density, Equation (2.14) instead of Equation (2.13) can be used to obtain Equation (2.18). For PM-based actuator applications, the $\mathbf{B}$ and Φ values in Equation (2.18) are

evaluated at an appropriate magnet surface. To avoid the singularity at the surface of a magnet $\mathbf{R} = \mathbf{R}'$, we choose

$$|\mathbf{R}| = \lim_{\varepsilon_R \to 0} \left(\left| \mathbf{R}' \right|_{\substack{\text{point} \\ \text{at surface}}} + \varepsilon_R \right)$$

(2.19)

where ε_R is a small positive number.

Three specific cases are worthy of mentioning:

1. If the relative permeability of the magnet is very large, the magnet surface can be approximated as equal potential, and Φ_A in Equation (2.16) is a constant.

2. If $\mathbf{M}$ is a constant implying $\nabla \bullet \mathbf{M} = 0$, the volume integral in Equation (2.16) is zero and the potential field can be computed from the surface integral in Equation (2.16).

3. If the magnet is axis-symmetric, the magnetic field is uniform in a particular direction (say θ). To minimize the field variation in the θ direction when modeling with a finite number of dipoles, the following constraint can be imposed:

$$\left. \frac{Max\left[\Phi(\theta)\right] - Mean\left[\Phi(\theta)\right]}{Mean\left[\Phi(\theta)\right]} \right|_{\text{at the edge}} \times 100\% \leq \varepsilon_\theta$$

(2.20)

where ε_θ is a specified (positive) error bound.

The procedure of the DMP method for a PM is summarized as follows:

Step 1: Compute Φ_A and B_A analytically along the magnetization vector from Equations (2.16) and (2.3) respectively

Step 2: Generate an initial set of spatial grid points (k, n).

Step 3: Formulate (2.18) from Equations (2.13) and (2.14) in terms of the unknowns, $\overline{\ell}$ and m_{ji}.

Step 4: Find $\overline{\ell}$ and m_{ji} by minimizing the objective function in Equation (2.15) subject to the constraint Equation (2.18). Error computed by Equation (2.15) is saved.

Step 5: Check the condition Equation (2.20). If Equation (2.20) is not satisfied, increase k or n, and repeat from Step 3. Once Equation (2.20) is met, the optimal parameters (k, n, $\overline{\ell}$ and m_{ji}) can be obtained by minimizing Equation (2.15) using Step 4.

2.4   EQUIVALENT ELECTROMAGNET

Magnetic forces exerted on current-carry conductors in a magnetic field are often calculated by the use of Lorentz force equation, which does not involve the magnetic flux generated by the current loop as the current density vector is directly used in the calculation. However, the 3D integral of the Lorentz force equation must account for each of the current-carrying conductors. For devices such as a spherical motor where a large number of coils (with multi layers of wires in each) are used, the field and force calculations are often very time-consuming for real time applications.

In this section, we introduce an alternative method, which is able to characterize the magnetic field of a multilayer (ML) coil by the DMP model by treating it as a PM. The process begins with finding an equivalent single-layer (ESL) model. The ESL model greatly reduces computation of magnetic forces, while the DMP model offers a means to visualize the interacting magnetic fields between a PM and an EM. Once the magnetic

fields of both the permanent magnets and voice coils are obtained in closed form, they can be computed in real-time for motion estimation.

2.4.1 Equivalent Single Layer Model

We derive here the effective radius and field density for the ESL coil and the effective magnetization of the equivalent PM to closely approximate the original ML coil.

For a thin wire with cross-section area S, the magnetic field density caused by the current I flowing along the wire can be determined by the Biot-Savart law.

$$\mathbf{B}_s = \oint d\mathbf{B}_s \tag{2.21}$$

where
$$d\mathbf{B}_s = \frac{\mu_o I}{4\pi} \frac{d\mathbf{s} \times \mathbf{e}_R}{\left|\mathbf{R} - \mathbf{R}'\right|^2} ;$$

where ds is an elemental length vector of the wire; $\mathbf{e}_R$ is the unit vector from the source point $\mathbf{R}'$ to the field point $\mathbf{R}$; $I = \oint_S J dS$; J is the current density; and μ_0 is free space permeability.

As mentioned previously, the Lorentz force exerted on the current-carry conductor due to the magnetic flux density $\mathbf{B}$ can be calculated using Equation (2.8) where the integral must account for each of the current-carrying conductors. The effective method to reduce computation time is to replace the multilayer (ML) coil with an equivalent single-layer (ESL) model. In general, the ESL model retains the shape of the original ML coil but with only one layer of wires. The process involves finding an effective radius a_e and current density J_e. The unknown parameters are chosen such that the errors of the magnetic flux along the centroidal axis are minimized, and that the same

34

magnetic flux density is generated at the end surface of the core. As will be shown, the field and force calculations of the ESL model do not increase with the number of turns.

Without loss of generality, we illustrate the modeling method with concentric coils as shown in Figure 2-2, where some analytical solutions are available for model validation. However, the method can be extended to coils of other customized shape.

(a) Cross sectional view   (b) Magnetic flux on the wire
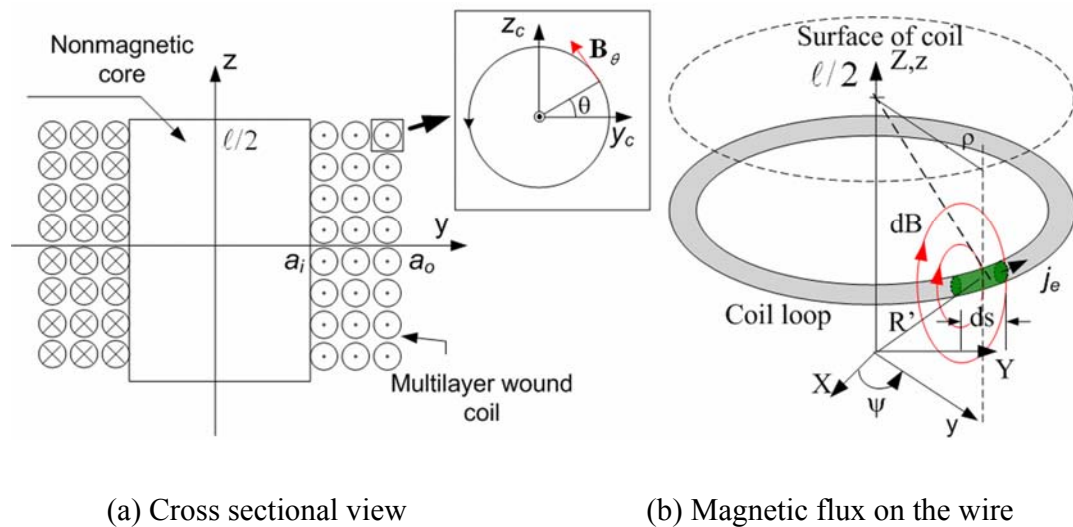
Figure 2-2 Multilayer EM coil

Consider a typical multilayer (axi-symmetrical) coil with a current density J, the sectional view of which is shown in Figure 2-2 (a). The current flowing in the wire towards the $+x$-axis generates a circular magnetic flux. As a result, the cumulative magnetic fluxes reverse its direction from $y=0$ to the location $a_i<y<a_o$. The radial location (where the flux reverses its direction) is called the switching radius ρ and is a function of z. The magnetic flux density of the multilayer coil can be closely approximated from that of the single layer coil with the effective radius a_e where the single wound coil is placed at the switching radius ρ on the surface of coil.

To find the effective radius, we consider the 2D magnetic flux density as shown in Figure 2-2 (a). For a single wire,

$$\mathbf{B}(y',z') = \frac{\mu_0}{2\pi r}\left(\mathbf{I}\times\mathbf{e}_r\right) \tag{2.22}$$

where $\qquad\qquad \mathbf{I}=I\mathbf{e}_x \text{ and } I=\displaystyle\int_S JdS$

The total magnetic flux densities at any point (distance vector **R)** can be calculated by integrating over the current-carrying conductor. For the original *ML* coil (with inner and outer radii, a_i and a_o, respectively)

$$\mathbf{B}_{ML}(y,z) = \frac{\mu_0 J}{2\pi}\int_{-\ell/2}^{\ell/2}\left(\int_{a_i}^{a_o}\frac{\mathbf{e}_\theta}{|\mathbf{R}-\mathbf{R'}|} + \int_{-a_i}^{-a_o}\frac{\mathbf{e}_\theta}{|\mathbf{R}-\mathbf{R'}|}\right)dy'dz' \tag{2.23}$$

where $\mathbf{e}_\theta = -\sin\theta\mathbf{e}_y + \cos\theta\mathbf{e}_z$ and $|\mathbf{R}-\mathbf{R'}| = \sqrt{(y-y')^2 + (z-z')^2}$.

Similarly, for a single layer coil,

$$\mathbf{B}_{SL}(y,z) = \frac{\mu_0 J_e d_w}{2\pi}\int_{-\ell/2}^{\ell/2}\frac{\mathbf{e}_{\theta+}}{|\mathbf{R}-\mathbf{R'}_+|} + \frac{\mathbf{e}_{\theta-}}{|\mathbf{R}-\mathbf{R'}_-|}dz' \tag{2.24}$$

where $|\mathbf{R}-\mathbf{R'}_\pm| = \sqrt{(y\mp a_e)^2 + (z-z')^2}$.

As the magnetic flux is dominant and symmetry along the centroidal axis (assumed *z*-axis), the unknown parameters (J_e and a_e) are determined to satisfy two conditions:

Condition I: Minimize the difference between the two models defined by:

$$E_y = \int_0^\infty |B_{Mz}(y,z) - B_{Sz}(y,z)|_{z=\ell/2}\, dy \tag{2.25}$$

where $B_{Mz}(y,z) = \mathbf{B}_{ML}(y,z)\bullet\mathbf{e}_z$ and $B_{Sz}(y,z) = \mathbf{B}_{SL}(y,z)\bullet\mathbf{e}_z$.

Note that $\cos\theta = (y-y')/|\mathbf{R}-\mathbf{R'}|$, we have

$$\frac{B_{Mz}(y,\ell/2)}{\mu_0 J\ell/(2\pi)} = \frac{1}{2}\ln\left[\left(\frac{1+\chi_{i-}^2}{1+\chi_{o-}^2}\right)\left(\frac{1+\chi_{i+}^2}{1+\chi_{o+}^2}\right)\right] + \chi_{i-}\vartheta_{i-} - \chi_{o-}\vartheta_{o-} + \chi_{i+}\vartheta_{i+} - \chi_{o+}\vartheta_{o+} \tag{2.26}$$

$$\frac{B_{Sz}(y,\ell/2)}{\mu_0 J\ell/(2\pi)} = -\frac{J_e d_w}{J\ell}\left(\cot^{-1}\chi_{e-} + \cot^{-1}\chi_{e+}\right) \tag{2.27}$$

where $\chi_{\pm} = (a\pm y)/\ell$; $\vartheta = \cot^{-1}\chi$; and the subscripts *i, o,* and *e* denote inner, outer and effective radius respectively.

Condition II: The effective current density J_e is determined such that

$$B_{ML}(0,\pm\ell/2) = B_{SL}(0,\pm\ell/2)$$

$$J_e d_w = \frac{J\ell}{\cot^{-1}(\chi_e)}\left[\chi_o\cot^{-1}\chi_o - \chi_i\cot^{-1}\chi_i - \frac{1}{2}\ln\left(\frac{1+\chi_i^2}{1+\chi_o^2}\right)\right] \tag{2.28}$$

where $\chi_i = a_i/\ell$; $\chi_o = a_o/\ell$ and $\chi_e = a_e/\ell$.

The unknown parameters (a_e and J_e) can be solved simultaneously from Equations (2.27) and (2.28). For an axi-symmetrical coil, a 2D model as shown in Figure 2-2 (a) is sufficient for deriving the unknown parameters of the ESL model. However, the 3D magnetic flux density is needed for field calculation, which can be obtained by applying the Biot-Savart law in Equation (2.21). For the original ML coil,

$$\mathbf{B}_{ML} = -\frac{\mu_0 J}{4\pi}\left[\int_{-\ell/2}^{\ell/2}\int_{a_i}^{a_o}\int_0^{2\pi}\frac{[\mathbf{R}-\mathbf{R}']\times rd\boldsymbol{\theta}}{|\mathbf{R}-\mathbf{R}'|^3}\mathbf{e}_\psi drdz'\right] \tag{2.29}$$

where $|R-R'| = (x-r\cos\theta)^2 + (y-r\sin\theta)^2 + (z-z')^2$;

$\mathbf{e}_\psi = -\sin\psi\,\mathbf{e}_y + \cos\psi\,\mathbf{e}_k$; and $\psi = \cos^{-1}\left(\sqrt{(x-r\cos\theta)^2 + (y-r\sin\theta)^2}/|\mathbf{R}-\mathbf{R}'|\right)$.

In Equation (2.29), the negative sign is due to the cross product in the coordinate system of Figure 2-2 (b). Similarly, once a_e and J_e are found the 3D magnetic flux density can be derived from the equivalent single layer (ESL) model:

$$\mathbf{B}_{SL} = \frac{-\mu_o J_e d_w}{2\pi} \left[\int_{-\ell/2}^{\ell/2} \int_0^{2\pi} \frac{[\mathbf{R} - \mathbf{R}'] \times a_e d\boldsymbol{\theta}}{|\mathbf{R} - \mathbf{R}'|^3} \mathbf{e}_\psi \, dz' \right] \tag{2.30}$$

2.4.2 Equivalent PM Model

The ESL model significantly reduces the computation time of the Lorentz force; however, the magnetic flux density must be integrated numerically. For real-time applications, it is desired to have the magnetic field solutions in closed form; this can be achieved by modeling the coil as an equivalent permanent magnet (PM) with an effective radius a_e, length ℓ, and an effective magnetization vector $\mathbf{M}_e = M_o \mathbf{e_z}$, the magnetic field solutions of which can then be presented in closed form using the DMP model. The effective magnetization vector $\mathbf{M}_e$ is determined to satisfy the following condition:

$$B_{Pz} = \mathbf{B}(0, 0, \ell/2) \cdot \mathbf{e}_z \tag{2.31}$$

where $\mathbf{B}(0, 0, \ell/2)$ is the magnetic field of the original coil.

The corresponding magnetic flux density can be derived from the constitutive relation in Equations (2.3) and (2.4). For a cylindrical PM, magnetic flux along the centroidal axis is given by

$$B_{Pz} = 0.5 \mu_o M_o \left[1 + \left(a_e / \ell \right)^2 \right]^{-1/2} \tag{2.32}$$

The magnitude of the effective magnetization vector can then be obtained by Equations (2.17), (2.31) and (2.32):

$$\mu_o M_o = 2\sqrt{1 + \left(a_e / \ell\right)^2}\, \mathbf{B}(0,0,\ell/2)\boldsymbol{\cdot}\mathbf{e}_z \tag{2.33}$$

where $\mathbf{B}(0,0,\ell/2)$ can be computed from either Equations (2.29) or (2.30).

General procedure for the steps of finding the DMP model for an EM is as follows:

Step 1: Find the specific geometry a_e and J_e of the equivalent single-layer EM in terms of the geometry of the coil and the current density J and formulate Equation (2.25).

Step 2: Calculate the effective radius a_e that satisfies its effective current density J_e from Equation (2.28).

Step 3: Model the EM as a PM that has the same geometry as the single-layer EM, the effective magnetization M is found using Equations (2.32) and (2.33).

Step 4: The DMP model of the multilayer EM can then be derived using the procedure given in the previous section.

Note that the 2D models in Equations (2.22) and (2.23) can be used in Steps 1 and 2 to simplify calculations for an axis-symmetrical EM. In addition, the 3D model in Equation (2.33) is validated to be equivalent to the magnetization $\mathbf{M}$ in Equation (2.23). Due to the symmetry, the tangential component of the flux along the centroidal axis is cancelled out automatically.

2.5   IMAGE METHOD

The DMP and ESL methods characterize the magnetic field of a PM or an EM in free space. When the magnetic field is involving a magnetic conducting material, the field of the PM or EM interacts with the material. The change of the field results in the

consequent change of the magnetic force and torque. To account for these effects, we introduce the image method.

The image method replaces the effects of a boundary or interface on an applied field by adding or subtracting elementary fields behind the boundary line called image. Provided image charges for the magnetic material boundary, the resultant field distribution with the material boundary can be expressed as the sum of the applied and the image fields. To compute the magnetic field with a boundary, each region of the boundary on the given field requires different images but one side of images leads to the other. Since the field distribution for the two regions are connected by the boundary condition, the solutions in each region can be achieved at once. In addition, the method provides certain solution forms for some important problems involving straight-line, circular and spherical boundaries in a simple manner which decrease the need for formal solutions of Laplace's and Poisson's equations

In this section, a novel approach combining the DMP method and the image method is discussed.

2.5.1 Formulation of Boundary Conditions

Figure 2-3 shows an arbitrary shape of boundary in the magnetic field. A region 1 with permeability μ_1 is separated from a region 2 with permeability μ_2 by the boundary. Supposed that H_n is the normal component of the applied magnetic field in the region 1. If the different material with permeability μ_2 is presented in the original region with μ_1, the magnetic flux is discontinuous at the boundary due to the surface current.

The effect of the surface current at the boundary can be accounted for by a normal component of field $\bar{H}_n$ and considered to act in the same direction as H_n in region 1 and the opposite direction in the region 2.
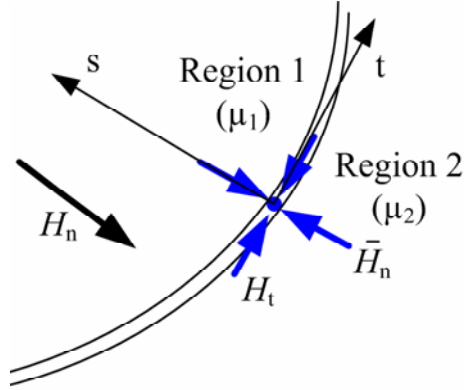
Figure 2-3 Magnetic flux with a material boundary

Thus, the resultant normal field at a point on the boundary is $H_n + \bar{H}_n$ in region 1 and $H_n - \bar{H}_n$ in region 2. The net field strength of the entire space with region 1 with source and 2 without source remain the same as the open space with a source region 1.

Since the normal component of flux is continuous across the boundary in Equation (2.11), it is necessary that

$$\mu_1\left(H_n + \bar{H}_n\right) = \mu_2\left(H_n - \bar{H}_n\right) \tag{2.34}$$

or

$$\bar{H}_n = \left(\frac{\mu_2 - \mu_1}{\mu_2 + \mu_1}\right)H_n \tag{2.35}$$

Hence, the net normal component of field H_{1n} at the interface of the region 1 is given by

$$H_{1n} = H_n + \bar{H}_n = \left(\frac{2\mu_2}{\mu_2 + \mu_1}\right)H_n \tag{2.36}$$

Similarly, H_{2n} at the interface of the region 2 is given by

$$H_{2n} = H_n - \bar{H}_n = \left(\frac{2\mu_1}{\mu_2 + \mu_1} \right) H_n \qquad (2.37)$$

From Equations (2.35) to (2.37), the net normal component of the field intensity at the interface of regions 1 and 2 is given in non-dimensional forms by

$$\left. \frac{H_{n1}}{H_n} \right|_{s=0} = \frac{2}{1+\rho} \quad \text{and} \quad \left. \frac{H_{n2}}{H_n} \right|_{s=0} = \frac{2\rho}{1+\rho} \qquad (2.38)$$

where $\rho = \mu_1 / \mu_2$; s denote the coordinate system shown in Figure 2-3.

From Equation (2.12), the tangential component of the magnetic field at the boundary can also be obtained as follows:

$$H_{1t} + \bar{H}_t = H_{2t} + \bar{H}_t \qquad (2.39)$$

Once the field **H** along the boundary is found, the scalar potential function can be inversely computed from Equation (2.3). Since the field in the region of interest should not include image charges, the general expression of the potential can be given by

$$\Phi_i = \Phi_u - \bar{\Phi}_i \qquad (2.40)$$

where the subscript "i" denotes the region of interest (normally $i=1,2$ between the boundary); the subscript "u" denotes the solution without the plane boundary.

In particular, the scalar potential in Equation (2.40) can be assumed as a constant if the boundary is the magnetic conducting material which the permeability μ is large. This characteristic can be shown as an illustrative example in the next section. In addition, it can be useful to account for the spherical magnetic conducting boundary in the three dimension space.

2.5.2 Plane Boundary

To illustrate the image method, we consider here a single source with a plane boundary shown in Figure 2-4. Since the DMP method satisfies superposition principle for the solution of Laplacian field, the single source model can be extended to the DMP model without loss of generality. In addition, the plane boundary provides the fundamental understanding of the image method and thus the results of this can be also extended to solve more complicated shape of boundaries by various combinations and conformal transformation.
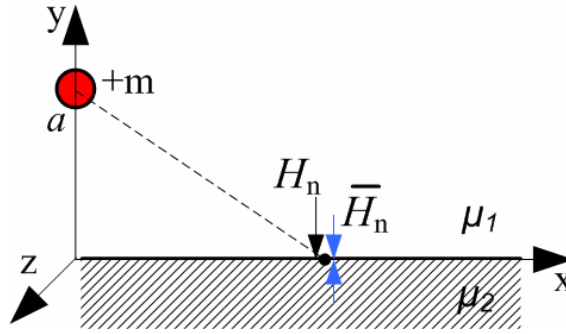
Figure 2-4 Source with plane boundary

From Equation (2.6), the net normal and tangent components of **H** at the interface of the regions 1 and 2 due to the source at the boundary point **P**(*x, 0, z*) are given by:

$$H_n(x,y,z) = \frac{\mp |m|(Y-1)}{4\pi a^2} \left[X^2 + (Y-1)^2 + Z^2 \right]^{-3/2} \tag{2.41}$$

$$H_t(x,y,z) = \frac{\mp |m| X}{4\pi a^2} \left[X^2 + (Y-1)^2 + Z^2 \right]^{-3/2} \tag{2.42}$$

where $X = x/a$; $Y = y/a$; and $Z = z/a$. Due to the effect of the induced surface charge at the boundary, the normal component $\bar{H}_n$ along the boundary is given by substation

from Equation (2.41) into Equation (2.35). In addition, the solution of each region is uniquely determined in such a way that the strength of the original source in the region 1 does not change by the boundary and also the region 2 does not have the source. Thus, the solution of each region can be explained by an equivalent image pole (source or sink) with $-m\left[(1-\rho)/(1+\rho)\right]$ as shown in Figure 2-5. The scalar potential Φ for each region can be given by summing the applied and image poles from Equation (2.40) as follows:

$$\frac{\Phi_1}{\Phi_u}=1-\frac{\overline{\Phi}\left(x,y+a,z\right)}{\Phi_u} \quad\text{and}\quad \frac{\Phi_2}{\Phi_u}=1-\frac{\overline{\Phi}\left(x,y-a,z\right)}{\Phi_u} \tag{2.43}$$
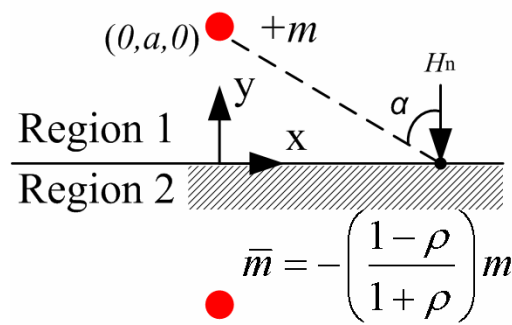
(a) Image source for region 1
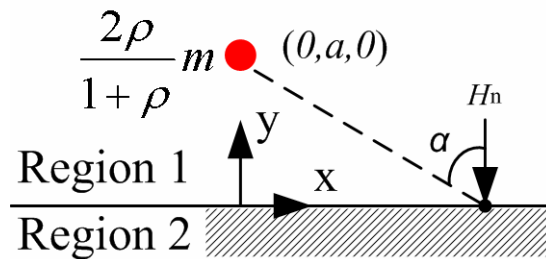
(b) Image source for region 2

Figure 2-5 Equivalent charge in each region

Finally, the field of each region can be summarized as follows:

For $Y \geq 0$

$$\frac{\Phi}{\Phi_u} = 1 - \left(\frac{1-\rho}{1+\rho}\right) S; \tag{2.44}$$

$$\frac{H_n}{H_{nu}} = 1 - \left(\frac{1-\rho}{1+\rho}\right)\left(\frac{Y+1}{Y-1}\right) S^3 \text{ where } Y \neq 1 \tag{2.45}$$

and

$$\frac{H_t}{H_{tu}} = 1 - \left(\frac{1-\rho}{1+\rho}\right) S^3 \tag{2.46}$$

For $Y < 0$

$$\frac{\Phi}{\Phi_u} = \frac{H_n}{H_{nu}} = \frac{H_t}{H_{tu}} = \frac{2\rho}{1+\rho} \tag{2.47}$$

where $S = \sqrt{\left[X^2 + (Y-1)^2 + Z^2\right] / \left[X^2 + (Y+1)^2 + Z^2\right]}$.

The solutions in Equations (2.45), (2.46) and (2.47), guarantee the two boundary conditions of Equations (2.11) and (2.12) at $Y=0$ (which leads to $S=1$):

$$B_{n1} = H_n \left(\frac{2\mu_1}{1+\rho}\right); \text{ and } B_{n2} = H_n \left(\frac{2\mu_2 \rho}{1+\rho}\right)$$

$$H_{t1} = H_{t2} = H_n \left(\frac{2\rho}{1+\rho}\right)$$

Some observations from Equation (2.44) to Equation (2.47) can be drawn.

1. If the boundary plane is highly magnetic conducting such that $\rho = \mu_2 / \mu_1 \to 0$, then B_{n1} is twice greater than the original strength of B_n ($=\mu_1 H_n$). In addition, the tangential component of **H** becomes $H_{t1} = H_{t2} \to 0$. This indicates the normal component of the magnetic flux is dominant along the boundary so that the magnetic flux is perpendicular to the surface boundary.

2. If the boundary plane were removed, and instead an image sink was placed a distance h behind the now missing conducting plane, then a vanishing potential can be found

at midway between the applied source and the image sink. Reinserting the conducting surface along this plane would make no difference as the potential already satisfies the boundary condition ($\Phi=0$ on a conductor).

Although the applied source *m* induces a nonzero source distribution on the conducting boundary in order to maintain a zero potential, the potential arising from this distribution is mimicked exactly by the image sink *-m* behind the boundary.

2.5.3   Spherical Boundary

Many engineering problems with PMs or EMs are often required to solve the three dimensional (3D) magnetic field including magnetic conducting interface. However, the 3D analysis is relatively difficult to solve using the previous method by which the magnetic field (**H**) was directly obtained. One of alternatives is using the scalar potential function since the surface of high conducting boundary can be assumed to be the equal potential. Based on this, it is possible to compute the modeling parameters of image charges inversely. We consider here a spherical boundary of a magnetic conducting material since it is commonly used for a spherical actuator illustrated later.

Without loss of generality, the surface assigned to the constant potential of the boundary can be expressed by

$$\Phi = 0 \tag{2.48}$$

Consider the magnetic source inside a magnetic conduction sphere as shown in Figure 2-6. Due to the symmetry of the sphere, it can be reduced to plane view in the *yz* plane.
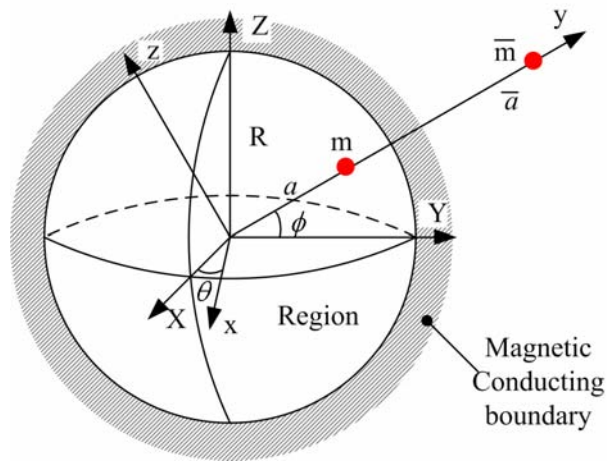
Figure 2-6 Image charge of Spherical boundary

Hence, the magnetic charge m at P(0, $b\cos\phi$, $b\sin\phi$) can be expressed in the *xyz* local frame and the potential on the spherical surface is given by

$$\Phi = -\frac{1}{4\pi}\left(\frac{m}{\sqrt{a^2 + R^2 - 2aR\cos\phi}} + \frac{\overline{m}}{\sqrt{\overline{a}^2 + R^2 - 2\overline{a}R\cos\phi}}\right) \quad (2.49)$$

To satisfy Equation (2.48), Equation (2.49) can be expressed by

$$m\sqrt{(\overline{a}^2 + R^2 - 2\overline{a}R\cos\phi)} + \overline{m}\sqrt{(a^2 + R^2 - 2aR\cos\phi)} = 0 \quad (2.50)$$

$$m^2(\overline{a}^2 + R^2 - 2\overline{a}R\cos\phi) = \overline{m}^2(a^2 + R^2 - 2aR\cos\phi)$$

Since Equation (2.50) must be independent of the ϕ coordinate, Equation (2.50) can be divided by two parts as follows:

$$m^2(\overline{a}^2 + R^2) = \overline{m}^2(a^2 + R^2) \quad (2.51)$$

and
$$\overline{a}m^2 = a\overline{m}^2 \quad (2.52)$$

Equation (2.52) is substituted into Equation (2.51). It gives unknown parameter h by.

$$(a\overline{a} - R^2)(\overline{a} - a) = 0$$

$$\overline{a} = R^2/a \quad \text{or} \quad \overline{a} = a \quad (2.53)$$

where $h = R^2 / b$ can be chosen since the image charge should be outside of the sphere.

From Equation (2.53), the strength of the image charge $\bar{m}$ can be given by

$$\bar{m} = -\frac{R}{a} m \tag{2.54}$$

Given the parameters in Equations (2.53) and (2.54), the scalar potential function inside circle can be expressed as follow:

For $0 \le r \le R$ region:

$$\Phi = -\frac{m}{4\pi} \left(\frac{1}{\sqrt{x^2 + (y-a)^2 + z^2}} - \frac{R/a}{\sqrt{x^2 + (y-(R^2/a))^2 + z^2}} \right) \tag{2.55}$$

Since an electromagnetic actuator generally consists of rotor, magnet and stator, three practical cases shown in Figure 2-7 are considered here to illustrate the combination of the DMP and image method.

(a) Iron rotor

(b) Iron stator   (c) Combination of both iron rotor and stator
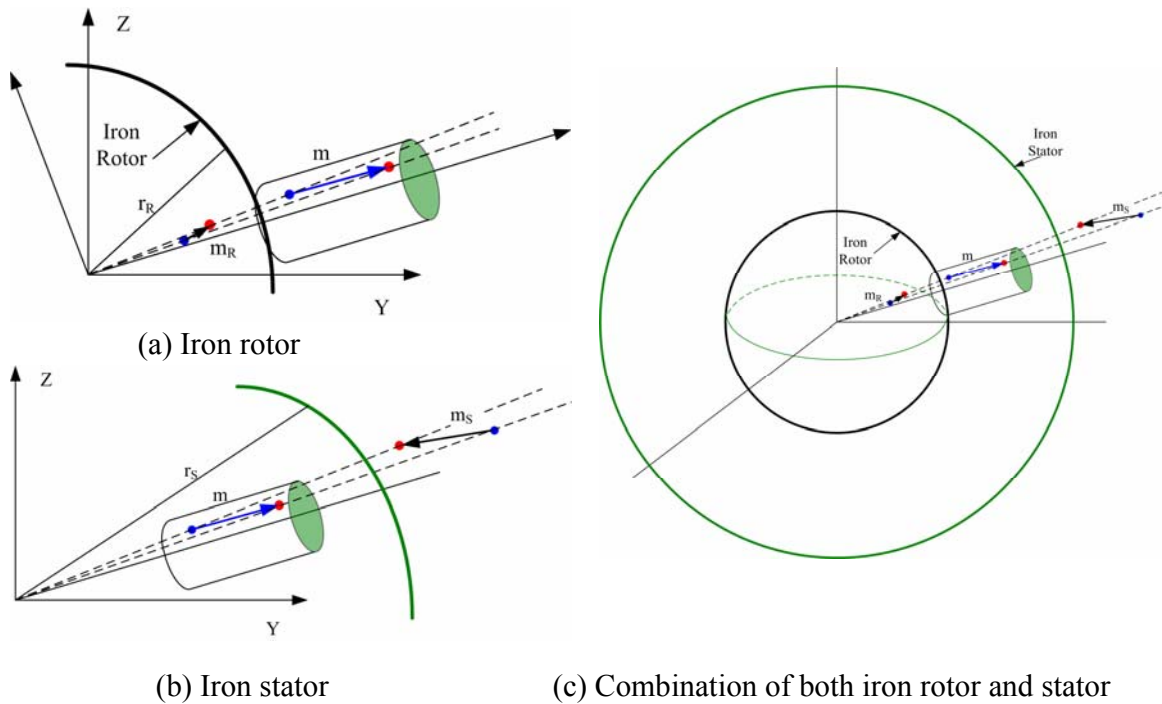
Figure 2-7 Spherical boundary of image method with DMP method

Case 1: Magnet is outside the conducting sphere (iron rotor)

Case 2: Magnet is inside the conducting sphere shell (iron stator shell)

Case 3: Combination of both iron rotor (Case 1) and stator (Case 2)

Case 1 considers a pair of the DMP model for a permanent magnet with the strength m and rotor boundary of a radius r_R in Figure 2-7 (a). In Equation (2.6), the position of each source/sink (x_1, y_1, z_1) can be expressed in the spherical coordinate as follows:

$$\begin{bmatrix} x_1 \\ y_1 \\ z_1 \end{bmatrix} = r_1 \begin{bmatrix} \cos\theta_1 \cos\phi_1 \\ \sin\theta_1 \cos\phi_1 \\ \sin\phi_1 \end{bmatrix} \tag{2.56}$$

where $r_1 = \sqrt{x^2 + y^2 + z^2}$; $\theta_1 = \tan^{-1}(y_1/x_1)$; $\phi_1 = \cos^{-1}(z_1/r)$

Since the image charge is along the line of the applied charge vector with the different distance r, the position of the image charge can be expressed in terms of the ratio of lengths Λ_R from Equation (2.53) and unit vector of the applied charge from Equation (2.56).

$$\begin{bmatrix} \overline{x}_1 \\ \overline{y}_1 \\ \overline{z}_1 \end{bmatrix}_R = \Lambda_R r_R \begin{bmatrix} \cos\theta_1 \cos\phi_1 \\ \sin\theta_1 \cos\phi_1 \\ \sin\phi_1 \end{bmatrix} \tag{2.57}$$

where $\Lambda_R = r_R/r_1$; r_R is the radius of the rotor (subscript R indicates the rotor).

From Equation (2.54), the strength of the image charge is also given in terms of Λ_R by

$$\overline{m}_R = -\frac{m}{\Lambda_R} \tag{2.58}$$

In Case 2, the image charge of the stator boundary with the outer radius r_S in Figure 2-7 (b) can be expressed in terms of the ratio $\Lambda_S = r_S/r_1$ as follows:

$$\begin{bmatrix} \bar{x}_1 \\ \bar{y}_1 \\ \bar{z}_1 \end{bmatrix}_S = \Lambda_S r_S \begin{bmatrix} \cos\theta_1 \sin\phi_1 \\ \sin\theta_1 \sin\phi_1 \\ \cos\phi_1 \end{bmatrix} \quad (2.59)$$

$$\bar{m}_S = -\Lambda_S m \quad (2.60)$$

where the subscript "S" indicates the stator.

Case 3 includes both the iron rotor and stator. Since the strength and position of image charge of each case are found, Case 3 can be obtained using the principle of superposition of the solution in Cases 1 and 2.

The potential functions including each boundary can be expressed as summing each potential function of image charges. Thus, the image method associated with the DMP model also provides the closed-form solutions about the three dimensional magnetic field with magnetic conducting boundaries.

2.6 SUMMARY

A general DMP modeling method which derives a closed–form solution for calculating the magnetic field of a permanent magnet or an electromagnet has been presented. This method, which extends the concept of a magnetic doublet beyond the context of physics, provides an effective means to account for the shape and magnetization (soft or hard magnet) of the physical magnet.

In the process of obtaining a DMP model for a multilayer electromagnet, we derive an equivalent single-layer model that significantly reduces the computational effort for calculating the magnetic force and torque. In addition, the advantage of being able to offer an inexpensive means to visualize the magnetic fields will make the DMP

modeling method an attractive alternative to the existing methods such as analytic, numerical, and lumped-parameter methods for actuator design.

Once the magnetic field is computed by the DMP method, the image method is applied to handle magnetic conducting material interfaces and the diverse shapes of the boundaries. As a first step, we recalled the image method with the plane boundary to illustrate the principle of image method. Then, the method is extended to the three dimensional spherical boundary to characterize a spherical wheel motor.

With the simplicity but accuracy of the method, the method can be used not only for the design of the material of the SWM but also the modeling of dynamics and controller system. Practical examples with model validation will be given in next chapter.

CHAPTER 3

VALIDATAION OF DMP MODEL

3.1   OVERVIEW

In many engineering applications, cylindrical permanent magnets and electromagnets are commonly used for design of an electromagnetic actuator, and also some analytical solutions and/or experimental results are available for model validation due to their simplicity [51]. Thus, they are used in this chapter along with a customized shaped PM to illustrate the DMP modeling procedure and validate the DMP method.

The remainder of this chapter is organized as follows:

1. We formulate the DMP models in dimensionless forms to facilitate practitioners in the design procedure of developing a DMP model. The illustration of the method begins with a cylindrical PM and a customized PM. The models are validated by comparing simulated fields against known solutions whenever possible, and/or published numerical and experimental results.

2. Three different methods for calculating magnetic forces using DMP models are compared, which provide a basis for evaluating the equivalent single layer and equivalent PM models. The first and second methods calculate the Lorentz force exerted on the current-carrying conductors using the original multilayer EM and its equivalent single-layer EM respectively. The third method treats the EM as a PM and uses Maxwell stress tensor to obtain the total force acting on the given field.

3. We demonstrate the use of DMP models to study the effect of different pole-shapes on the magnetic fields and forces of electrometrical systems. Three examples are demonstrated to validate the image method along with the DMP method.

3.2 DMP MODEL OF PERMANENT MAGNET

3.2.1 Cylindrical permanent magnet

Consider a cylindrical magnet (radius a, length ℓ and $\mathbf{M} = M_o\mathbf{e}_z$) as shown in Figure 3-1. The potential and flux density field solutions along the z-axis are given in

$$\frac{\Phi_A(Z)}{M_o\ell} = \frac{1}{4}\left[\left(A_- - |B_-|\right) - \left(A_+ - |B_+|\right)\right] \tag{3.1}$$

$$\frac{B_A(Z)}{\mu_o M_o} = \frac{1}{2}\left[\frac{|B_+|}{A_+} - \frac{|B_-|}{A_-} + c\right] \text{where } c = \begin{cases} 0 & \text{if } |Z| \geq 1 \\ 2 & \text{if } |Z| < 1 \end{cases} \tag{3.2}$$

where $Z = 2z/\ell$; $\gamma = 2a/\ell$; $A_\pm = \sqrt{\gamma^2 + B_\pm^2}$ and $|B_\pm| = |Z \pm 1|$.
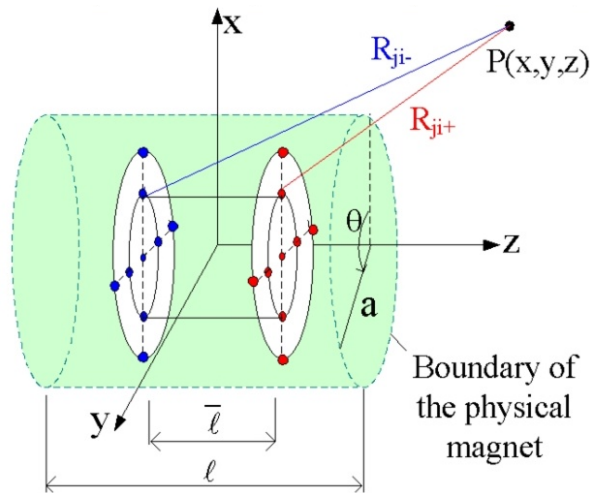
Figure 3-1 DMP model of a cylindrical magnet

We model the PM using k circular loops of n dipoles parallel to the magnetization vector as shown in Figure 3-1. The loops (each with radius $\overline{a}_j$) are uniformly spaced:

$$\overline{a}_j = aj/(k+1) \text{ at } z = \pm\overline{\ell}/2 \ (0 \le j \le k); \text{ and } 0 < \overline{\ell} < \ell \tag{3.3}$$

For the cylindrical magnet, the field is uniform circumferentially and hence $m_{ji}=m_j$. To minimize the field variation in the θ direction, we impose on n the constraint in Equation (2.20) evaluated at $r=a$ and $z = \ell/2$. The unknowns ($\overline{\ell}$, m_j, n and k) are solved by minimizing Equation (2.15) with Φ_A and Φ given by Equations (2.16) and (2.13) respectively subject to the constraints imposed by Equations (2.17), (2.18) and (2.20). For the DMP model shown in Figure 3-1,

$$R^2_{ji\pm} = \left[x-\overline{a}_j\cos i\theta_n\right]^2 + \left[y-\overline{a}_j\sin i\theta_n\right]^2 + \left(z\mp\overline{\ell}/2\right)^2 \tag{3.4}$$

$$\frac{\mathbf{a}_{Rji\pm}}{R^2_{ji\pm}} = \frac{\left(x-\overline{a}_j\cos i\theta_n\right)\mathbf{a}_x + \left(y-\overline{a}_j\sin i\theta_n\right)\mathbf{a}_y + \left(z\mp\overline{\ell}/2\right)\mathbf{a}_z}{\left[\left(x-\overline{a}_j\cos i\theta_n\right)^2 + \left(y-\overline{a}_j\sin i\theta_n\right)^2 + \left(z\mp\overline{\ell}/2\right)^2\right]^{3/2}} \tag{3.5}$$

where $i\theta_n$ indicates the angular position of the ith dipole on the jth loop and $\theta_n = 2\pi/n$.

To provide some insight and clarity in illustration, we derive and compare the following two cases; one for the single dipole and the other for the DMP model with $k=1$ and $n=4$.

Case A: Single dipole model

The simplest approximation is to model the field with a single dipole at $x = y = 0$, which can be derived from Equation (2.16),

$$\frac{\Phi(Z)}{(m/\ell)} = \frac{1}{2\pi}\left(\frac{1}{|Z-\delta|} - \frac{1}{|Z+\delta|}\right) \tag{3.6}$$

and
$$\frac{\mathbf{B}(Z)}{\mu_o m/\ell^2} = \frac{4\delta Z}{\pi\left(Z^2 - \delta^2\right)^2}\mathbf{a}_z \tag{3.7}$$

where $\delta = \overline{\ell}/\ell$. However, as shown in Equations (3.6) and (3.7) the single dipole model cannot account for the shape of the PM (or more specifically, the large aspect ratio γ of the cylindrical PM).

Case B: DMP model (*n*=4)

To account for the shape,

$$\frac{\Phi(Z)}{m_0/\ell} = \sum_{j=1}^{k}\frac{2m_j}{\pi m_0}\left(\frac{1}{\overline{A}_{j-}} - \frac{1}{\overline{A}_{j+}}\right) + \frac{1}{4\pi}\left(\frac{1}{|\overline{Z}_-|} - \frac{1}{|\overline{Z}_+|}\right) \tag{3.8}$$

and
$$\frac{\mathbf{B}(Z)}{\mu_o m_o/\ell^2} = \frac{1}{\pi}\sum_{j=1}^{k}\frac{m_j}{m_o}\left[\frac{\overline{Z}_-}{\overline{A}_{j-}^3} - \frac{\overline{Z}_+}{\overline{A}_{j+}^3}\right] + \left(\frac{1}{\overline{Z}_-^2 - \overline{Z}_+^2}\right) \tag{3.9}$$

where $\overline{A}_{j\mp} = \sqrt{\overline{\gamma}_j^2 + \left(\overline{Z}_\mp\right)^2}$; $\overline{Z}_\mp = Z \mp \delta$; and $\overline{\gamma}_j = 2\overline{a}_j/\ell$.

The results are given in Figure 3-2, and Table 3-1 where

$$\% \text{ Error} = 100 \times \int_z |\Phi(z) - \Phi_A(z)|\,dz / \int_z |\Phi_A(z)|\,dz \tag{3.10}$$

Results in Table 3-1 were computed using MATLAB Optimization Toolbox. Since Equation (2.16) is singular at the surface of a magnet, the Φ_A values for Equation (3.10)

are solved numerically with $\left|\mathbf{R}'\right|+10^{-6}$; no significant difference in results was found when $\varepsilon_R \leq 10^{-3}$.

Table 3-1 Values of the parameters in cylinder PM

Model	$\delta = \overline{\ell}/\ell$	m (A·m)	%Error
Single (n= k=0)	0.20	206.91	55.49
DMP (n=4, k=1)	0.39	m_o=-33.31; m_{1i}=78.13	1.76

$\mu_0 M_0 = 1\text{T}$, a=6.35mm, $\ell = 12.7$ mm, ε_R =10e-6.

Some other observations are discussed as follows:

1. For a given aspect ratio $\gamma = 2a/\ell$, the parameters, $\delta = \overline{\ell}/\ell$ and m_j/m_o, can be calculated. The results for $\gamma \leq 1$ (with k=1 and n=4) are given in Figures 3-2 (a) and (b). Once k, n, δ, and m_j/m_o are known, m_o can be determined for a specified **B** from Equation (3.9). In Figure 3-2 (a), δ decreases as γ increases as expected. For a given δ, the curve m_1/m_o in Figure 3-2 (b) depends only on the first term of Equations (3.8) or (3.9). Figure 3-2 (b) also shows that the case m_1/m_o=0 (or only a single dipole) is very limited.

2. The DMP model is compared against the single dipole model and analytical solution in Figures 3-2 (c)-(f). The analytical solution agrees well with the DMP model that uses only five dipoles (n=4 and k=1) to characterize the potential field and flux density of a PM with a unity aspect ratio (γ=1). The single dipole, on the

other hand, only provides a reasonable estimate of the magnetic flux density along the z-axis.

3.   The discrepancy in Figure 3-2 (f) occurs primarily around the corner ($r=a$, $z = \ell/2$) of the PM due to field discontinuity; the errors in the magnetic flux density can be reduced by using more loops k. Figures 3-3 and 3-4 illustrate the effects of n and k on modeling accuracy.

4.   Figure 3-3 (b) shows the effect of increasing n in the circular loop, which effectively improves the uniformity circumferentially. The variation is about 5% with only five dipoles ($n=4$ and $k=1$), and nearly eliminated with $n \geq 6$.

5.   As shown in Figures 3-4 (a) and (b) where the absolute differences between the analytical and DMP modeled potentials are graphed in $\log_{10}$ scale, the model (with an increase in k) can be extended to account for the effect of larger aspect ratios.
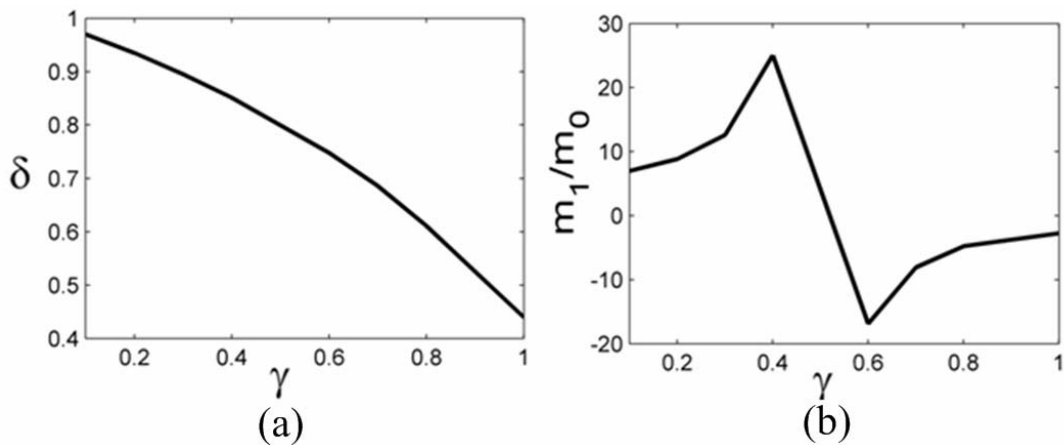
Figure 3-2 Potential and flux density along the Y and Z axes (continuous)
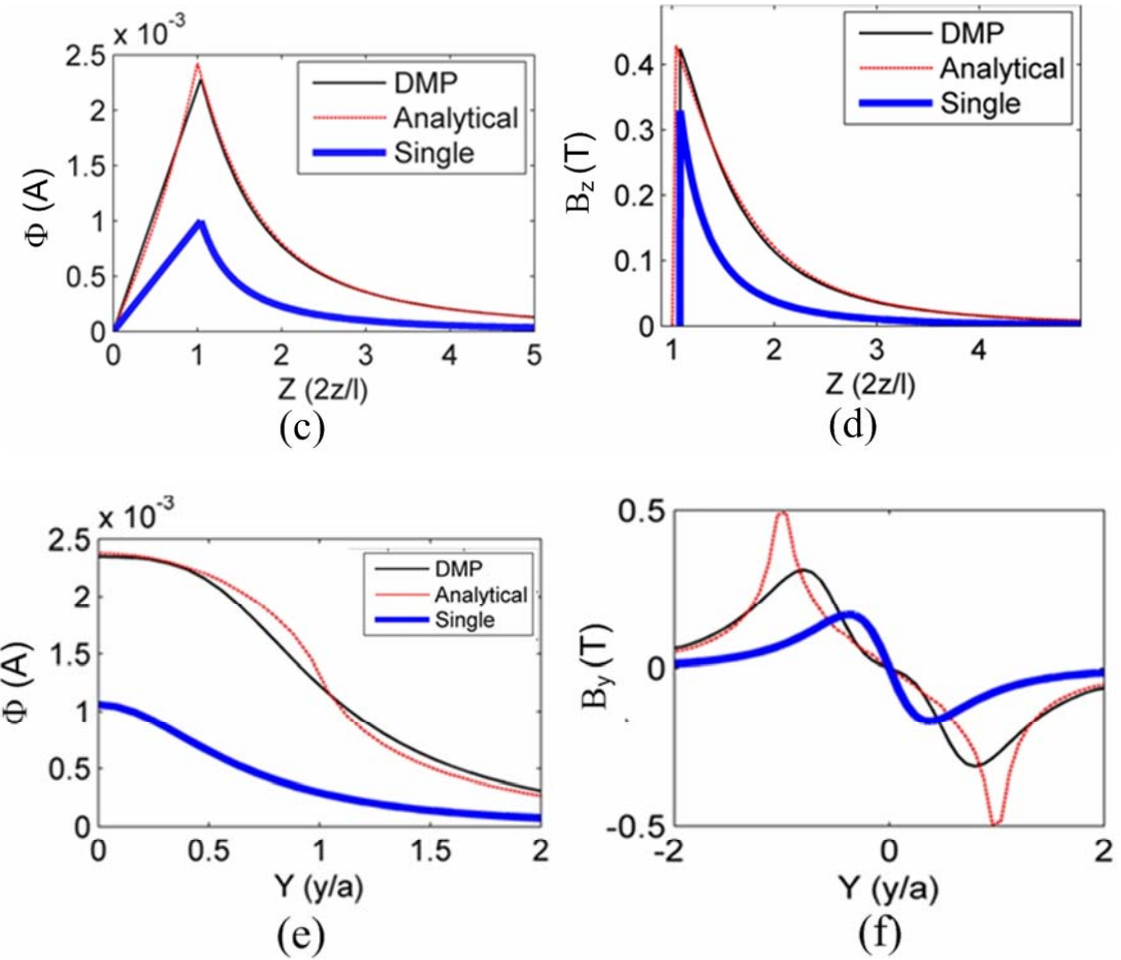
Figure 3-2 Potential and flux density along the Y and Z axes

for all plots: $n=4$ and $k=1$; and for (c)-(f), $\gamma = 2a / \ell = 1$
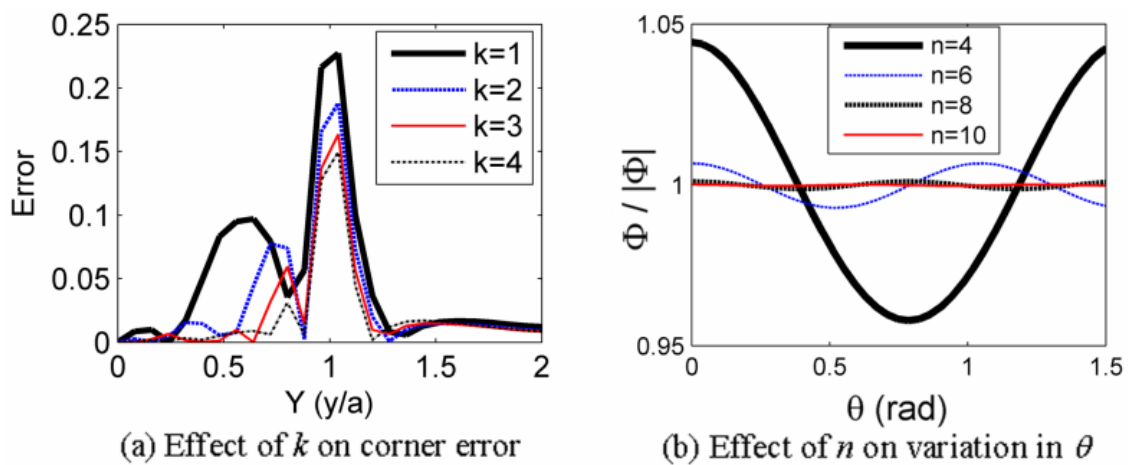
Figure 3-3 Effect of n and k on modeling errors ($\gamma = 2a / \ell = 1$)
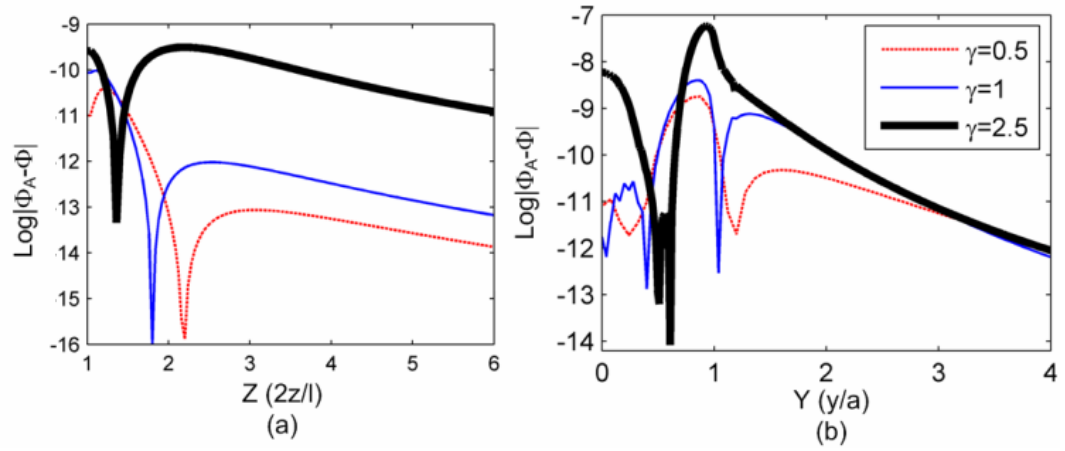
Figure 3-4 Effect of the aspect ratio on modeling errors (n=4)

for $\gamma = 2a/\ell \leq 1$, k=1; and for γ=2.5, k=2

3.2.2 Customized shape permanent magnet

We illustrate two examples here to extend the DMP method. The first example shows the DMP modeling method to characterize a PM of customized shape. The second investigates the effect of three different pole-shapes on the magnetic torque using DMP models.

Figure 3-5 shows an example of customized PM used in a prototype spherical motor [32] where the magnet (shaped as a segment of a sphere) was magnetized in the positive x-axis. The potential field solution can be derived analytically from Equation (2.16). Since $\mathbf{M} = M_o \mathbf{e}_x$ implying $\nabla \bullet \mathbf{M} = 0$, the volume integral in Equation (2.16) is zero. With the differential surface and unit normal for each of the surfaces given in Table 3-2 where spherical coordinates (r, θ, ϕ) are defined in Figure 3-5, the potential field can be computed from the surface integral in Equation (2.16).
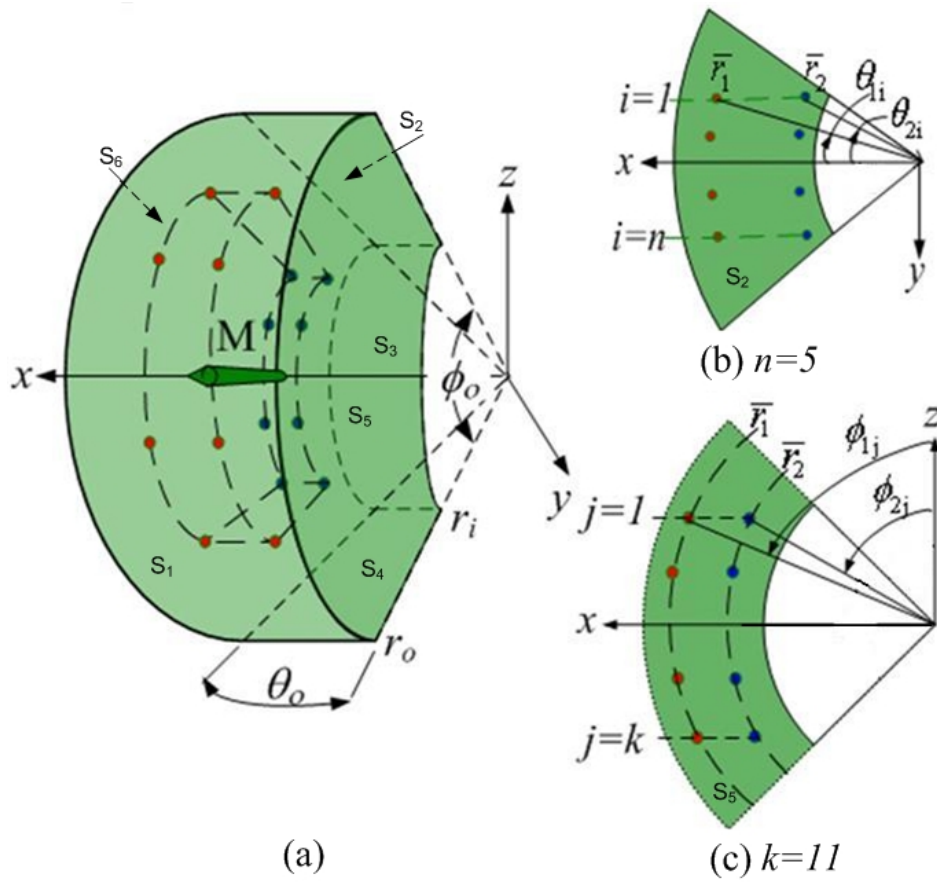
Figure 3-5 Customized PM geometry

(r_o=46.5mm, r_i=23mm, θ_o=40°, ϕ_o=70°, and $\mu_o M_o$=0.62T)

Table 3-2 Parameters for surface integral in Equation (2.16)

Surfaces	Differential	Surface normal
$r=r_o,\ r=r_i$	$dS_{1,3} = r_{o,i}^2 \sin\phi\, d\theta\, d\phi$	$\hat{n}_1 = -\hat{n}_3 = \mathbf{e_r} = \sin\phi\cos\theta\mathbf{e_x}$ $+\sin\phi\sin\theta\mathbf{e_y} + \cos\phi\mathbf{e_z}$
$\phi=\phi_2,\ \phi=\phi_4$	$dS_{2,4} = r\,dr\,d\theta$	$\hat{n}_2 = -\sin\phi_1\mathbf{e_x} +\cos\phi_1\mathbf{e_z}$ $\hat{n}_4 = -\sin\phi_2\mathbf{e_x} -\cos\phi_2\mathbf{e_z}$
$\theta=\theta_5,\ \theta=\theta_6$	$dS_{5,6} = r\sin\phi\,dr\,d\phi$	$\hat{n}_5 = -\sin\theta_1\mathbf{e_x} +\cos\theta_1\mathbf{e_y}$ $\hat{n}_6 = \sin\theta_2\mathbf{e_x} -\cos\theta_2\mathbf{e_y}$

As shown in Figure 3-5, the dipoles of the DMP model for the customized PM are uniformly along the *x*-axis located in a $\bar{r}_1 \times \bar{r}_2$ region where $r_o > \bar{r}_1 > \bar{r}_2 > r_i$ such that they form a $k \times n$ lattice as defined in Figures 3-5 (b) and (c). Their locations are given by

$$\phi_{2j} = j\phi_o/(k+1); \quad \theta_{2i} = i\theta_o/(n+1) \tag{3.11}$$

Since the dipoles are parallel to the x-axis, from Figure 3-5 (c), we have

$$\bar{r}_1 \cos\phi_{1j} = \bar{r}_2 \cos\phi_{2j} \quad \text{or} \quad \phi_{1j} = \cos^{-1}\left(\bar{r}_2 \cos\phi_{2j}/\bar{r}_1\right) \tag{3.12}$$

Similarly, from the projections on the x-axis in Figure 3-5 (b),

$$\theta_{1i} = \sin^{-1}\left[\frac{\bar{r}_2 \sin\phi_{2j}}{\bar{r}_1 \sin\phi_{1j}} \sin\theta_{2i}\right] \tag{3.13}$$

Since the magnet is symmetric about the *xy* and the *xz* planes, only one quarter of the dipole moments m_{ji} are found numerically using the optimization toolbox in MATLAB. The values are given in Table 3-3. To allow for one more degree of freedom to describe the location of the dipoles, we define the source-sink spacing using two variables:

$$\delta_1 = \frac{\bar{r}_1 - r_c}{r_o - r_c} \quad \text{and} \quad \delta_2 = \frac{\bar{r}_2 - r_c}{r_o - r_c}; \quad \text{where } r_c = \frac{r_o + r_i}{2} \tag{3.14}$$

The customized magnet was studied experimentally in [54] and [55] giving measured magnetic flux density along the *x*-axis, and the ϕ direction in the *yz* plane. These data are used here as a basis for comparison. We compute the flux density of the customized magnet using three different models, and compare the computed results to published data in Figure 3-6.

i) Analytical integral of Equation (2.16) with $\mathbf{M} = M_o\mathbf{e}_x$ and Table 3-2.

ii) Analytical integral (*r*-only): same as (i) but neglects ϕ and θ components of the magnetization; this model assumes a uniform radial field $\mathbf{M} \approx M_o \cos\theta \sin\phi\, \mathbf{e}_r$ [54].

iii) The 11×5 DMP model in Table 3-3 and $\mathbf{M} = M_o\mathbf{e}_x$ as in (i).

Table 3-3 Parameters m_{ji} of the 11×5 DMP model

	j=1	j=2	j=3	j=4	j=5	j=6
i=1	7.0594	-0.0453	4.1249	2.0897	3.2027	2.5187
i=2	-0.9223	-1.0204	-0.1404	-0.7011	-0.2487	-0.5497
i=3	1.7825	0.3004	1.0298	0.6462	0.8940	0.7231

δ_l =0.3951; δ_2=0.1702

Some observations from the comparisons are summarized:

As shown in Figure 3-6 (a), the computed $B_x(x,0,0)$ of the DMP model along the x-axis closely agrees with both the analytical solution and experimental data. Note that since $\mathbf{M} = M_o\mathbf{e}_x$, $B_y = B_z = 0$ along the x-axis.

The three components of **B** field that were measured at locations ($r=r_o+0.5$mm, $\theta=0$) in terms of ϕ are given in Figures 3-6 (b)-(d). The DMP computed B_x and the results of the first analytical integral agree well with the measured B_x data.

The magnetic fields $B_y(\phi)$ and $B_z(\phi)$ of the DMP model lie between the analytical integral model and the experimental data. Some discrepancies are observed between the computed and measured $B_y(\phi)$ and $B_z(\phi)$, which may be explained as follows. Since Φ is symmetric about the yz plane, analytically we should have

$$B_y = -\mu_0 \left[\partial \Phi / \partial y \right]_{y=0} = 0 \text{ and } B_z \big|_{y=z=0} = 0 . \tag{3.15}$$

However, measured B_y in Figure 3-6 (c) and B_z at $y=z=0$ in Figure 3-6 (d) are not zero suggesting that the customized PM may not have been uniformly magnetized or that there could be some systematic errors in measurements of $B_y(\phi)$ and $B_z(\phi)$.
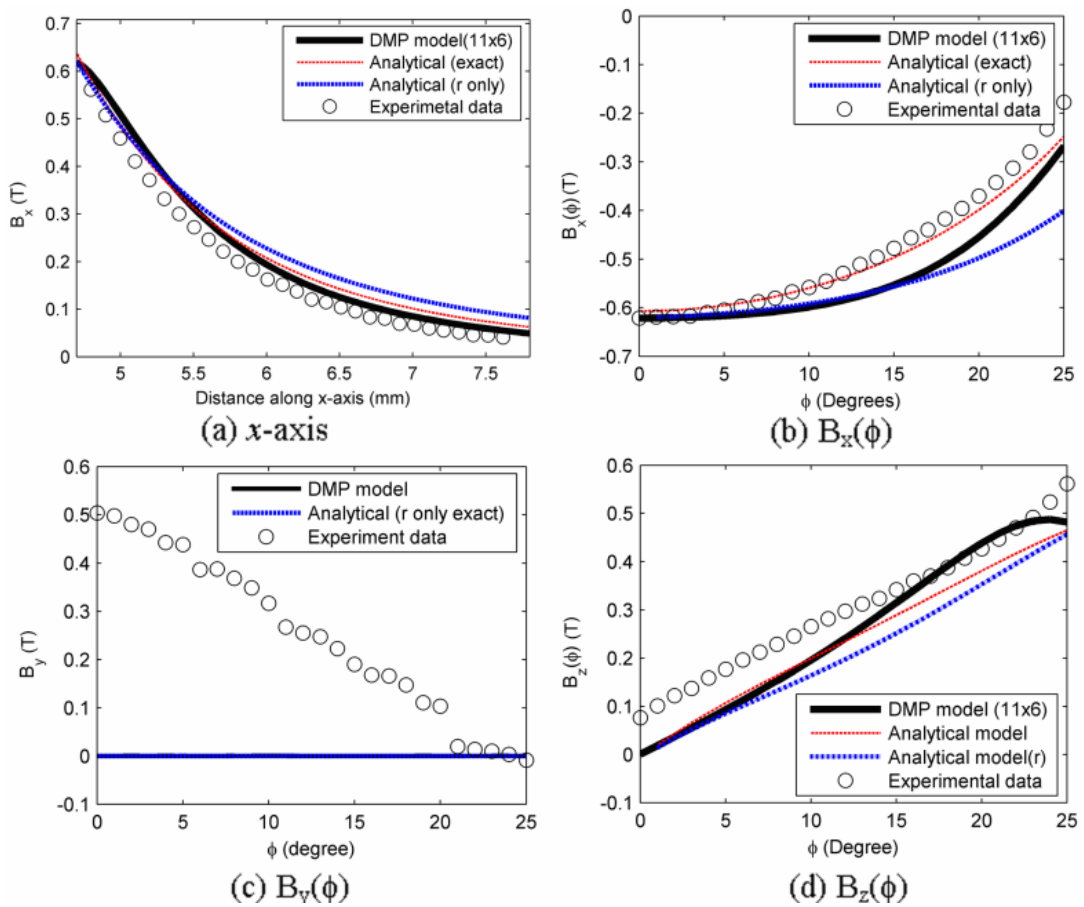
Figure 3-6 Comparisons of magnetic flux density

3.3 DMP MODEL OF ELECTROMAGNET

As shown in section 2.4, the geometry (a_o, a_i, ℓ) of the cylindrical ML coil considered here is defined in Figure 2-2. We present two sets of simulation results. The first simulation illustrates the ESL model, and examines its effects of coil geometries on the magnetic flux density and the Lorentz force. The second simulation validates the equivalent models and compares the computed forces against published data.

ESL model of cylindrical voice coil

Table 3-4 compares three different coil geometries and their effects on the magnetic flux density for the same wire volume of 5.41cm^3 (0.33in^3) and length $\ell = 25.4$mm (1 inch). With the current of 4 Amperes, the effective radius a_e and current density J_e in Table 3-4 were found numerically using the optimization toolbox in MATLAB. Since the magnetic flux density of the ESL model is singular at the surface ($z = \ell/2$), we compare $B_{Sz}(y, \ell/2 + \varepsilon)$ at ε=1μm and 1mm in Figures 3-7 (a) and (b) respectively for three different ratios a_i/a_o = 0.1, 0.5 and 0.9.

Table 3-4 Effects of the ML coil geometry on ESL model

Geometry			Current density	% Error at $z = \ell/2 + \varepsilon$	
a_i/a_o	a_o/ℓ	a_e/a_o	$J_e d_w$ (A/mm)	$\varepsilon = 1\mu m$	$\varepsilon = 1mm$
0.1	0.3256	0.582	137.1	32.0%	19.0%
0.5	0.3740	0.766	136.7	13.4%	6.6%
0.9	0.7437	0.951	136.2	1.3%	0.6%

Volume=5.41cm^3 (0.33 in^3); $\ell = 25.4$mm (1in); 29AWG wire with 4A currents.

Original ML (ε=1μm) Original ML (ε=1mm)

a_i / a_o = 0.1(ε=1μm) a_i / a_o = 0.1 (ε=1mm)

a_i / a_o = 0.5(ε=1μm) a_i / a_o = 0.5 (ε=1mm)
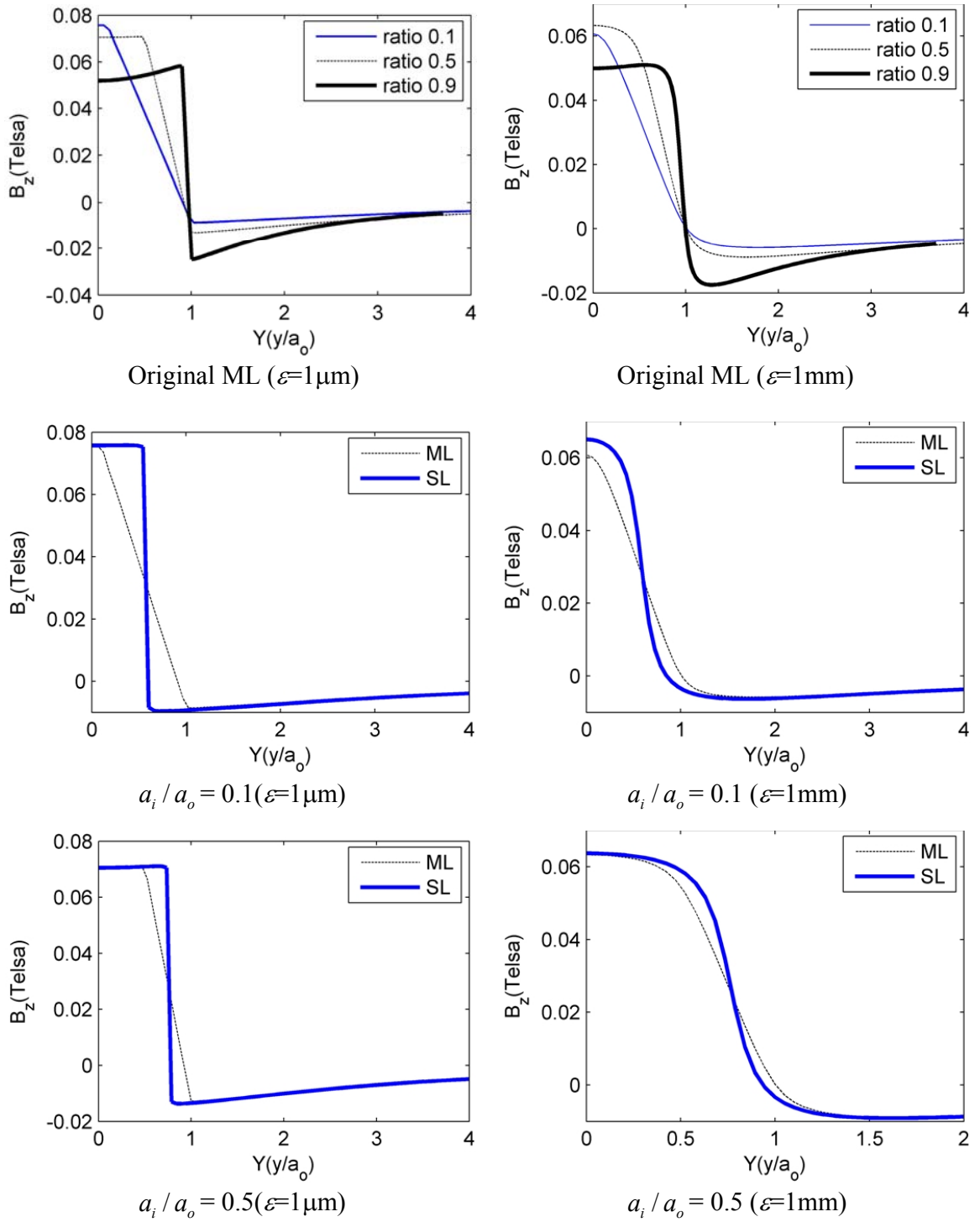
Figure 3-7 Effect of the effective radius on the different geometry of EMs (continuous)

$a_i / a_o = 0.9 \ (\varepsilon{=}1\mu m)$

(a) $B_{Sz}(y, \ell/2 + 1\mu m)$

$a_i / a_o = 0.9 \ (\varepsilon{=}1mm)$

(b) $B_{Sz}(y, \ell/2 + 1mm)$
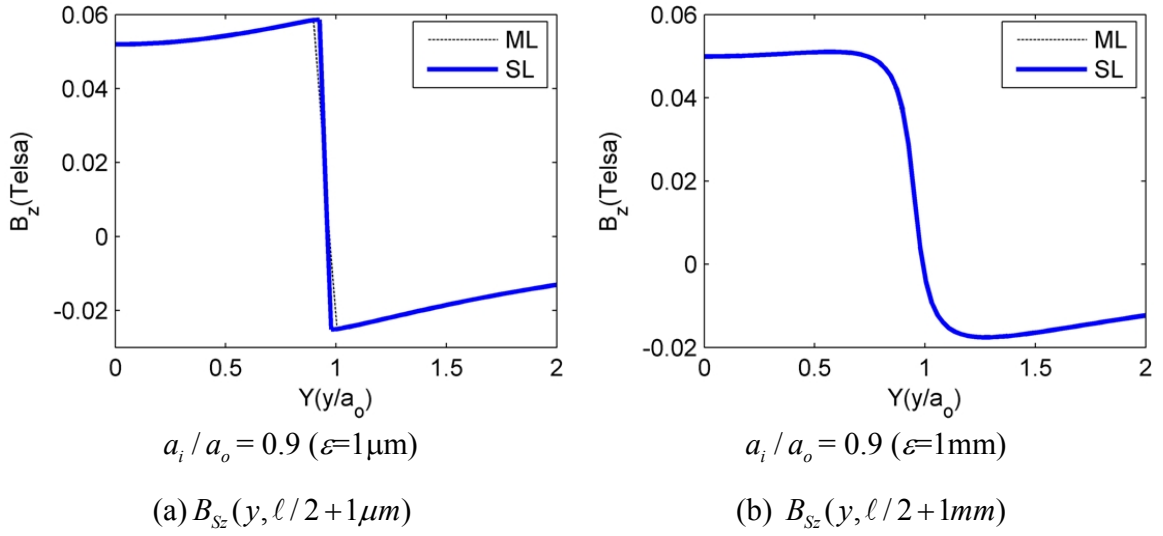
Figure 3-7 Effect of the effective radius on the different geometry of EMs

The errors of the ESL models are summarized in Table 3-4 where the % Error is defined

$$\% \text{ Error} = \left[\int_0^\infty \left| B_{Mz}(y,z) - B_{Sz}(y,z) \right|_{z=\ell/2} dy \right] \Big/ \left[\int_0^\infty \left| B_{Mz}(y,z) \right|_{z=\ell/2} dy \right] \qquad (3.16)$$

Comparison of results in Figure 3-7 and Table 3-4 shows that the ESL model well approximates the magnetic fields of coils with $a_i / a_o \geq 0.5$. As expected, discrepancies between the ML and ESL models occurs primary at the surface ($z = \ell/2$), particularly for coils with a very small a_i / a_o ratio. This implies that one or more additional wire layers may be needed to improve the approximation. For the same volume of wires and coil length, thin coils ($a_i / a_o \approx 1$) tend to have a more uniform but lower magnetic flux density along the centroidal axis than that of the thick coil ($a_i / a_o \ll 1$).

Figure 3-8 (a) shows the setup used to compare the torque computed with the 3D field of the ESL model against that based on the 3D field of the original ML coil by

Lorentz formulation. The cylindrical PM is rotated in the *xz* plane towards the ML coil. The parameters of the PM and coil are given in Figure 3-8 (a). Computation with the ESL model requires only 5% of the computation time with the original ML coil in MATLAB. As shown in Figure 3-8 (b), the two computed torque are in excellent agreement.

Permanent magnet (PM):

$2a = \ell = 12.7$mm ; $\mu_0 M_0 = 1.27$ Tesla

coil: 29AWG wire

a_o=9.5, a_i=4.76, $\ell = 25.4$mm

# of turns = 1050; Current= 4A

Gap between PM and coil = 0.5mm
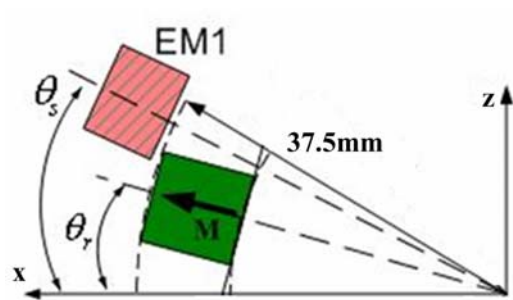
(a) Parameters used in simulation
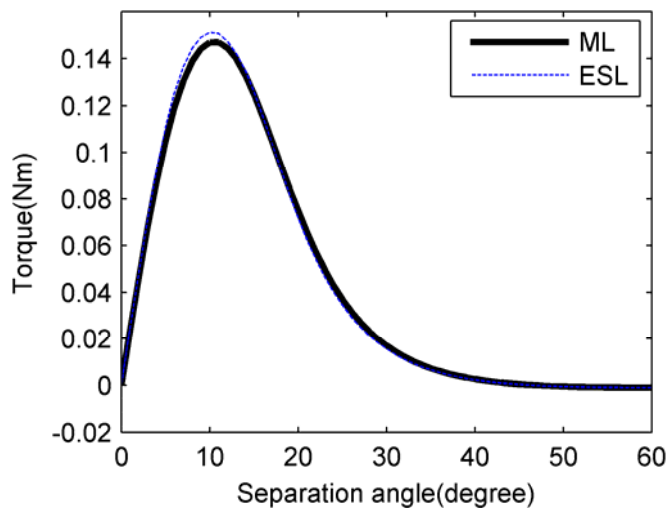
(b) Torque vs. separation angle ($\theta_s - \theta_r$) with 3D fields

Figure 3-8 Effect of equivalent models on the torque

3.3.1 Model validation with force computation

To illustrate the method and validate the DMP models, we model the setup (with two different size combinations) as shown in Figure 3-9, and compare the computed forces against numerical solutions [9] [56] and published experimental data [57].

Size	Large	Small
d_1 (mm)	3.048	1.524
d_2 (mm)	3.962	3.175
d_3 (mm)	2.998	1.6
L (mm)	1.6	0.813
Coil res. (Ω)	57	32
Wire length (m)	3	1.68

Samarium-Cobalt magnet; $\mu_0 M_0$=1.02 T

Coil: 280 turns of #47 wire; Current=0.05A
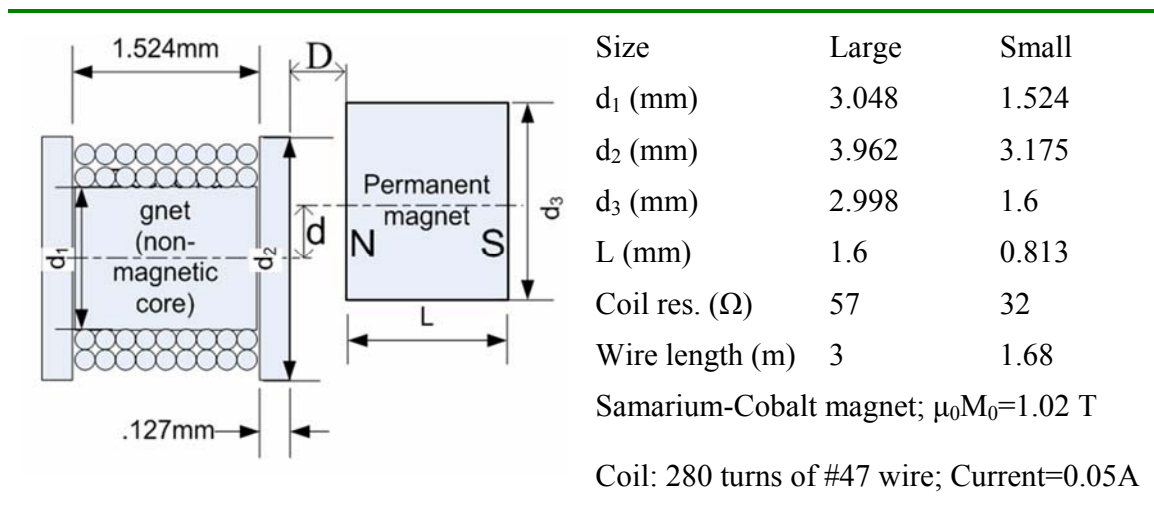
Figure 3-9 Experimental setup and parameters

As an illustration, Figure 3-10 (a) shows the normalized switching radius as a function of Z for the larger coil, where the effective radius is defined at Z=1. Table 3-5 lists the calculated effective radii and field intensity of the ESL models, and the corresponding parameters of the DMP models.

Figure 3-10 (b) compares the three different methods for calculating the corresponding magnetic flux density along the z-axis; namely, the original ML coil, the ESL model, and the DMP model of the EM. The comparisons are remarkably close.

(a) Switching radius (large coil)   (b) B_z at ($\ell/2+1$ mm)
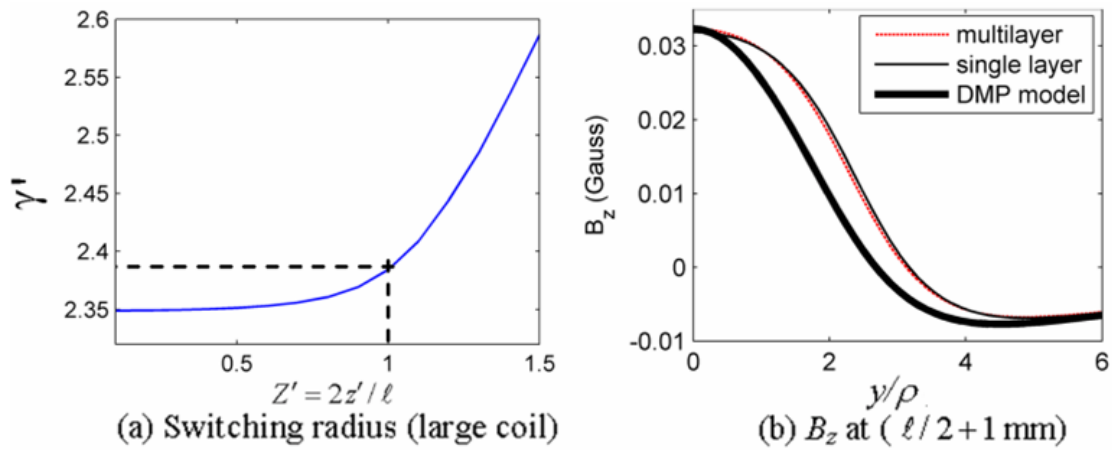
Figure 3-10 Switching radius and magnetic flux density B_z

Table 3-5 Parameters of the equivalent models

	Parameters	Large	Small
PM (DMP)	δ	0.3140	0.3122
($k=2$; $n=6$)	m_j (μA·m)*	1.65, 0.02, 3.80	0.43, 0.02, 1.07
EM	ρ (mm)	1.8168	1.456
(Single-layer)	$J_e d_w$ (A/m)	2.2750 e-5	3.8975 e-5
EM(DMP)	δ	0.3833	0.56
($k=2$; $n=6$)	m_j (nA·m)	11.31, 2.59, 38.80	7.5, 1.3, 21.2

*m_j, j=1, 2, 3; m is same for n.

The magnetic forces (between a PM and an EM in Figure 3-9) were computed using the three different EM models: (i) original ML coil, (ii) ESL model, and (iii) equivalent PM (DMP model).

Models (i) and (ii) use the Lorentz force equation to calculate the magnetic force exerted on the current-carry conductors of the ML and the ESL coils respectively. Model (iii) treats the EM as a PM, and uses Maxwell stress tensor to calculate the force on the

given field of the effective PM. The modeled axial and tangential forces are compared in Figures 3-11 (a, b) and (c, d) respectively against published experimental data and numerical results computed using mesh-less method (MLM).

Table 3-6 Maximum differences from published experimental data

	Lorentz force equation		Maxwell stress tensor
	Multilayer	Single layer	Equivalent PM
Tangential	5.79 %	3.57 %	8.92 %
Axial	8.21 %	8.14 %	9.04 %

As shown in Figure 3-11, both the Lorentz-force computation models (the original ML coil and its ESL model) very closely agree with each other and with the MLM one. Maximum differences from the experimental data, $100 \times |F_m - F_{\exp}| / |F_{\exp}|$, are within 10% as shown in Table 3-6. As compared in Figure 3-11, the force prediction using the DMP model with Maxwell stress tensor is as good as the experimental data. In addition, the computational times of each method for the large PM and EM detailed in Table 3-7. Since the ESL modeling method only requires the surface integral of Lorentz formulation, the computational time of the ESL is 21 times faster than original volume integral of Lorentz formulation.
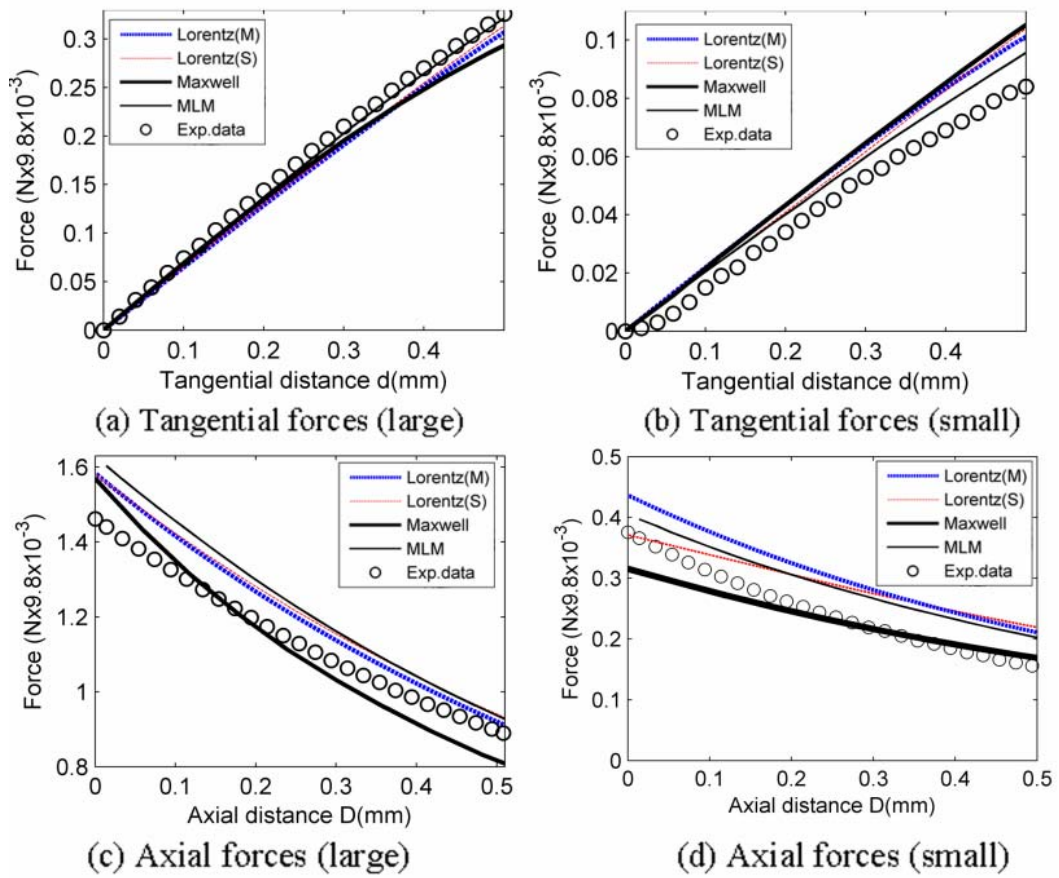
Figure 3-11 Comparisons between computed and experimental results

Table 3-7 Computational time (seconds) for the large size

Lorentz (multilayer)	Lorentz (ESL)	Maxwell tensor
15.6	0.83	4.2

3.3.2 Effect of pole-shape and design configuration

The geometry and layout of the PMs have a significant influence on the magnetic torque of a PM-based actuator. This example illustrates the use of DMP models to

investigate the effect of pole-shapes on the magnetic torque of a spherical motor. The PM pole-shapes used in the following designs are considered:

Design A [47] consists of 2 rows of 8 cylindrical PMs with $\gamma =1$.

Design B [54] uses a row of 8 assemblies of 5 cylindrical PMs with $\gamma >1$.

Design C [55] is similar to Design B but the customized PMs (Figure 3-5) are used as rotor poles.

We focus on comparing the net magnetic torque per unit magnet-volume for a given rotor radius and under the same influence of the stator electromagnets. Detailed geometries of the three PM pole-shapes are compared in Figure 3-12, where the bold arrow indicates the polarity of the PMs. The parameters used in the simulation are summarized in Table 3-8.

The simulated magnetic flux and potential lines are plotted in Figure 3-14; as expected, the potential and flux lines are orthogonal. Figure 3-14 (a), or the left column, compares the magnetic fields of the three different PM designs. Unlike Designs B and C where only one row of PMs is used, a significant portion of the flux lines in Design A forms a closed path between two PMs. Once the magnetic field of the PMs is found the force acting on the current-carrying conductors can be calculated using the Lorentz force equation.

Figure 3-13 compares the torque per unit volume of the three designs. The calculation in Figure 3-13 uses the ESL model with the magnetic field given in Figure 3-14 (a). In calculating the torques, ±1A current profiles in Figure 3-13 (a) are given to the EMs such that a positive torque in +y-direction is generated.

Table 3-8 Parameters used in simulation

Common Parameters				
Rotor radius, mm	Stator EM ($2\theta_s=26°$)			Air gap (mm)
	$(2a_o)\times(2a_i)\times\ell$ (mm)	# of turns	Current (A)	
$r_1=37.5$	$19.05\times9.53\times25.4$	1050	±1	0.5
PM Pole Designs				
	$\mu_o M_o$ (T)	PM pole shape (mm)		Volume (cm^3)
Design A	1.27	$2a=\ell=12.7$, $2\theta_r=20°$		3.22
Design B	1.27	$2a\times\ell$: 25×10, 20×5, 16×6, 12×3, 8×3		8.2
Design C	0.62	Fig.10 ($r_o=46.5$, $r_i=23$, $\phi_o=70°$, $\theta_o=40°$)		23.6

(a) Design A   (b) Design B   (c) Design C
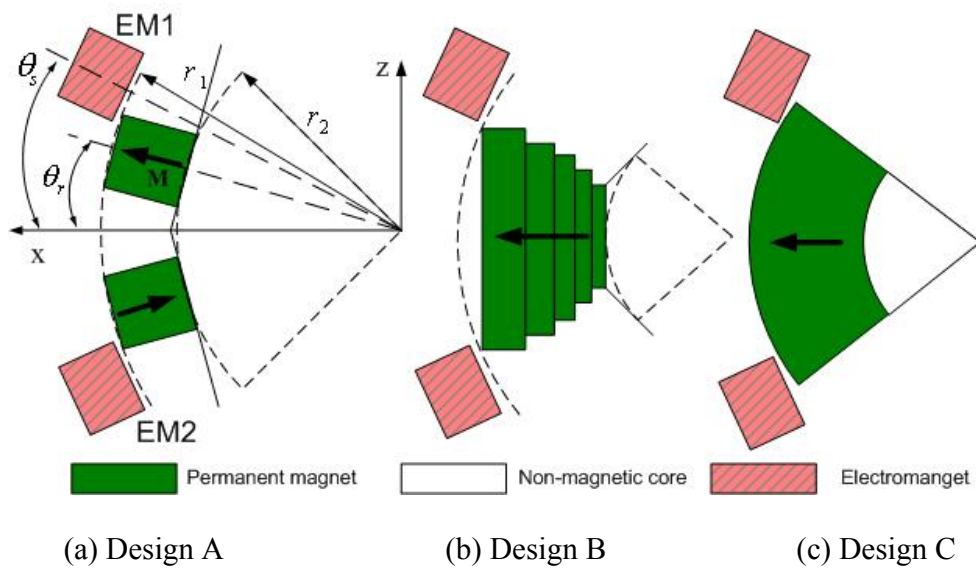
Figure 3-12 PM pole-shape designs

Figure 3-13 (b) shows that Design A offers the largest electromagnetic energy to mechanical energy (area under the torque-displacement curve) conversion, and that

Design C has the smallest torque-to-volume ratio. These observations can be explained by comparing the magnetic fields of the designs. As an illustration, snap-shots of the combined (PM and EM) fields for the three designs are compared in Figure 3-14 (b), where ±1 Ampere of current is given to the pair of EMs such that a magnetic torque is generated in +y-direction with the same applied input power. In other words, the upper EM is repulsive while the lower EM is attractive. The comparison shows that Design A has significantly less leakage fluxes in the attractive PM or EM, and less attractive fluxes in the repulsive EM than Designs B and C. The leakage fluxes in the attractive PM or EM are considered losses as they do not contributes to mechanical torques. Due to the large exposed surfaces in Designs B and C, a relatively strong closed path of magnetic flux is formed between the repulsive EM and the single PM, which would produce an opposing torque, and thus reduce the net torque. In addition, significantly large leakage fluxes from the customized magnet (region between the two EMs) can be seen in Design C indicating the PM is oversized for the specified EMs.

(a) current input   (b) torque comparison
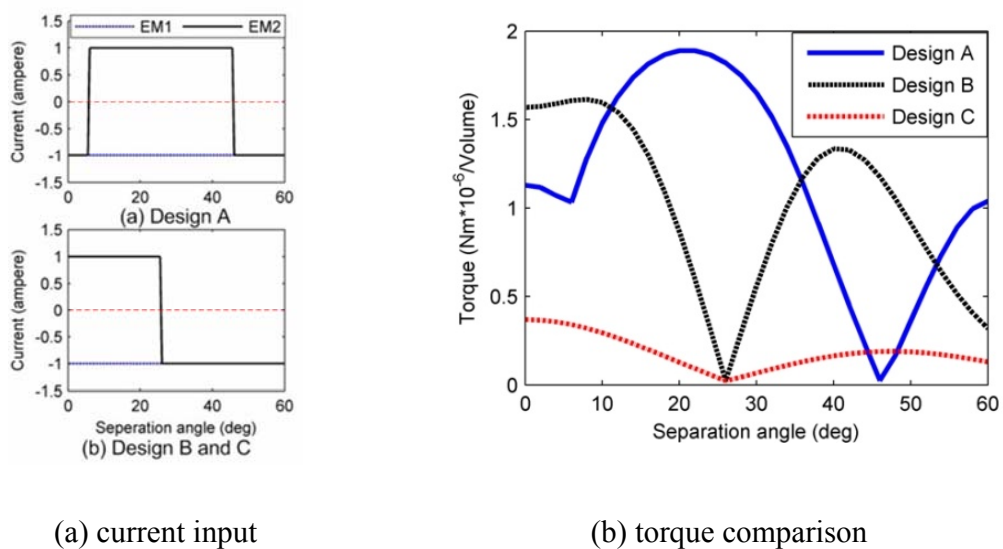
Figure 3-13 Comparison of torque/volume

(a) PM only   (b) Combined PM and EM (±1A)
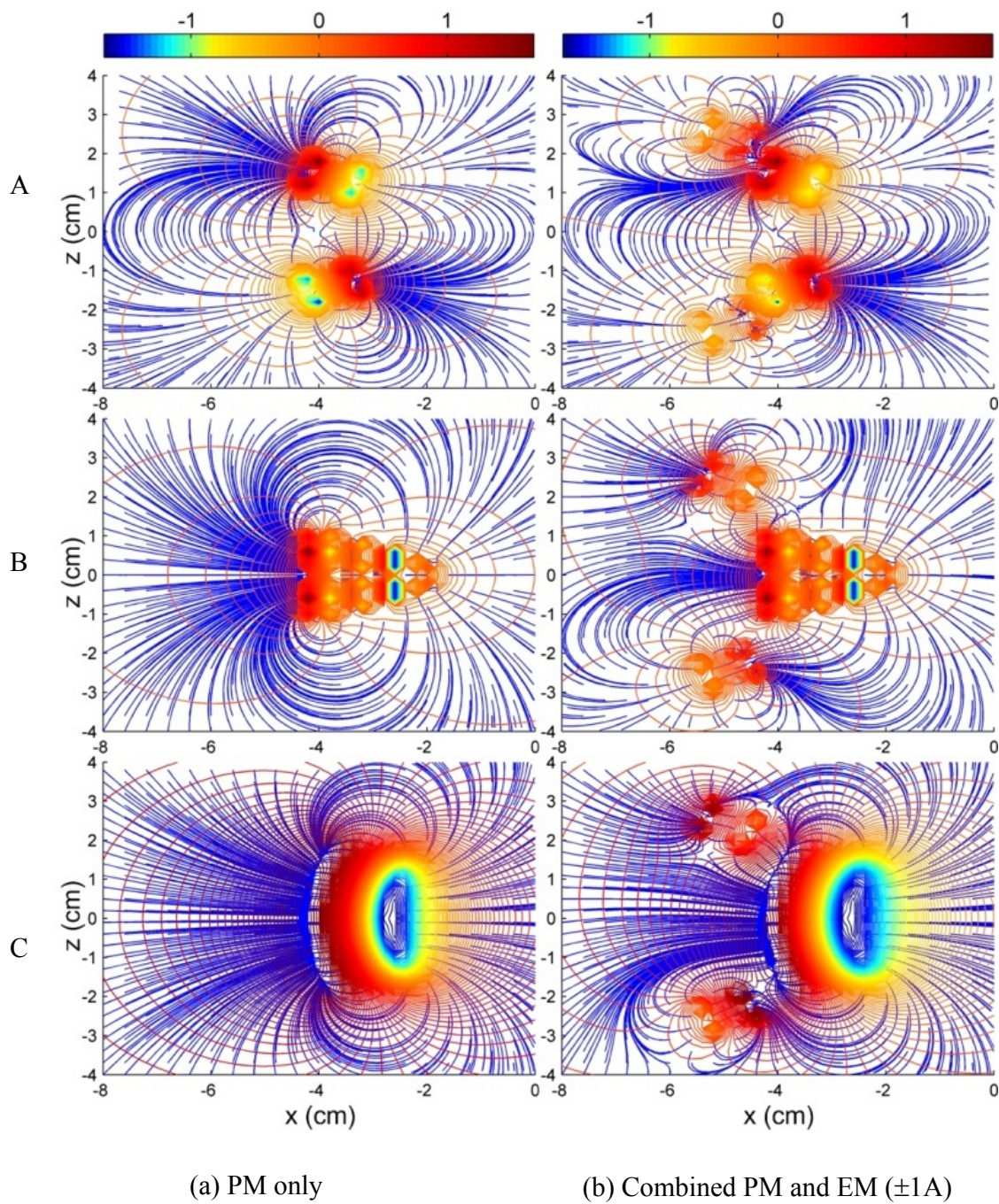
Figure 3-14 Magnetic fields (Orange line: potential; blue lines: magnetic flux)

Top: Design A; middle: Design B; bottom: Design C

As illustrated in Figure 3-14 (b), the closed-form solution of the DMP models can offer an inexpensive means to visualize and analyze the effect of the EM fields on the leakage and unexpected flux paths that have significant influences on the magnetic torque.

3.4   EFFECT OF MAGNETIC BOUNDARY CONDITIONS

Three examples are simulated to illustrate the procedure using the image method to account for the effects of magnetic boundary conditions.

3.4.1   Example 1: comparison with ANSYS results

Figure 3-15 shows the electromagnetic system with a pair of PMs and EMs. Two system configurations with and without magnetic conducting boundaries are simulated and compared against the numerical method using ANSYS.

Design A: Both rotor and stator are non-magnetic conductors.

Design B: Both rotor and stator are magnetic conductors.

For simplicity, ANSYS model uses the cylinder iron boundary but the DMP model uses the spherical boundary. The rotor rotates at the same plane parallel to the plane of the cylinder. The simulations are based on the parameters detailed in Table 3-9.
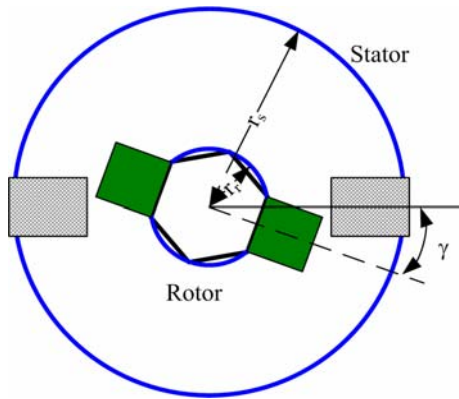
(a) Top view

Table 3-9 System configuration

r_R	0.75 inch
r_S	2.5 inch
PM	
length	0.75 inch
Radius	0.375 inch
$\mathbf{M}_o$	1.12 T
EM	
Outer radius	0.75 inch
Inner radius	0.375 inch
Length	1 inch
# of turn	1040
I	4 Amp
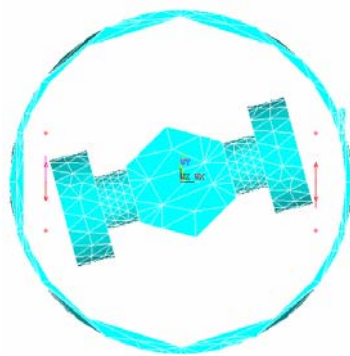
(b) Mesh in ANSYS
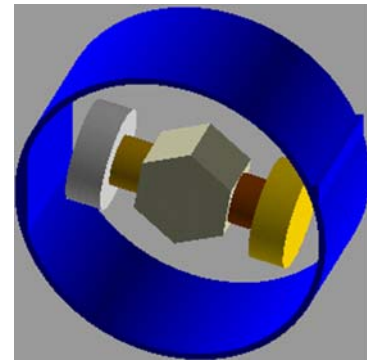
(c) 3D model in ANSYS

Figure 3-15 Validation Image method against ANSYS simulation

Figure 3-16 shows the simulation results of the torque computation which have good agreement and the maximum errors for each configuration is less than 7% and 5% respectively. However, some discrepancies occurred from the initial position. In the FE method, the free space must be bounded; particularly in 3D, the computation cost increases drastically with the size of the free space. This, along the distortion of the automatically generated FE mesh, contributes to some discrepancy (of less than 5%

difference) between the two models. The mesh distortion could be the cause of the FE

error (offset) when the separation angle is zero.
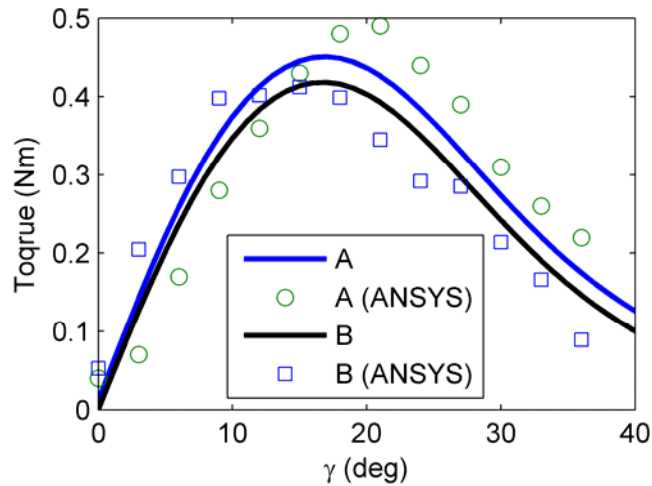
Figure 3-16 Comparisons between DMP and ANSYS

In addition, the computational time of the results in Figure 3-16 are compared.

ANSYS took about 12 minutes to compute Design A, and 20 minutes for Design B using

a Windows-based PC (dual core processor 2.21Ghz CPU and 1GB memory), while the

DMP based models require less than 17 seconds to compute each of the cases as

compared in Table 3-10. The time of the DMP-based torque calculation can be further

reduced by modeling the multilayer EM as an equivalent single-layer EM or PM as

shown in Table 3-7.

Table 3-10 Computational time (seconds)

DMP		ANSYS	
Design A	Design B	Design A	Design B
0.0128T(16.14)	0.013T(16.9)	0.5484T(702.0)	T=1480.0

3.4.2   Example 2: Effect of magnetic field on the iron boundaries

Figure 3-17 shows a magnetic system which consists of two permanent magnets on the spherical rotor and one electromagnet in the stator, which is used here to investigate the effects of the iron boundaries on the magnetic field and the torque. The values of parameters used in the simulation are detailed in Table 3-11. In addition, the parameters of the DMP modeling for the PM and image charges are given in Table 3-12. Four different configurations are compared:

Case A: Non-magnetic boundaries of both the rotor and stator

Case B: Magnetic conducting boundary of the rotor

Case C: Magnetic conducting boundary of the stator

Case D: Magnetic boundaries of both the rotor and stator

Figure 3-18 visualizes the magnetic field of each design. The black and red bold circles indicate the boundaries of the rotor and the stator to identify each boundary. Figure 3-18 (a) shows the non magnetic boundaries of rotor and stator, which serves as a basis for comparing any effect of the boundaries. Figures 3-18 (b), (c) and (d) show the influence of the magnetic field due to the iron rotor, iron stator and both iron rotor and stator respectively.   Since the current through the coil conductor interacts with the magnetic field in this region, it is most critical to analyze the effects of the magnetic field on the force/torque computation. The magnetic field of Case B makes smaller change than Case C in the region of the air gap and EM. In addition, the magnetic fields from the PMs for Case C go to the stator through the shortest path. This indicates that the

leakage flux in the iron stator is much less than the non-magnetic stator or even the iron rotor.

Figure 3-19 shows that torque acting on the EM for each case. The results of torque computation are consistent with the behavior of the magnetic field as expected. Table 3-13 shows the maximum increasing torque % of each design compared to Case A. Based on the results, the EM can generate 10% larger torque with the same structure but the different materials.
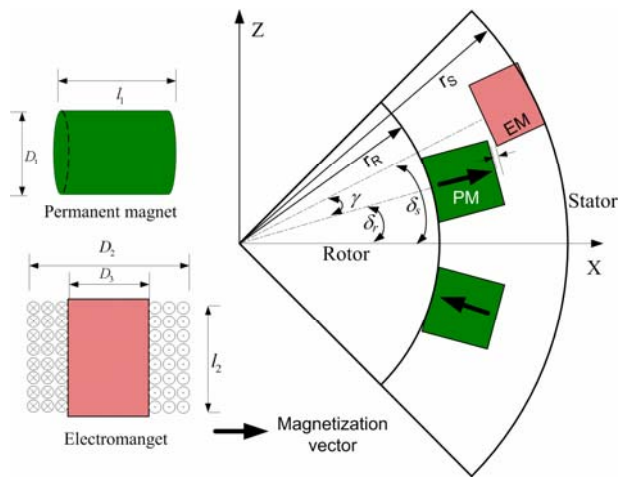
Figure 3-17 Two PMs and EMs

Table 3-11 Simulation parameters

rotor	r_R	1 inch
	δ_r	20 deg
stator	r_S	2.5 inch
	δ_s	26 deg
PM	l_1	0.5 inch
	D_1	0.5 inch
	$\mathbf{M}_o$	1.34 T
EM	D_2	0.75 inch
	D_3	0.375 inch
	L_2	1 inch
	# of turn	1040
	I	4 Amp

Table 3-12 DMP parameters of PM ($n=6, k=1$)

$m_j\ (j=0,1)$	PM($\times 10^5$)	Image charges of rotor	Image charge of stator
m_o	-2.29	3.16	4.20
m_1	6.18	-8.55	-11.30

(a) Case A   (b) Case B

(c) Case C   (d) Case D
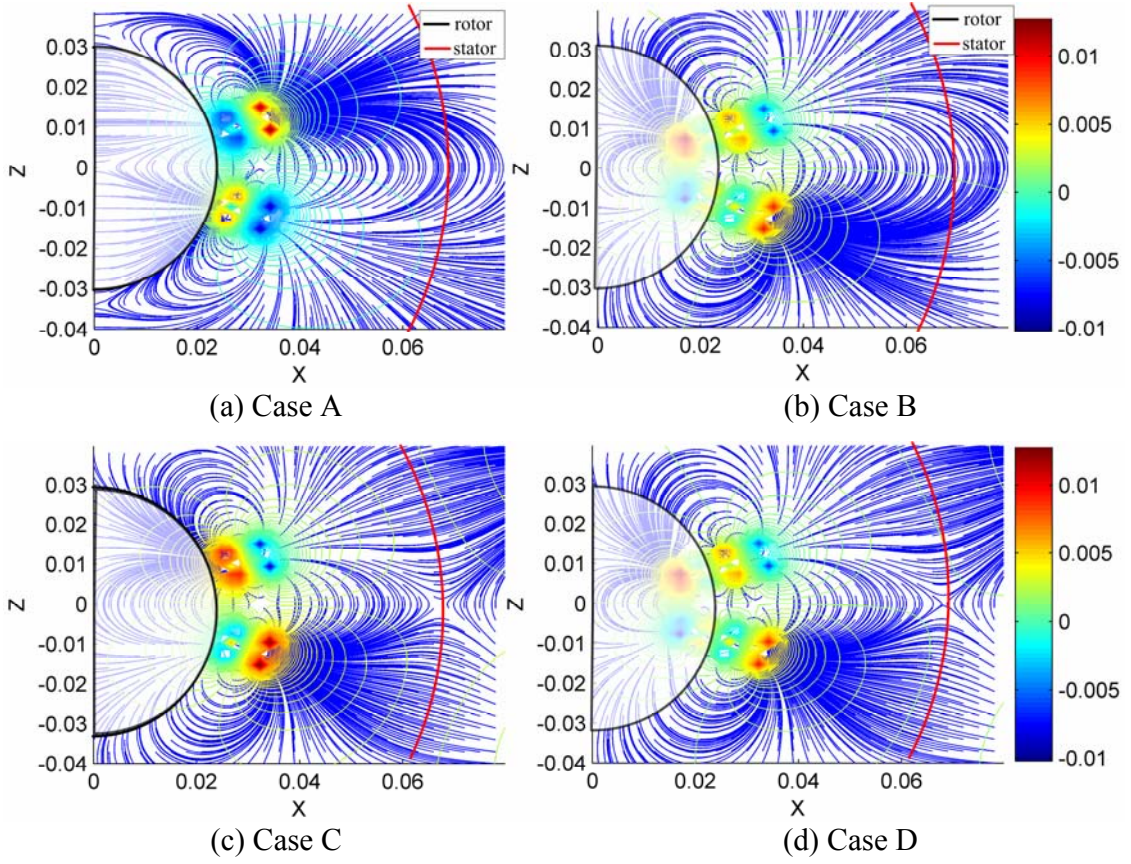
Figure 3-18 Effect of the iron boundaries on magnetic field
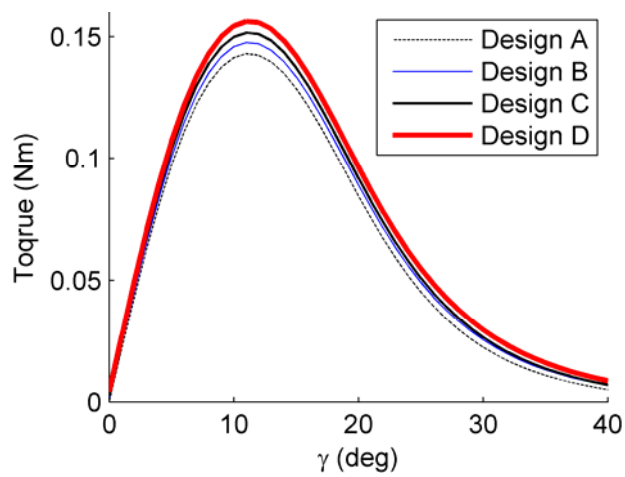
Figure 3-19 Effect of the iron boundaries on torque of the SWM

Table 3-13 Maximum torque (%)

Designs	B	C	D
Torque (%)	3.2	6.0	9.2

3.4.3   Example 3: Design of actuators

This example illustrates the effect of the rotor design on the torque of SWM. Figure 3-20 shows two different rotor size but the same stator size designs, which are constructed by magnetic materials. Design A has larger rotor than Design B.

Figure 3-20 Effect of the rotor size on torque of the SWM

As the radius of rotor r_R increases with the given stator size, the shape of PM and EM in Design A is allowed to be flat compared to Design B. The area of coil wound is same in both designs such that the number of turns can be same for comparison. The detail parameters of the DMP model for each PM and the system are given in Tables 3-14 and 3-15 respectively.

Table 3-14 Simulation parameters (mm) of example 3

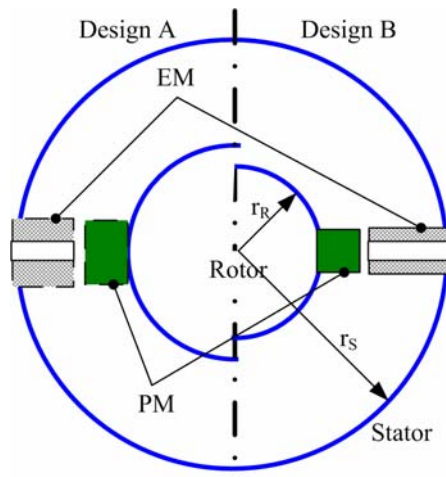|	Design A	Design B		Design A	Design B
r_R	31.8	25.4	**EM**		
r_S	64.3	64.3	D_2	20.32	19.05
gap	0.76	0.76	D_3	7.62	9.525
PM			L_2	19.05	25.4
l_1	12.7	12.7	# of turn	1040	1040
D_1	19.05	17.78	I	4 Amp	4 Amp
M_o	1.34 T	1.34 T			

Table 3-15 DMP parameters of PM ($n=6$)

m_j	Design 1 ($k=1$)	Design 2 ($k=2$)
PM ($\times 10^{-5}$)	-2.29/6.18	4.95/0.10/12.59
Modeling Error	1%	3.4%

Figure 3-21 (a) shows the magnetic field inside the stator. The blue line is magnetic flux distribution and the red contour is the equal-potential. Since the shape of both the iron rotor and stator is sphere, the potential is also sphere but the B-field is normal to the spherical potential. Figure 3-21 (b) shows the torque comparison of each design. The torque generated by Design A is 58% larger than Design B with the same magnitude of input current.

Some other observations are discussed as follows:

1. As shown in Figure 3-21 (a), normal component of magnetic field along the spherical boundary is dominant with present of the iron boundary. It increases the interaction of the normal magnetic flux and the current flow to generate the effective torque

since torque is the outcome of cross product between current density and **B**-field.

2. Design A has smaller air region between the rotor and stator. It reduces magnetic flux leakage in the region so that it becomes more efficient. In addition, we reduce the length of EM but increase the width. It also results in more current wound which interact strong magnetic field.

3. For the mechanical structure, Design A has a larger moment arm since the radius of rotor is long. It also helps to increase the resultant torque.

(a) Magnetic field   (b) Torque comparison
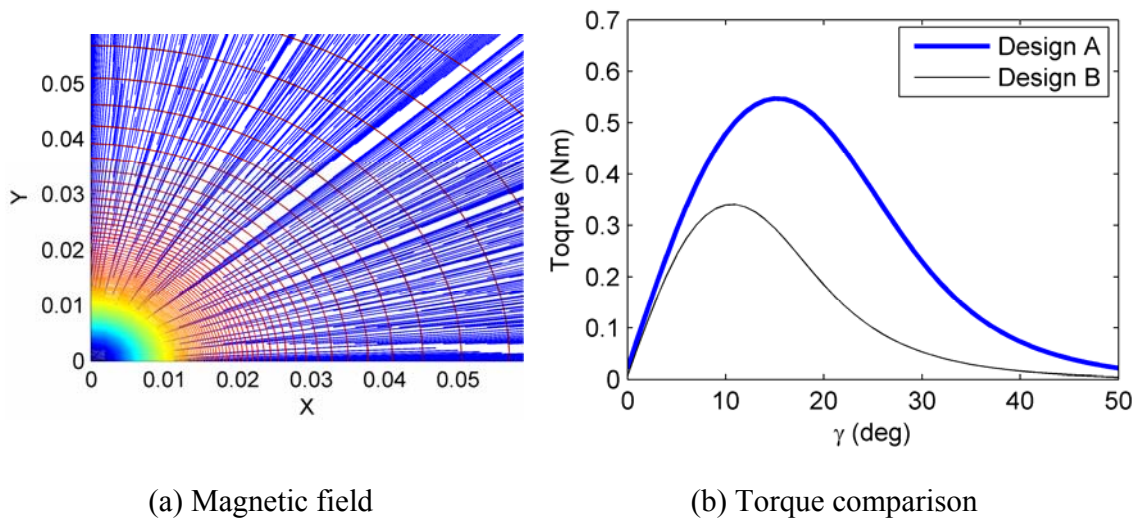
Figure 3-21 Magnetic flux in the air gap region and torque comparison

3.5   EXPERIMENTAL VALIDATIONS

Two illustrative examples are here used to validate the DMP model against the experimental results. The first example provides the comparisons between the DMP model and the experimental results of the magnetic field directly measured by a Hall effect sensor and torque computation. The second example demonstrates the practical

design of a PM-based repulsion actuator for non-contact rotation of moving devices at high-speed as an application in automation and manufacturing industries.

3.5.1 Magnetic field and force

To illustrate and validate the DMP models experimentally, the magnetic field **B** and magnetic force computation using the DMP model and Maxwell stress tensor formulation is verified using the set up as shown in Figure 3-22. The pair of permanent magnets is separately mounted on two cantilever beams, one of which is driven by a precision NSK ball-screw while the other carries a strain gage that measures the magnetic force. The same PM in the previous example 2 is used here whose parameters are in Tables 3-11 and 3-12. The computed forces are compared in Figure 3-23 against the experimental, numerical, and analytical data with two identical permanent magnets. Similarly, the magnetic field B is measured by the Hall effect sensor using the same set-up but the one end is replaced by the Hall effect sensor. Since the output of sensor is voltage, the conversion constant k of the sensor to minimize the error in Equation (3.17) is computed, which results in k=0.148.

$$E_B = \sum_{i=1}^{N_S} \left(B_z - kS_i \right)^2 \tag{3.17}$$

where B_z is the computed field by the DMP model; S_i is senor output voltage; and N_s is the total number of the sampled data.

Figure 3-24 compares the experiment and simulation results of the magnetic flux density. Figure 3-24 (a) measured the magnetic field along the magnetization axis. Since the end surface B-field of the PM is strong, the measured flux density is saturated and

thus the output voltage is a constant. However, the comparisons in the other range are remarkably close.
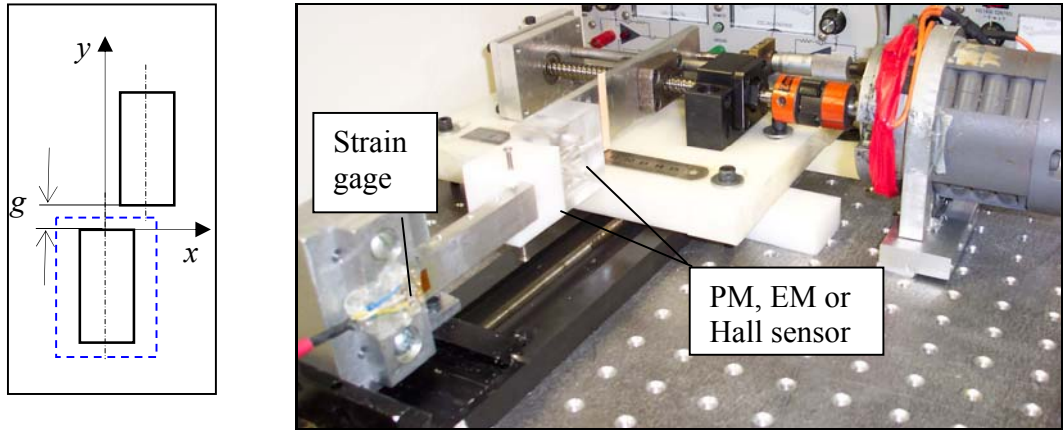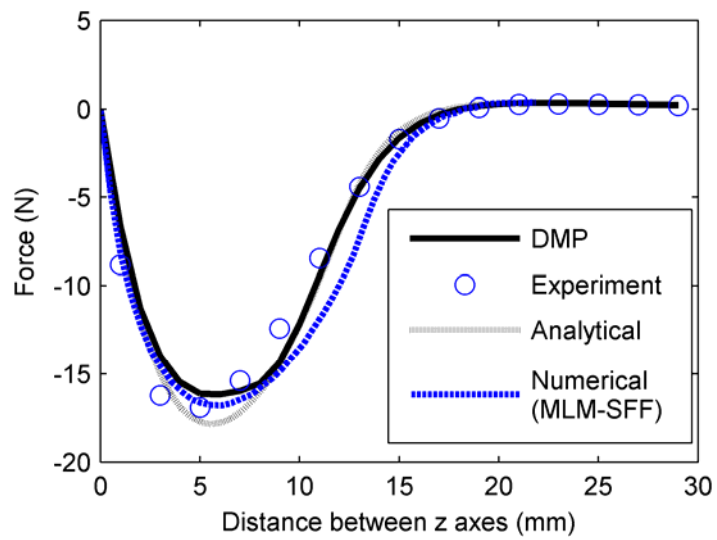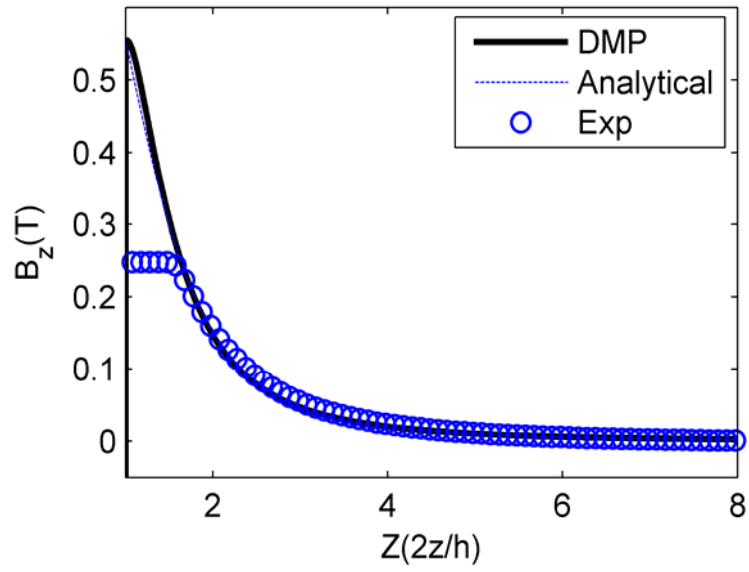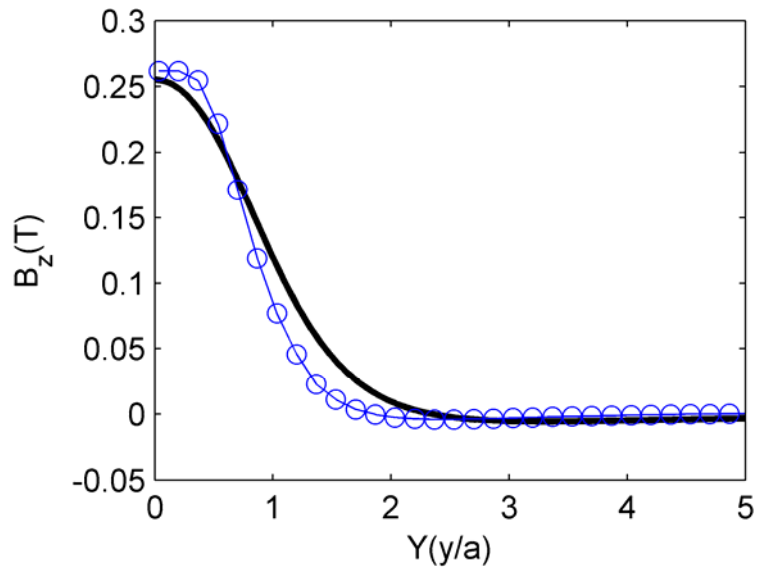

Figure 3-22 Experimental setup

Figure 3-23 Force comparison of a pair of PMs

(a) $B_z(z)$ along the z-axis


(b) $B_z(y)$ along the y-axis

Figure 3-24 Comparisons of magnetic flux density

### 3.5.2 PM based actuator for handling a live object

To illustrate the application of the DMP models, Figure 3-25 shows a PM-based orientation correction mechanism, which uses high coercive PM as energy-efficient actuators. The mechanism travels along a high-speed production line to orient moving graspers so that the grasped objects will face a unique direction for subsequent handling. The parameters used in this example simulation, Table 3-16, are based on a live-bird transfer system [58] so that computed results can be validated experimentally.

As shown in Figure 3-25 (a), the grasper (moving at a constant speed v along a motorized chained track) is initially locked mechanically by a PM-coil trigger preventing it from any rotation. Upon receiving a command from a vision system to make an orientation correction, the trigger unlocks allowing the device to rotate the grasper (in θ direction) by a repulsive force (of two PM of like-polarities) to a specified orientation (defined by the pair of alignment PM of opposite polarities) within an often very short cycle time while the grasper moves continuously. The only energy input required in this PM-based device is a finite pulse of energy to unlock the trigger, which relocks by gravity. The mechanism has six identical PMs; two pairs of fixed PM (N1/N2 with an offset D_o, and S1/S2) mounted on the track and a pair of PM (M1/M2) moving with the grasper. In Figure 3-25 (c), the shading of the magnets indicates their polarities; S1/S2 has opposite polarity of N1/N2 and M1/M2. The values designed for the graspers are summarized in Table 3-16. The offset D_o and the magnet geometry are designed to meet two objectives:

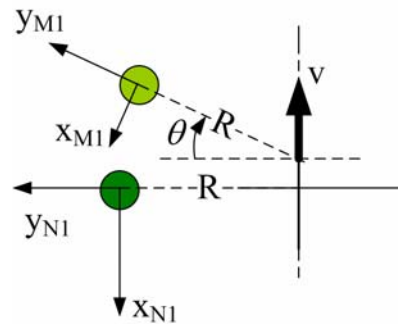1. The trigger unlocks at the instant when the two opposing forces are equal, and thus the static friction is a minimum.

2. The mechanical torque is maximized to complete a (180°) rotation with a specified distance and time.
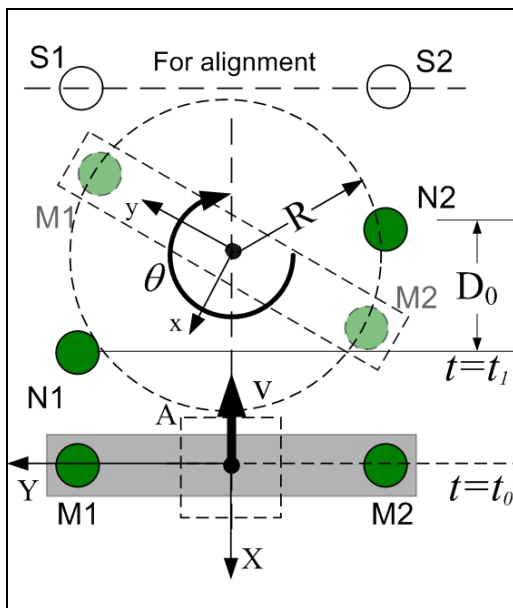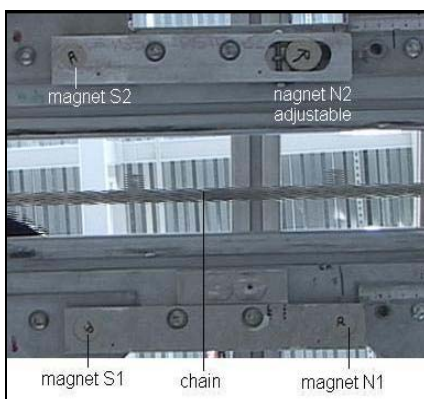

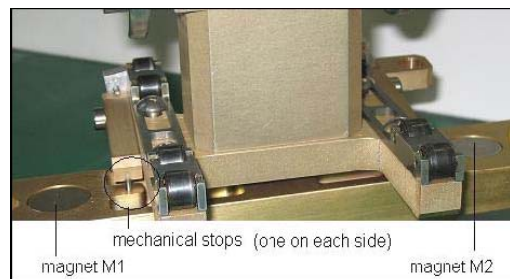(a) Layout of permanent magnets
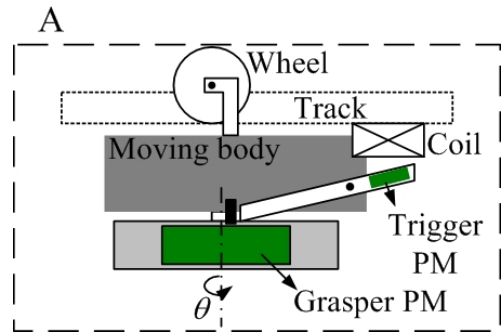
(b) Side view of A

(c) Coordinate systems

(d) PM on underside of the track

(e) PM on grasper

Figure 3-25 Schematics of an orientation correction device

Table 3-16 Parameters of the PM-based orientation correction mechanism

Grasper	I=0.0316kg-m^2; c= 0.01N-s/m; v=0.45m/s
Actuator configuration	D_o=20, 25mm; $2R$=175mm
Vertical gap between M_i and N_i	g=6.25mm
Neodymium PM (grade N38)	B_r=1.24Tesla; $2a$=25mm; ℓ=12.5mm

In order to verify the computed trajectory of the grasper using the DMP models, we compute the net repulsive torques and simulate motion of the rotating magnet M1 and compare against the motion data digitally recorded experimentally using a 3-CCD video camera. The coordinate of M1 is given by:

$$\mathbf{x}_{M1} = \begin{pmatrix} \cos\theta & \sin\theta & 0 \\ -\sin\theta & \cos\theta & 0 \\ 0 & 0 & 1 \end{pmatrix}\left(\mathbf{x}_{N1} + \begin{bmatrix} vt - v(t_1 - t_0) \\ R \\ 0 \end{bmatrix} \right) - \begin{pmatrix} 0 \\ R \\ 0 \end{pmatrix}$$
(3.18)

The dynamic equation of the grasper motion $\theta(t)$ is given by

$$I\ddot{\theta} + c\dot{\theta} = T_z$$
(3.19)

where I is the grasper inertia about the rotational axis; c is the friction coefficient determined experimentally; and T_z is the net torque acting on the rotating grasper by the permanent magnets.

Table 3-17 DMP model of the magnet

$\gamma = 2a/\ell$	n	k	$\delta = \bar{\ell}/\ell$	$m_i(T/m^2)\times1.0e\text{-}3, i=0,1,2$	%Error
0.25	6	1	0.9445	0.0091, 0.9097	4.66
		2	0.3105	0.1291, 0.0087, 0.3277	2.47

The DMP parameters for the magnets ($\gamma = 0.25$) are summarized in Table 3-17. Once **B** is obtained by summing the magnetic flux densities of the DMP models, the torque can be computed by the Maxwell stress tensor in Equation (2.10). The computed

torque and simulated trajectory of the moving magnets are shown in Figure 3-26. Two moving magnets M1 and M2 on the grasper are marked as circles, which move with respect to the fixed magnet N1 marked as asterisk. As compared in Figure 3-27, the simulated trajectory θ(t) agrees well with experimental data obtained using a 3-CCD digital camera.

(a) Torque on the rotating grasper   (b) Trajectory of the moving PM
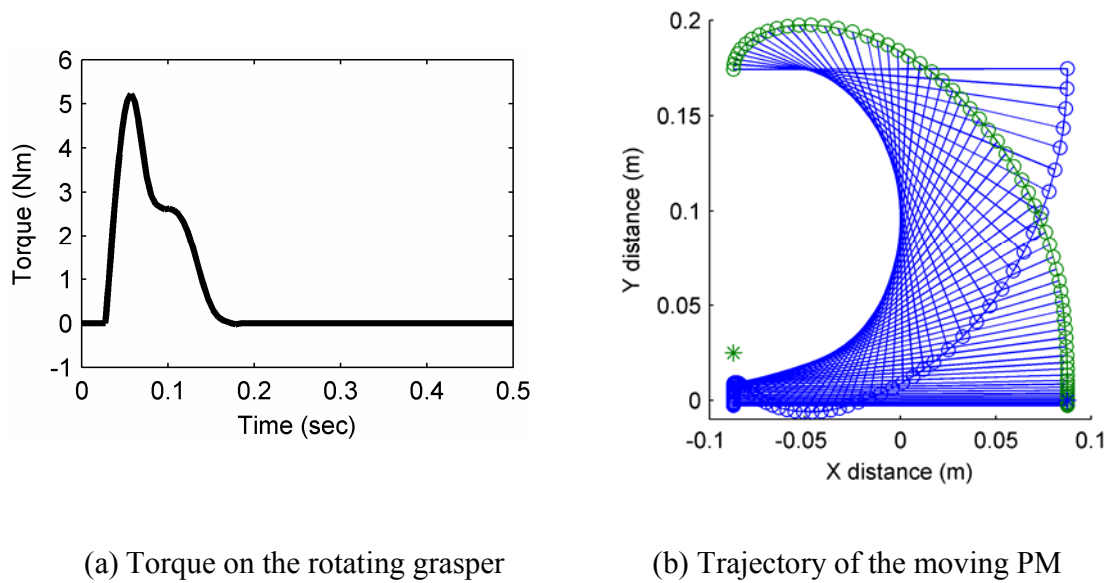
Figure 3-26 Simulated torques and trajectory
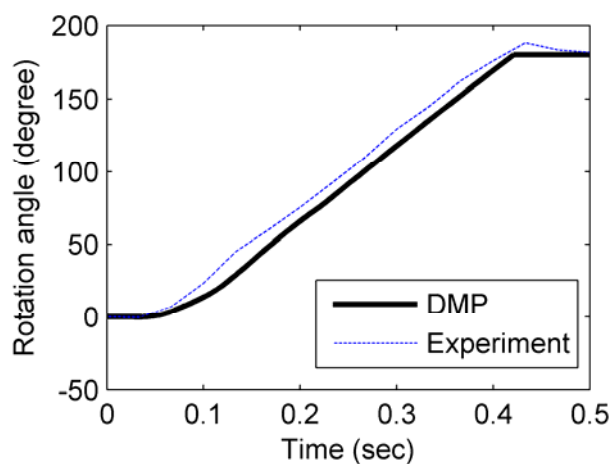
Figure 3-27 Experimental setup and simulated trajectories $\theta(t)$

In addition, the method can be easily shown for the design change such that the grasper of 180 degree rotation can be improved to control the different angle and direction such as 90 degree shown in Figure 3-28. Similarly, the motion trajectory of the grasper corresponding to the required torques is simulated in Figure 3-29.
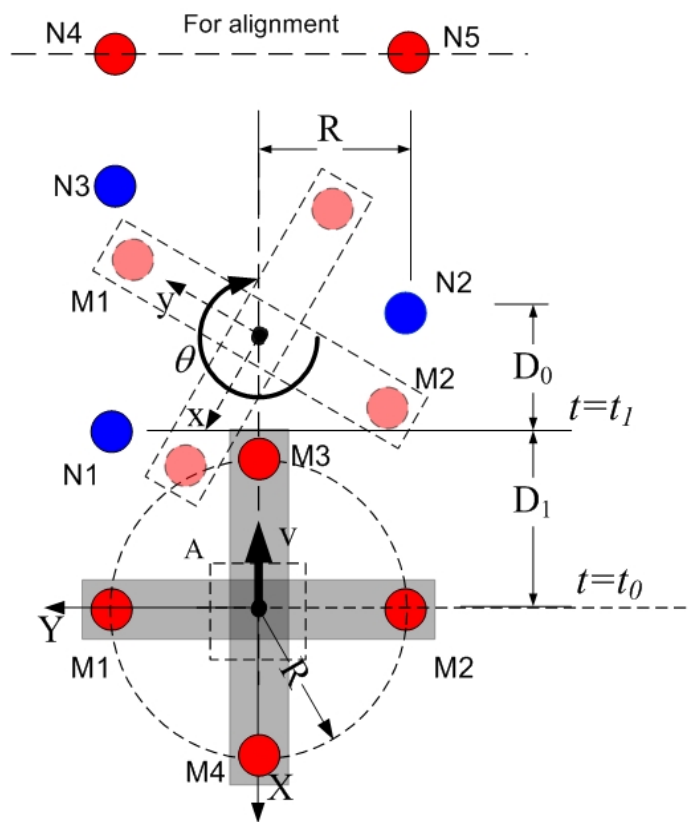
Figure 3-28 Design for the 90degree rotation and direction

(a) Trajectory

(b) Trajectory

(c) Angle

(d) Angle

(e) Torque

(f) Torque
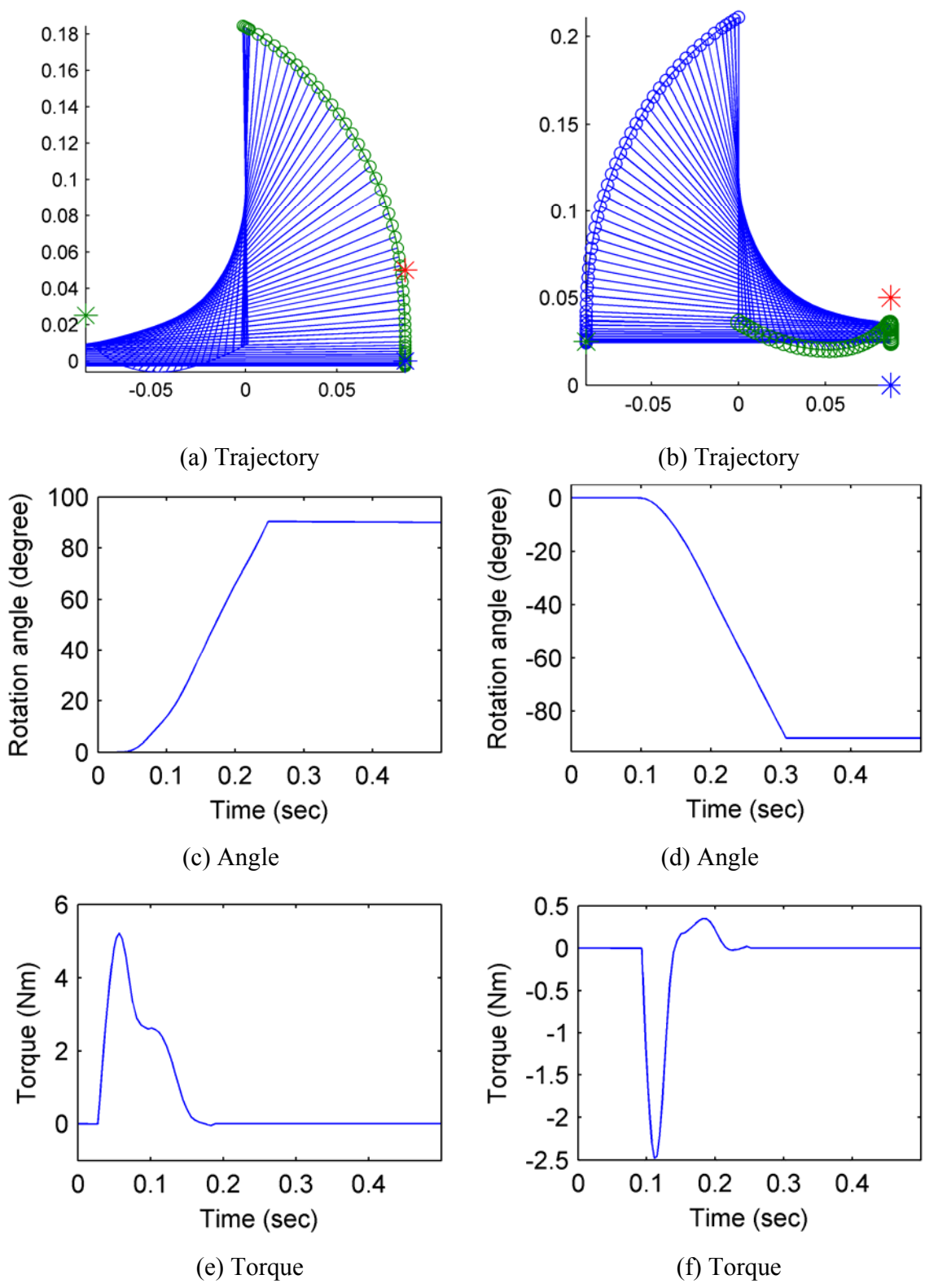
Figure 3-29 Simulations of 90 degree rotation

3.6   DISCUSSION AND SUMMARY

A number of examples have been illustrated to validate the DMP method. A relatively complete DMP model has been derived for general cylindrical magnets with axial magnetization, and validated by comparing computed results against published experimental and numerical data. The simplicity of the closed-form solution, along with precise (and yet intuitive) magnetic fields of the DMP models, has been demonstrated with four practical examples including the modeling of customized shape of PM. The results have proven that the model can be extended to a general shape of PM.

Figures 3-30 (a) and (b) illustrate further extension of the DMP method for arbitrary shape of PMs. Permanent Magnets can be separated into each shape PMs and characterized by the DMP method respectively. However, the same shape like the PM shown in Figure 3-30 (c) does not need to be separated by parts shown in Figure 3-30 (d) since the internal magnetic fields will be cancelled by each other.
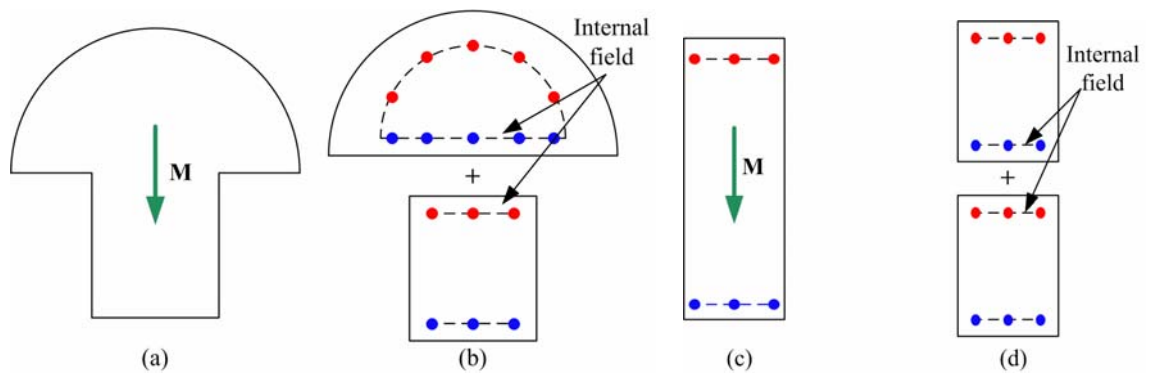
Figure 3-30 General DMP method using discretization of PMs

In the procedure of obtaining a DMP model for a multilayer electromagnet, we derive the equivalent single-layer model and the equivalent PM model that significantly reduces the computational effort for calculating the magnetic force and visualize the field interaction between the PM and the EM.

The simulated field and force are compared to the experimental results. In addition, we have illustrated the design concept, dynamic analysis of a practical PM based actuator; manipulator for live object orientation control. The DMP modeling method has been facilitated to characterize the magnetic fields, from which the magnetic force and torque are derived using the Maxwell stress tensor. The comparisons against the experimental results show excellent agreement.

CHAPTER 4

DMP BASED ORIENTATION SENSOR

4.1   OVERVIEW

This chapter describes a method to determine the orientation and position of a magnetic system consisting of a set of permanent magnets and electromagnets using the DMP model. Despite the completeness and simplicity of the DMP method, the real time computation of the orientation renders the problem more demanding in practice. The closed-form solutions of the magnetic field are nonlinear and orientation dependent. Thus, a special approach must be applied to estimate the measurable magnetic field distribution to determine the orientation and position.

The remainder of this chapter is organized as follows:

1. We introduce orientation measurement system consists of a PM and a set of magnetic sensor arrays.

2. Two methods are presented to determine the orientation of a PM in real time; absolute sensing system and an incremental approximation.

3. The simulation results of two methods are compared to the conventional dipole approximation which commonly used to analyze engineering applications. The comparison provides not only the accuracy of the developed methods but also the effectiveness.   In addition, we examine the effects of system parameters on the accuracy of the orientation measurement.

4. We illustrate a spherical wheel motor as a practical example and compute the magnetic field generated by a number of PMs of a rotor. The example offers an alternative means to validate the DMP method and also the feasibility of the sensing method.

4.2   DMP MODEL FOR SENSING MECHANISM

Figure 4-1 shows the PM based measuring system with its coordinate systems where a and ℓ are the radius and length of the cylindrical PM; and **M** is its magnetization.
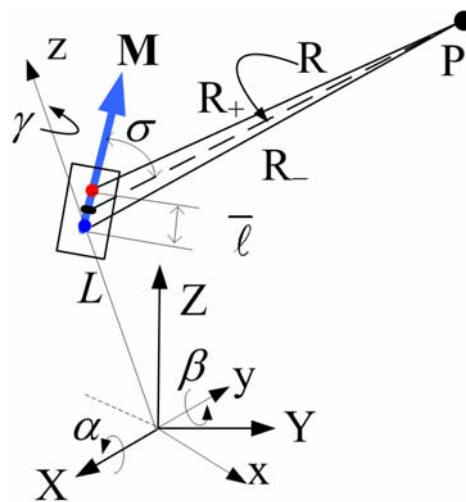

Figure 4-1 Permanent magnet based measuring system

As shown in Figure 4-1, the body-fixed xyz frame attached at the bottom (same origin as the XYZ frame), and L is a known distance from the origin to the center of the PM. The location and orientation with respect to the XYZ reference frame are described by the coordinate transformation:

$$\mathbf{P} = \Gamma(\mathbf{q})\mathbf{p} \tag{4.1}$$

$$\text{and } \Gamma(\mathbf{q}) = \begin{bmatrix} \cos\gamma\cos\beta\cos\alpha - \sin\gamma\sin\alpha & -\sin\gamma\cos\alpha - \cos\gamma\cos\beta\sin\alpha & -\cos\gamma\sin\beta \\ \sin\gamma\cos\beta\cos\alpha + \cos\gamma\sin\alpha & \cos\gamma\cos\alpha - \sin\gamma\cos\beta\sin\alpha & \sin\gamma\sin\beta \\ \sin\beta\cos\alpha & -\sin\alpha & \cos\beta\cos\alpha \end{bmatrix}$$

where $\mathbf{q} = \begin{bmatrix} \alpha & \beta & \gamma \end{bmatrix}^{\mathrm{T}}$ is the *xyz* Euler angles describing the orientation of the xyz frame.

The unit vector $\hat{\mathbf{z}}$ along the rotational shaft of the PM can be expressed in the XYZ frame as

$$\hat{\mathbf{z}} = \begin{bmatrix} \sin\beta\cos\alpha & -\sin\alpha & \cos\beta\cos\alpha \end{bmatrix}^{\mathrm{T}} \tag{4.2}$$

As discussed in Chapter 2, the cylinder PM is modeled analytically using k circular loops (each with radius $\bar{a}_j$, $j = 0, \ldots, k$) of n dipoles (strength m_j) separated by a distance $\bar{\ell}$ in parallel to its magnetization vector. The coordinates of its source and sink, $\mathbf{p}_{ji+}$ and $\mathbf{p}_{ji-}$ respectively, are known constants in the *xyz* frame. In Figure 4-1, R_{ji+} and R_{ji-} are the distances from the source and sink in the ith dipole in the jth loop, to a sensor located point $\mathbf{P}$ respectively. Based on the given parameters of the DMP method, the magnetic field expressed in XYZ reference frame can be given by

$$\mathbf{B} = \frac{\mu_o}{4\pi} \sum_{j=0}^{k} m_j \sum_{i=1}^{n_k} \left(\frac{\mathbf{a}_{Rji+}}{R_{ji+}^2} - \frac{\mathbf{a}_{Rji-}}{R_{ji-}^2} \right) \tag{4.3}$$

where $\quad R_{ji\pm} = \left| \mathbf{P} - \mathbf{P}_{ji\pm} \right|; \ \mathbf{P}_{ji\pm} = \Gamma(\mathbf{q})\mathbf{p}_{ji\pm}$

$$\mathbf{p}_{ji\pm} = \begin{bmatrix} x_{ji} & y_{ji} & z_{ji\pm} \end{bmatrix}^{\mathrm{T}}; \text{ and } \ \frac{\mathbf{a}_{Rji\pm}}{R_{ji\pm}^2} = -\frac{\mathbf{P} - \Gamma(\mathbf{q})\mathbf{p}_{ji\pm}}{\left| \mathbf{P} - \Gamma(\mathbf{q})\mathbf{p}_{ji\pm} \right|^3}$$

Equation (4.3) provides a means to determine the unknown orientation $\mathbf{q}(\alpha, \beta, \gamma)$ from the measured magnetic flux density $\mathbf{B}$ using field-based sensors. However, the unknown orientation $\mathbf{q}$ must be solved explicitly for the real-time computation.

We consider a two-sensor-pairs array on the plane $Z_s=L$ symmetrically such that the magnetic flux densities B_X and B_Y along the X and Y directions can be measured by the sensor pair $\mathbf{S}_1$ and $\mathbf{S}_2$ and the sensor pair $\mathbf{S}_3$ and $\mathbf{S}_4$ respectively.

As will be shown, the inverse problem can be formulated and solved from $B_{X\pm}$ and $B_{Y\pm}$ measured using two sensor-pairs located respectively at

$$\mathbf{S}_{1\pm} = \begin{bmatrix} \pm S & 0 & Z_s \end{bmatrix}^{\mathrm{T}} \text{ and } \mathbf{S}_{2\pm} = \begin{bmatrix} 0 & \pm S & Z_s \end{bmatrix}^{\mathrm{T}} \tag{4.4}$$

where the subscript $i\pm$ denotes the ith sensor pair.

4.3 FORMULATION OF ORIENTATION SENSOR

To allow a broader application of magnetic sensors for measuring the orientation of a three-DOF actuator in real time, two different alternatives which relax the single dipole assumption are derived in this section; incremental and absolute orientation.

4.3.1 Incremental Sensing Mechanism

One of approaches for a real time application to reduce Equation (4.3) is to compute the incremental change in orientation for every sampled time step,

$$\hat{\mathbf{q}} = \mathbf{q}_{k+1} - \mathbf{q}_k \tag{4.5}$$

such that the orientation $\mathbf{q}_{k+1}$ at the $(k+1)^{th}$ time step is computed from its previous step $\mathbf{q}_k$ based on the perturbation model of Equation (4.3):

$$[\mathbf{A}]\hat{\mathbf{q}} = \mathbf{b} \tag{4.6}$$

where $\quad \hat{\mathbf{q}} = \begin{bmatrix} \hat{\alpha} & \hat{\beta} & \hat{\gamma} \end{bmatrix}^{\mathrm{T}}$; $\mathbf{b} = \begin{bmatrix} \mathbf{B}(\mathbf{q}_{k+1}) - \mathbf{B}(\mathbf{q}_k) \end{bmatrix}$

and
$$[\mathbf{A}] = \begin{bmatrix} \dfrac{\partial \mathbf{B}}{\partial \alpha} & \dfrac{\partial \mathbf{B}}{\partial \beta} & \dfrac{\partial \mathbf{B}}{\partial \gamma} \end{bmatrix}_{\mathbf{q}=\mathbf{q}_k} \in \mathbb{R}^{j \times 3}$$

For a sensor located at $\mathbf{P}$,

$$\frac{\partial \mathbf{B}}{\partial q} = -\frac{\mu_o}{4\pi} \sum_{j=0}^{k} m_j \sum_{i=1}^{n_k} \frac{\partial}{\partial q} \left(\frac{\mathbf{R}_{ji+}}{|\mathbf{R}_{ji+}|^3} - \frac{\mathbf{R}_{ji+}}{|\mathbf{R}_{ji+}|^3} \right) \tag{4.7}$$

where q denotes Euler angles α, β or γ, and $\mathbf{R}_{ji\pm} = \mathbf{P} - \mathbf{P}_{ji\pm}$.

The partial derivative in Equation (4.7) is given by

$$\frac{\partial}{\partial q} \left(\frac{\mathbf{R}_{ji\pm}}{|\mathbf{R}_{ji\pm}|^3} \right) = -\frac{1}{|\mathbf{R}_{ji\pm}|^3} \frac{\partial \mathbf{P}_{ji}}{\partial q} + \left(3 \begin{bmatrix} \mathbf{R}_{ji\pm} \end{bmatrix}^{\mathrm{T}} \frac{\partial \mathbf{P}}{\partial q} \right) \frac{\mathbf{R}_{\pm}}{|\mathbf{R}_{ji\pm}|} \tag{4.8}$$

where $\qquad \partial \mathbf{P}_{ji\pm} / \partial q = \nabla \begin{bmatrix} \Gamma(\mathbf{q})\mathbf{p}_{ji\pm} \end{bmatrix}$

and $\qquad \nabla = \partial / \partial \alpha + \partial / \partial \beta + \partial / \partial \gamma$

The detail expression of Equation (4.8) is presented in Appendix A.

Once the matrix $[\mathbf{A}]$ in Equation (4.6) is computed, the updated orientation can be obtained:

$$\mathbf{q}_{k+1} = \mathbf{q}_k + \left([\mathbf{A}]^{\mathrm{T}} [\mathbf{A}] \right)^{-1} [\mathbf{A}]^{\mathrm{T}} \mathbf{b} \tag{4.9}$$

Equations (4.3) and (4.9) provide a general formulation of a field-based sensor for incremental orientation measurement in the real-time computation. However, incremental measurement, in general, is susceptible to cumulative errors and updating rate of measurement. Thus, an absolute orientation measurement is discussed in the next section.

4.3.2   Absolute Orientation with Polynomial Approximation

To provide a means to determine the absolute orientation in real time, we express the magnetic field density $\hat{B}$ as a special from of a polynomial function which can be accurately approximated the field in the range of motion. In addition, this function is desired explicitly to solve the inverse problem of computing the rotor orientation from the measured magnetic field.

Measured B-field approximation

In general, the magnetic field of a rotating PM $\hat{B}$ can be approximated as the nth order polynomial form:

$$\hat{B}_k(\alpha, \beta) = \sum_{i=0}^{n} \sum_{j=0}^{n} c_{ij} C_k^j S_k^i \tag{4.10}$$

where the subscript k denotes the kth sensor; and n is the order of the approximation. For the sensor pairs defined in Equation(4.4), $B_{X\pm}$ is an even function of α but odd function of β, and vice versa for $B_{Y\pm}$. Thus, C_k and S_k have the form:

For $B_{X\pm}$: $\qquad\qquad C_1 = C_2 = \cos\alpha$ and $S_1 = -S_2 = \sin\beta \tag{4.11}$

For $B_{Y\pm}$: $\qquad\qquad C_3 = C_4 = \cos\beta$ and $S_3 = -S_4 = \sin\alpha \tag{4.12}$

Using the least-square method, the coefficients c_{ij} in Equation (4.10) can be obtained by minimizing the summed squared error

$$E_k = \sum_{i=1}^{n_i} \sum_{j=1}^{n_j} \left[B_k(\alpha_i, \beta_j) - \hat{B}_k(\alpha_i, \beta_j) \right]^2 \tag{4.13}$$

where $B_k(\alpha, \beta)$ is the analytical solution of the magnetic field at points from Equation (4.3).

Solutions to the Inverse Problem

Once $\hat{B}$ is modeled, the orientation (α, β) can be obtained by solving the inverse problem; the solution depends on the order of the approximation. In general, two equations can be obtained for each of sensor pairs:

$$\bar{B} = \frac{\hat{B}_+ + \hat{B}_-}{2} = \sum_{i=0}^{n}\left(\sum_{j=0}^{n} c_{ij} C^j\right) S^i \quad \text{where } i \text{ is even.} \tag{4.14}$$

$$\tilde{B} = \frac{\hat{B}_+ - \hat{B}_-}{2} = \sum_{i=1}^{n}\left(\sum_{j=0}^{n} c_{ij} C^j\right) S^i \quad \text{where } i \text{ is odd.} \tag{4.15}$$

Two independent sets of inverse solutions, $\left[\hat{\alpha}_1, \hat{\beta}_1\right]$ and $\left[\hat{\alpha}_2, \hat{\beta}_2\right]$, can be solved from the pair of equations; one from each sensor pair. The orientation angles are estimated as follows:

$$\begin{bmatrix} \hat{\alpha} \\ \hat{\beta} \end{bmatrix} = \mathbf{W_1} \begin{bmatrix} \hat{\alpha}_1 \\ \hat{\beta}_1 \end{bmatrix} + \mathbf{W_2} \begin{bmatrix} \hat{\alpha}_2 \\ \hat{\beta}_2 \end{bmatrix} \tag{4.16}$$

where $\mathbf{W_1}$ and $\mathbf{W_2}$ are the 2×2 weighting matrices of given sensor pair respectively. For the sensor pair defined in Equation (4.3), the following matrices are chosen since a pair of sensors along x-axis are independent to the other along the y-axis :

$$\mathbf{W_1} = \begin{bmatrix} 1 & 0 \\ 0 & 0 \end{bmatrix}, \mathbf{W_2} = \begin{bmatrix} 0 & 0 \\ 0 & 1 \end{bmatrix} \tag{4.17}$$

Illustrative Example

For the first order approximation ($n=1$), the inverse solutions are given by:

$$\bar{B}_X = \left(\hat{B}_{X+} + \hat{B}_{X-}\right)/2 = c_{00} + c_{01}\cos\alpha \tag{4.18}$$

$$\tilde{B}_X = \left(\hat{B}_{X+} - \hat{B}_{X-}\right)/2 = \left(c_{10} + c_{11}\cos\alpha\right)\sin\beta \tag{4.19}$$

$$\overline{B}_Y = \left(\hat{B}_{Y+} + \hat{B}_{Y-} \right)/2 = c_{00} + c_{01} \cos \beta \qquad (4.20)$$

$$\tilde{B}_Y = \left(\hat{B}_{Y+} - \hat{B}_{Y-} \right)/2 = \left(c_{10} + c_{11} \cos \beta \right) \sin \alpha \qquad (4.21)$$

Two estimated solutions are obtained independently from Equations (4.18), (4.19) and (4.20), (4.21) independently:

$$\hat{\alpha}_1 = \cos^{-1}\left[\left(\overline{B}_X - c_{00} \right)/c_{01} \right] \; ; \; \hat{\beta}_1 = \sin^{-1}\left[\tilde{B}_X / \left(c_{10} + c_{11} \cos \hat{\alpha}_1 \right) \right]$$

Similarly, from Equations (4.14) and (4.15),

$$\hat{\alpha}_2 = \cos^{-1}\left[\left(\overline{B}_Y - c_{00} \right)/c_{01} \right] \; ; \; \hat{\beta}_2 = \sin^{-1}\left[\tilde{B}_Y / \left(c_{10} + c_{11} \cos \hat{\alpha}_2 \right) \right]$$

Higher order approximations, though lengthy, can be solved similarly. In general, the inverse solutions become complex as the order increases.

4.4   COMPUTATIONAL RESULTS AND DISCUSSIONS

To provide some insights to the orientation measurement systems, we simulate here the performance of the sensing methods by computing the measurement errors, and compare the absolute orientation against the single–dipole approximation method and incremental measurement with the apparatus of the single PM. In addition, we also investigate the effects of sensor location and orientation on the measurement performance through simulations.

4.4.1   Effect of the polynomial order

We simulate the magnetic field of two sensor-pairs defined in Equation (4.4). The values of the apparatus parameters used in the simulation are listed in Table 4-1. Figure 4-2 (a) graphs the analytical solutions of the magnetic field B_Y at point P(0, S, Z_s) using

Equation (4.3) over the (α, β) range of $\pm20°$, for which the simulated measurements of constant $B_{X\pm}$ and $B_{Y\pm}$ contours (in Tesla) are plotted in Figure 4-2 (b). Since the sensors are placed symmetrically about the X and Y axes in the reference frame, only one sensing quadrant is here presented to show the **B**-field. As expected, the contours are circular in nature and sensor readings decrease nonlinearly as the PM moves towards the center or further away.

Table 4-1 System parameters

Permanent Magnet
M=1.35T, a=0.25inch, L=0.5inch

Dipole parameters (k=1,n=6)
δ=0.5136
m_o=-0.229; m_{1i}=0.618
Model error = 1%

Sensor location and orientation
S=0.85inch, Z_s=1.25inch
Measured magnetic flux
$s_{1\pm} = \pm B_x\, e_x$
$s_{2\pm} = \pm B_y\, e_y$

Table 4-2 Coefficients of **B** field

c_{ij}	1st	2nd	3rd
c_{00}	-0.3187	0.2440	13.0731
c_{01}	0.3439	-0.6157	-40.2560
c_{02}		0.3984	41.2166
c_{03}			-14.0072
c_{10}	1.5028	-24.63	-39.7679
c_{11}	-1.6099	52.1366	117.58
c_{12}		-27.6219	-114.792
c_{13}			36.89
c_{20}		92.9403	-1733.83
c_{21}		-195.3960	5449.07
c_{22}		102.7010	-5709.5
c_{23}			1994.51
c_{30}			5812.28
c_{31}			-18211.4
c_{32}			19019.7
c_{33}			-6621.01
Max. error	17.6%	8.3%	0.9%

For the given sensor pairs, the coefficients in Equation (4.10) are computed using Matlab Optimization toolbox minimizing the error in Equation (4.13); the results of three different orders of approximation are given in Table 4-2. Figures 4-3 (a), (b) and (c) compare the magnetic field densities and errors approximated using the 1st, 2nd and 3rd orders respectively.
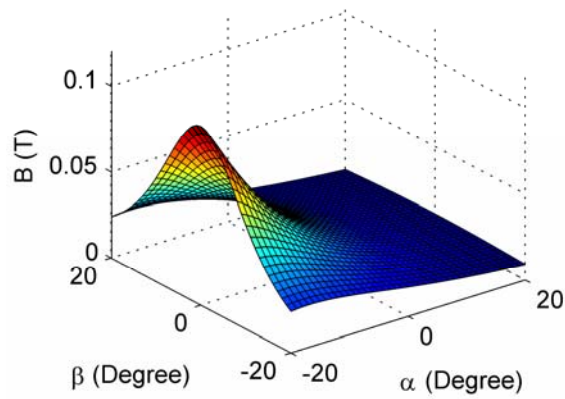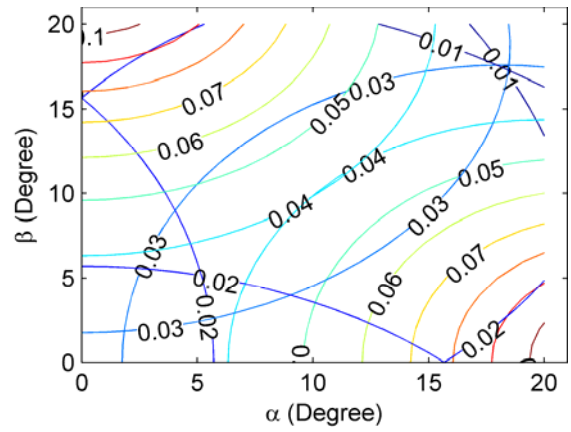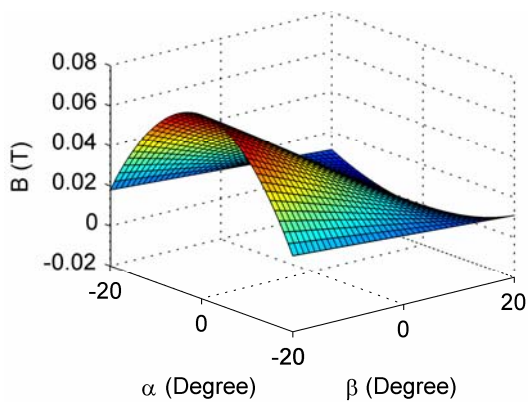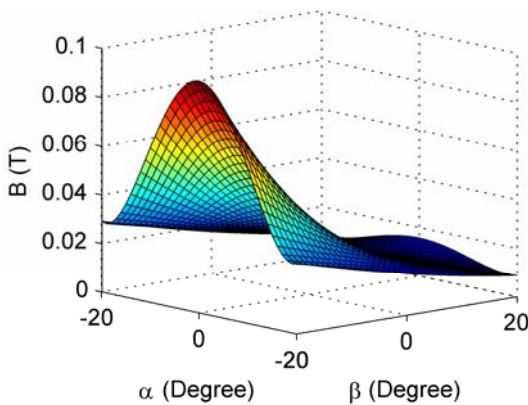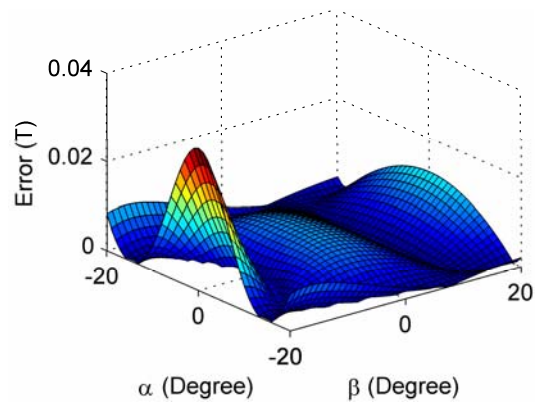
(a) Analytical solution　　　　　　　(b) Simulated B_{x+} and B_{y+} measurements

Figure 4-2 Exact solutions and simulated measurement*s*

(a) First order approximation
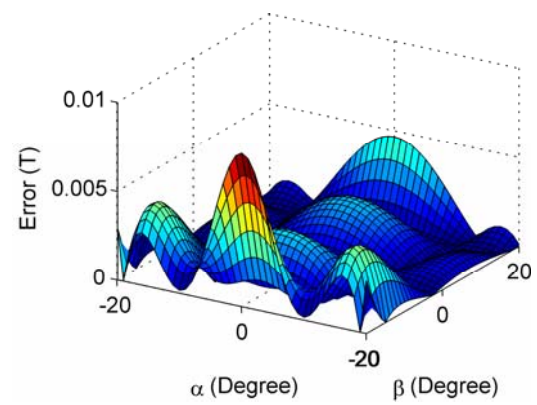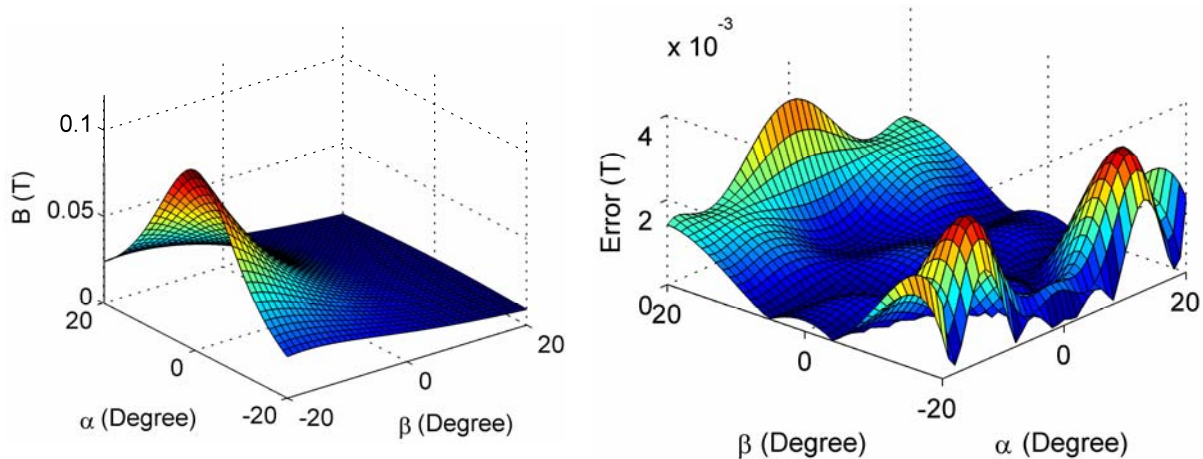

(b) Second order approximation

Figure 4-3 Approximated magnetic field density (continuous)

(c) Third order approximation

Figure 4-3 Approximated magnetic field density

As shown in Figure 4-3 (a), the first order approximation, which is linear in the change of α and β, relatively poor in capturing sharp changes. The maximum error, however, can be reduced by increasing the order of the approximation as compared in Table 4-2. With the third order approximation, the maximum error can be kept within 1% as shown in Figure 4-3 (c) where the errors are relatively uniform over the measured range.

Figure 4-4 (a) shows the circular trajectory of the shaft inclined at 10° from the Z-axis. The measurement errors (in radians) corresponding to the three different orders (n=1, 2, 3) of the approximation are plotted in Figures 4-4 (b), (c) and (d) respectively. Figure 4-5 compares the maximum errors of the absolute orientation measurement against two other methods of approximation; single–dipole approximation and incremental orientation measurement.

Several observations can be made from the results:

i)   Single dipole approximation, which neglects the physical dimension of the magnet, offers limited accuracy as shown in Figure 4-5.

ii)   As compared in Figure 4-5 and Table 4-2, the measurement errors based on polynomial approximation decrease as the order increases. For the range of ±20°, errors less than 5 *μradians* can be obtained with the third order approximation.

iii) The errors of the incremental measurement depend on step size as shown in Figure 4-6. Generally, the step size is various as sampling time and speed of motion. However, the small step size is preferred to increase the accuracy of sensors.

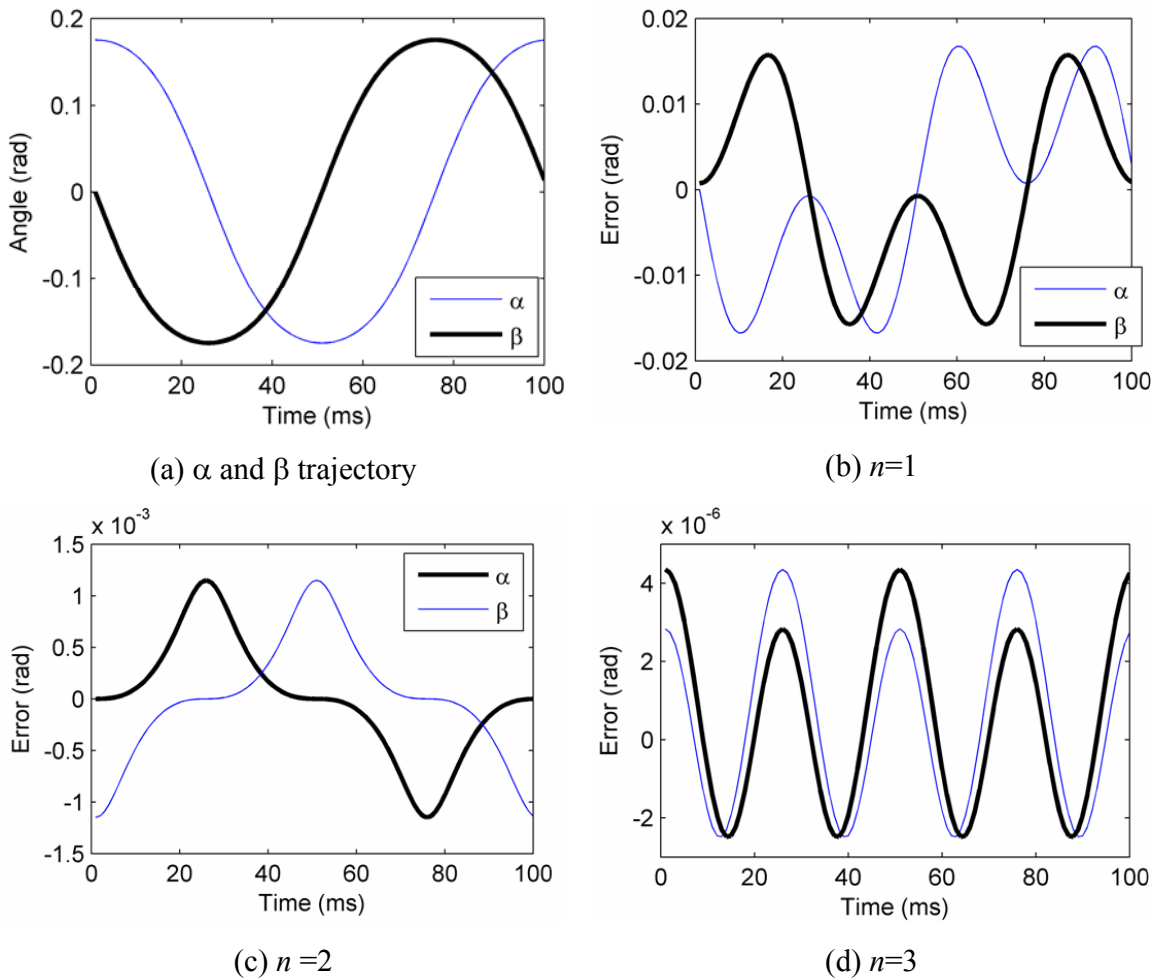(a) α and β trajectory   (b) *n*=1

(c) *n* =2   (d) *n*=3

Figure 4-4 Absolute orientation measurement errors (10° inclination)
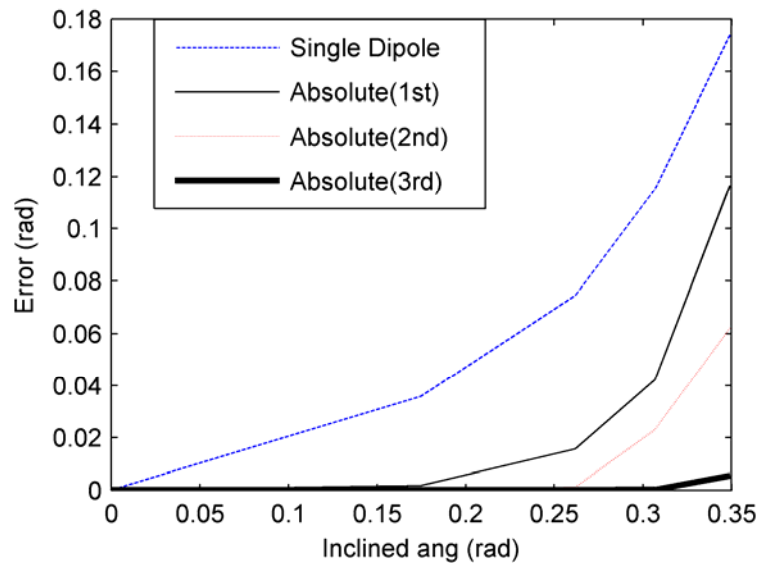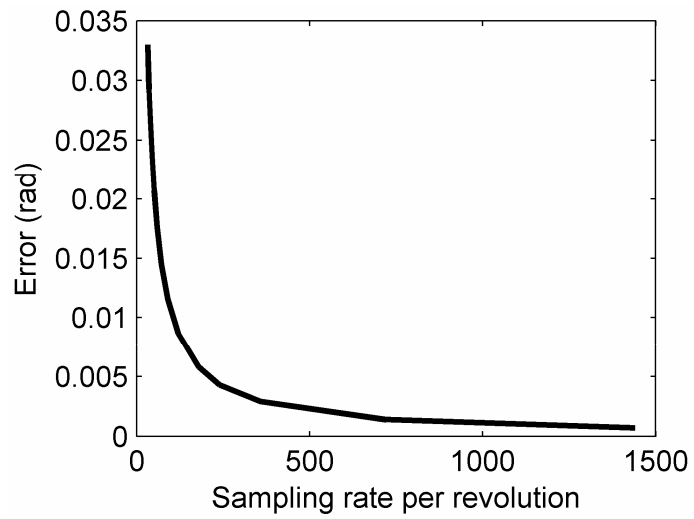
Figure 4-5 Comparison of maximum errors

Figure 4-6 Effects of sampling rate on incremental measurement (10° inclination)

4.4.2 Effect of Sensor Location and Orientation

The two orientation angles α and β can be theoretically computed from any two of four equations. We exploit the redundancy for improving the sensor performance. To provide some insights to the choice of the weighting matrices in Equations (4.16) and (4.17), we simulate the setup where both pairs of sensors measure the magnetic field density in the Y-direction $\hat{B}_{Y\pm}$ located on the following coordinates:

$$\mathbf{S}_{1\pm} = \begin{bmatrix} \sqrt{2}S & \pm\sqrt{2}S & Z_s \end{bmatrix}^{\mathrm{T}}$$

$$\mathbf{S}_{2\pm} = \begin{bmatrix} \pm\sqrt{2}S & \sqrt{2}S & Z_s \end{bmatrix}^{\mathrm{T}}$$

(4.22)

where $C_1 = C_2 = -C_3 = -C_4 = \sin\alpha$ and $S_1 = -S_2 = -S_3 = S_4 = \sin\beta$

Figure 4-7 summarizes the results of the simulation, where the corresponding coefficients in Equations (4.14) and (4.15) are given in Figure 4-7 (b). Figure 4-7 (a) shows the exact solution of the magnetic field. Figure 4-7 (c) graphs the magnetic field based on the 2$^{\text{nd}}$ order approximation and its modeling error of the magnetic field. As compared in Figures 4-7 (d) and (e), since both pairs of sensors measure the magnetic field density in the Y-direction $\hat{B}_{Y\pm}$, the β angles are measured much more accurately than the α angle.
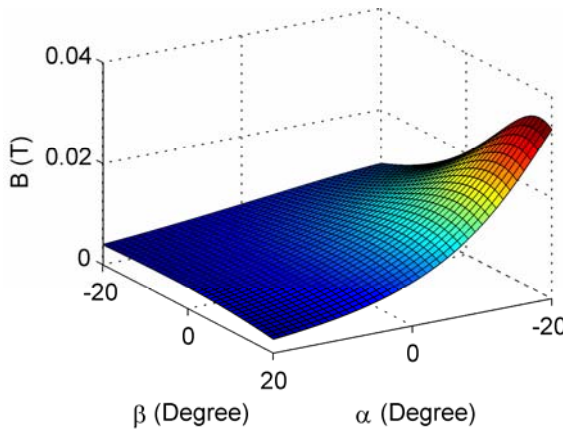
c_{ij}	1st	2nd
c_{00}	0.0104	0.0099
c_{01}	-0.0254	-0.0249
c_{02}		0.0243
c_{10}	0.0104	0.0047
c_{11}	-0.0584	-0.0583
c_{12}		0.1352
c_{20}		-0.0188
c_{21}		-0.0130
c_{22}		0.1875

(a) Analytical solutions
(b) coefficients
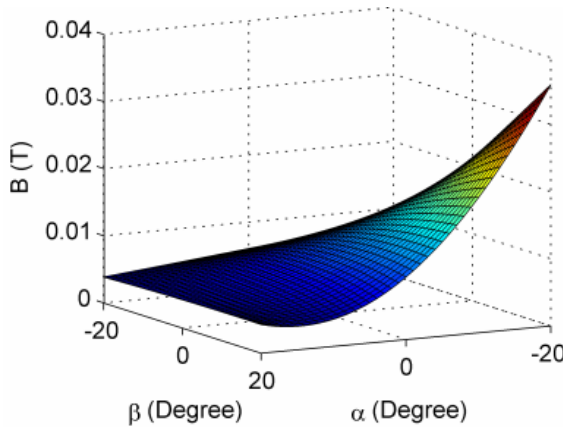
(c) Second order approximation of magnetic field density
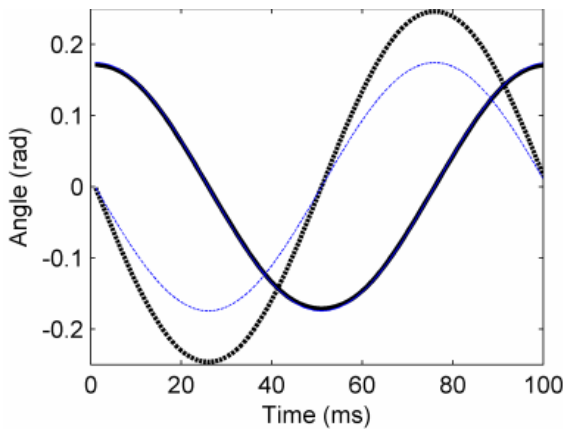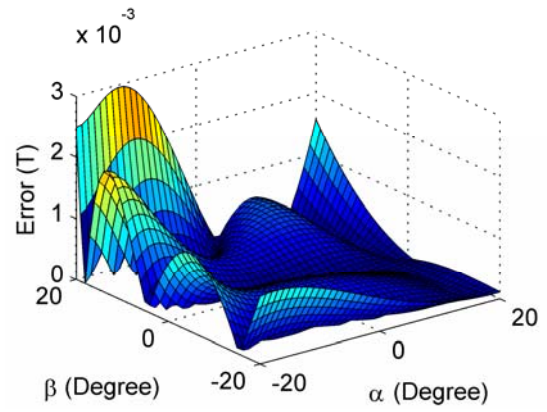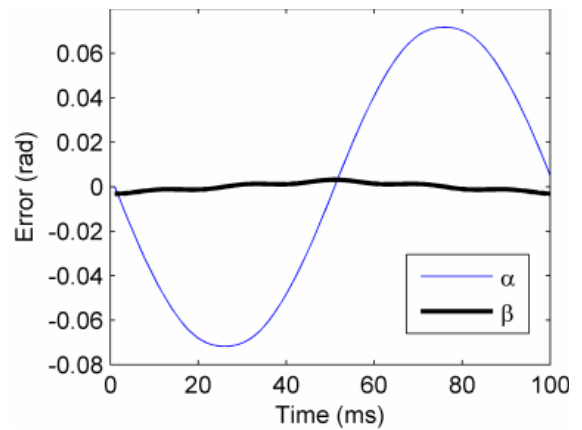
(d) Orientation angles
(e) α and β measurement errors

Figure 4-7 Effects of sensor locations on measurement errors

4.5   ORIENTATION SENSOR OF SWM

4.5.1   Absolute orientation

The sensing methodology is directly applied to measure the orientation as shown in Figure 4-8. Since the magnetization of a permanent magnet installed on the top is parallel to the rotor shaft, only orientation of the rotor can be measured. However, if the length of L_e is short, the rotor PMs make an influence to the sensor measurement which cause decreasing the accuracy. In order to avoid the interaction of both orientation PM and rotor PMs and thus obtain accurate measurement, the height of the orientation PM should be long enough. However, if it is too long, it may cause an effect on the dynamic response as well as the stability of rotor since the center of gravity is higher than the center of rotation. For this, L_e should be appropriately chosen.
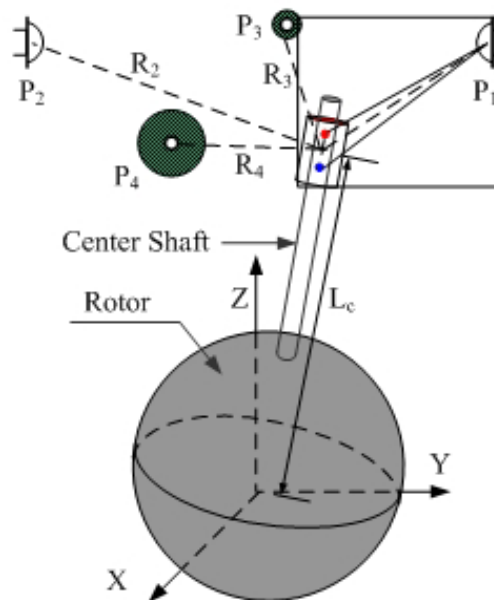
Figure 4-8 Spherical Wheel Motor and its sensors

Figures 4-9 and 4-10 show potential field and magnetic field **B** with and without the interaction of rotor PMs on the sensor measurement with L_e=2.75 inch respectively. The length L_e here is chosen to minimize the effects of rotor poles on the sensor sensitivity which of Hall Effect sensor is on average less than one Gauss.
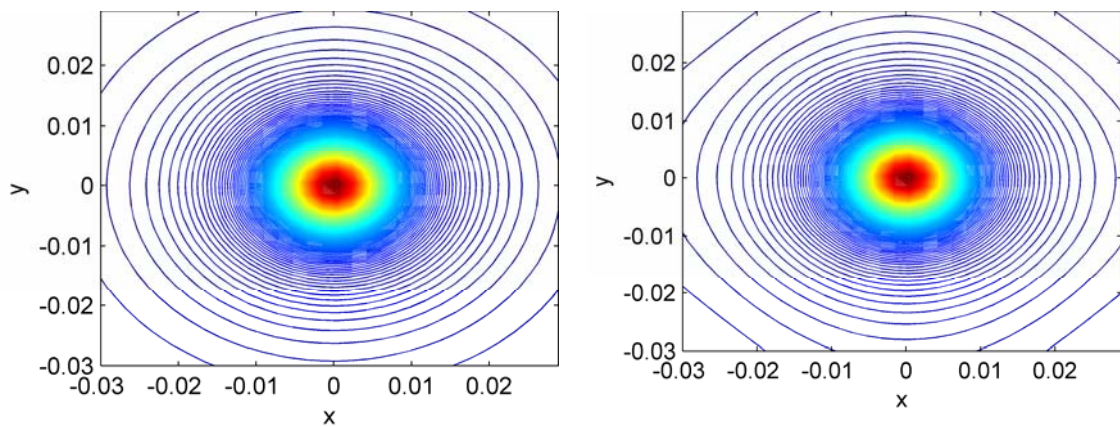
(a) Potential field without the rotor PMs   (b) Potential field with the rotor PMs

Figure 4-9 Potential field at (α=β=0)

Similarly, Figures 4-10 (a) and (b) show the influence of the rotating rotor on the sensor with and without the SWM respectively. The polarity change of the spinning rotor results in the oscillatory measurement as expected. However, the error in the range of motion in Figure 4-10 (c) is relatively small such that the maximum error is at the maximum inclination within the resolution of the sensor.

Once we validate the effect of rotor poles on the orientation PM, the sensor sensitivity and its resolution, the orientation can be measured by both the absolute and the incremental methodology.
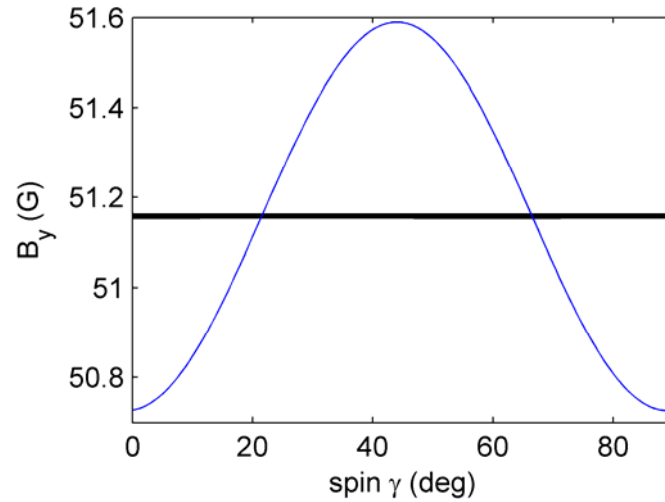
(a) Field interaction for spin
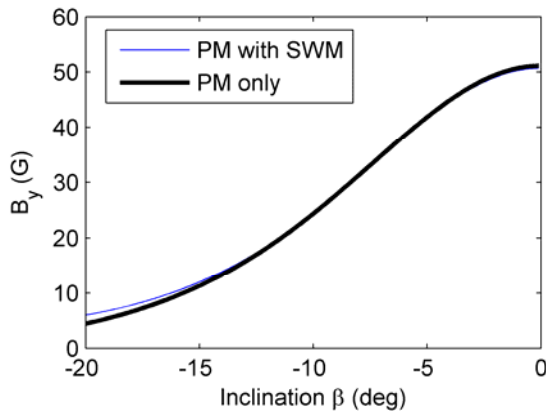
(b) Field interaction for inclination
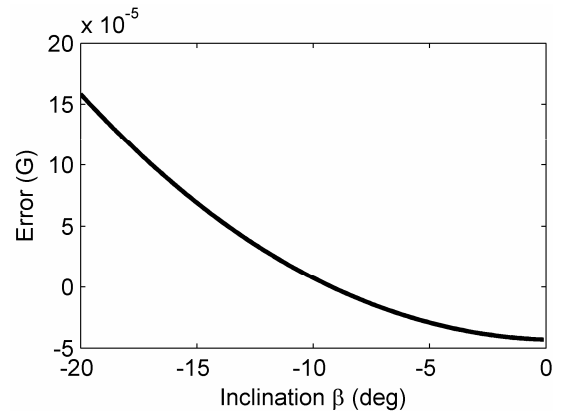
(c) Error of field for inclination

Figure 4-10 Magnetic field interaction of rotor PMs

4.5.2　Incremental orientation with spinning

The absolute measurement is difficult to measure the spin rate/angle since the field variation becomes more complicated as the number of unknown orientation is increasing. In addition, the formulations may not be explicitly solved to acquire the orientation for the real-time even if it formulates the closed form of the magnetic field.

However, the incremental method offers to measure the orientation without the change of the fundamental formulation.

Figure 4-11 shows the set of Hall Effect sensors directly measuring the magnetic field of rotor PMs on the top. The system doesn't require an additional magnet for measurement, which retain the system simple but it offers to measure not only the orientation of the shaft but also the spinning angle.
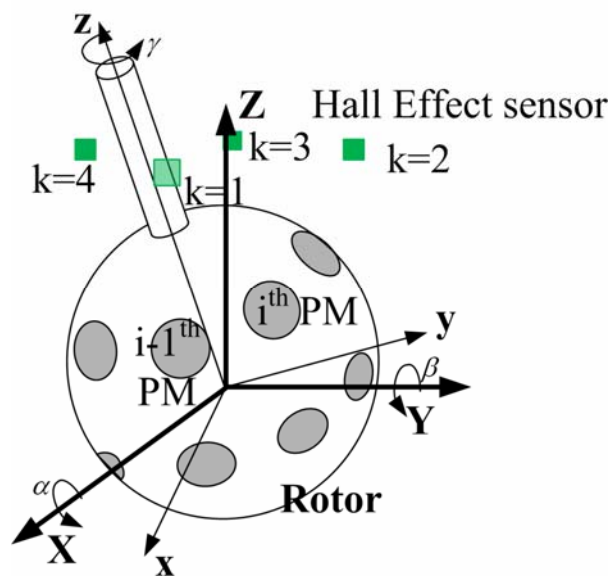
Figure 4-11 Hall Effect sensors for directly measuring the field of the SWM

The magnetic field inside the SWM can be expressed by the DMP model in Chapter 2 and the simulated **B** fields in a quadrant plane from the top view and in the vertical plane are shown in Figure 4-12. Compared to the **B**-field of the single PM, the SWM has a number of PMs and three orientation angles (α, β, γ) must be measured in real-time. These make the problems very challenging. For this, we extend the incremental orientation. In addition, we further investigate the effects of sensor location and sampling rate on the performance of incremental method.

(a) XY Plane	(b) XZ plane
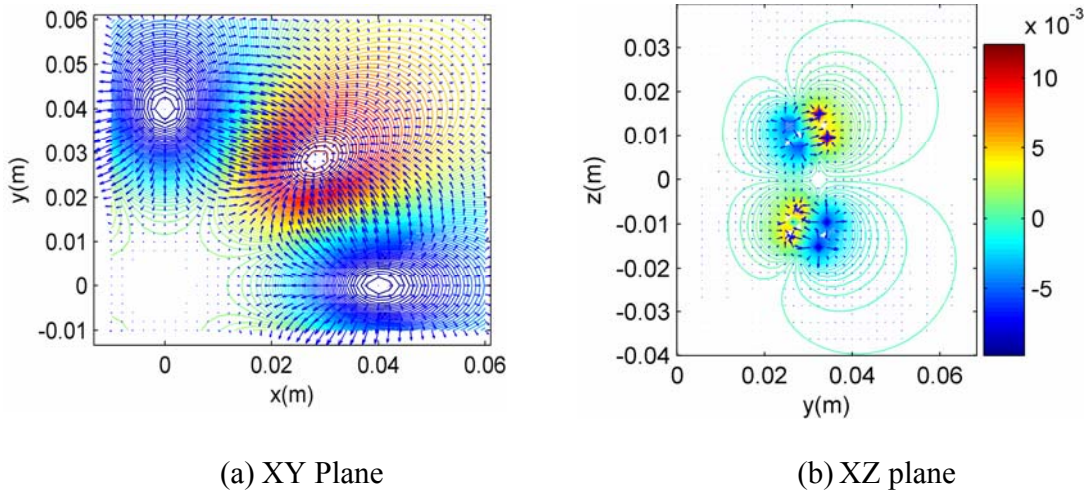
Figure 4-12 Magnetic flux density of SWM

Figure 4-13 shows two different setups of sensor locations for the spherical motor. The sensors are located in [±a 0 h] and [0 ±a h] where a=0.0305, h= 0.033 on the top and h=0.0016 in the middle respectively. Hexagons represent the surface of PMs and asterisks are Hall Effect sensors. To demonstrate the performance, the SWM rotates one revolution about the Z-axis with the inclination angle α between z-axis (rotor shaft) and Z-axis without the rotating shaft. Figure 4-14 shows the measured **B**-field in a sensor since the location of sensors is symmetric in the XY plane and the estimated error of orientation angle respectively. As expected, the **B**-field measured in the middle is five times stronger than on the top and thus, its error becomes small. In practical implementation, it also increases the signal and noise ratio. Similarly, Figure 4-15 is simulation results of two pairs and four pairs of sensors respectively. The additional two pairs sensors are located at [$a\cos(i\pi/2+\pi/4)$ $a\sin(i\pi/2+\pi/4)$ h] where i=1, 2, 3, 4 on the top and in the middle respectively. As the number of sensors increases, the accuracy of the orientation is accordingly increased. Both four pairs in Figure 4-15 offer more accurate measurement compared to the two pairs in Figure 4-14.

(a) Design A   (b) Design B
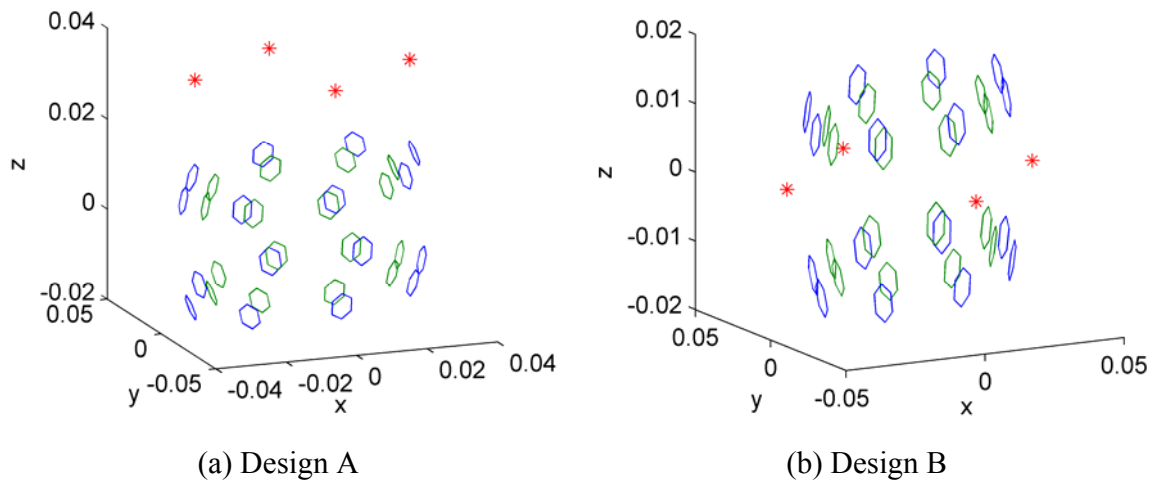
Figure 4-13 Sensors of spherical wheel motor

(a)B-field on the top   (b) B-field in the middle

(c) Error on the top   (d) Error in the middle
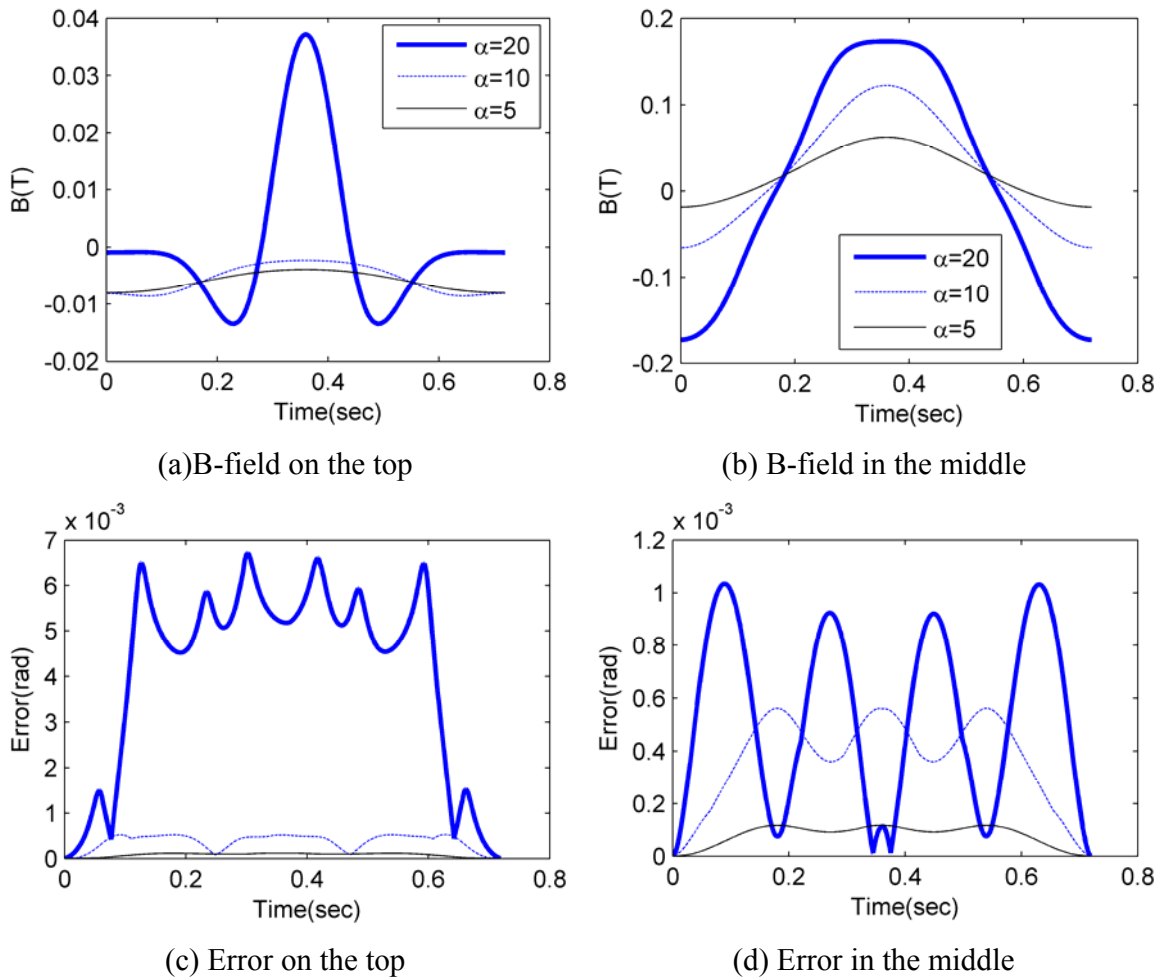
Figure 4-14 Computed **B**-field measured by a sensor and orientation error (γ=0)

(a) Four pairs on the top   (b) Four pairs in the middle
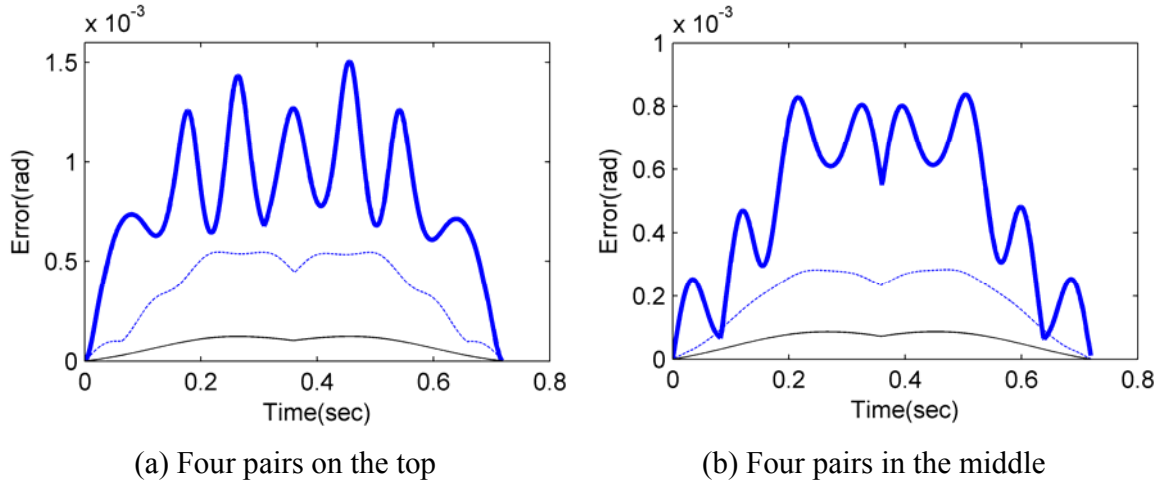
Figure 4-15 Effect of error on the number of sensor

Effect of the sampling frequency

In the incremental sensing method, the sampling rate is an important factor for accurate measurement since the current measurement is continuously computed from the previous. Thus, the measurement error is accumulated for every step. To investigate the effect of the sampling rate on the sensor performance, non-dimensional parameter is defined as

$$\varpi = \frac{f_{Sensor}}{f_{PM}} \tag{4.23}$$

where f_{sensor} is the sampling frequency of the sensor and f_{PM} is rotor angular velocity .
The parameter ϖ physically means the number of sampled data per unit angle of orientation change. In the similar to the previous examples, the orientation without the spinning is first simulated. Figure 4-16 shows the simulation results for the two and four pair's sensors respectively. The error is inversely decreasing as the ratio ϖ is increasing. Since the rate of the orientation change is relatively slow compared to the spinning and

also the rotor polarity doesn't change with respect to each sensor, the measurement for the orientation is not required to high sampling rate.

(a) Two pairs   (b) Four pairs
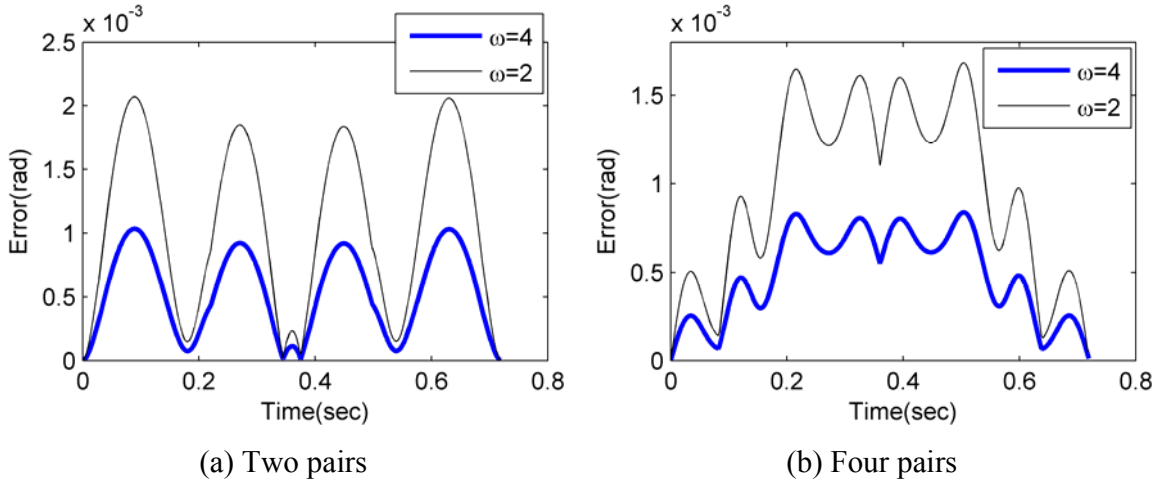
Figure 4-16 Effect of Error on sampling frequency (f_{PM}=2.78Hz, α=20°)

Figure 4-17 shows the performance of the orientation measurement of the rotating shaft with $\varpi = 2$ which indicates two sampled data per unit change of spin angle. Unlike the previous results with only change of the orientation, the **B**-field is changed at the high frequency which has the same period as the change of rotor polarity with respect to the sensor. Thus, the error of the orientation with spinning is increasing with the same ϖ compared to the error without spinning in Figure 4-14.

Some observation can be further discussed as follows:

1. The frequency of the measured **B**-field depends on the spin of the rotor and it becomes higher frequency at the same spin rate as the number of poles increases. The accuracy can be improved as increasing the sampled rate.

2. The orientation of the rotor is related to the magnitude of the measured signals. When the rotor is inclined and rotor poles are close to the sensor, the magnitude of the output voltage become large as shown in Figure 4-7 (a).

3. The accuracy of the spin angle affects the orientation since the Jacobian matrix [**A**] in Equation (4.6) is fully coupled. In addition, the method has an intrinsic disadvantage that the error is accumulated for every computation. As the spin rate of the rotor is increasing, errors of both spin and orientation are coupled and increasing. To reduce the effect, the accumulated error in the spin motion must be periodically reset to be zero.
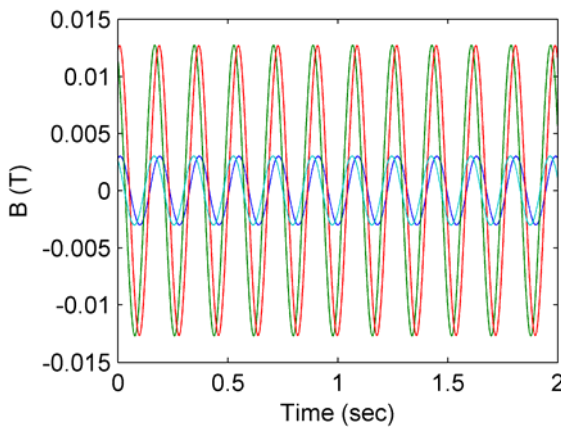
(a) Magnetic flux **B**
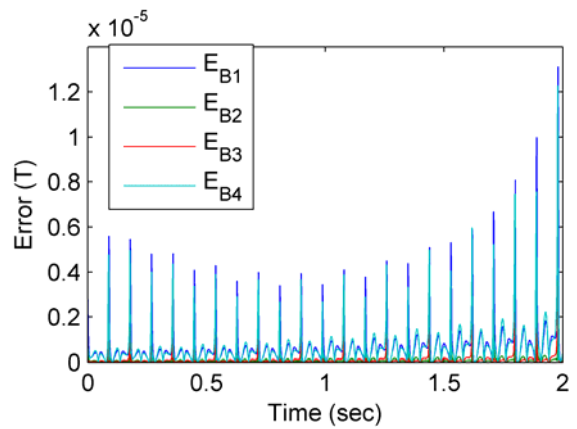
(b) Error of B
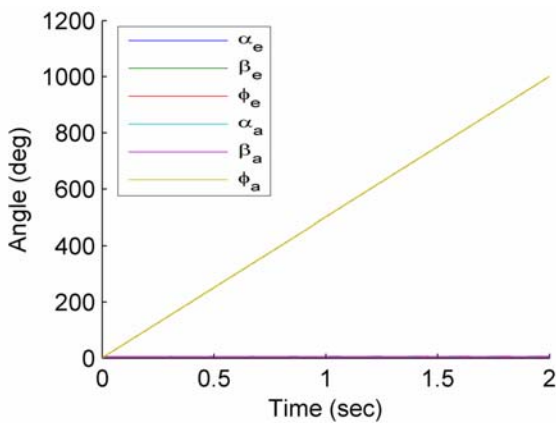
(c) Angle measurement
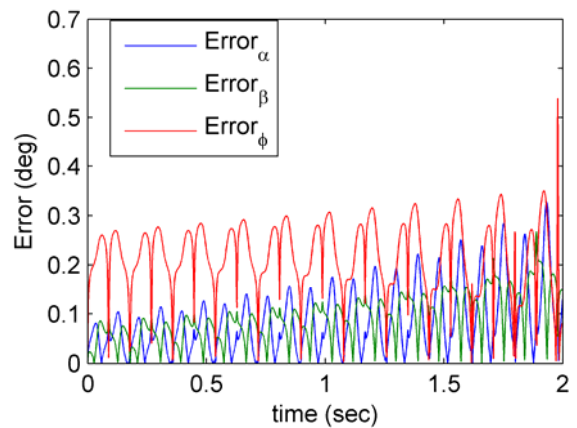
(d) Error of measurements

Figure 4-17 Simulated sensor measurement of spinning ($\varpi = 2$ and $\alpha=\beta=5°$)

4.6 SUMMARY

This chapter has presented a novel approach to measure an orientation of a PM-based device. Since the method exploits the DMP model which predict accurate magnetic field, it can utilize magnetic sensors to measure existing magnetic field and obtain the orientation by inversely solving the DMP model. The ability to characterize magnetic fields and forces in addition to orientation sensing can offer a number of advantages the force and torque computations and control in real-time. In addition to it, a number of advantages of this method can be summarized as follows:

- Mechanical contact free which eliminates mechanical friction and backlash.

- Compact design since its size is relative small and also a mechanical structure such as linkage is not needed.

- Cost efficiency since a magnetic sensor such as Hall Effect sensor is generally inexpensive.

- High accuracy with real-time computation since the magnetic field can be uniquely and fast predicted by the DMP model.

The single PM apparatus has been illustrated to demonstrate the feasibility of the sensing method. The simulation results are given to provide insights to the performance of the methods by computing and comparing the measurement errors. With successful validation, the method has immense potential for diverse engineering measurement applications and it will demonstrate a spherical wheel motor in next chapter.

CHAPTER 5

DMP BASED CONTROL OF SPHERICAL MOTOR

5.1   OVERVIEW

This chapter presents a control system design for the SWM. An effective control scheme is developed to decouple the spin motion from the inclination. This leads to a practical an open-loop (OL) control system that combines a switching (spin-rate) controller and a model-based inclination controller that uses the principle of push-pull operation. The OL system presented here provides the fundamental control structure for the SWM. To account for un-modeled external torques, we extend the design to allow feedback with a PD controller and a high-gain observer.

The remainder of this chapter is organized as follows:

1. We present the DMP-based torque calculation of the SWM for dynamics modeling and controller design.

2. Three controllers for the SWM are presented and their characteristics are compared; namely, OL, PD, and PD with a high-gain observer. The OL controller consists of two parts. The first part is a switching controller based on the principle of a VR stepper for regulating the spin rate, while the second part is based on the inverse torque model for manipulating the inclination. The OL controller provides the fundamental design structure for the SWM and thus serves as a basis for the other two feedback controller designs.

3. We illustrate the effectiveness of the controllers by performing simulations under the influence of an unknown external torque and then comparing their performance to experimental data.

5.2   SYSTEM MODELING

5.2.1   Torque Model

The Spherical wheel motor has the m_r rotor PM pole pairs and m_s stator EM pole-pairs as shown in Figure 5-1 . Each magnetization axe can be given by Equations (5.1) and (5.2) respectively in their own body coordinate frames:

$$\mathbf{x_{m}}_i = (-1)^{i-1}\left[\cos\phi_r\cos\delta_{ri} \quad \cos\phi_r\sin\delta_{ri} \quad \sin\phi_r\right]^{\mathrm{T}} \tag{5.1}$$

where $i = 1, 2 \dots m_r$; $\delta_{ri} = (i-1)\delta_r$; and $\delta_r = 2\pi/m_r$.

$$\mathbf{x_s}_j = \left[\cos\phi_s\cos\delta_{sj} \quad \cos\phi_s\sin\delta_{sj} \quad \sin\phi_s\right]^{\mathrm{T}} \tag{5.2}$$

where $j = 1, 2\dots m_s$; $\delta_{sj} = (j-1)\delta_s$; and $\delta_s = 2\pi/m_s$. Unlike m_s which may be odd or even, $m_{r,}$ is always an even number.

In Equations (5.1) and (5.2), ϕ_r and ϕ_s are the angles between the magnetization axes and the XY plane and δ is the angle between the two adjacent poles (PMs or EMs) on the circumference defined in Figure 1-6.
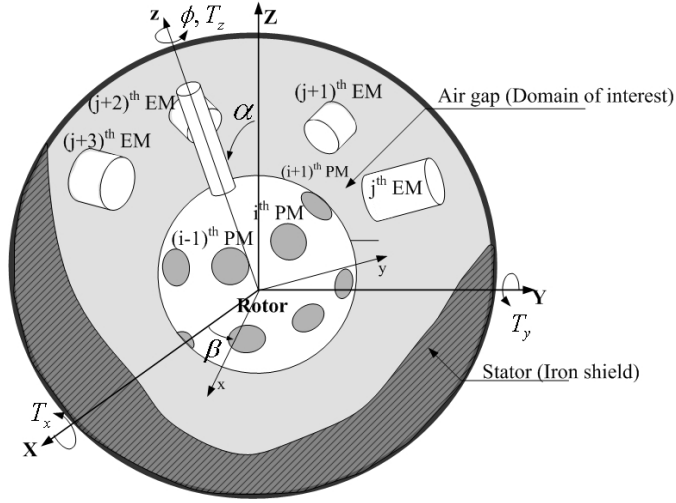
Figure 5-1 Schematic spherical wheel motor configuration

The magnetic forces involved in the SWM can be calculated using the *Lorenz* force formulation. Lorenz force calculation involves only the residual **B**-fields of the permanent magnets of the rotor. The magnetic field **B** of the rotor PMs can be computed by the DMP method, which gives the solution of the **B**-field in closed form. However, the PMs rotate with respect to the stator EMs. The total magnetic field **B** should be expressed in the jth EM coordinates $\mathbf{x}_{cj}$ to compute the force acting on the current-carrying the jth EM. Figure 5-2 shows rotation in the XYZ Euler angles (α, β, γ); no singularities in the domain of interest, for the coordinate transformation from the rotor $\mathbf{x_r}$ to the stator $\mathbf{x_s}$. In the local coordinate system of the jth EM, the position of the ith PM is given by

$$\mathbf{x}_{cj} = \left[\mathbf{L}_{cj\mathbf{s}} \right]\left[\mathbf{L_{sr}} \right]\mathbf{x}_{mi} \tag{5.3}$$

where $\left[\mathbf{L_{sr}}\right] = \begin{pmatrix} C_\gamma C_\beta & C_\gamma S_\alpha S_\beta & -C_\gamma C_\alpha S_\beta + S_\gamma S_\alpha \\ -S_\gamma C_\beta & C_\alpha C_\gamma - S_\gamma S_\alpha S_\beta & S_\gamma C_\alpha S_\beta + C_\gamma S_\alpha \\ S_\beta & -S_\alpha C_\beta & C_\alpha C_\beta \end{pmatrix}$;

123

$$\begin{bmatrix} \mathbf{L}_{cjs} \end{bmatrix} = \begin{pmatrix} C_{\phi_s} & -S_{\phi_s} & 0 \\ S_{\theta_{sj}}S_{\phi_s} & S_{\theta_{sj}}C_{\phi_s} & C_{\theta_c} \\ -C_{\theta_{sj}}S_{\phi_s} & -C_{\theta_{sj}}C_{\phi_s} & S_{\theta_c} \end{pmatrix};$$ C and S represent cosine and sine respectively; and

the subscripts of C and S denote their respective angles.
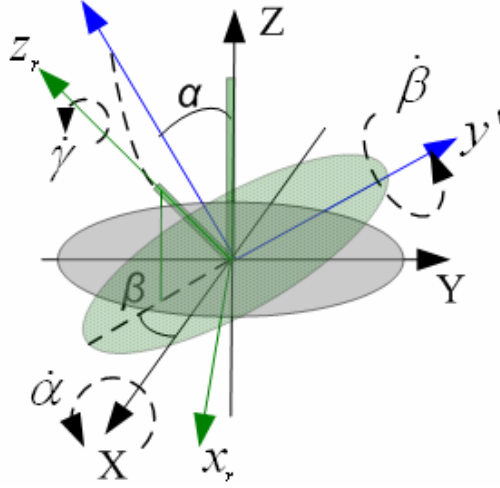
Figure 5-2 XYZ Coordinate transformation

Once the force acting on the jth EM is computed, the resultant torque for all EMs can be computed from:

$$\mathbf{T}_{\text{total}} = \begin{bmatrix} T_X & T_Y & T_Z \end{bmatrix}^{\text{T}} = \begin{bmatrix} \tilde{\mathbf{T}}_1 & \tilde{\mathbf{T}}_2 & \dots & \tilde{\mathbf{T}}_{\mathbf{m}_s} \end{bmatrix} \mathbf{u} \tag{5.4}$$

where $$\tilde{\mathbf{T}}_{\mathbf{j}}\left(\in \mathbb{R}^{3 \times 1} \right) = \mathbf{L}_{\mathbf{cjs}}^{\text{T}} \left(\oint_{EM} \mathbf{R}_c(S,L) \times \left[\sum_i m_i \beta_i(\alpha,\beta,\gamma) \right] dSdL \right); \tag{5.5}$$

and $$\mathbf{u} = \begin{bmatrix} J_1 & J_2 & \dots & J_{m_s} \end{bmatrix}^{\text{T}} \tag{5.6}$$

where $\mathbf{R}_c(S,L)$ is a position vector of every coil wound in the EM.

The torque vector in Equation (5.5) is orientation-dependent and must be evaluated numerically from the volume integral in real time. To reduce the computation

to a tractable form, we take advantage of the fact that the torque is linearly proportional to the current and hence we apply the principle of superposition to compute the total magnetic torque acting on the rotor as follows:

$$\mathbf{T}_{total} \approx \begin{bmatrix} \hat{\mathbf{K}}_1 & \cdots & \hat{\mathbf{K}}_j & \cdots & \hat{\mathbf{K}}_{\mathbf{m}_s} \end{bmatrix} \mathbf{u} \tag{5.7}$$

$$\hat{\mathbf{K}}_j = \begin{cases} -\sum_{k=1}^{m_r} \left\{ \hat{f}(\varphi) \Big|_{\varphi = \varphi_{jk}} \dfrac{\mathbf{s}_j \times \mathbf{r}_k}{\left| \mathbf{s}_j \times \mathbf{r}_k \right|} \right\} & \text{if } \mathbf{s}_j \times \mathbf{r}_k \neq 0 \\[4mm] 0 & \text{if } \mathbf{s}_j \times \mathbf{r}_k = 0 \end{cases} \tag{5.8}$$

where $\hat{f}(\varphi)$ curve-fits the torque between a PM pole-pair and an EM pole-pair in terms of the separation angle φ given by

$$\varphi_{jk} = \cos^{-1}\left(\mathbf{s}_j \bullet \mathbf{r}_k \right) / \left(\left| \mathbf{s}_j \right| \left| \mathbf{r}_k \right| \right). \tag{5.9}$$

5.2.2 Dynamic Equation of Motion

The equation of motion can be derived using the Lagrangian formulation in terms of the XYZ Euler angles as generalized coordinates:

$$\begin{bmatrix} \mathbf{M} \end{bmatrix} \dot{q}_2 + \mathbf{C}(q_1, q_2) + \mathbf{C}_f = \mathbf{Q} + \mathbf{T}_{ext} \tag{5.10}$$

where $q_1 = [\alpha\ \beta\ \gamma]^T$; $q_2 = \dot{q}_1$; $\mathbf{T}_{ext}$ is the disturbance torque; $\mathbf{C}_f$ is the frictional torque of mechanical bearing; and where

$$\mathbf{M} = \begin{bmatrix} I_t C_\beta^2 + I_a S_\beta^2 & 0 & -I_t S_\beta \\ 0 & I_t & 0 \\ -I_t S_\beta & 0 & I_a \end{bmatrix} \tag{5.11}$$

$$C(\dot{q},q) = \begin{bmatrix} 2(I_a - I_t)S_\beta C_\beta \dot{\alpha}\dot{\beta} - I_a C_\beta \dot{\beta}\dot{\gamma} \\ (I_t - I_a)S_\beta C_\beta \dot{\alpha}^2 + I_a C_\beta \dot{\alpha}\dot{\gamma} \\ -I_a C_\beta \dot{\alpha}\dot{\beta} \end{bmatrix}$$ (5.12)

and
$$\mathbf{Q} = \begin{bmatrix} -S_\beta C_\gamma & S_\beta S_\gamma & C_\beta \\ S_\gamma & C_\gamma & 0 \\ 0 & 0 & 1 \end{bmatrix} \begin{Bmatrix} T_X \\ T_Y \\ T_Z \end{Bmatrix}$$ (5.13)

In Equations (5.11) and (5.12), $I_a = I_{zz}$; $I_t = I_{xx} = I_{yy}$; and the mass center of the rotor is assumed to coincide with the center of rotation. In Equation (5.13), $\mathbf{Q}$ is expressed in *xyz* rotor coordinates and represents the contributions of the applied (magnetic) torque to the generalized moments. Since the inertia matrix [$\mathbf{M}$] is positive-definite in the range of inclination motion (-20°≤ α, β≤ 20°), the nonlinear dynamics can be expressed in the standard state forms as

$$\dot{q} = \begin{bmatrix} q_1 \\ q_2 \end{bmatrix} = \begin{bmatrix} 0_{3\times3} & I_{3\times3} \\ & f(q) \end{bmatrix} + \begin{bmatrix} 0_{3\times3} \\ [\mathbf{M}]^{-1} \end{bmatrix}\mathbf{Q}$$ (5.14)

where $f(q) = [\mathbf{M}]^{-1}\mathbf{C}(q) \in R^{3\times1}$ is given by

$$f(q) = \frac{1}{I_t}\begin{bmatrix} q_5 \sec q_2 \left(I_a q_6 + (2I_t - 3I_a)q_4 S_{q_2}\right) \\ q_4 C_{q_2}\left(-I_a q_6 + (I_t - I_a)q_4 S_{q_2}\right) \\ q_5\left\{-I_t q_4 C_{q_2} + \left[I_a q_6 + (2I_t - 3I_a)q_4 S_{q_2}\right]\tan q_2\right\} \end{bmatrix}$$ (5.15)

which is linearized to the desired state $\mathbf{q}_d$ for controller and observer design:

$$[\mathbf{A}] = \left(\frac{\partial f_j}{\partial q_i}\right)\Bigg|_{q=q_d} = \frac{1}{I_t}\begin{bmatrix} [\mathbf{A}_1] & [\mathbf{A}_2] \\ [\mathbf{A}_3] & [\mathbf{A}_4] \end{bmatrix}_{q=q_d}$$ (5.16)

where $[\mathbf{A}_1] = [0_{3\times3}]$; $[\mathbf{A}_2] = I_t[\mathbf{I}_{3\times3}]$; $\mathbf{I}$ is the identity matrix;

$$[\mathbf{A}_3] = \begin{bmatrix} 0 & A_{42} & 0 \\ 0 & A_{52} & 0 \\ 0 & A_{62} & 0 \end{bmatrix}_{q=q_d} ; \quad [\mathbf{A}_4] = \begin{bmatrix} A_{44} & A_{45} & A_{46} \\ A_{54} & 0 & A_{56} \\ A_{64} & A_{65} & A_{66} \end{bmatrix}_{q=q_d} ;$$

$A_{42} = q_5 \left(2I_t q_4 - 3I_a q_4 + 3I_a q_6 \sin q_2 \right) \sec^2 q_2$; $A_{52} = q_4 \left[(I_1 - I_3) q_4 \cos 2q_2 + I_3 q_6 \sin q_2 \right]$;

$A_{62} = q_5 \left[I_a q_6 \sec^2 q_2 + 3(I_t - I_a) q_4 \sin 2q_2 + (2I_t - 3I_a) q_4 \sec q_2 \tan q_2 \right]$;

$A_{44} = (2I_t - 3I_a) q_5 \tan q_2$; $A_{54} = \left[2(I_1 - I_3) q_4 \sin q_2 - I_3 q_6 \right] \cos q_2$;

$A_{64} = q_5 \left[(2I_t - 3I_a) \sin q_2 \tan q_2 - I_t \cos q_2 \right]$; $A_{45} = \left[I_a q_6 + (2I_t - 3I_a) q_4 \sin q_2 \right] \sec q_2$;

$A_{65} = \left[I_a q_6 + (2I_t - 3I_a) q_4 \sin q_2 \right] \tan q_2 - I_t q_4 \cos q_2$; $A_{46} = I_a q_5 \sec q_2$;

$A_{56} = -I_3 q_4 \cos 2q_2$; and $A_{66} = I_a q_5 \tan q_2$

5.3 CONTROLLER DESIGN OF SWM

We illustrate three SWM controllers; OL, PD, and PD with a high-gain observer. The OL controller provides the fundamental design structure for the SWM and thus serves as a basis for the other two feedback controller designs. The controller designs are here focusing on the orientation control of a rotating shaft.

5.3.1 Design Parameters

To facilitate this discussion of the design of a SWM and its control system, we define design parameters; plane angle of symmetry, and minimum phase angle:

Plane angle of symmetry

$$\psi_{sym} = LCM(\delta_{r,} \delta_s) \leq 180° \tag{5.17}$$

where ψ_{sym} is in degrees; and *LCM* is the least common multiplier of its arguments. There are n_{sym} symmetric regions:

$$n_{sym} = \text{int}\left(360°/\psi_{sym}\right) \tag{5.18}$$

For example, the design (m_s =12 and m_r =18) has three symmetric regions (ψ_{sym}=60°) and that (m_s =10 and m_r =8) has two (ψ_{sym}=180°).

Minimum Phase angle

$$\psi_{min} = GCD(\delta_r, \delta_s) \tag{5.19}$$

where *GCD* is the greatest common divisor of its arguments. The number of drive modes is equal to

$$n_{max} = \text{int}\left(\delta_r/\psi_{min}\right) \tag{5.20}$$

Different switching sequences for the z-axis rotation can be designed based on *n* number of ψ_{min} or

$$\gamma = \varphi_{11} = n\psi_{min} \tag{5.21}$$

where $n \le n_{max}$.

Each *n* corresponds to a *quasi-static* location of the rotor spin, at which at least one pair of PMs and EMs on the *XY*-plane are aligned. The resolution of the spin motion depends on the drive mode for given design configurations.

5.3.2 Open-loop Controller

A model-based OL controller (that is designed to perform orientation control of a continuously spinning rotor as shown in Figure 5-3) consists of two parts; one for the

(α,β) inclination, and the other for the spin rate $\dot{\gamma}$ (or switching control). The amplitude-modulated current inputs of the SWM have the following form:

$$u_{sj} = \text{sat}\left[u_{\gamma j}\left(1+u_{\alpha\beta j}\right)\right] \tag{5.22}$$

where $j=1,2,...m_s$; $u_{\gamma j}$ governs the spin-rate; $u_{\alpha\beta j}$ is an incremental factor regulating the rotor inclination about the X and Y axes; and sat[•] indicates saturation of current vector.
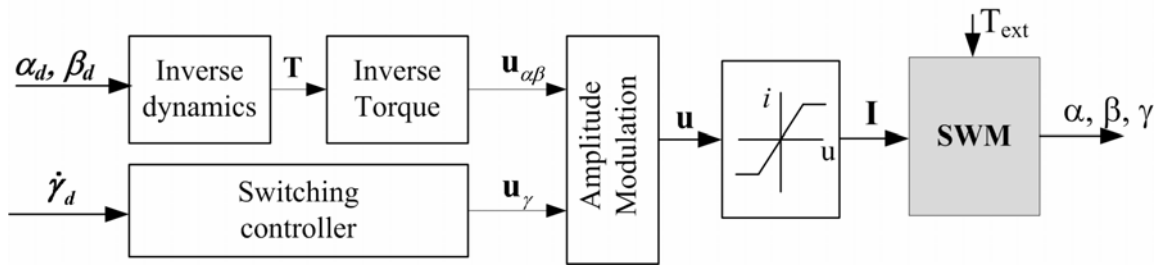
Figure 5-3 OL controller of SWM

Switching (spin motion) Controller

A switching controller can be developed based on the design parameters in section 5.3.1. The EM pole-pairs can be grouped into $n_{sym} = \text{int}\left(360°/\psi_{sym}\right)$ phases, and only m_s/n_{sym} input currents need to be calculated due to the symmetry of the EMs' and PMs' pole layout. At each of the switching steps, n_{sym} PM pole-pairs align with the EM pole-pairs when projected on the XY-plane.

For a given $\psi_{\min}$, $n_{\max} = \text{int}(\delta_r/\psi_{\min})$ levels of electronic "gear" transmission can be designed. The $n_{\max}$ speed levels are based on different step sizes which are an integer factor of ψ_{min} given in Equation (5.21).

For the pole-pairs defined by Equations (5.1) and (5.2), the switching sequences with the minimum step size $\psi = \psi_{\min}$ have the form given in Table 5-1, where all the rows repeat after every $S_N = 2m_s / n_{sym}$. By deduction, other different switching sequences with a step size $n\psi_{\min}$ can be made up from the sequence number S_N defined as follows:

$$S_N = nj - (n-1) \tag{5.23}$$

where $j = 1, \ldots, m_s$.

If $S_N > m_s$, $S_N = S_N - m_s$. The S_N row in Table 5-1 specifies the polarities of the EMs for that sequence (or time step).

Table 5-1 Minimum-step switching

S_N	EM pole-pairs				
	1	**2**	**3**	...	m_s / n_{sym}
1	N	S	N	⋮	N
2	N	S	N		S
⋮	N	S	N		S
$m_s / n_{sym} - 1$	N	S	S		S
m_s / n_{sym}	N	N	S		S
$m_s / n_{sym} + 1$	S	N	S		S
$m_s / n_{sym} + 2$	S	N	S		N
⋮	S	N	S		N
$2m_s / n_{sym} - 1$	S	N	N		N
$2m_s / n_{sym}$	S	S	N		N

From Table 5-1, the input regulating the spin takes the form:

$$u_{\gamma j} = (-1)^j \left| u_{mj} \right| \mathrm{sgn}\left[\sin(\omega_s t + \theta_j) \right]$$ (5.24)

$$\omega_s = n\pi / \left(n_{\max} \Delta t_s \right) \text{ and } \theta_j = -\pi(n-1)/n_{\max} - jn\psi_{\min} - \theta_o$$

where $j = 1, 2, \ldots, m_s$; $n=1, 2, \ldots, n_{max}$; Δt_s=update sampling rate; $0 < \theta_o < \psi_{\min}$; $\mathrm{sgn}(x) = 1, -1$ corresponding to $x{\geq}0$ and $x{<}0$ respectively; and ω_s is the switching frequency of the square wave.

The steady-state spin-rate $\dot{\gamma}_{ss}$ is linearly proportional to ω_s and ψ while the choice of the current magnitude $\left| u_{mj} \right|$ depends on the rotor dynamics (transient response for every switching sequence).

Inclination controller

As illustrated in Figure 1-6, the rotor, which is structurally symmetric and operated on the push-pull principle, is open-loop stable since the rotor becomes stable due to torque feedback by the applied switching controller. The rotor tends to be at the local minimum field energy states; these are local stable equilibrium positions to which the rotor would move from any perturbed position within the local boundary through the *shortest* path during the transient. The inclination control is designed about the local equilibrium ($\alpha{=}\beta{=}\gamma{=}0°$). Given the desired orientation [α_d β_d], the required torque at this state is computed at $\gamma{=}0$ ($T_z{=}0$) from:

$$\left[\tilde{\mathbf{T}}(\boldsymbol{\alpha}, \boldsymbol{\beta}) \right] \mathbf{u}_{\alpha\beta} = \mathbf{T_d}$$ (5.25)

The current vector to generate this torque is given by the inverse torque model in:

$$\mathbf{u}_{\alpha\beta} = \left[\tilde{\mathbf{T}}\right]^{\mathrm{T}} \left(\left[\tilde{\mathbf{T}}\right]\left[\tilde{\mathbf{T}}\right]^{\mathrm{T}}\right)^{-1} \mathbf{T}_d \tag{5.26}$$

Once the inclination and spin currents are computed from Equations (5.24) and (5.26) respectively, the total current inputs can be determined from Equation (5.22).

In order to express the inclination control law in closed-form based on the DMP model, we describe the inclination of a continuously spinning rotor using the ZYZ Euler angles ($\bar{\alpha}, \bar{\beta}, \gamma$). It offers a user-friendly interface to control the orientation. In this representation, $\bar{\alpha}$ is the rotation of the rotor shaft (or z axis) about the Z axis; $\bar{\beta}$ is the angle of inclination between the rotor shaft and the Z axis, and γ is the spin of the rotor shaft about its own z axis. Thus, for real-time computation of the coordinate transformation, we define $[\bar{\alpha}\ \bar{\beta}\ \gamma]$ in Equation (5.27):

$$\bar{\beta} = \cot^{-1}\left(-\sin\beta\cot\alpha\right)$$

and
$$\bar{\alpha} = \sin^{-1}\left(-\sin\alpha / \sin\bar{\beta}\right) \tag{5.27}$$

The inclination controller can be designed as follows:

1. Due to the linear relation between torques and currents, the magnitude of the spin current in Equation (5.24) is normalized to unity, $|u_{mj}|=1$, which maintains the spinning rotor at $\alpha=\beta=0$. The required current vector to incline the rotor at other angles is given by Equation (5.26).

2. The inclination control input of the full torque model is expressed in a closed form. To do this, we decouple the $\bar{\alpha}$ and $\bar{\beta}$ motion control by defining two Fourier series functions $f_{j1}(\bar{\alpha})$ and $f_{j2}(\bar{\beta})$ in Equation (5.28):

$$\hat{u}_{\alpha\beta,j} = f_{j1}(\overline{\alpha})f_{j2}(\overline{\beta}) \tag{5.28}$$

where $\quad f_{j1}(\overline{\alpha}) = \sum_{i=1}^{2}\left[a_{ji}\cos(i\overline{\alpha})+b_{ji}\sin(i\overline{\alpha})\right]$

and $\quad f_{j2}(\overline{\beta}) = c_{jo} + \sum_{i=1}^{3}\left[d_{ji}\cos(i\overline{\beta})+e_{ji}\sin(i\overline{\beta})\right]$

3. The coefficients of the two Fourier series are found by minimizing the following square-error function:

$$E_j = \left(u_{\alpha\beta,j} - \hat{u}_{\alpha\beta,j}\right)^2 \tag{5.29}$$

The ZYZ Euler angle representation has a singularity at $\overline{\alpha} = \overline{\beta} = 0$ and is used only to obtain Equation (5.26) in closed form for inclination control.

4. The inclination current can also be directly computed by using the torque constant vector and inverse torque model in Equations (5.7) and (5.26).

5.3.3 PD controller

PD controllers have been widely used to eliminate the effect of uncertainty and track the desired command for the control of electromagnetic actuators in a number of robotic areas. Figure 5-4 shows the classical PD controller with the nonlinear dynamics of the SWM.
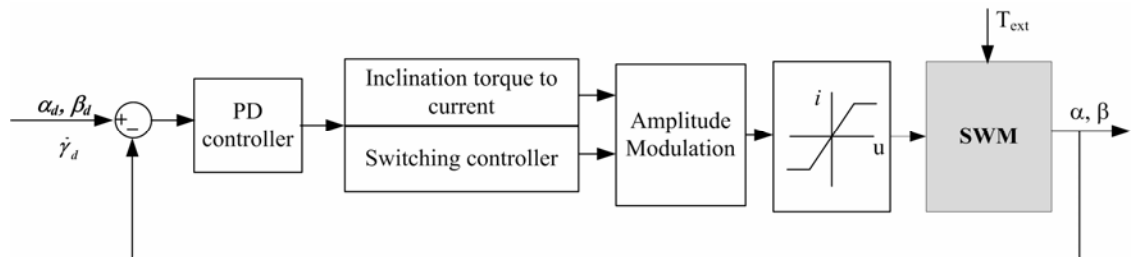

Figure 5-4 PD controller of SWM

The desired torque for the PD controller is given in terms of the position tracking error as follows:

$$\mathbf{T} = [\mathbf{K_p}]\tilde{\mathbf{x}}_1(t) + [\mathbf{K_d}]\tilde{\mathbf{x}}_2(t) \tag{5.30}$$

where $\tilde{\mathbf{x}}_1(t) = \mathbf{q_{1d}} - \mathbf{q_1}(t)$; and $\tilde{\mathbf{x}}_2(t) = \mathbf{q_{2d}} - \mathbf{q_2}(t)$.

The matrices **[K$_p$]** and **[K$_d$]** are positive definite. Since only orientation angle can be measured, angular velocities may be mathematically obtained from differentiating angles for feedback. Once the desired torque is calculated, the actual current input vector is computed from the inverse torque model in Equation (5.26) to control inclination and with Equation (5.24) to control spin rate.

Stability of PD controller

The stability of the PD controller is analyzed using the Lyapunov candidate function [8], given in

$$V = \frac{1}{2}\left(\tilde{\mathbf{x}}_2^T[\mathbf{M}]\tilde{\mathbf{x}}_2 + \tilde{\mathbf{x}}_1^T[\mathbf{K_p}]\tilde{\mathbf{x}}_1\right) \tag{5.31}$$

The time derivative of the Lyapunov function in the Hamiltonian form [59] is

$$\dot{V} = \frac{1}{2}\frac{d}{dt}\left(\tilde{\mathbf{x}}_2^T[\mathbf{M}]\tilde{\mathbf{x}}_2 + \tilde{\mathbf{x}}_1^T[\mathbf{K_p}]\tilde{\mathbf{x}}_1\right) = -\tilde{\mathbf{x}}_2^T\left(\mathbf{T} - [\mathbf{K_p}]\tilde{\mathbf{x}}_1\right) \tag{5.32}$$

which can be shown to be

$$\dot{V} = -\tilde{\mathbf{x}}_2^T[\mathbf{K_d}]\tilde{\mathbf{x}}_2^T \leq 0 \tag{5.33}$$

Along with Equation (5.30), Equation (5.33) implies that the Lyapunov function is only zero at $\tilde{\mathbf{x}}_2 = 0$. Therefore, the SWM with the PD controller is stable and converges to the desired state.

5.3.4 High gain observer with linear approximation

The angular velocities in the PD controller are estimated from the differentiating angle measurements which often compromise the signal to noise ratio. This would decrease the accuracy of the feedback since sensor noise generally fluctuates more rapidly than the command input. To avoid differentiating sensor measurement, an observer to estimate unmeasured outputs for a practical control design has been developed as shown in Figure 5-5. Due to the complexity of rotor dynamics, the observer has been based on a linear approximation model appliying the nonlinear dynamics in Equation (5.10) to the desired (final) states. With the rotor orientation is measured by an assembly of Hall Effect sensors, the forward torque model in Equation (5.4) can be computed to estimate the applied torque in real-time.
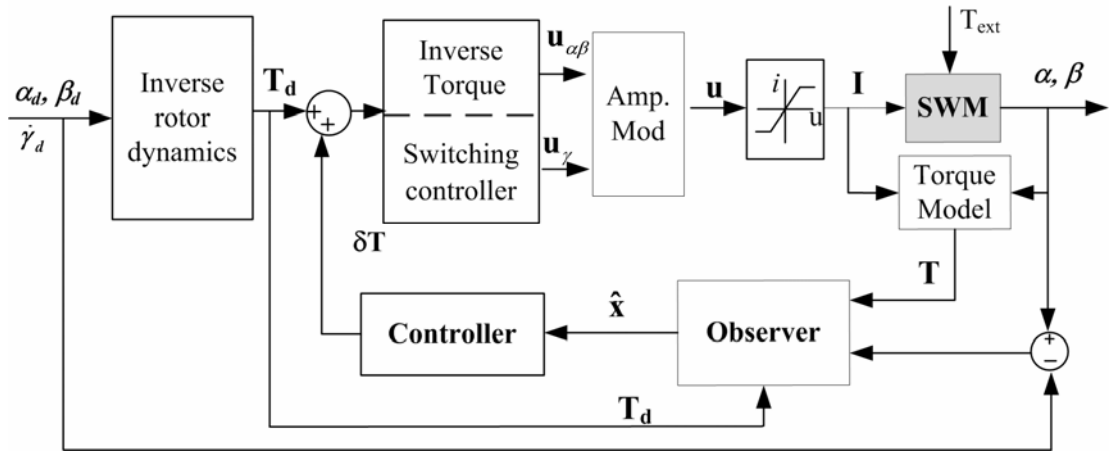

Figure 5-5 High gain observer with linear approximation for error dynamics

The linear error ($\tilde{\mathbf{x}} \triangleq \mathbf{q}_d - \mathbf{q}$) dynamics from Equation (5.16) is given in

$$\dot{\tilde{\mathbf{x}}} = [\mathbf{A}]\tilde{\mathbf{x}} + [\mathbf{B}]\tilde{\mathbf{Q}}$$

$$\mathbf{z} = [\mathbf{C}]\tilde{\mathbf{x}}$$

(5.34)

where $[\mathbf{B}]=[0_{3\times3} \quad [\mathbf{M}]^{-1}]^{\mathrm{T}}$; $\tilde{\mathbf{Q}}=\mathbf{T}_d-\mathbf{T}$; and $[\mathbf{C}]=[\mathbf{I}_{3\times3} \quad 0_{3\times3}]$. To provide an estimate of the unmeasured error signals (angular velocities) around the desired state, a linear high-gain (full state) observer for the tracking error dynamics is designed. In terms of estimated error state $\hat{\mathbf{x}}\triangleq\mathbf{q}_d-\hat{\mathbf{q}}$,

$$\dot{\hat{\mathbf{x}}}=[\mathbf{A}]\hat{\mathbf{x}}+[\mathbf{B}]\tilde{\mathbf{Q}}+[\mathbf{H}](\mathbf{z}-\hat{\mathbf{z}})$$

$$\hat{\mathbf{z}}=[\mathbf{C}]\hat{\mathbf{x}}$$

(5.35)

The dynamics of the estimated error $\mathbf{e}=\tilde{\mathbf{x}}-\hat{\mathbf{x}}$ is then given by

$$\dot{\mathbf{e}}=\big([\mathbf{A}]-[\mathbf{H}][\mathbf{C}]\big)\mathbf{e}=[\Lambda]\mathbf{e}$$

(5.36)

In Equations (5.35) and (5.36), $[\mathbf{H}]=\text{Block Diag}[\mathbf{H_1} \quad \mathbf{H_2}]^{\mathrm{T}}$.

where $[\mathbf{H_j}]=\text{Diag}[\alpha_j^1/\varepsilon^j \quad \alpha_j^2/\varepsilon^j \quad \alpha_j^3/\varepsilon^j]$; ε^j (j=1,2) is a positive constant to be specified; and the positive constants α_j^i are chosen such that the roots of Equation (5.37) satisfy time response specifications in the left-half plane of the complex domain. It guarantees asymptotic error convergence $\lim_{t\to\infty}\mathbf{e}(t)=0$. This indicates the stability of the observer dynamics.

$$\det\big|s\mathbf{I}-[\Lambda]\big|=0$$

(5.37)

In addition, the separation principle allows us to design the controller and observer separately to guarantee the stability of the overall system. The stability of the PD controller has been shown in Equation (5.33), and can be extended to include the high gain observer. Once the full state of error is estimated, the estimated state vector can be used in the state feedback to generate the desired input torque vector.

5.4   SIMULATION RESULTS AND DISCUSSION

The effectiveness of the controllers for the SWM shown in Figure 5-1 has been examined by computational simulation. The parameters of the SWM used in the simulation are detailed in Tables 5-2 and 5-3.

Table 5-2 Stator and rotor pole pair

Stator EM pole	OD = 0.75 in, 1050 turns
Coil wire and resistance	29 AWG, 6.46 Ohms
Current (2 EMs in series)	4 Amperes
Rotor radius	76.2 mm (3 inches)
Cylindrical PM	OD=L=12.5mm (0.5in)
Air-gap between EM & PM	0.762mm (0.03in)

Table 5-3 Values used in the setup

Rotor radius	76.2 mm (3 inches)
Offset of mass centre	$\bar{r} = 0$
M. of Inertia, (kg-m^2)	I_a = 6.0576e-005; I_t =3.8628e-005
Frictional coefficient C_f	0.3 Nm•sec
Stator EMs	20 (2 layers of 10)
Magnetization	ϕ_s = 26º; δ_s = 36º
Current limit	u_{sat} = 1 Ampere
Rotor PMs	16 (2 layers of 8)
Magnetization	ϕ_r = 20º; δ_r = 45º

$R=d$=6.35mm, g=0.5mm, and $\mu_0 M_0$=1.35Tesla

5.4.1 Torque model in closed form

Torque calculation is crucial to the design of a controller for the SWM in real time. Since the SWM consists of the iron rotor and stator, the DMP-based torque using image method presented in chapter 2 is computed to design the controllers. Figure 5-6 graphs the torque constant between a PM pole-pair and an EM pole-pair in Equation (5.8). The seventh order polynomial of the torque curve fit function can be given by

$$\hat{f}(\varphi) = \sum_{k=0}^{7} c_k \varphi^k \qquad (5.38)$$

where $c_0 = -53.18$; $c_1 = 232.51$; $c_2 = -402.68$; $c_3 = 343.74$; $c_4 = -142.27$; $c_5 = 20.61$; $c_6 = 1.25$; and $c_7 = 0.01$
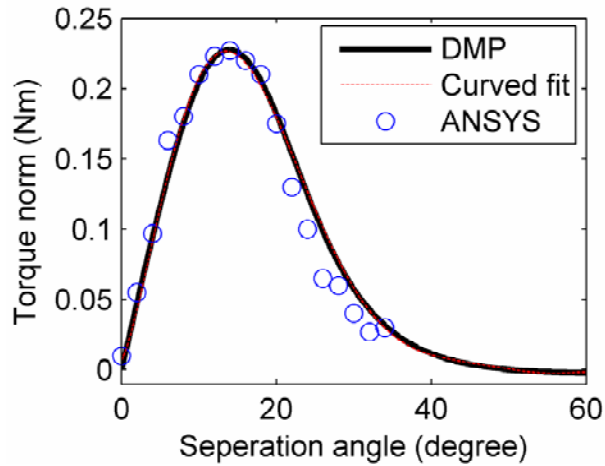

Figure 5-6 Torque between a PM pole-pair and an EM pole-pair

The result is compared to those obtained using ANSYS. We note that the accuracy of the ANSYS results depends significantly on the resolution of the mesh. The FE analysis must cover a relatively large free space to include the magnetic fields, and thus it demands significant computational time. Unlike ANSYS results where only a few

data are available, the torque computed using the DMP model is smooth and can be easily curve-fitted as shown in Figure 5-6, where the average error sum of the 7th order polynomial curve-fit is less than 1%.

Torque Validation

Two cases of torque validation are presented:

(1)   Superposition of DMP-based torque model

(2)   Exact and approximated torque model in Equations (5.5) and (5.7)

For case 1: In [47], the superposition of torque computations has been numerically validated using ANSYS simulation, which is the superposition of the two individual cases against the single EM and the two combined rotor poles. Figure 5-7 shows the results of the superposition principle using the DMP method against numerical solutions from ANSYS. The simulation parameters are given in Tables 5-2 and 5-3. The maximum difference is within 5% of both the DMP model and ANSYS.
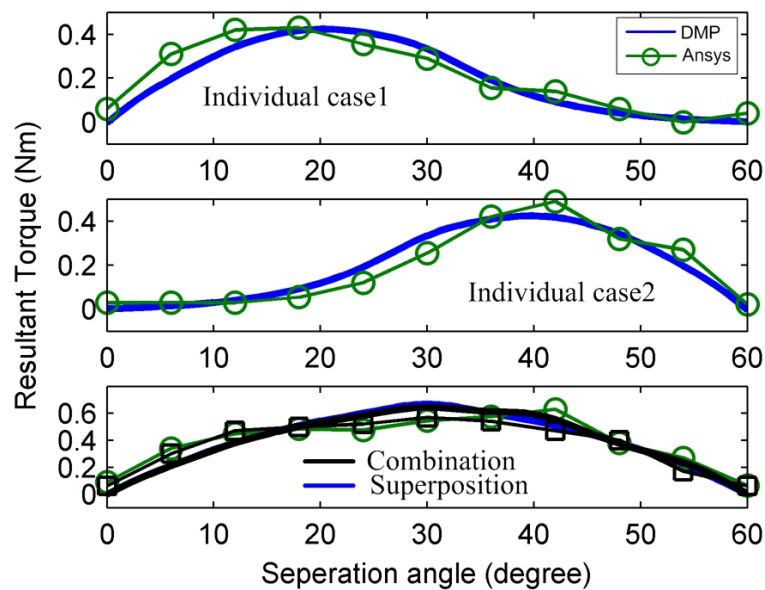

Figure 5-7 Validation of the torque superposition principle

For case 2: the exact torque model in Equation (5.5) and the approximated torque Equation (5.7) are compared using the simulated responses of the PD controller [47] in Figure 5-8.
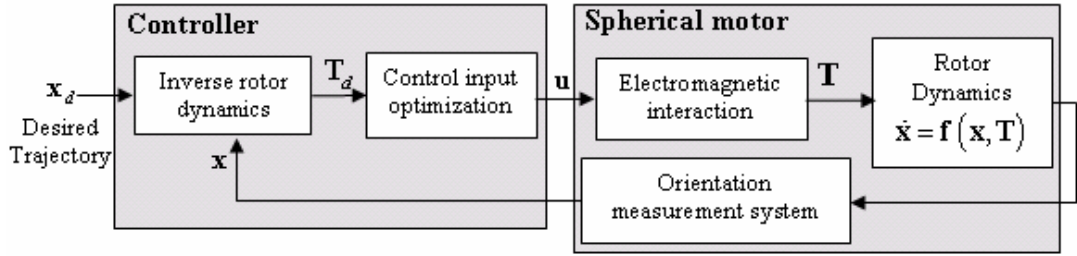

Figure 5-8 Closed-loop control of the spherical motor

The gain matrices of the PD controller in Equation(5.30) are given by

$$[\mathbf{K_p}] = \begin{bmatrix} 0.5 & 0 & 0 \\ 0 & 0.3 & 0 \\ 0 & 0 & 0.5 \end{bmatrix} \text{ and } [\mathbf{K_d}] = .05[\mathbf{I}] \tag{5.39}$$

where [$\mathbf{I}$] is 3x3 identity matrix.

The simulation results for a step change in rotor orientation from its initial upright position ($\alpha=\beta=\gamma=0°$) to a final state ($\alpha=0°$, $\beta=10°$ and $\gamma=60°$) are given in Figure 5-9. As shown in Table 5-4, the comparisons show excellent agreement with less than 15% error in both the computed torque and the simulated motions. Thus, the simplified torque model is verified to correctly design controllers and to correctly estimate the torque generated by the SWM in real-time.

Table 5-4 Maximum percentage (%) error

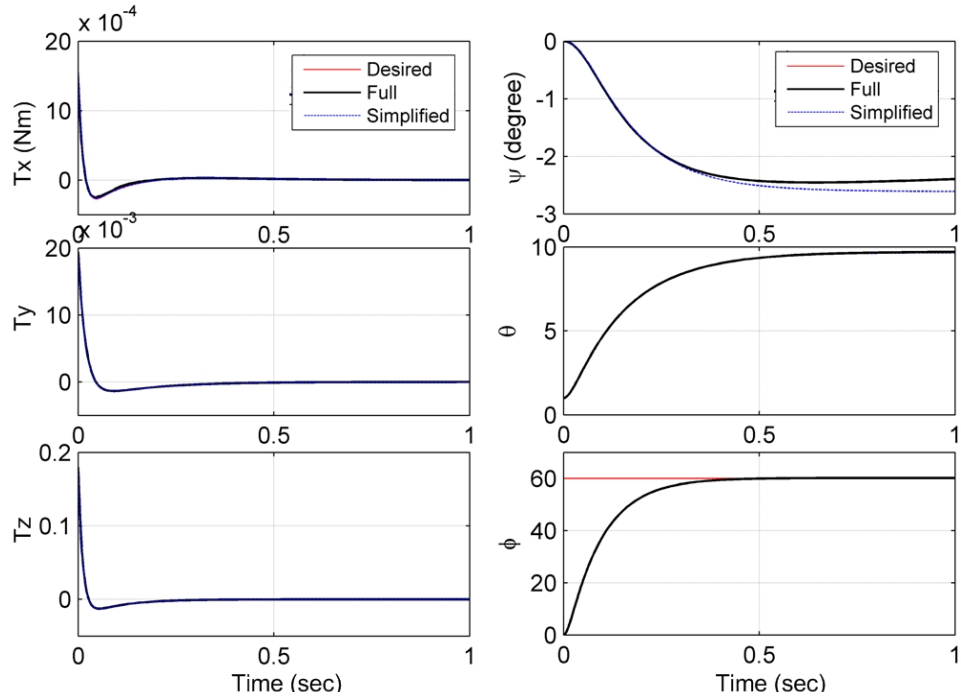| Torques (%)			Angles (%)		
Tx	Ty	Tz	α	β	γ
9.78	4.37	6.02	13.9	7.6	10.4

Figure 5-9 Step response of spherical motor

5.4.2 Spin motion

From the design parameters in section 5.3.1, $\psi_{sym} = 180°$ implies that the 10 (pole-pairs of) EMs can be divided into $n_{sym} = 2$ phases; the sixth to tenth EMs have the same current profiles as the first to fifth EMs respectively. Additionally, the minimum step size of $\psi_{min} = 9°$ suggests that $n_{max} = 5$ different spin-speed levels can be designed for the OL control. The plan view showing the EM layout and the switching sequences for five different spin-speed levels ($n = 1, 2...5$) are given in Table 5-5, from which the switching current can be intuitively derived as follows:

1. From Table 5-1, the switching current vector $\mathbf{u}_\gamma$ is obtained and shown in Figure 5-10, whee the horizontal axis indicates S_N (which is also the time step).

141

2. For a particular speed level n, the switching current has a period T which depends on the number of sequences S_N and is given in terms of sampling interval Δt_s.

3. In each time step, the rotor spins $\psi = n\psi_{min}$ degrees while the rotor makes $360/\psi$ steps to complete one revolution. Thus, the spin rate (in rpm) directly depends on n and Δt_s. Table 5-6 shows an example for $\Delta t_s = 1$ ms.

Table 5-5 Switching controller for $n = 1, 2...5$ spin-speed levels
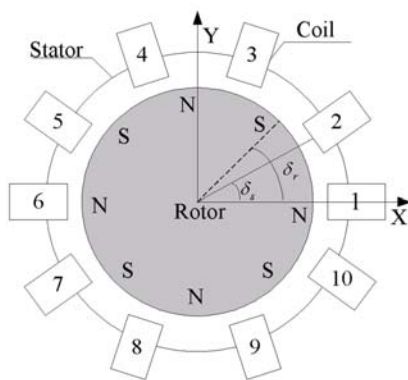
Plan view of coil layout

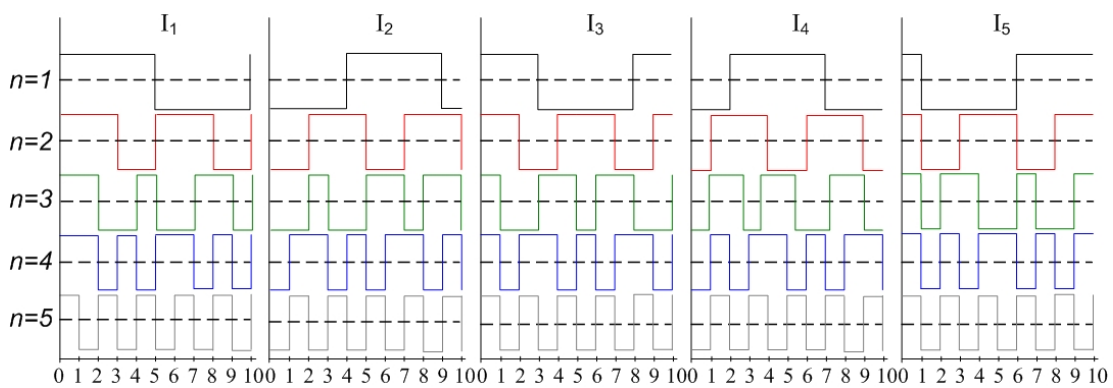| n	ψ	S_N	Period, T
1	9°	1, 2, 3, 4, 5, 6, 7, 8, 9, 10	90°, 10Δt_s
2	18°	1, 3, 5, 7, 9	90°, 5Δt_s
3	27°	1, 4, 7, 10, 3, 6, 9, 2, 5, 8	270°, 10Δt_s
4	36°	1, 5, 9, 3, 7	180°, 5Δt_s
5	45°	1, 6, 1, 6	90°, 2Δt_s

Figure 5-10 Timing diagram for five different spin-speed levels

The switching current can also be expressed mathematically in Equation (5.24), where ω_s and θ_j are given in Table 5-6 ($\theta_o = 5°$, $\Delta t_s = 1$ ms).

Table 5-6 Parameters of switching controller ($\theta_o=5°$, $\Delta t_s=1ms$)

n	θ_j	ω_s (rad/s)	T(ms)	$\dot{\gamma}_{ss}$ rpm
1	*-0.1571j-0.0873*	628	10	1500
2	*-0.3142j-0.7156*	1,257	5	3000
3	*-0.4713j-1.3439*	1,885	10	4500
4	*-0.6284j-1.9723*	2,513	5	6000
5	*-0.7855j-2.6006*	3,142	2	7500

5.4.3 Inclination

The OL inclination controller can be derived from either using Equation (5.28) or (5.26). The computed unknown parameters in Equation (5.28) are detailed in Tables 5-7 and 5-8 for $\bar{\alpha}$ and $\bar{\beta}$ respectively.

Table 5-7 Constants of $f_{j1}(\bar{\alpha})$ ($u_{\alpha\beta,5}=u_{\alpha\beta,2}$, $u_{\alpha\beta,4}=u_{\alpha\beta,3}$ due to the symmetry)

j	1	2	3
a_{i1}	-134.896	-144.083	-101.69
a_{i2}	134.89	144.074	101.682
b_{i1}	6374.87	5162.52	3843.15
b_{i2}	-3185.02	-2579.32	-1919.34

Table 5-8 Constants for $f_{j2}(\bar{\beta})$

j	1	2	3	4	5
c_{io}	.035466	-0.091224	-0.003365	-0.003365	-0.091224
d_{i1}	.02134	-0.130895	0.013119	-0.036560	-0.12672
d_{i2}	-0.09967	0.040402	0.005075	-0.003483	0.055141
d_{i3}	-0.01214	-0.054836	0.003483	-0.005075	-0.048777
e_{i1}	-0.47508	0.126491	0.03656	0.013119	-0.142679
e_{i2}	-0.02024	0.165207	-0.032600	0.032600	-0.158953
e_{i3}	.118731	0.032188	-0.023501	0.023501	-0.037096

(a)

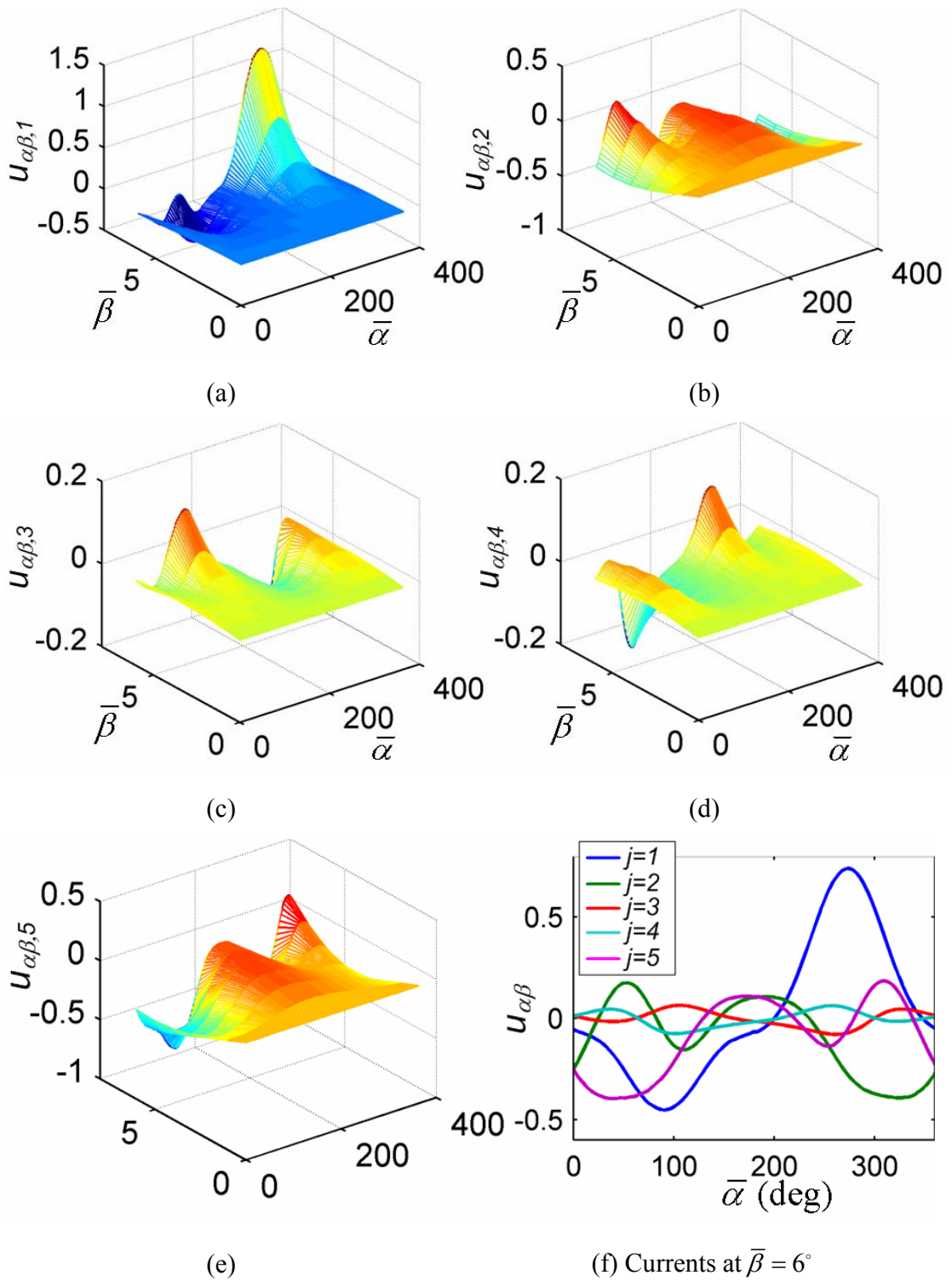(b)

(c)

(d)

(e)

(f) Currents at $\bar{\beta} = 6°$

Figure 5-11 Inclination current inputs

144

The currents of the OL inclination controller are plotted in Figures 5-11 (a)-(e) showing the current profiles of the first to fifth EMs. Figure 5-11 (f) shows the current components at $\bar{\beta} = \phi_s - \phi_r = 6^o$ in Figure 1-6 (b) when the first pair of EMs aligns with the PMs. Due to the symmetrical structure designed to operate on the push-pull principle, it can be easily shown in that the currents to the sixth to tenth EMs have equal magnitudes but opposite directions the current supplied to the first to fifth EMs. Similar arguments can be made for the pairs j=2, 5 and j=3, 4 as shown in Figure 5-11 (f).

5.4.4 Orientation control

Figures 5-12 (a) and (b) show simulation results for the orientation control. To validate both the inclination control and the switching control inputs, two simulations are compared. The first one sets the rotor trajectory from an arbitrary initial position (α=β=0, γ=30°) to the desired position (α=5°, β=γ=0°) with an initial switching controller. The second command applies the same trajectory except that the desired position γ=45° with the next switching control from the initial, which moves the rotor to the 45° angle. Figures 5-12 (c) and (d) are corresponding torque inputs respectively.
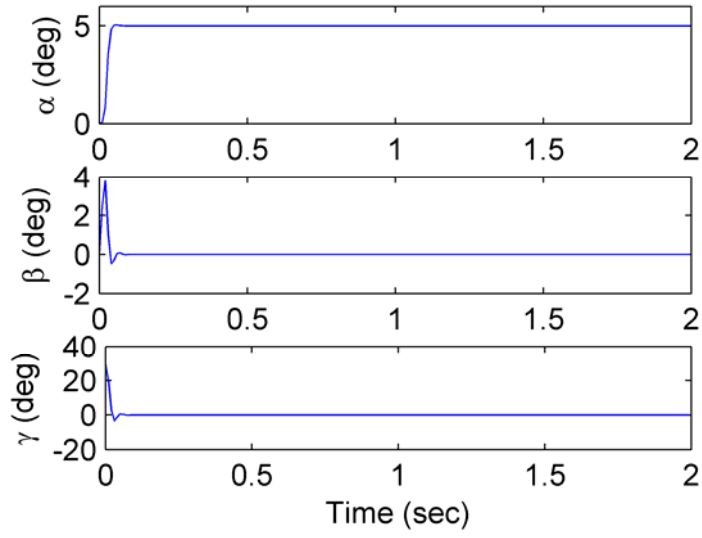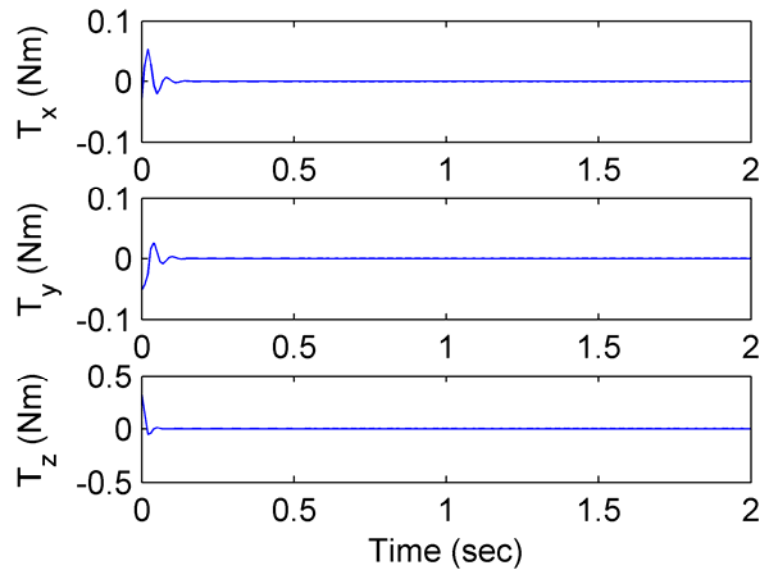
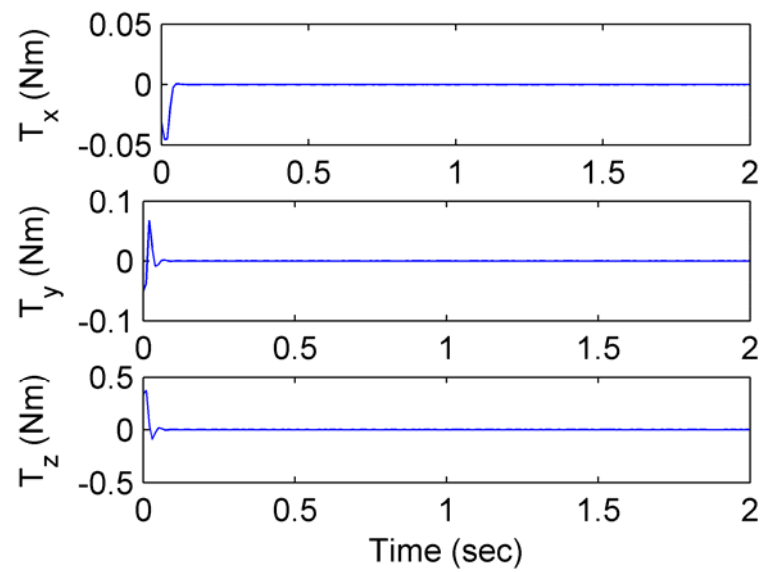(a) Position with an initial switching controller
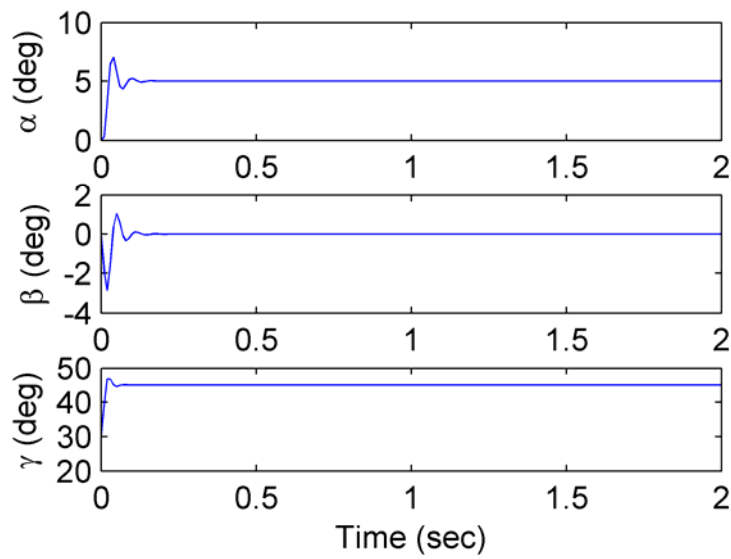
(b) Position with the next set of switching controller

Figure 5-12 Initialization to the desired position (continuous)

(c) Torque corresponding to position control in (a)


(d) Torque corresponding to position control in (b)

Figure 5-12 Initialization to the desired position ($\alpha=5°$, $\beta=\gamma=0$ and 45°)

### 5.4.5 Orientation control with spinning rotor

The controller gain matrices for the PD controller in Equation (5.30) are set to $[K_p]= 23[\mathbf{I}]$ and $[K_d]=[\mathbf{I}]$, which maximize the performance and also minimize the current input saturation. For the high-gain observer, the parameters $\varepsilon^1=\varepsilon^2=0.01$ and $\alpha_j^i = 5$ (i=1, 2 and j=1, 2, 3) are used. Thus, the observer dynamics is faster than that of the controller. Both eigenvalues of the linear dynamic model are compared as follows:

PD: -0.98±31.52j; -0.02±0.73j; -0.50±4.77j

Observer (×100):   -1.34±j0.49; -3.66±j0.18; -3.62; -1.38

The orientation control without spinning can be used to initialize the rotor which is then commanded to spin at the specified inclination. Figure 5-13 shows the simulation results at α=5° (0.0873 radians), β=0° and $\dot{\gamma}=19.6$ rad/sec (187.5 rpm) with a constant external torque $\mathbf{T}_{ext} = [0.05 \ 0 \ 0]^T$ Nm. The simulation results of the model-based OL controller and the PD controller with/without the high-gain observer are compared. As expected, the OL alone cannot compensate an unknown torque. The addition of a feedback loop successfully drives the rotor to the desired orientation, and attenuates oscillations. The maximum steady state error of the controllers is compared in Table 5-9. The error dynamics with a high gain observer converge to zero faster than the classical PD controller.
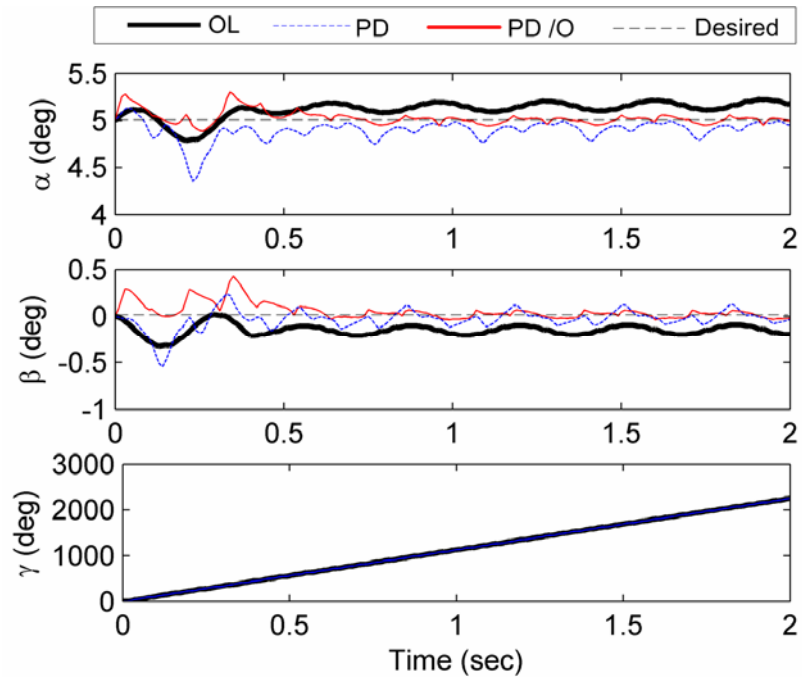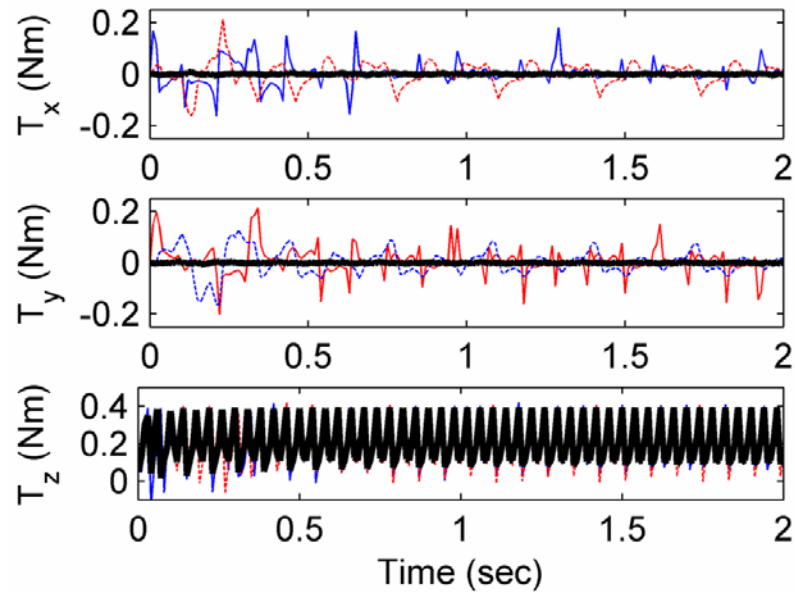
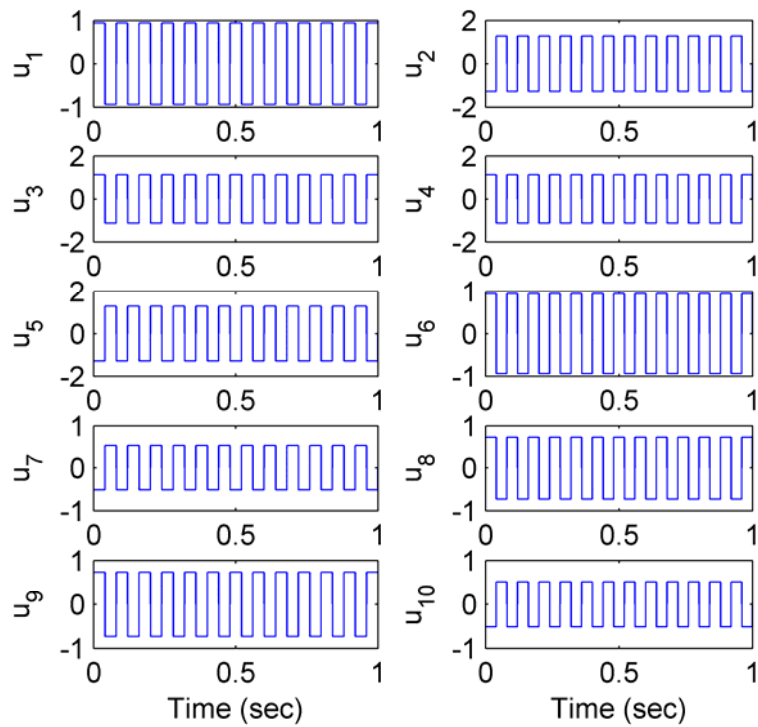(a) Output tracking for desired Euler angles (α=5°, β=0)
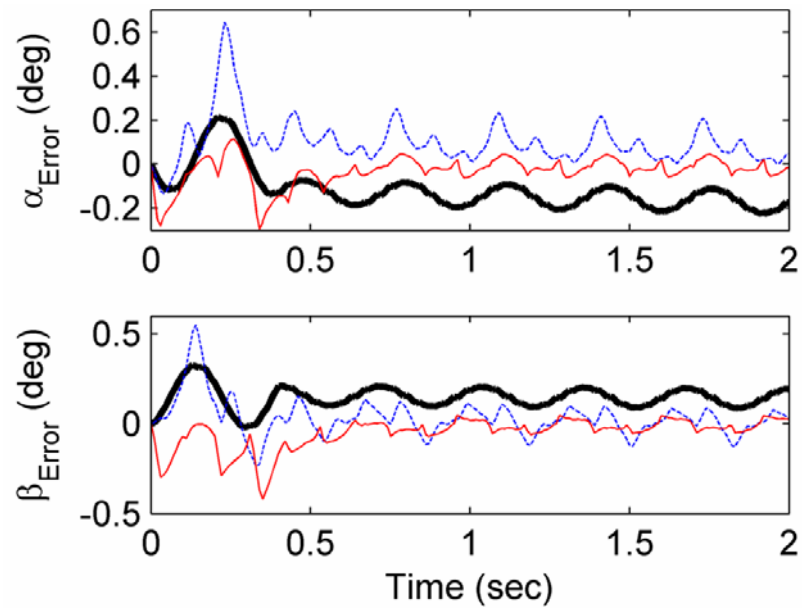
(b) Error of inclination

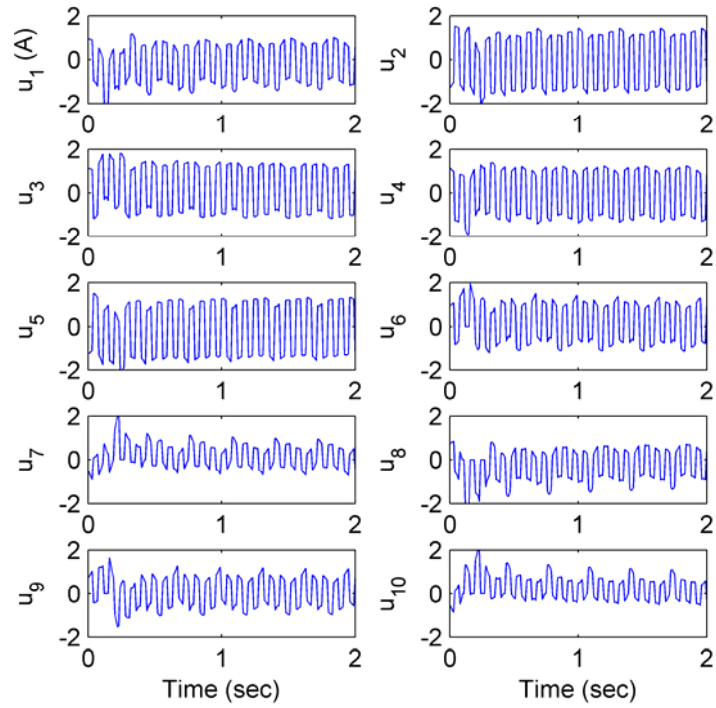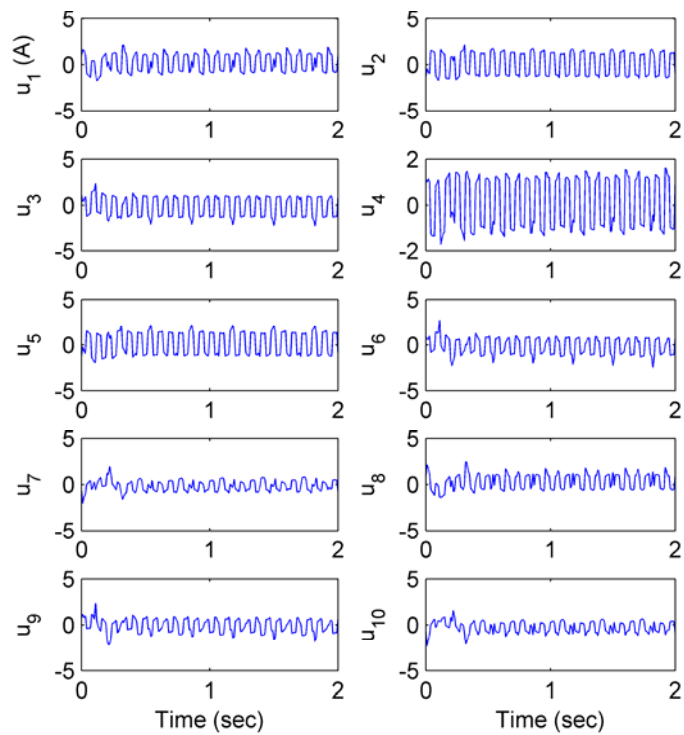Figure 5-13 Simulation comparisons (continuous)

(c) Torque

(d) OL current

Figure 5-13 Simulation comparisons (continuous)

(e) Current of PD controller

(f) Current of PD with high gain observer

Figure 5-13 Simulation comparisons

Table 5-9 Maximum steady state Error ($|E_{ss}|$)

Max($|E_{ss}|$) (deg)	OL	PD	PD with Observer
α	0.24	0.20	0.05
β	0.19	0.07	0.04

5.5 SUMMARY

The mechanical characteristics of the spherical wheel motor are presented to design the orientation control of a rotating shaft. To design the model-based controllers, torque formulation and dynamic model are prerequisite to design the control system and employ them in the real-time control.

Once the torque is computed in the closed form, three controller designs for the SWM are followed. The first is a model-based open-loop controller which serves as an essential basis for feedback control system designs. The OL control presented here offers an effective method to decouple the control of the spin rate from that of the inclination and thus allow the OL controller to consist of two kinds of independent parts; a switching (spin-rate) controller based on the principle of a stepper, and an inclination controller based on the inverse torque model. The OL controller shows the feasibility of operation. We further extend the design to allow two feedback; PD with and without a high gain observer. Finally, we simulate the orientation control of rotating the rotor for output tracking and disturbance rejection.

CHAPTER 6

EXPERIMENTAL RESULTS AND DISCUSSION

6.1 OVERVIEW

This chapter presents the experimental results of the absolute orientation measurement and control systems of the SWM, which have been presented in the previous chapters. The absolute orientation method is chosen here for the inclination measurement because it is less sensitive to measurement noise and sampling time. We also focus on illustrating two unique features of the controller design detailed in Chapter 5 for the SWM. (1) The control of the shaft inclination and the spin motion is decoupled. (2) The performance of the OL and PD controllers with and without an observer is investigated.

Two sets of experiments were conducted: control of the shaft inclination with and without the spin motion. In each set, the experiments aim at demonstrating the mobility and the performance of the SWM. The un-modeled parameters of the system's dynamics were experimentally obtained to shape the reference inputs. In addition, we compare three reference (step, combined two-step and ramp) inputs. Since the OL controller fully relies on the torque model, its performance offers a way to examine the effect of the DMP model on accuracy. Then, the three controllers (OL, PD and PD with an observer) for positioning the shaft inclination (with and without the spin motion) are presented. Finally, a discussion of experimental results is given.

6.2   EXPERIMENT SETUP AND CALIBRATION

The experimental setup of the SWM and each component are presented. Then, Hall effect sensors are calibrated for measuring the shaft inclination. Finally, we experimentally examine the dynamic model of the SWM to find the optimal reference input.

6.2.1   Experiment setup

Figure 6-1 shows the experimental test-bed which consists of the spherical wheel motor, orientation measurement and control system. The mechanical structures of the rotor and stator are shown in Figures 6-1 (a) and (c).

The measurement system consists of four Hall effect sensors mounted one PM shown in Figure 6-1 (b). Hall effect sensors (UGN3505) measure a wide range of positive and negative magnetic fields and the output voltage proportional to the strength of the magnetic field. Its sensitivity is 2.5mV/Gauss with 5 supply voltage. In addition, the sensor is not affected by environmental disturbances such as dirt, lighting and vibration.

The control systems are implemented on a personal computer (PC) which has a 16 channel D/A converter (KPCI-3130), a 16 channels of A/D converter (PCI-DAS6036), a signal amplifier and a power amplifier. The KPCI-3130 has eight channels of analog output current which can be controlled by software. The updating time and settling time for transient responses in each channel are 10ms and 15ms respectively [60]. These update speeds limit the maximum spin rate that issued to generate the switching control signal in Equation (5.22). The signals from the Hall Effect sensor through the amplifier

are measured by the PCI-DAS6036. The PCI-DAS6036 provides 16 bit resolution up to 16 analog inputs. They are all bipolar and range from ±500mV to ±10V. In addition, the important parameters of the experimental setups are summarized in Table 6-1.
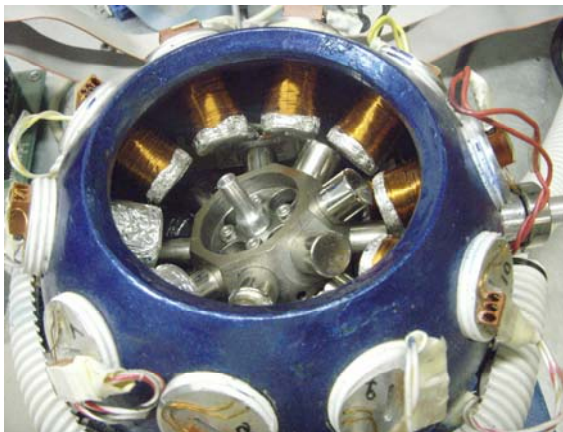
Figure 6-1 (d) shows the control user interface written in Microsoft Visual C++ to interface the PC and the I/O cards of the SWM. The GUI has several functions that not only control the orientation of the rotor but also that monitor the current inputs and the estimated torque in the real-time computation.
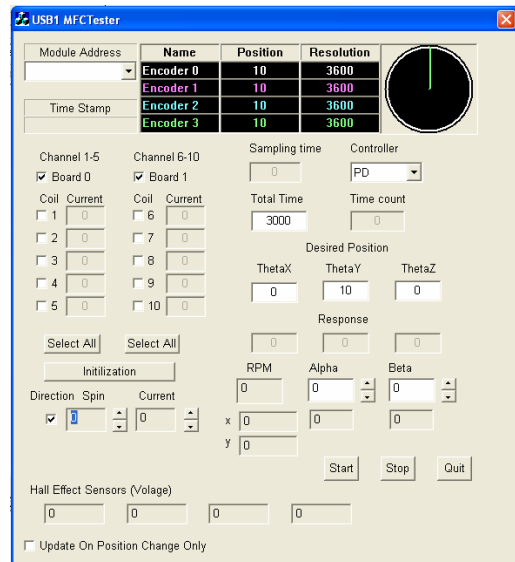

(a) Rotor
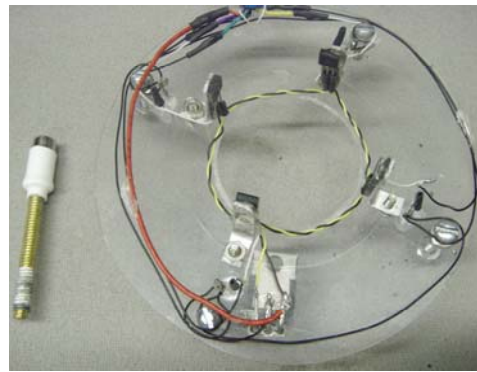
(b) Orientation PM and sensors

(c) Spherical Wheel Motor

(d) GUI control program

Figure 6-1 SWM and control system

Table 6-1 System parameters

SWM	# of poles / # of layers		Pole dim. OD×L (m)	
Rotor	8 / 2		0.0127×0.0127	
Stator	10 / 2		0.019×0.0254	
System I/O	**# channels**	**Range**	**Update time**	**Data Bit**
KPCI-3130 (D/A)	8	-3.5- 3.5A	15ms	8 bit (reg)
PCI-DAS6036 (A/D)	16	-10 - 10V	5µs	16 bit
Measurement system	**# axis**	**V_{cc}**	**V_{out}**	**Sensitivity**
UGN3505	1	5V	0.2V - 4.7V	2.5mV/G

V_{cc} is the supply voltage; V_{out} is the output voltage range
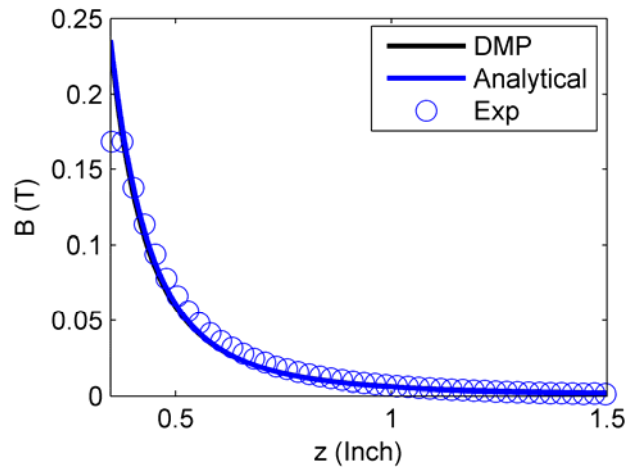
6.2.2 Hall Effect sensor calibration

The PM mounted on a rotating shaft has an aspect ratio (= $h/2a$) of 2. The geometric parameters of the sensors and the DMP modeling parameters of the PM are detailed in Table 6-2.

Using the experimental setup shown in Figure 3-22, a conversion factor k (voltage to flux density) of the Hall effect sensor was experimentally calibrated, and yielded k=0.148. Figures 6-2 (a) and (b) compare the B_z component along the z-axis parallel to the magnetization vector **M** and along the y-axis respectively where the z position is specified to be the position where the maximum error occurred in Figure 6-2 (a). The maximum difference between the values measured B_z and the DMP model is less than 5% for both the y and z axes.

Table 6-2 DMP parameters of the PM and system parameters

| PM		DMP	
Radius (mm)	3.2	$\delta = \bar{\ell}/\ell$	0.8392
Length (mm)	12.7	m_o; m_1 (mA·mm)	0.588 ; 8.622
$\mathbf{B}_r$ (T)	1.32	Error (%)	1.286
L_e (mm)	53.3	Sensor position S, Z(mm)	22.9, 69.8
Coefficients (1st) c_{ij} of $\hat{B}$ (i,j=0,1)		-0.023258, 0.024883, 0.090525, -0.094489	

(a) B$_z$ along z-axis
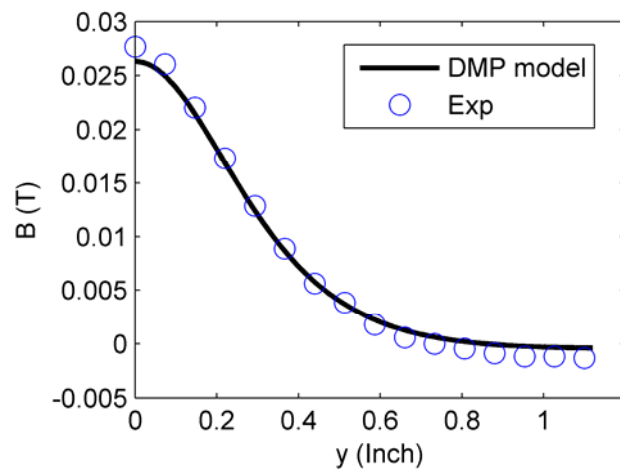
(b) B$_z$ along y-axis at (z=0.65inch)

Figure 6-2 Hall effect sensor calibration

The rotor orientation was measured using the absolute orientation method presented in Chapter 4.3.2. Four sensors were mounted on the top of the SWM and each pair faced toward the X and Y axis in the stator frame.
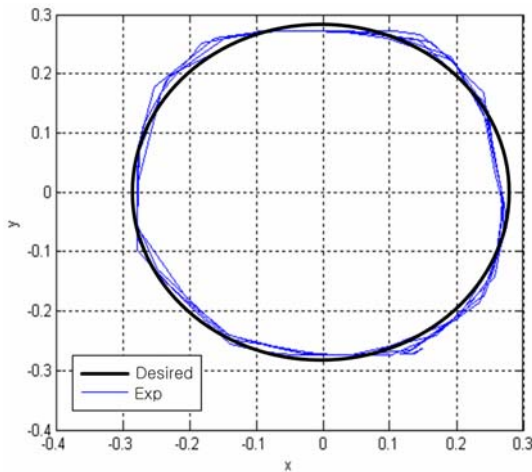
(a) Experiment of circular contour
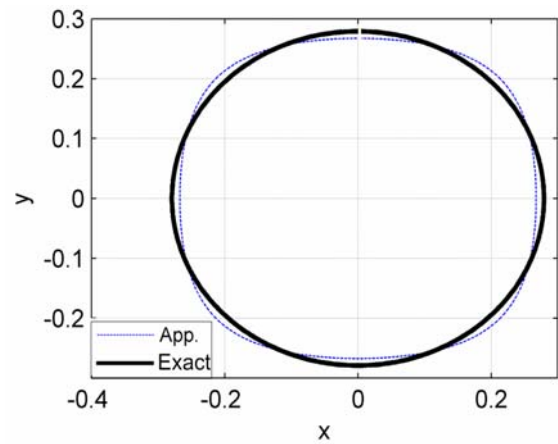
(b) Simulation of circle contour
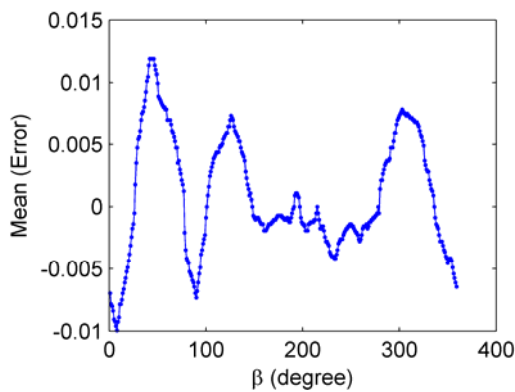
(c) Average error

(d) Error

Figure 6-3 Sensor measurement

Figure 6-3 shows the experimental and simulation results obtained for circular motions using the absolute orientation method based on the 1st order approximation and using the parameters given in Table 6-2. To validate the sensor performance accurately,

we repeated the same circle contour three times. As shown in Figures 6-3 (a) and (b), the maximum error occurred at every 45n (deg), (n=1, 2, 3, 4), where the sensor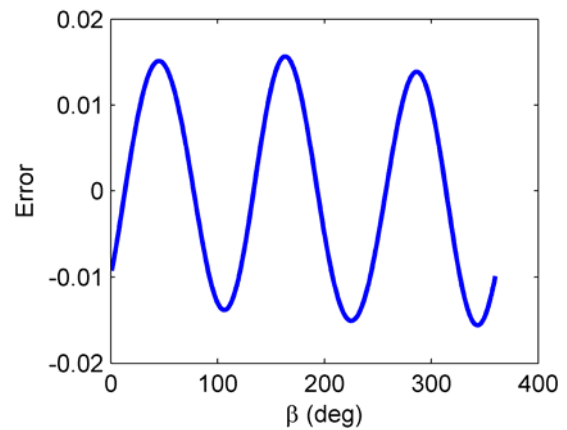 signal is weak. Compared to the errors in Figures 6-3 (c) and (d), these error regions can be predicted by simulation since their trends agrees well. The maximum mean of the errors is 0.012rad which is an error of less than 10% of the desired inclination.

6.2.3   System Parameter Identification

Accurate orientation control requires a good understanding of the system, which is relatively difficult to measure in practice. However, the dynamic motion of orientation can be decoupled and simplified with the assumption that the rotation motion is isotropic and the bearing friction is constant. Thus, the equation of motion can be approximated as the standard 2nd order system:

$$I_t \ddot{\alpha} + c_b \dot{\alpha} + k_e(\alpha, \mathbf{I})\alpha = T_\alpha \tag{6.1}$$

where α is the inclination angle; c_b is the unknown bearing friction constant; k_e is the unknown equivalent spring constant, and T_α is magnetic torque. In Equation (6.1), c_b and k_e can be experimentally determined. However, k_e varies with the current input magnitude and the rotor orientation. Thus, k_e is approximated from the steady state response and the torque computation.

$$k_e(\alpha, \mathbf{I}) = T_\alpha / \alpha \tag{6.2}$$

Figure 6-4 compares the simulation result against the experimentally obtained result with $\alpha = 5°$, $\mathbf{I}$=0.35Amp, which result in c_b= *0.0012* and k_e=0.4425. Some discrepancies can be seen in Figure 6-4, which could be due to the model uncertainties,

including the moment of inertia, approximation of the torque computation and sensor measurement errors and noise. Comparison indicates that accurate modeling prediction is difficult in practice.
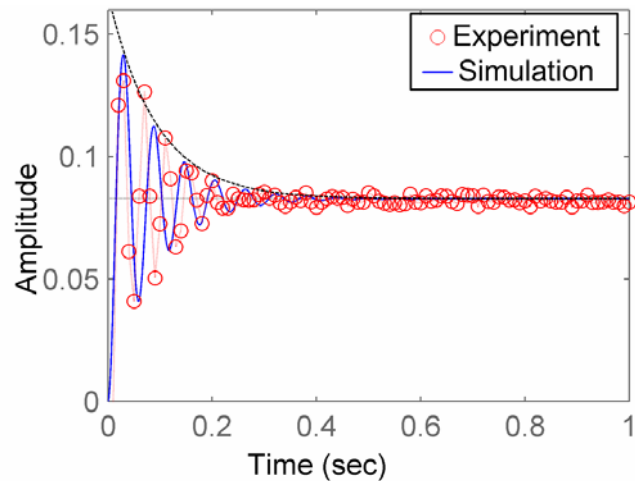
Figure 6-4 Step response

6.2.4 Model based input shaping

The inclination is controlled with three different input shapes (step, input shaping and ramp-step) as shown in Figure 6-5 to compare transient responses such as oscillation and overshoot. The coupled dynamics between the rate of inclination change and spin motion results in gyroscopic moment and Coriolis force, which destabilize the SWM. The controllers tend to minimize the effect of the coupling on both inclination and spin motion. For robust control, it is desired that the control system be insensitive to modeling error and that it be easy to adjust control parameters for any system change.

(a) step input   (b) Two step of input shaping   (c) ramp-step input

Figure 6-5 Inputs of orientation control

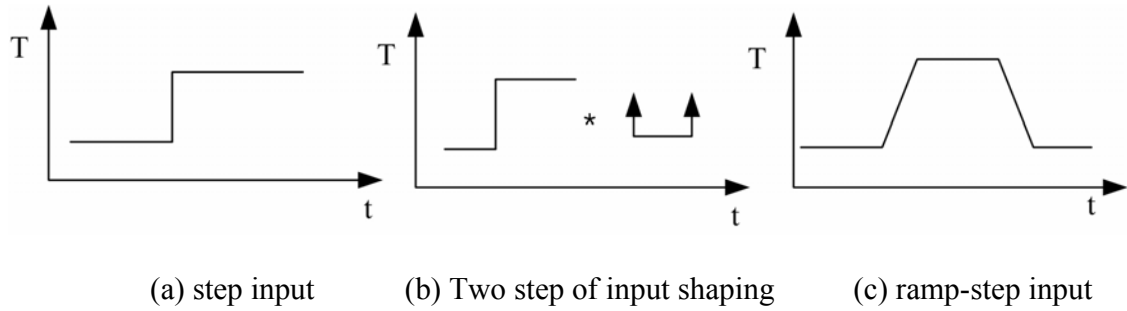The step input is commonly used as a test signal to characterize the system parameters. Based on step responses, Input shaping techniques [61] can be used effectively to design the model-based open loop controller. A combined two-step input was widely used to reduce the undesired responses. In addition, we also explore the effect of a ramp input on transient responses.

Based on the parameters in section 6.2.3, the damping coefficient is small and negligible. With this assumption, Equation (6.1) is simulated to compare the performance with two control inputs from the input shaping technique. The first input consists of two steps with a period equal to π / ω_n, which has the shortest response time (rise time). The second input is a stepwise ramp.

Figure 6-6 compares the simulated dynamic responses based on Equation (6.1) corresponding to two inputs, where the bold lines are the responses and the thin lines denote the specified inputs respectively. The combined two step inputs result in faster response than the ramp input. Figure 6-6 (b) shows the responses in the presence of modeling uncertainty, which is 10% larger than the natural frequency. The ramp response results in a smaller maximum overshoot, which is expected since the ramp input results in

a smaller discrepancy from the applied torque than does the step. The finding leads us to design the maximum slope of the ramp for the model based controller:

$$\mathrm{Max}\left[\partial \mathbf{T}/\partial t\right] = \frac{\left|\mathbf{T}\right|_{\mathbf{q}=\mathbf{q}_d}}{2\pi/\omega_n} \qquad (6.3)$$

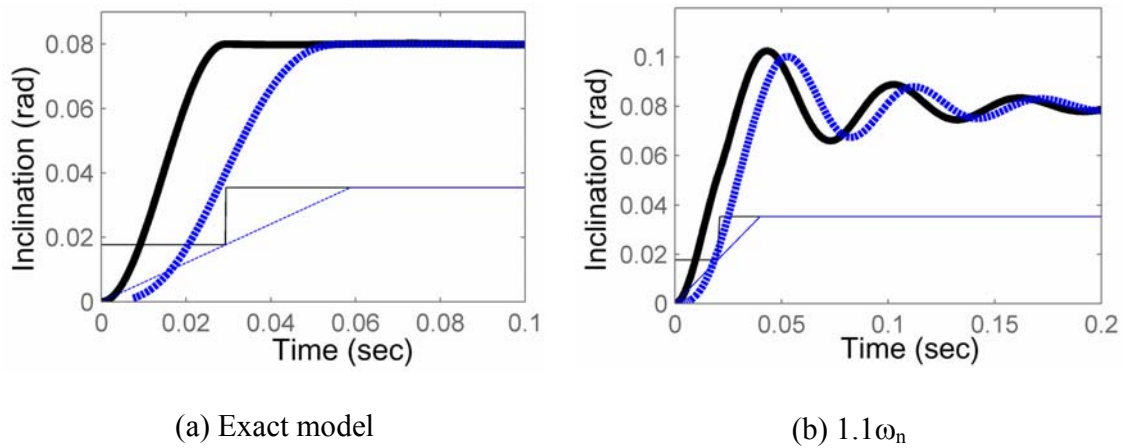(a) Exact model   (b) $1.1\omega_n$

Figure 6-6 Input shaping technique (thin line: input and bold line: output)

The experimental results using three control inputs are compared to investigate the effect of inputs on the transient response. Figures 6-7 (a), (b), and (c) show the results of position-to-position control using three different inputs; a step, two combined steps and ramp respectively. As expected, the response of a single step input in Figure 6-7 (a) shows a large overshoot with a long settling time. Figure 6-7 (b) shows the combined two step input, which results in a smaller overshoot in the first response than the second. The result indicates that exact timing for the input is very difficult in practice since the dynamics of the SWM are stiff (fast dynamic response) and nonlinear (the principle of superposition does not hold). Finally, Figure 6-7 (c) shows the ramp and the results show no overshoot in the transient responses and they also show that rotor follows a desired

path/trajectory. In addition, we observe the accuracy and effectiveness of these desired inputs from the small steady state error.
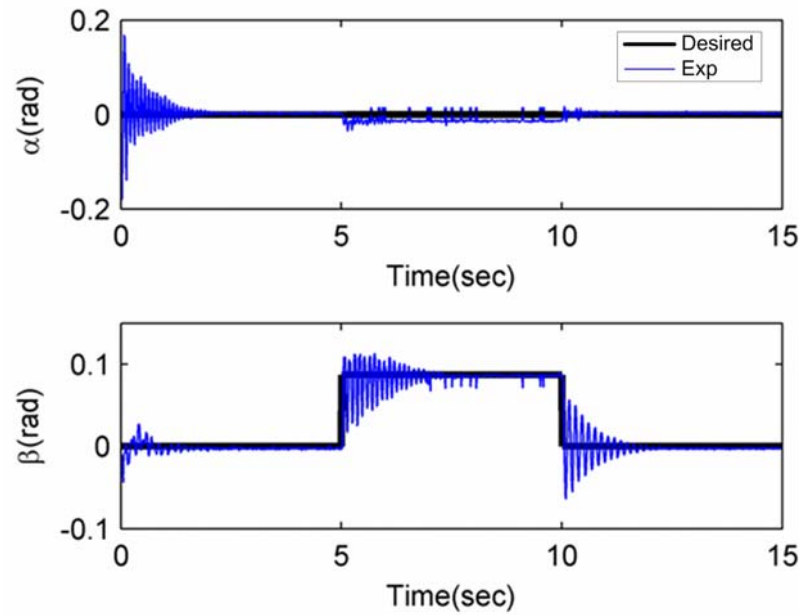
(a) Single step input for orientation control
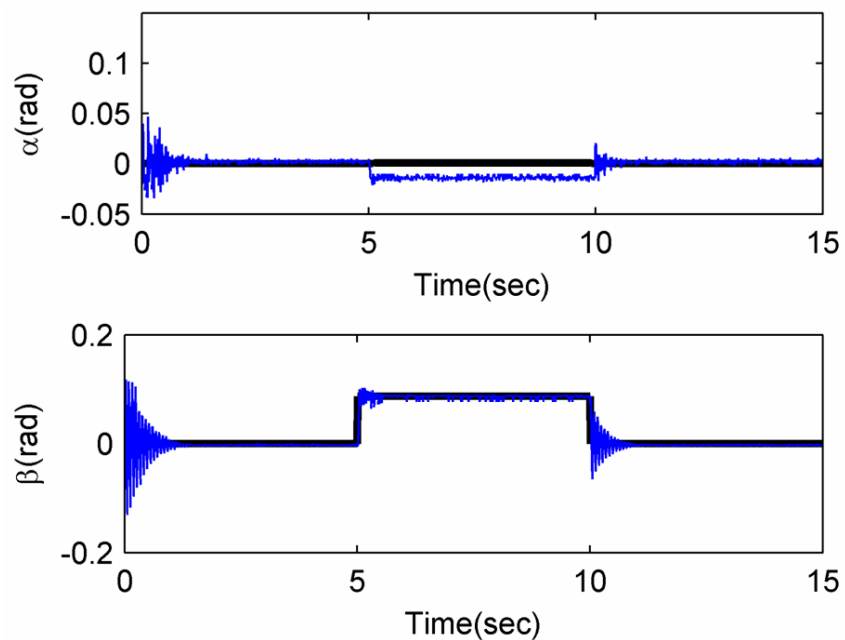
(b) Two step inputs using input shaping

Figure 6-7 Three inputs for orientation control (continuous)
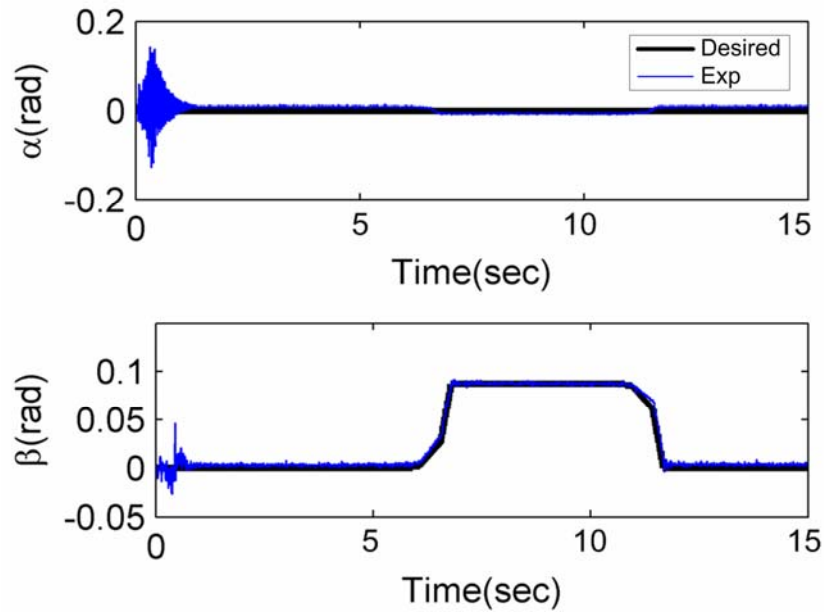
(c) Ramp inputs

Figure 6-7 Three inputs for orientation control

6.3 EXPERIMENTAL RESULTS

The performances of the three controllers (OL, PD and PD with an observer) were investigated experimentally.

6.3.1 Control of shaft inclination

The point-to-point trajectory is as follow:

The SWM is commanded from an initial upright position ($\alpha=\beta=0$) to the state ($\alpha=5°$, $\beta=0$), which is 5 degree inclination of Y-axis. Next, the SWM is commanded to the final state ($\alpha=5°$, $\beta=5°$).

Each command uses the step input to the final desired position for apparent comparison. The maximum current input for normal operation is limited to 0.7 ampere to

avoid heat commutation in the coil. For the feedback controllers, the proportional and derivative gain matrices are experimentally tuned based on the simulation presented in Chapter 5:

$$[\mathbf{K_p}]=0.3[\mathbf{I}] \quad \text{and} \quad [\mathbf{K_d}]=0.01[\mathbf{I}]$$

The parameters of the observer are chosen so that the control inputs on the desired trajectory are within the saturation limit of 0.7 ampere, which yields $\alpha_i=5$ ($i=1, 2$) and $\varepsilon=0.1$ for the shaft inclination control.

The performances are compared in Table 6-3 which summarizes the results graphed in Figures 6-8, 6-9 and 6-10. Some observations are discussed as follows:

- The OL Inclination control without spin motion has a highly accurate response as the predicted DMP method.

- The OL control has a large overshoot and oscillation during the transient response. However, both feedback controllers fulfilled the fast response and desired transient response simultaneously.

- All controllers have steady state errors. The static friction of the ball bearing is expected as one of the dominant factors.

Table 6-3 Transient responses

	t_r(sec)	M_p (%)	t_s (sec)	SS error (rad)
OL	0.04	95	1.67	0.03
PD	0.04	58	0.53	0.01
PD wOB	0.028	38	0.32	0.01

t_r is rise time; M_p is the maximum overshoot; t_s is the settling time; SS denote the steady state.

Open-loop controller

Figures 6-8 (a), (b) and (c) show the commanded torque, applied current and the corresponding experimental results of the OL control respectively. As shown in Table 6-3 and Figure 6-8, the steady state error is very small, 0.003rad, showing that the DMP-based models give an accurate prediction of the torque required. However, the response of each individual step exhibits a large overshoot and oscillations, as expected.
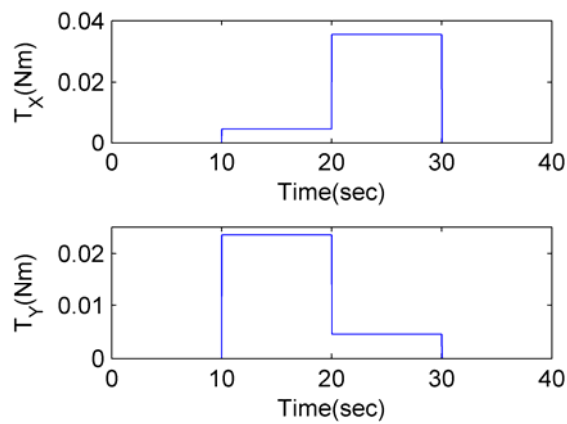
(a) Commanded torque in open loop control
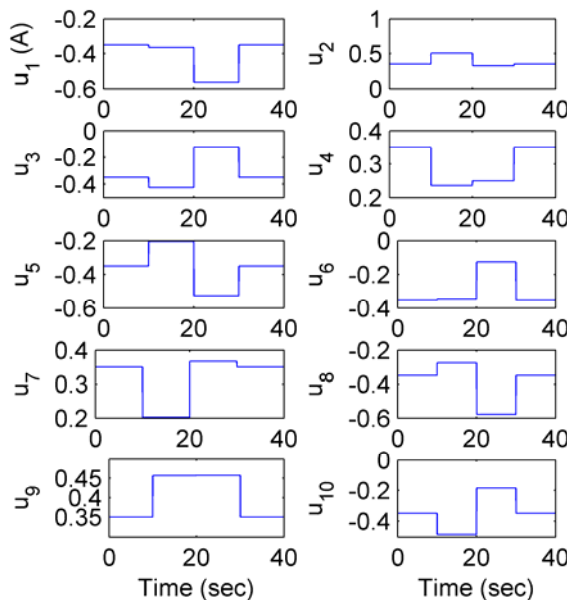
(b) Applied current inputs in open loop control

Figure 6-8 Open loop control using step input (continuous)
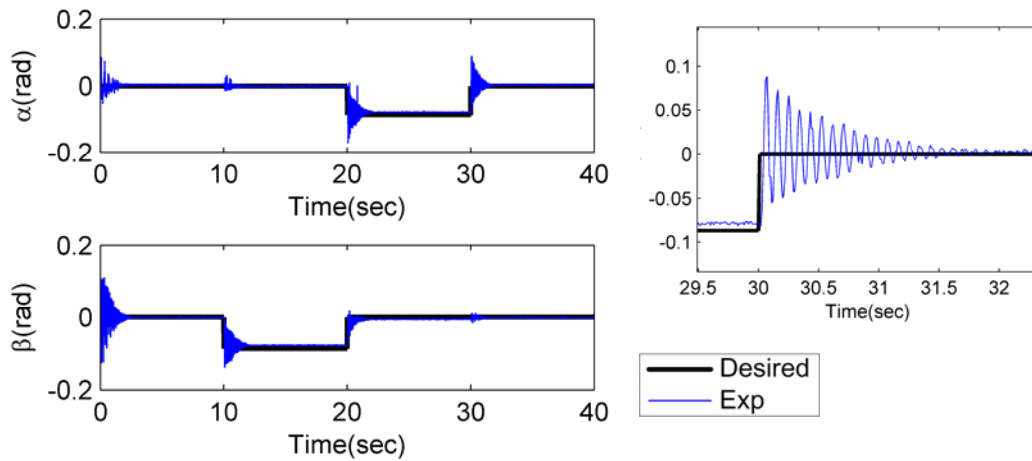
(c) Step response in open loop control

Figure 6-8 Open loop control using step input

PD controller

Similarly, Figures 6-9 and 6-10 show the experimental results that were obtained for the closed loop controllers; PD and PD with a high gain observer. As compared to Figure 6-8, the overshoot and settling time in the initialization and the transient response for every step input are dramatically reduced using the closed loop controller. In addition, the steady state error decreases to 0.001rad.
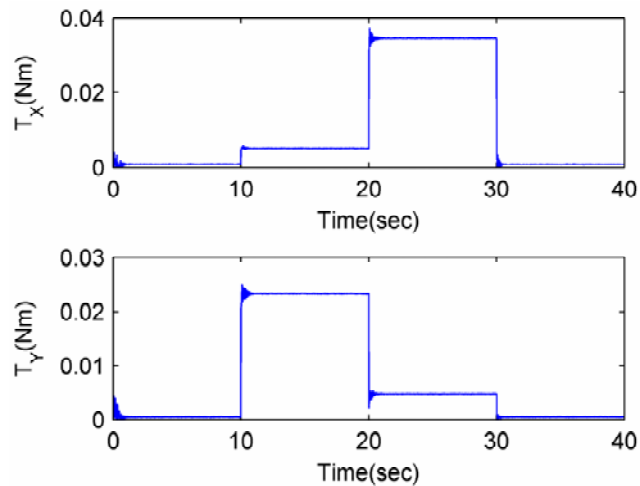
(a) Commanded torque in PD control

Figure 6-9 PD control using step input (continuous)
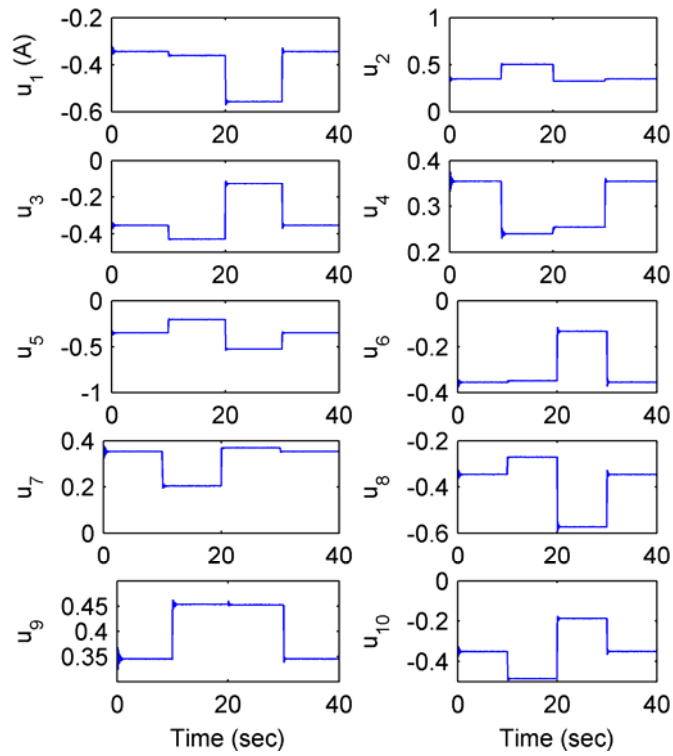
(b) Applied current inputs in PD control
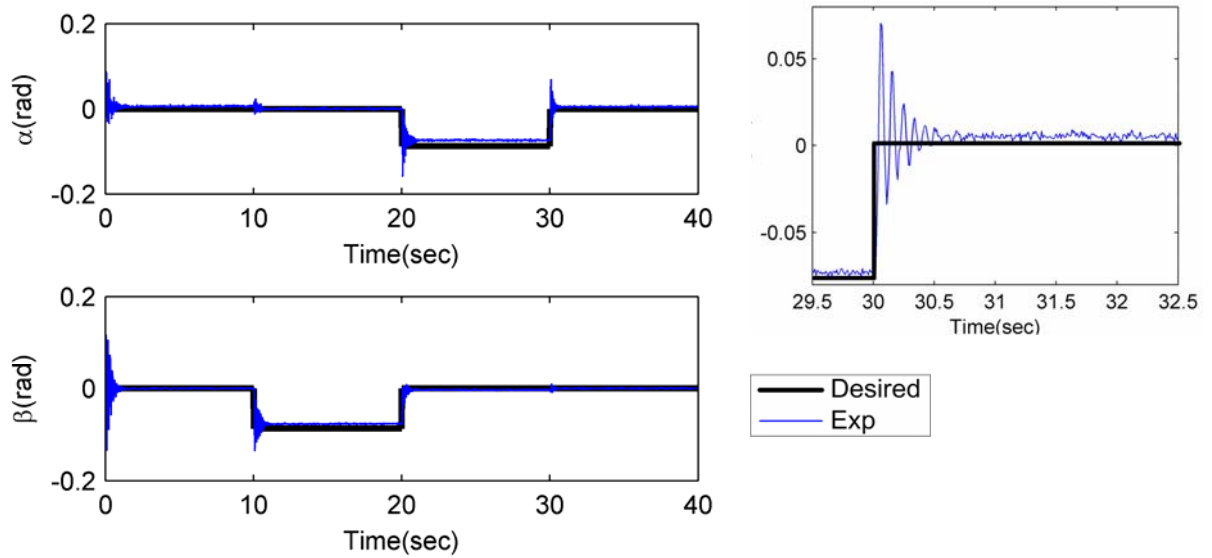
(c) Step response in PD control

Figure 6-9 PD control using step input

PD with observer

     The high gain observer exerts a dominant influence on the settling time and the overshoot by increasing the instantaneous torque. However, it does not improve the steady state error, which is the same as was observer for PD control.
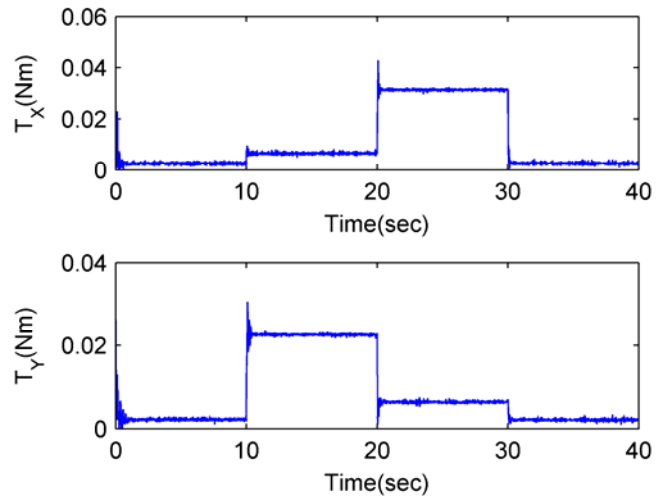
(a) Commanded torque in PD control with high gain observer
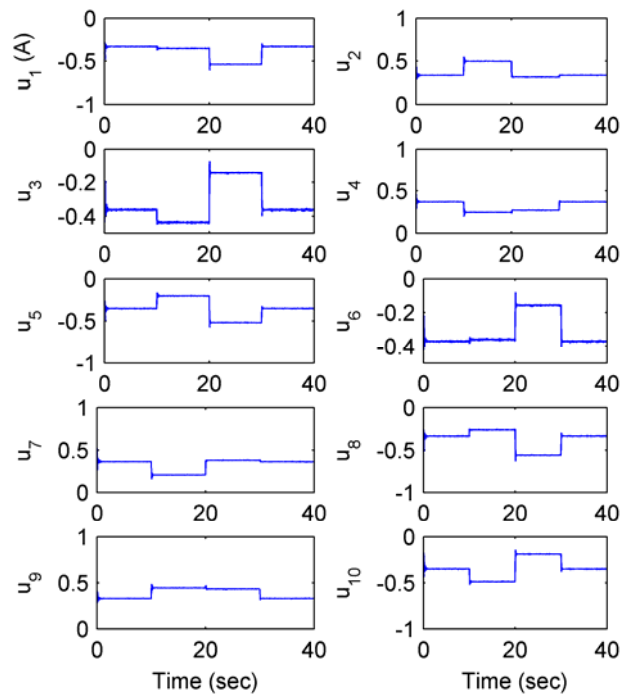
(b) Applied current inputs in PD control with high gain observer

Figure 6-10 PD control with a high gain observer using step input (continuous)
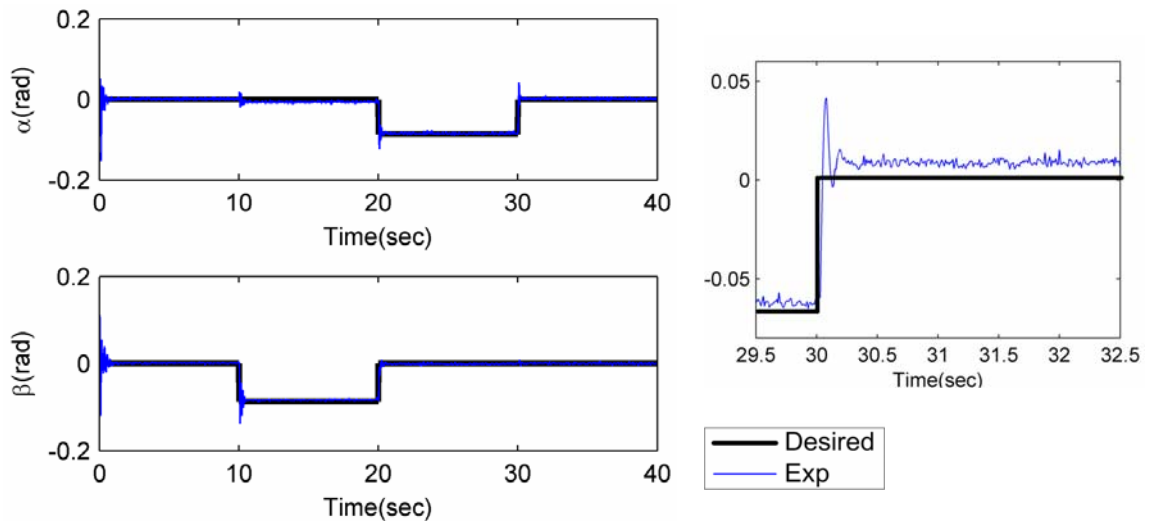
(c) Step response in PD control with high gain observer

Figure 6-10 PD control with a high gain observer using step input

6.3.2 Inclination control of spinning rotor

This section presents the experimental results for tests of the inclination control of a continuously spinning shaft. Since the spin motion is controlled in the open-loop, the effect of inclination motion on the spin must be minimized so that the rotor motion is stable. For this reason, the ramp inputs for orientation control (previously designed) are applied to minimize the effect of the undesired transient response. The same gain matrices for the closed loop control are used to compare the effects of the square wave for the spin control on the inclination control. The trajectory used in this test is as follows:

After initialization of the rotor, the 45 degree spinning controller is applied and spinning starts at 185 rpm. The spin rate slowly increases up to 300 rpm. A high spin rate helps the rotor stabilize. Then the inclination input is applied to

α=5° and β=0°. Once the rotor reaches the desired position, it moves to the desired circle trajectory (black solid line) while maintaining a constant spin rate.

The experimental results of all controllers in Figures 6-11, 6-12 and 6-13 have oscillation, which is also seen in the simulation results as shown in Figure 5-13. The period of the oscillation is proportional to the spinning velocity, which implies that the square wave for the switching controller has effect on the spin motion.

In addition, some undesired motion and errors are shown in the experimental results. The possible causes could be:

- The spin motion is controlled by the open loop.

- The rotor has an eccentricity.

- The system has mechanical imperfections such as the coil is wound unevenly and there is non uniform air gap spacing.

- The rotor motion was also found to be non concentric.

Open loop control
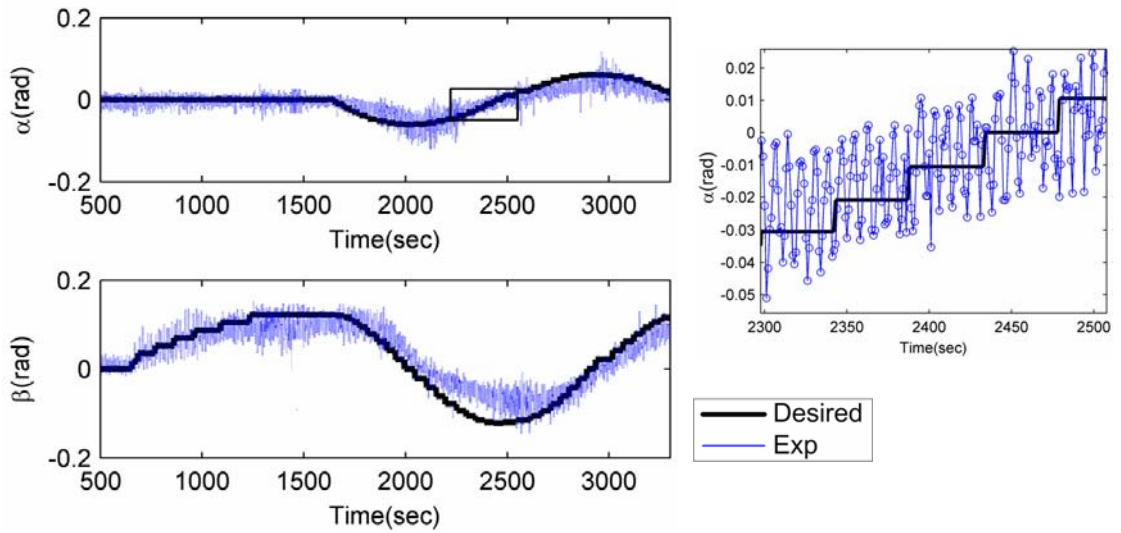
(a) Orientation   (b) Enlargement of box in (a)
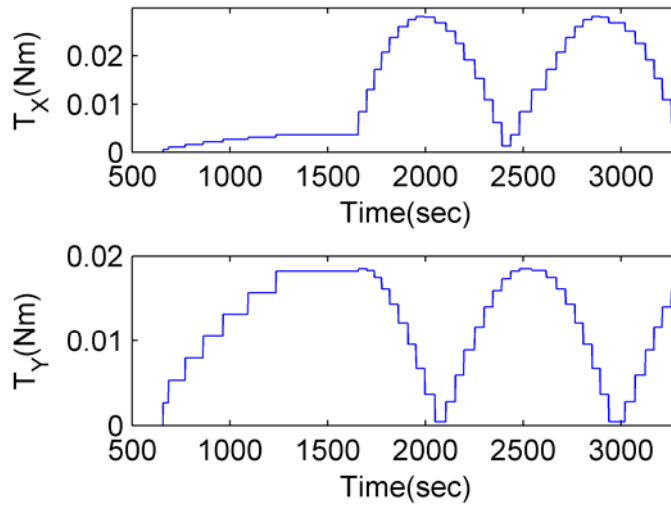
(c) Desired torque

Figure 6-11 Model based open loop controller (continuous)

172
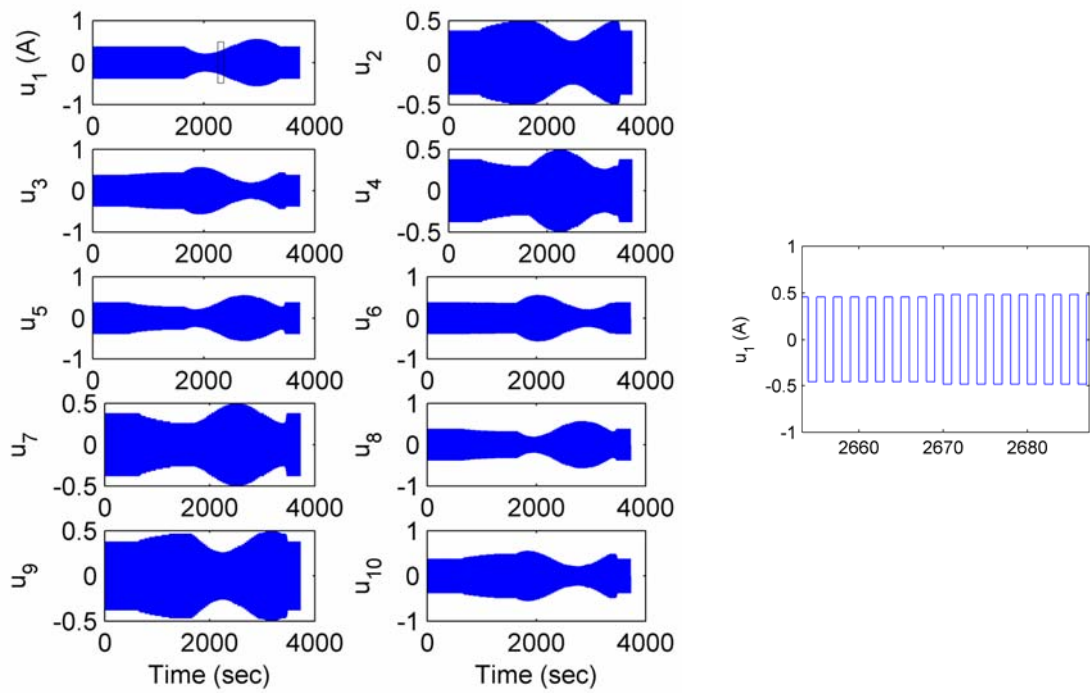
(d) Applied currents   (e) Enlargement of box in (d)

Figure 6-11 Model based open loop controller

PD control
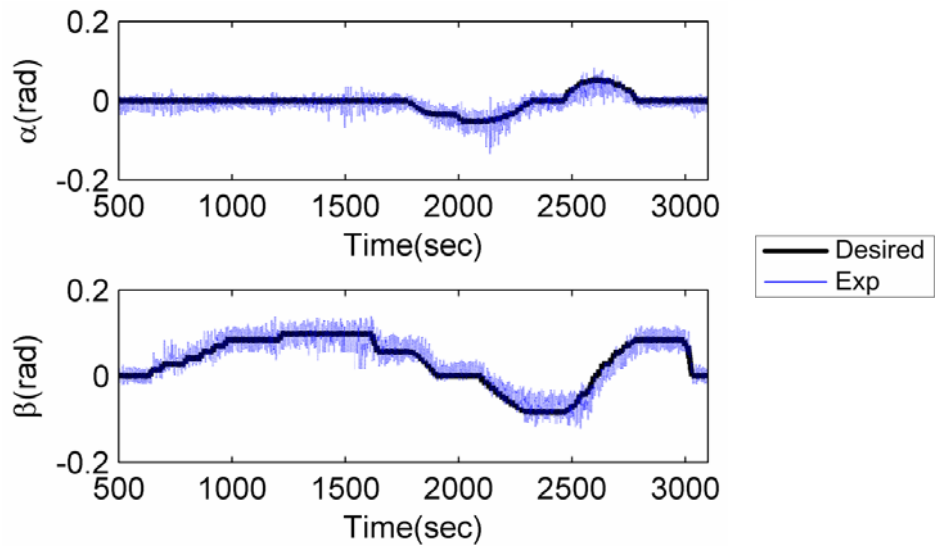
(a) Orientation

Figure 6-12 PD controller (continuous)
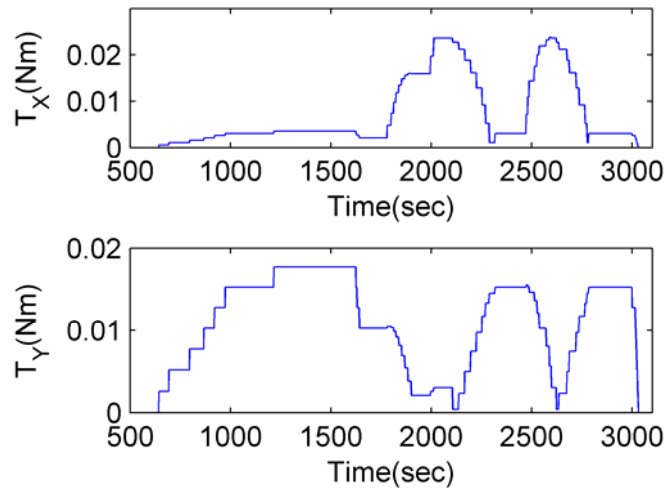
(b) Desired torque
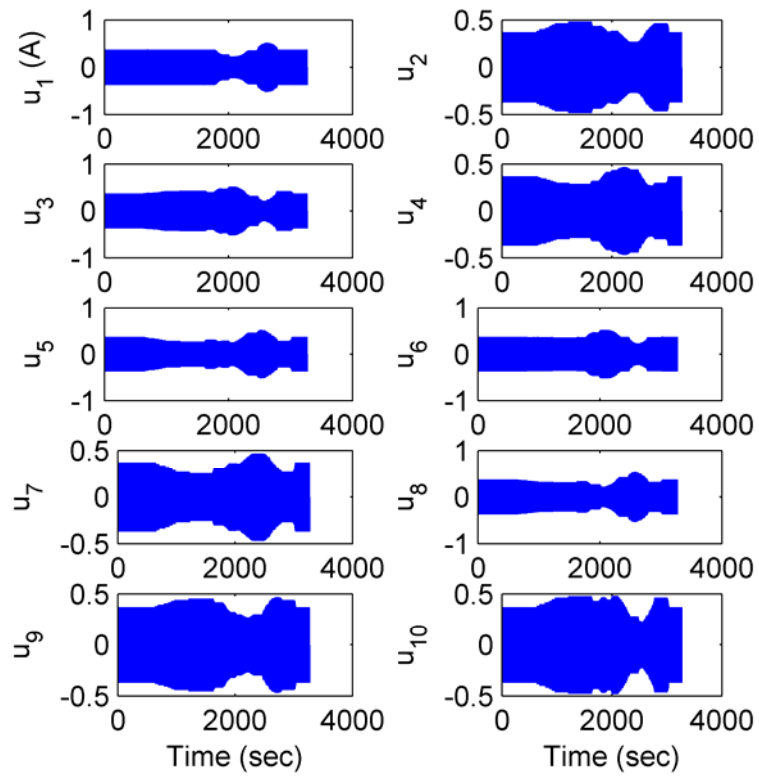
(c) Applied currents

Figure 6-12 PD controller

PD with a high gain observer
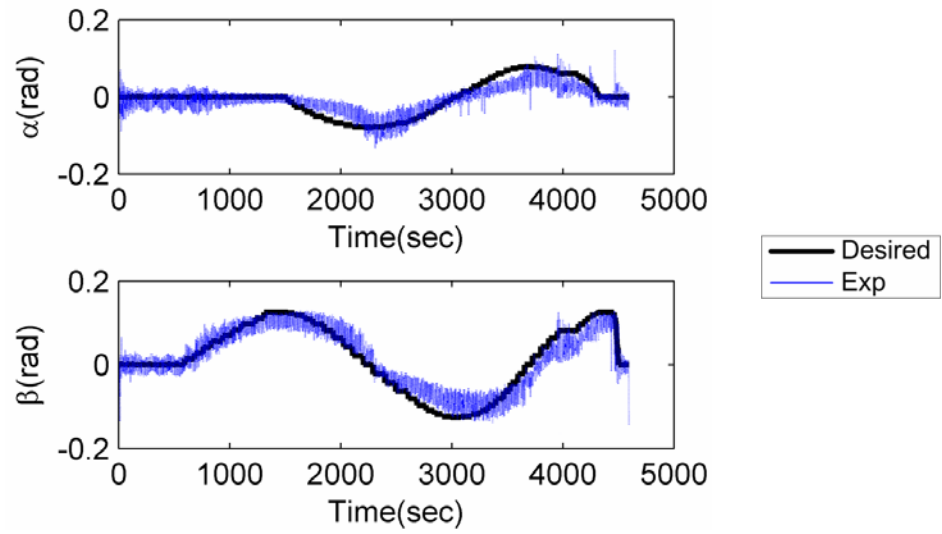
(a) Orientation
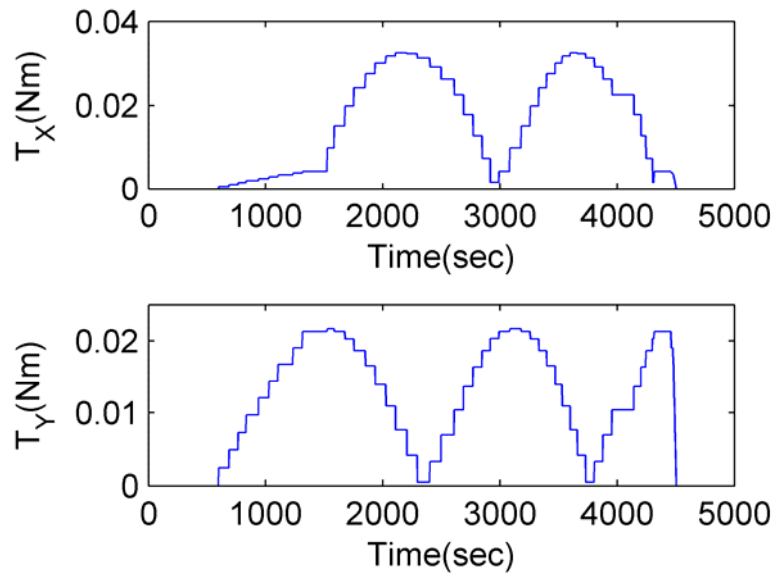
(b) Desired torque

Figure 6-13 PD controller with high gain observer (continuous)
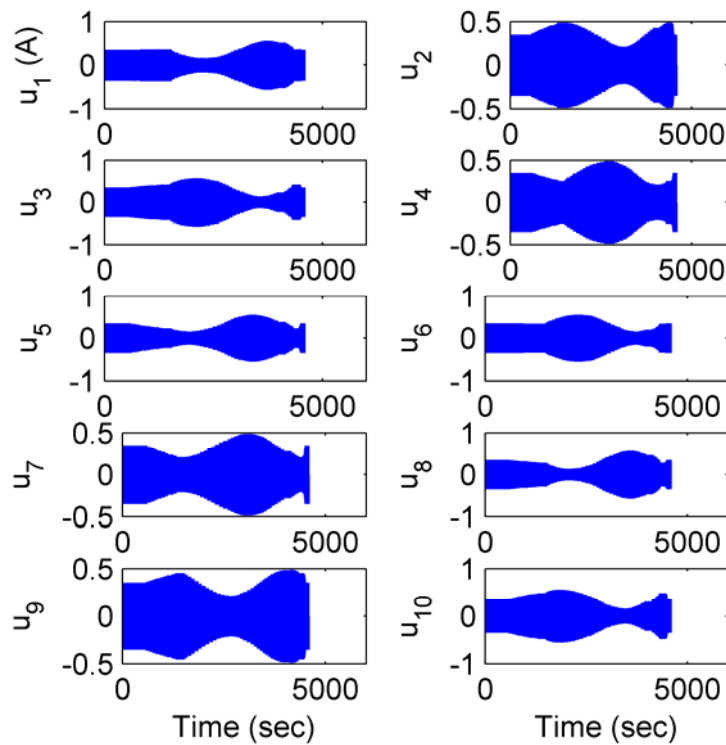
(c) Applied currents

Figure 6-13 PD controller with high gain observer

6.4   SUMMARY

This chapter has presented the real-time control designs of the SWM. In particular, experimental results and practical implementation of the sensor measurement for the orientation control of the SWM have been presented. The simulation results and the experimental results show excellent agreement.

Three different controllers have been implemented to the SWM; OL and PD controller with and without the observer. Model based OL controllers along with three control input shapes have been examined for the inclination control without spin motion.

Their results offer physical intuition, practical effectiveness, and demonstrate the accuracy of the DMP model. In addition, the feedback controllers have also implemented and various position control experiments have been performed.

The experimental results verify the design of control systems and demonstrate the motion capability of the SWM. While the experimental results illustrate the ability to move, they also reveal the constraints and limitations of the controller design and provide insights for future design of the SWM.

CHAPTER 7

CONCLUSION AND FUTURE WORKS

7.1   ACCOMPLISHMENTS AND CONTRIBUTIONS

This thesis presented a new control-oriented method to model magnetic fields and their application in non-contact orientation sensing and control of a spherical wheel motor. Three specific contributions have been made:

I. Magnetic field analysis for design and control of an electromagnetic actuator

A general modeling method which derives the magnetic field closed–form solution of a permanent magnet or an electromagnet has been presented. This method consists of three parts; the DMP model, equivalent PM model, and combined DMP and image method.

● The DMP model, which extends the concept of a magnetic doublet beyond the context of physics, provides an effective means to account for the shape and magnetization of the physical magnet. The model has been validated by comparing simulation results with published data for a cylinder PM and a customized shape PM.

● The DMP model has been further extended to analyze the field of a multilayer electromagnet. In the process of modeling the multilayer electromagnet as a PM (and hence a DMP model), we derive an equivalent single-layer model that

significantly reduces the computation time for calculating the magnetic force. In addition, the DMP model of the multilayer electromagnet offers a means to visualize the magnetic fields. Once the entire magnetic field is computed, the magnetic force can be calculated using either Lorentz force or Maxwell stress tensor.

- Through the use of the image method, we show how the DMP model can be extended to account for the effect of magnetic material interfaces. Two practical examples illustrated the principle of the image method; the plane boundary and the spherical boundary in the 3D space. Then, these methods were extended to characterize the spherical wheel motor which has an iron-cored rotor and iron stator.

These simple but accurate methods can be used not only to optimize the design of the SWM (including material selection) but also to help analyze the dynamics of its control system.

II. Non contact orientation sensing methodology

The simple magnetic field models have been exploited to develop novel orientation sensors by inversely solving the DMP model. Two orientation sensing methods, incremental and absolute, were developed. The incremental method is based on the Jacobian of the magnetic field and it provides the current shaft orientation from its past orientation. However, the method is susceptible to cumulative errors and updating rate of measurement. The absolute method, which approximates the magnetic field using closed-form polynomial functions, is independent of the sampling rate and is also

insensitive to the sensor noise. For these reasons, a method was chosen for measuring the shaft inclination of the SWM.

The ability to characterize magnetic fields and forces, in addition to determining the orientation using Hall effect sensors, offers a number of advantages in real-time computation and control. These include

- small and compact design without mechanical linkages that must be incorporated if the three DOF orientation is measured independently using the single axis encoder.

- low cost, since Hall effect sensors are generally inexpensive, and

- accurate measurement with real-time computation.

A single PM-based device has been designed to demonstrate the feasibility of sensing methods, and to provide insight for optimizing the sensor design. It is expected that such method will have immense potential for a spectrum of engineering applications such as gyroscopes, haptic devices and MEMS devices, etc.

III. Control of the SWM

Three controllers (OL, PD and PD with an observer) using the DMP models have been designed and implemented on an existing spherical motor: Unlike prior methods that focused on orientation control, this thesis presents a control design that decouples the inclination control of the shaft from its spin motion. The decoupling property allows the OL controller to consist of two independent parts; a switching (spin-rate) controller and an inclination controller. The switching (spin-rate) controller is based on the principle of a stepper and an inclination controller is based on the inverse torque model. In addition,

three inputs (step, combined two steps and ramp) for the model based OL controller are applied to minimize the overshoot and oscillation in the transient response.

The OL controller which serves as a basis for feedback control system designs has been shown (both in simulation and experiments) to be capable of controlling a desired trajectory. To account for the un-modeled dynamics or external disturbances, the orientation sensor (with and without an additional observer) is implemented to allow for closed loop control with a PD controller. The feedback controlled systems were experimentally evaluated.

7.2   FUTURE WORKS

The outcome of this thesis research has extended the knowledge base for analysis, design and control of PM based actuators. The results are encouraging. Further research and possible directions are briefly summarized as follows:

1.   Effects of nonlinearity on the magnetic field such as iron saturation, eddy current

The DMP modeling method has been based on the assumption that the superposition principle holds. Recently, the magnetization of a modern permanent magnet is very strong and dense. It well satisfies the linearity for general applications in the electromagnetic actuator. However, the demand for accuracy in the computation often requires accounting for a nonlinear effect.

For applications where the rotor spins at high speed and voltage controls an EM, time varying effect may not be neglected. The DMP model can be extended to account for the time varying magnetic field. The image method can be used to characterize the

eddy current in magnetic conducing boundary with the time varying DMP model. A number of researchers have already explored the use of the image method to investigate the eddy current effect.

In addition, the DMP method can be further extended in the microscopic magnetic field namely, using the motion of a magnetic particle, which is the dynamic model of a dipole, for damped gyromagnetic precession. Since the DMP method is developed from the concept of magnetic particle momentum called 'magnetic dipole', the precession motion can be introduced from the spin magnetic momentum of electrons and their angular momentum in the dipole theory.

As a potential application, this study includes biomedical devices such as magnetic resonance imaging (MRI), magnetocardiography (MCG) and storage devices such as a thin film and head of computer storage system.

2. Sensor optimization and implementation.

Due to the limited sampling rate, we implemented the orientation measurement system using an additional permanent magnet. The method has been successfully tested through simulation as well as through experiments using the SWM. However, the spin angle and its rate were not measured. To extend the method to measure the spin motion, the total magnetic field of the SWM should be directly estimated. The simulation results for the rotor poles have shown the feasibility of measuring the orientation of a rotating shaft without additional PM. It requires a higher sampling rate to maintain accuracy.

Currently, the minimum $1msec$ sampling rate restricts to the maximum spin rate since the software control (Window OS) is limited. However, this restriction can be overcome by using a separate measurement system from a controller system.

An optimal sensor configuration can be found to estimate the magnetic field quantitatively, which systematically determines the sensor location, the number of sensors, and the measurable axis. Since the measurement is critical to the design of the control system and also to computing the torque, the research work will have significant contributions of practical precision applications.

3. Hardware and software controller design

Both analytical and experimental results have shown that accurate timing is a key of the control parameter. Control Performance is mostly sensitive to the update rate of the feedback loop. Currently, D/A converters in the experimental setup have a 15ms limitation for the updating rate, which in turn is a major limiting factor on spin control. Improving the control update rate is therefore considered to be the immediate next step. The ultimate or ideal approach is to use a smooth sine wave instead of the square wave for the spin motion. The same control strategy can be used for the smooth wave to control the orientation and spin motion respectively, which produces a smooth motion and reduces the undesired torque ripple.

In addition, the control system used a single processor to compute the optimizing current inputs and to measure the orientation. As the speed of the spin motion increases, the processor requires faster computation and handles a number of measurement data. A quick alternative is to use fast multiple processors and thus, each core processor carries out its own computation independently.

The SWM used a spherical ball bearing at the center joint. It caused some mechanical problems such as rotor eccentricity, mechanical wearing, and bearing

magnetization. To overcome these difficulties, the bearing can be replaced by a magnetic

levitation bearing which is currently investigated.

APPENDIX A

The Jacobin Matrix of the magnetic field $\mathbf{B} = f(X, Y, Z, \alpha, \beta, \gamma)$ for Equation (4.7) in terms of the inertial XYZ frame is given by

$$\nabla \bullet \mathbf{B} = \begin{bmatrix} B_{X\alpha} & B_{X\beta} & B_{X\gamma} \\ B_{Y\alpha} & B_{Y\beta} & B_{Y\gamma} \\ B_{Z\alpha} & B_{Z\beta} & B_{Z\gamma} \end{bmatrix} \tag{A.1}$$

where $B_{X\alpha} = \dfrac{\partial B_X}{\partial \alpha} = \dfrac{\mathrm{Num}_{X\alpha}}{\mathrm{Den}}$;

$\mathrm{Den} = 2((Z - z\cos\alpha\cos\beta + y\cos\beta\sin\alpha - x\sin\beta)^2 +$
$((-X + \cos\gamma(x\cos\beta + (-z\cos\alpha + y\sin\alpha)\sin\beta) + (y\cos\alpha + z\sin\alpha)\sin\gamma)^2 +$;
$(Y - \cos\gamma(y\cos\alpha + z\sin\alpha) + x\cos\beta\sin\gamma + (-z\cos\alpha + y\sin\alpha)\sin\beta\sin\gamma)^2)^{5/2}$

$\mathrm{Num}_{X\alpha} = (m(-2(-\cos\gamma(y\cos\alpha + z\sin\alpha)\sin\beta + (-z\cos\alpha + y\sin\alpha)\sin\gamma)$
$((Z - z\cos\alpha\cos\beta + y\cos\beta\sin\alpha - x\sin\beta)^2 +$
$(-X + \cos\gamma(x\cos\beta + (-z\cos\alpha + y\sin\alpha)\sin\beta) + (y\cos\alpha + z\sin\alpha)\sin\gamma)^2 +$
$(Y - \cos\gamma(y\cos\alpha + z\sin\alpha) + x\cos\beta\sin\gamma + (-z\cos\alpha + y\sin\alpha)\sin\beta\sin\gamma)^2) +$;
$6(X - x\cos\beta\cos\gamma + \cos\gamma(z\cos\alpha - y\sin\alpha)\sin\beta - (y\cos\alpha + z\sin\alpha)\sin\gamma)$
$(\sin\alpha(zZ\cos\beta + yY\cos\gamma - zX\cos\gamma\sin\beta + yX\sin\gamma + zY\sin\beta\sin\gamma) +$
$\cos\alpha(yZ\cos\beta - z(Y\cos\gamma + X\cos\gamma) + y\sin\beta(-X\cos\gamma + Y\sin\gamma)))))$

$B_{X\beta} = \dfrac{\mathrm{Num}_{X\beta}}{\mathrm{Den}}$;

$\mathrm{Num}_{X\beta} = (m(-2\cos\gamma(z\cos\alpha\cos\beta - y\cos\beta\sin\alpha + x\sin\beta)$
$((Z - z\cos\alpha\cos\beta + y\cos\beta\sin\alpha - x\sin\beta)^2 +$
$(-X + \cos\gamma(x\cos\beta + (-z\cos\alpha + y\sin\alpha)\sin\beta) + (y\cos\alpha + z\sin\alpha)\sin\gamma)^2 +$
$(Y - \cos\gamma(y\cos\alpha + z\sin\alpha) + x\cos\beta\sin\gamma + (-z\cos\alpha + y\sin\alpha)\sin\beta\sin\gamma)^2) -$;
$6(X - x\cos\beta\cos\gamma + \cos\gamma(z\cos\alpha - y\sin\alpha)\sin\beta - (y\cos\alpha + z\sin\alpha)\sin\gamma)$
$(\sin\beta(-zZ\cos\alpha - xX\cos\gamma + yZ\sin\alpha + xY\sin\gamma) +$
$\cos\beta(xZ - (z\cos\alpha - y\sin\alpha)(X\cos\gamma - Y\sin\gamma)))))$

$B_{X\gamma} = \dfrac{\mathrm{Num}_{X\gamma}}{\mathrm{Den}}$;

$$\text{Num}_{X\gamma} = (m(6(X - x\cos\beta\cos\gamma + \cos\gamma(z\cos\alpha - y\sin\alpha)\sin\beta$$
$$-(y\cos\alpha + z\sin\alpha)\sin\gamma)(x\cos\beta(Y\cos\gamma + X\sin\gamma) + (-z\cos\alpha + y\sin\alpha)$$
$$\sin\beta(Y\cos\gamma + X\sin\gamma) - (y\cos\alpha + z\sin\alpha)(X\cos\gamma - Y\sin\gamma)) - 2(-\cos\gamma$$
$$(y\cos\alpha + z\sin\alpha) + (x\cos\beta + (-z\cos\alpha + y\sin\alpha)\sin\beta)\sin\gamma)$$
$$((Z - z\cos\alpha\cos\beta + y\cos\beta\sin\alpha - x\sin\beta)^2 +$$
$$(-X + \cos\gamma(x\cos\beta + (-z\cos\alpha + y\sin\alpha)\sin\beta + (y\cos\alpha + z\sin\alpha)\sin\gamma)^2 +$$
$$(Y - \cos\gamma(y\cos\alpha + z\sin\alpha) + x\cos\beta\sin\gamma + (-z\cos\alpha + y\sin\alpha)\sin\beta\sin\gamma)^2))) \quad ;$$

$$B_{Y\alpha} = \frac{\partial B_Y}{\partial\alpha} = \frac{\text{Num}_{Y\alpha}}{\text{Den}} \ ;$$

$$\text{Num}_{Y\alpha} = (m(-2(-\cos\alpha(-z\cos\gamma + y\sin\beta\sin\gamma) +$$
$$\sin\alpha(y\cos\gamma + z\sin\beta\sin\gamma))$$
$$((Z - z\cos\alpha\cos\beta + y\cos\beta\sin\alpha - x\sin\beta)^2 +$$
$$(-X + \cos\gamma(x\cos\beta + (-z\cos\alpha + y\sin\alpha)\sin\beta + (y\cos\alpha + z\sin\alpha)\sin\gamma)^2 +$$
$$(Y - \cos\gamma(y\cos\alpha + z\sin\alpha) + x\cos\beta\sin\gamma + (-z\cos\alpha + y\sin\alpha)\sin\beta\sin\gamma)^2) + \quad ;$$
$$6(Y - \cos\gamma(y\sin\alpha + z\cos\alpha) + x\cos\beta\sin\gamma + (-z\cos\alpha + y\sin\alpha)\sin\beta\sin\gamma)$$
$$(\sin\alpha(zZ\cos\beta + yY\cos\gamma - zX\cos\gamma\sin\beta + yX\sin\gamma + zY\sin\beta\sin\gamma) +$$
$$\cos\alpha(yZ\cos\beta - z(Y\cos\gamma + X\cos\gamma) + y\sin\beta(-X\cos\gamma + Y\sin\gamma)))))$$

$$B_{Y\beta} = \frac{\text{Num}_{1\,Y\beta}}{(\text{Den}/2)^{3/5}} + \frac{\text{Num}_{2\,Y\beta}}{\text{Den}} \ ;$$

$$\text{Num}_{1\,Y\beta} = m(z\cos\alpha\cos\beta - y\cos\beta\sin\alpha + x\sin\beta) \ ; \text{ and}$$

$$\text{Num}_{2\,Y\beta} = (6m(Y - \cos\gamma(y\cos\alpha + z\sin\alpha) + x\cos\beta\sin\gamma +$$
$$(-z\cos\alpha + y\sin\alpha)\sin\beta\sin\gamma)$$
$$(\sin\beta(-zZ\cos\alpha - xX\cos\gamma + yZ\sin\alpha + xY\sin\gamma) + \quad ;$$
$$\cos\beta(xZ - (z\cos\alpha - y\sin\alpha)(X\cos\gamma - Y\sin\gamma))))$$

$$B_{Y\gamma} = \frac{\text{Num}_{Y\gamma}}{\text{Den}} \ ;$$

$$\text{Num}_{Y\gamma} = (m(6(Y - \cos\gamma(y\cos\alpha + z\sin\alpha) + x\cos\beta\sin\gamma$$
$$+ (-z\cos\alpha + y\sin\alpha)\sin\beta\sin\gamma)$$
$$(x\cos\beta(Y\cos\gamma + X\sin\gamma) + (-z\cos\alpha + y\sin\alpha)\sin\beta(Y\cos\gamma + X\sin\gamma) -$$
$$(y\cos\alpha + z\sin\alpha)(X\sin\gamma - Y\cos\gamma)) -$$
$$2(\cos\gamma(x\cos\beta + (-z\cos\alpha + y\sin\alpha)\sin\beta) + (y\cos\alpha + z\sin\alpha)\sin\gamma) \quad ;$$
$$((Z - z\cos\alpha\cos\beta + y\cos\beta\sin\alpha - x\sin\beta)^2 +$$
$$(-X + \cos\gamma(x\cos\beta + (-z\cos\alpha + y\sin\alpha)\sin\beta + (y\cos\alpha + z\sin\alpha)\sin\gamma)^2 +$$
$$(Y - \cos\gamma(y\cos\alpha + z\sin\alpha) + x\cos\beta\sin\gamma + (-z\cos\alpha + y\sin\alpha)\sin\beta\sin\gamma)^2)))$$

$$B_{Z\alpha} = \frac{\text{Num}_{Z\alpha}}{\text{Den}};$$

$$\text{Num}_{Z\alpha} = (m(-2(-\cos\beta(y\cos\alpha + z\sin\alpha)$$
$$((Z - z\cos\alpha\cos\beta + y\cos\beta\sin\alpha - x\sin\beta)^2 +$$
$$(-X + \cos\gamma(x\cos\beta + (-z\cos\alpha + y\sin\alpha)\sin\beta + (y\cos\alpha + z\sin\alpha)\sin\gamma)^2 +$$
$$(Y - \cos\gamma(y\cos\alpha + z\sin\alpha) + x\cos\beta\sin\gamma + (-z\cos\alpha + y\sin\alpha)\sin\beta\sin\gamma)^2) + ;$$
$$6(Z - z\cos\alpha\cos\beta + y\cos\beta\sin\alpha - x\sin\beta)$$
$$(\sin\alpha(zZ\cos\beta + yY\cos\gamma - zX\cos\gamma\sin\beta + yX\sin\gamma + zY\sin\beta\sin\gamma) +$$
$$\cos\alpha(yZ\cos\beta - z(Y\cos\gamma + X\cos\gamma) + y\sin\beta(-X\cos\gamma + Y\sin\gamma)))))$$

$$B_{Z\beta} = \frac{\text{Num}_{Z\beta}}{\text{Den}};$$

$$\text{Num}_{X\beta} = (m(-2(-x\cos\beta + (z\cos\alpha - y\sin\alpha)\sin\beta)$$
$$((Z - z\cos\alpha\cos\beta + y\cos\beta\sin\alpha - x\sin\beta)^2 +$$
$$(-X + \cos\gamma(x\cos\beta + (-z\cos\alpha + y\sin\alpha)\sin\beta + (y\cos\alpha + z\sin\alpha)\sin\gamma)^2 +$$
$$(Y - \cos\gamma(y\cos\alpha + z\sin\alpha) + x\cos\beta\sin\gamma + (-z\cos\alpha + y\sin\alpha)\sin\beta\sin\gamma)^2) - ;$$
$$6(Z - z\cos\alpha\cos\beta + y\cos\beta\sin\alpha - x\sin\beta)$$
$$(\sin\beta(-zZ\cos\alpha - xX\cos\gamma + yZ\sin\alpha + xY\sin\gamma) +$$
$$\cos\beta(xZ - (z\cos\alpha - y\sin\alpha)(X\cos\gamma - Y\sin\gamma)))))$$

$$B_{Z\gamma} = \frac{\text{Num}_{Z\gamma}}{\text{Den}};$$

$$\text{Num}_{Z\gamma} = (-6m(Z - z\cos\alpha\cos\beta + y\cos\beta\sin\alpha - x\sin\beta)$$
$$(-x\cos\beta(Y\cos\gamma + X\sin\gamma) +$$
$$(z\cos\alpha - y\sin\alpha)\sin\beta(Y\cos\gamma + X\sin\gamma) \qquad .$$
$$+ (y\cos\alpha + z\sin\alpha)(X\sin\gamma - Y\cos\gamma)))$$

APPENDIX B

B.1 Magnetic Dipole model for the orientation sensor

To illustrate the use of DMP model for designing an orientation sensor and investigate the effects of some parameters on the design, the following simplifications are made for the clarity in explanation:

(a) The sensors are located such that $R \gg \overline{\ell}, \overline{a}$.

$$R_{\pm}^{-3} \approx \left(R \mp \overline{\ell} \cos\sigma / 2 \right)^{-3} \approx R^{-3} \left[1 \pm 3\overline{\ell} \cos\sigma / (2R) \right] \tag{B.1}$$

(b) Sensor are oriented such that $\sigma \approx 90°$; $\overline{\ell} \cos\sigma / R \ll 1$.

Assumption (a) reduces the expression for the magnetic field **B** to

$$\mathbf{B} \approx \frac{\mu_o}{4\pi R^3} \left(1 - \frac{3\overline{\ell}\cos\sigma}{2R} \right) \sum_{j=0}^{k} \sum_{i=1}^{n_k} m_j \left(\mathbf{P_{ji+}} - \mathbf{P_{ji-}} \right) \tag{B.2}$$

where $\cos\sigma = \mathbf{M} \cdot \mathbf{R} / \left(|\mathbf{M}||\mathbf{R}| \right)$ as shown in Figure 4-1. In Equation (B.2), $\mathbf{P_{ji+}} - \mathbf{P_{ji-}}$ is the vector of length $\overline{\ell}$ in XYZ frame. Hence, with assumption (b) and the sensor locations defined in,

$$\rho_X = \frac{B_{X+}}{B_{X-}} = \frac{R_{1-}^3}{R_{1+}^3} \text{ and } \rho_Y = \frac{B_{Y+}}{B_{Y-}} = \frac{R_{2-}^3}{R_{2+}^3} \tag{B.3}$$

where the sensor location $R_{i\pm} = |\mathbf{S}_{i\pm} - \mathbf{P_m}|$ is given by

$$R_{1\pm}^2 = \left(\pm S - X_m \right)^2 + Y_m^2 + \left(Z_s - Z_m \right)^2 \tag{B.4}$$

$$\text{and } R_{2\pm}^2 = X_m^2 + \left(\pm S - Y_m \right)^2 + \left(Z_s - Z_m \right)^2$$

In Equation (B.4), $\mathbf{P_m} = \begin{bmatrix} X_m & Y_m & Z_m \end{bmatrix}^T$ defines the center of the PM;

$$X_m^2 + Y_m^2 + Z_m^2 = L^2 \tag{B.5}$$

Equations (B.2) to (B.5), which implicitly relate $\mathbf{B}$ to $\hat{\mathbf{z}}$ through R and σ, can be used to solve X_m, Y_m and Z_m in closed form. Expanding Equation (B.3) with Equation (B.5),

$$R_{1+}^2 \left(\rho_X^{2/3} - 1 \right) = 4X_m S \tag{B.6}$$

$$R_{1+}^2 \left(\rho_X^{2/3} + 1 \right) = 2 \left(S^2 + Z_s^2 - 2Z_m Z_s + L^2 \right) \tag{B.7}$$

$$R_{2+}^2 \left(\rho_Y^{2/3} - 1 \right) = 4Y_m S \tag{B.8}$$

$$R_{2+}^2 \left(\rho_Y^{2/3} + 1 \right) = 2 \left(S^2 + Z_s^2 - 2Z_m Z_s + L^2 \right) \tag{B.9}$$

Eliminating R_{1+}^2 from Equations (B.5) and (B.7). Similarly, R_{2+}^2 from Equation (B.5) and (B.8) leads to Equation (B.10):

$$X_m = m_X \left(hZ_m - H \right)$$
$$Y_m = m_Y \left(hZ_m - H \right) \tag{B.10}$$

where $m_X = \left(1 - \rho_X^{2/3} \right) / \left(1 + \rho_X^{2/3} \right)$; $m_Y = \left(1 - \rho_Y^{2/3} \right) / \left(1 + \rho_Y^{2/3} \right)$; $h = Z_s / S$;

and $H = S \left(1 + h^2 + L^2 / S^2 \right) / 2$.

From Equations (B.5) and (B.10),

$$Z_m = \frac{hH}{1 + \left(m_X^2 + m_Y^2 \right) h^2} \left\{ 1 \pm \sqrt{1 + \left[1 + \left(m_X^2 + m_Y^2 \right) h^2 \right] \left(\frac{L^2}{H^2} - \frac{1}{h^2} \right)} \right\} \tag{B.11}$$

In Equations (B.10) and (B.11), the parameters m_X and m_Y are measured quantities; and h and H are constants characterizing the placement of the sensor pairs. Once $\mathbf{P_m} = \begin{bmatrix} X_m & Y_m & Z_m \end{bmatrix}^T$ is known, the orientation (α, β) can be solved from the unit vector $\hat{\mathbf{z}}$ in Equation (4.2).

This example demonstrates that the shaft inclination can be determined from two orthogonal magnetic sensor-pairs. While the assumption that essentially approximates the PM as a single dipole permits the orientation (α, β) to be solved in closed form, it has some practical limitations where R and $\overline{\ell}$ are in the same order.

REFERENCES

[1] W. Clarke, "Mercedes-Benz F-400 Carving", http://www.edmunds.com, 2002.

[2] J. Peter, "The Wave of the Future?," Automotive Industries, 2004.

[3] W. Wang, J. Jewell, and D. Howe, "Design and Control of a Novel Spherical Permanent Magnet Acutator With Three Degrees of Freedom," *IEEE/ASME Trans. on Mechatronics,* vol. 8 no4, p. 457, 2003.

[4] L. Yan, I. M. Chen, G. Yang, and K.-M. Lee, "Analytical and experimental investigation on the magnetic field and torque of a permanent magnet spherical actuator," *IEEE/ASME Transactions on Mechatronics,* vol. 11, pp. 409-418, 2006.

[5] R. F. Hanington, "Matrix methods for fields," in *Proc. IEEE.* vol. 55, 1967, pp. 136-149.

[6] T. J. Cui and C. H. Liang, "Perturbation technique for matrix equations and its application in the computation of internal fields in a three-dimensional arbitrarily shaped biological body," *IEEE Transactions on Antennas and Propagation,* vol. 42, pp. 569-573, 1994.

[7] J. M. Johnson and Y. Rahmat-Samii, "Genetic algorithms and method of moments (GA/MOM) for the design of integrated antennas," *IEEE Transactions on Antennas and Propagation,* vol. 47, pp. 1606-1614, 1999.

[8] K.-M. Lee, R. A. Sosseh, and Z. Wei, "Effects of the torque model on the control of a VR spherical motor," *Control Engineering Practice,* vol. 12, pp. 1437-1449, 2004.

[9] Q. Li and K.-M. Lee, "An adaptive meshless computation method for design of electromechanical actuators," Beijing, China, 2006, pp. 5453-5458.

[10] D. J. Craik, "Magnetostatics of axially symmetric structure," *J. of Physics,* vol. 7, p. 1566, 1974.

[11] T. H. Boyer, "The force on a magnetic dipole," *American J. of Physics,* vol. 56, pp. 688-92, 1988.

[12] M. A. Green, "Modeling the behavior of oriented permanent magnet material using current doublet theory," *IEEE Trans. on Magnetics,* vol. 24 no.2, p. 1528, 1988.

[13] W. S. Bennett, "Basic sources of electric and magnetic fields newly examined," *IEEE Antennas and Propagation Magazine,* vol. 43, pp. 31-5, 2001.

[14] S. Nedelcu and J. H. P. Watson, "Mangetic dipole model of a permanent magnet based device," *J. of Physics,* vol. 34, pp. 2622-2628, 2001.

[15] T. Amano, T. Ishii, K. Nakamura, and S. Ueha, "Ultrasonic actuator with multi-degree of freedom using bending and longitudinal vibrations of a single stator," *Proc. of the IEEE Ultrasonics Symposium,* vol. 1, pp. 667-670, 1998.

[16] D. Visschere and Patrick, "An exact two-dimensional model for a periodic circular array of head-to-head permanent magnets," *J. of Physics D: Applied Physics,* vol. 38, pp. 355-362, 2005.

[17] A. Foggia, E. Oliver, and F. Chappuis, "New Three Degrees of Freedom Electromagnetic Actuator," in *IAS Annual Meeting*, New York, 1988.

[18] G. Vachtsevanos, K. Davey, and K.-M. Lee, "Development of a Navel Intelligent Robotics Manipulator," *IEEE Control Systems Magazine,* vol. 7, pp. 9-15, June 3 1987.

[19] K. Davey and G. Vachtsevanos, "The Analysis of Fields and Torques in a Spherical Induction Motor " *IEEE Trans. on Magnetics,* vol. MAG-23, MARCH 1987.

[20] L. Neto, R. Mendes, and D. A. Andrade, "Spherical Motor-A three-dimensional position servo," in *Proc. of IEEE Conf. on Electrical Machines and Drives*, 1995, pp. 227-231.

[21] R. L. Hollis, S. E. Salcudean, and A. P. Allan, "A Six-Degree-of-Freedom Magnetically Levitated Variable Compliance Fin-Motion Wrist: Design, Modeling, and Control," *IEEE Trans. Robot. Automat.,* vol. 17, pp. 320-332, June 1991.

[22] K. Kaneko, I. Yamada, and K. Itao, "A Spherical DC Servo Motor with Three Degrees of Freedom," *ASME, Dyn. Sys. And Control Div,* pp. 398-402, 1988.

[23]   K.-M. Lee and C. Kwan, "Design Concept Development of a Spherical Stepper for Robotic Applications," *IEEE Trans. on Robotics and Automation,* vol. 7, February 1991.

[24]   J. Wang, G. Jewel, and D. Howe, "Modeling of a novel spherical permanent magnet actuator," in *Proc. of IEEE Inter. Conf. On Robotics and Automation*, Albuquerque, 1997, pp. 1190-1195.

[25]   K.-M. Lee, G. Meyouhas, and R. Blenis, "Direct Sensing of Three DOF Orientation of a Spherical Wrist Actuator," in *Proc. of the 1993 NSF Design and Manufacturing Systems Conference*, Charlotte, NC,, 1993.

[26]   T. Shigeki, Z. Guoqiang, and M. Osamu, "Development of New Generation Spherical Ultrasonic Motor," in *Proc. of the 1996 IEEE International Conf. on Robotics and Automation*, 1996, pp. 2871-2876.

[27]   F. C. Williams, E. R. Laithwaite, and J. F. Eastham, "Development and design of spherical induction motors," *Institution of Electrical Engineers Proc.Part A. Power Engineering,* vol. 106, pp. 471-484, 1959.

[28]   K.-M. Lee and P. J., "Kinematic Analysis of a Three Degree-of-Freedom Spherical Wrist Actuator," in *The Fifth Inter. Conf. on Adv. Robotics*, Italy, 1991.

[29]   J. Wang, G. Jewel, and D. Howe, "Analysis, design and control of a novel spherical permanent magnet actuator," *IEE Proc. of Electr. Power Appl.,* vol. 154, 1998.

[30]   G. S. Chirikjian and D. Stein, "Kinematic design and commutation of a spherical stepper motor," *IEEE/ASME Trans. on Mechatronics,* vol. 4, pp. 342-353, DEC 1999.

[31]   K. Kahlen and R. W. De Doncker, "Current regulators for multi-phase permanent magnet spherical machines," in *Industry Applications Conference*, 2000, pp. 2011-2016.

[32]   C. Yang and Y. S. Baek, "Design and control of the 3 degrees of freedom actuator by controlling the electromagnetic force," *IEEE Trans. on Magnetics,* pp. 3607-3609., May 1999.

[33]   Y. Liang, I. M. Chen, L. Chee Kian, Y. Guilin, L. Wei, and L. Kok-Meng, "Experimental investigation on the magnetic field of a permanent magnet spherical actuator," Monterey, CA, USA, 2005, pp. 347-52.

[34]   R. Ueda, H. Takata, S. Nakagaki, and S. Takata, "On the Estimation of Transient State of Power System by Discrete Nonlinear Observer," *IEEE Trans. on Power Apparatus and Systems,* vol. PAS-94, pp. 2135-2140, 1975.

[35]   L. A. Jones and J. H. Lang, "State observer for the permanent-magnet synchronous motor," *IEEE Trans. on Industrial Electronics,* vol. 36, pp. 374-382, 1989.

[36]   R. B. Sepe and J. H. Lang, "Real-time observer-based (adaptive) control of a permanent-magnet synchronous motor without mechanical sensors," *IEEE Trans. on Industry Applications,* vol. 28, pp. 1345-52, 1992.

[37]   J. N. Chiasson and R. T. Novotnak, "Nonlinear speed observer for the PM stepper motor," *IEEE Trans. on Automatic Control,* vol. 38, pp. 1584-1588, 1993.

[38]   A. M. Dabroom and H. K. Khalil, "Output feedback sampled-data control of nonlinear systems using high-gain observers," *IEEE Trans. on Automatic Control,* vol. 46, pp. 1712-1725, 2001.

[39]   G. Zhu, A. Kaddouri, L. A. Dessaint, and O. Akhrif, "A nonlinear state observer for the sensorless control of a permanent-magnet AC machine," *IEEE Trans. on Industrial Electronics,* vol. 48, pp. 1098-1108, 2001.

[40]   K.-M. Lee, Pei. J., "Kinematic Analysis of a Three Degree of Freedom Spherical Wrist Actuator," in *The Figth International Conference on Advanced Robotics*, Italy, 1991.

[41]   K.-M. Lee, Wang, X., "Dynamics Modeling and Control of a Ball-joint-like Variable Reluctance Spherical Motor," in *Proceeding of the 1992 NSK Design and Manufacturing System Grantees Conf.*, Atlanta, 1992.

[42]   Z. Zhou and K.-M. Lee, "High precision torque control of a self magnetically-levitated six-degree-of-freedom variable-reluctance spherical motor," Chicago, IL, USA, 1994, pp. 775-780.

[43]   J. Pei, "Methodology of Design and Analysis of Variable Reluctance Spherical Motor," in *The George W. Woodruff School of Mechanical Engineering*. vol. Ph.D.: Georgia Institute of Technology, 1990.

[44]   R. B. Roth and K.-M. Lee, "Design optimization of a three degrees-of-freedom variable-reluctance spherical wrist motor," *Journal of Engineering for Industry, Transactions of the ASME,* vol. 117, pp. 378-388, 1995.

[45]   K.-M. Lee, Meyouhas, G. and Blenis, R., "Direct Sensing of Three DOF Orientation of a Spherical Wrist Actuator," in *Proc. of the 1993 NSF Design and Manufacturing Systems Conf.*, Charlotte, NC, 1993.

[46]   H. Garner, "Development and Analysis of an Absolute Three Desgree of Freedom Vision Based Orientation Sensor," in *The George W. Woodruff School of Mechanical Eng.* vol. Ph.D Atlanta: Georgia Institute of Technology, 2001.

[47]   R. A. Sosseh, "Finite Element Torque Modeling and Backstepping Control of A Spherical Motor," in *The George W. Woodruff School of Mechanical Eng.* vol. Ph.D Atlanta: Georigia Institute of Technology, 2001.

[48]   Q. Li, "Effects of Adaptive Discretization on Numerical Computation using Meshless Mehtod with Live-object Handling Applications," in *School of Mechanical Engineering.* vol. Ph.D Atlanta: Georgia Institute of Technology, May. 2007.

[49]   K.-M. Lee, H. Son, and J. Joni, "Concept development and design of a spherical wheel motor (SWM)," Barcelona, Spain, 2005, pp. 3652-3657.

[50]   K.-M. Lee and H. Son, "Torque model for design and control of a spherical wheel motor," Monterey, CA, United States, 2005, pp. 335-340.

[51]   K.-M. Lee and H. Son, "Distributed multipole model for design of permanent-magnet-based actuators," *IEEE Transactions on Magnetics,* vol. 43, pp. 3904-3913, 2007.

[52]   K. Lee and K. Park, "Modeling eddy currents with boundary conditions by using Coulomb's law and the method of images," *IEEE Transactions on Magnetics,* vol. 38, pp. 1333-1340, 2002.

[53]   I. Dufour and D. Placko, "Original approach to Eddy current problems through a complex electrical image concept," *IEEE Transactions on Magnetics,* vol. 32, pp. 348-365, 1996.

[54]   Y. Liang, I-M. Chen, C. K. Lim, G. Yang, W. Lin, K-M. Lee, "Experimental Investigation on the Magnetic Field of a Permanent Magnet Spherical Actuator," in *IEEE/ASME AIM2005 Proc.*, 2005, pp. 347-352.

[55]   Y. Liang, "Modeling and Design of a three degree-of-freedom Permanent Magnet Spherical Actuator," in *Mechanical Eng.* vol. Ph.D: Nanyang Technological University, 2005.

[56]   K.-M. Lee, Q. Li, and H. Son, "Effects of numerical formulation on magnetic field computation using meshless methods," *IEEE Transactions on Magnetics,* vol. 42, pp. 2164-2171, 2006.

[57]   N. I. J. P. A. Bastos, "Forces in permanent magnets team workshop problem 23."

[58]   K.-M. Lee, Q. Li, and W. Daley, "Effects of classification methods on color-based feature detection with food processing applications," *IEEE Transactions on Automation Science and Engineering,* vol. 4, pp. 40-51, 2007.

[59]   W. L. Jean-Jacques Slotine, *Applied Nonlinear Control*: Prentice Hall, 1990.

[60]   Keithley Instruments Inc., http://www.keithley.com, 2005.

[61]   W. Singhose, L. Porter, M. Kenison, and E. Kriikku, "Effects of hoisting on the input shaping control of gantry cranes," *Control Engineering Practice,* vol. 8, pp. 1159-1165, 2000.

VITA

Hungsun Son was born in Seoul, South Korea. He received his B.S degree in Aerospace and Mechanical Engineering from Inha University. After finishing his undergraduate, he came to the Unite States of America in 2000. He joined to Stanford University to pursue graduate study and he received M.S. degree in Aero& Astronautical Engineering in 2002. Then, he transferred to Georgia Tech and studied in Aerospace Engineering for a year. From 2003 to 2007, he is a Ph.D candidate in the George W. Woodruff School of Mechanical Engineering.

His research interests in the area of mechatronics include design and control of electromechanical systems, dynamic and vibration analysis and sensing methodology. He received Korea National Scholarship from 2000 to 2002 and he is also a recipient of Who's Who Award for best student in America University and Collage in 2005. Hungsun Son is a student member of IEEE.